

Measurement of CP Violation in

$B^0 \rightarrow J/\psi K_L$ Decays

Sven Einar Vahsen

A DISSERTATION

PRESENTED TO THE FACULTY

OF PRINCETON UNIVERSITY

IN CANDIDACY FOR THE DEGREE

OF DOCTOR OF PHILOSOPHY

RECOMMENDED FOR ACCEPTANCE

BY THE DEPARTMENT OF

PHYSICS

November 2003

UMI Number: 3102228

UMI[®]

UMI Microform 3102228

Copyright 2003 by ProQuest Information and Learning Company.
All rights reserved. This microform edition is protected against
unauthorized copying under Title 17, United States Code.

ProQuest Information and Learning Company
300 North Zeeb Road
P.O. Box 1346
Ann Arbor, MI 48106-1346

© Copyright by Sven Einar Vahsen, 2003.

All rights reserved.

Abstract

We present a measurement of a time-dependent difference between the rate of the weak decay $B_d^0 \rightarrow J/\psi K_L$, and the rate of its charge-parity (CP) conjugate $\overline{B}_d^0 \rightarrow J/\psi K_L$.

In the standard model of particle physics, such CP violation in the weak interactions can be accommodated via the Kobayashi-Maskawa (KM) mechanism, which allows an irreducible complex phase in the weak quark-mixing matrix, which is known as the Cabibbo-Kobayashi-Maskawa (CKM) matrix. This model predicts the measured asymmetry, $A(t)$, to take the form

$$A(t) = \frac{\Gamma_{\overline{B}_d^0 \rightarrow J/\psi K_L} - \Gamma_{B_d^0 \rightarrow J/\psi K_L}}{\Gamma_{\overline{B}_d^0 \rightarrow J/\psi K_L} + \Gamma_{B_d^0 \rightarrow J/\psi K_L}} = -\sin 2\phi_1 \sin(\Delta m_d t), \quad (1)$$

where $\phi_1 = \arg(-V_{cd}V_{cb}^*/V_{td}V_{tb}^*)$ is a convention-independent combination of CKM matrix elements, and Δm_d is the mass difference between the B_d meson mass eigenstates. ϕ_1 , also known as β , can be interpreted as one of the three inner angles of the “CKM Unitarity Triangle” or “Bjorken Triangle,” which is the graphical representation of the unitarity condition

$$V_{ud}V_{ub}^* + V_{cd}V_{cb}^* + V_{td}V_{tb}^* = 0. \quad (2)$$

Using 78 fb^{-1} of e^+e^- collision data, collected with the Belle detector at the KEKB accelerator, we reconstruct 1330 $B^0 \rightarrow J/\psi K_L$ candidates, with an estimated signal purity of $62 \pm 3\%$. Using 1230 of these candidates, we measure

$$\sin 2\phi_1 = 0.77 \pm 0.16 \text{ (statistical)} \pm 0.07 \text{ (systematic)}. \quad (3)$$

$B_d^0 \rightarrow J/\psi K_L$ is one of several B_d^0 meson decays where CP -violating effects have recently been observed. These are the first observations of CP violation outside the neutral K meson system, where it was first discovered almost 40 years ago [1]. At present, all observations of CP violation are consistent with the

KM mechanism.

Acknowledgements

I joined Belle in the spring of 1999, just a few months before the experiment began to take data. It did not take long until hadronic events started to trickle in, and I remember our great excitement when the first potential $B^0 \rightarrow J/\psi K_L$ decays appeared.

The subsequent years of work on the $B^0 \rightarrow J/\psi K_L$ analysis were exciting. Especially the $\sin 2\phi_1$ measurement felt like a bit of an adventure—we were very curious about what we would find. Due to the hard work of several hundred physicists, the experiment performed over all expectation. Soon there were hundreds of signal candidates.

It was a pleasure to meet and work with all the talented and interesting individuals in the KLM and CP -fit groups. The analysis presented in this thesis builds on, and incorporates the work of many. Among them are Kazuo Abe, Kazu Hanagaki, Itaru Higuchi, Kirill Korotushenko, Dan Marlow, Mitsushiro Yamaga, and Masashi Yokoyama, who all worked directly on the $B^0 \rightarrow J/\psi K_L$ analysis. Masashi Hazumi and Yoshihide Sakai coordinated and guided the CP violation measurement efforts at KEK. Tomonobo Tomura and Kazutaka Sumisawa wrote the CP -fitting and vertexing software, and I greatly appreciate their kind assistance on many occasions.

I thank my advisor, Dan Marlow, for his kind and patient guidance during my Belle years. He taught me not only about high-energy physics, but also other lessons, as diverse as stress management and the climbing of radio antennas.

The measurement of $\sin 2\phi_1$ involved a “blind” analysis, where one does not look at the result until the very end. When this is combined with a tight schedule, and frequent updates with new data, the result can be nerve-racking. For the updates, we typically would take data until right before the conferences where our results were shown, in order to keep up with our chief competitors at the BaBar experiment in California. I am thankful for William Trischuck, who was at KEK during several such analysis marathons, and looked out for me.

During the early Princeton years, I enjoyed the fellowship with the other graduate students, especially Justin Albert, although he eventually joined the

enemy. Kirill Korotushenko was my faithful office mate for many years. From behind our terminals in Jadwin 380, we would yell our latest ideas back and forth, or remind each other that it was time for yet another run to the coffee machine. Our many discussions influenced my work, and I used several of his ideas in this thesis. Lately, Alexei Tchouvikov has accompanied me on many a late-night computing session, and generously shared his supply of Russian cookies with me.

Finally, my love goes out to friends and family who supported me when times were tough, many of whom I feel that I somewhat neglected, when there was too much work. My friend Arang deserves special mention for his support during my first year in Princeton. I thank my parents for their love and support, and Claire for her patience, love and understanding.

I would also like to extend my gratitude to Kirk McDonald and Eric Prebys who took good care of me during my first year at Princeton, and Andrew Bazarko, for his careful reading of this thesis.

Contents

| | |
|---|------------|
| Abstract | iii |
| Acknowledgements | v |
| 1 Introduction and Overview | 1 |
| 1.1 Introduction | 1 |
| 1.2 Overview of the Measurement | 2 |
| 2 Historical and Theoretical Background | 6 |
| 2.1 Introduction | 6 |
| 2.2 Symmetries and Invariance Principles | 7 |
| 2.3 Discrete symmetries | 8 |
| 2.3.1 Charge Conjugation | 9 |
| 2.3.2 Parity | 10 |
| 2.3.3 Experimental Developments | 11 |
| 2.4 The Kobayashi Maskawa Mechanism | 15 |
| 2.4.1 Parameter Counting: One Irreducible Phase | 17 |
| 2.4.2 Wolfenstein Parameterization | 19 |
| 2.4.3 Unitarity Triangles | 19 |
| 2.4.4 Measurable CP Violation Requires Interference | 21 |
| 2.5 CP violation in the neutral B Meson System | 23 |
| 2.5.1 CP Violation Purely in the Mixing, a.k.a. “Indirect CP Violation” | 24 |
| 2.5.2 Decay of B_d^0 and \bar{B}_d^0 Mesons into CP Eigenstates | 25 |
| 2.5.3 CP Violation in the Decay Amplitudes, a.k.a. “Direct CP Violation” | 27 |
| 2.5.4 Mixing-induced CP Violation in B Decays, a.k.a. “Interference CP Violation” | 28 |

| | | |
|----------|---|------------|
| 3 | Experimental Considerations | 32 |
| 3.1 | Introduction | 32 |
| 3.2 | The KEKB Accelerator | 33 |
| 3.3 | The Belle Detector | 36 |
| 3.3.1 | Coordinate System | 40 |
| 3.3.2 | Beam Pipe & Silicon Vertex Detector (SVD) | 40 |
| 3.3.3 | Central Drift Chamber (CDC) | 43 |
| 3.3.4 | Aerogel Cherenkov Counter System (ACC) | 48 |
| 3.3.5 | Time of Flight System(TOF) | 51 |
| 3.3.6 | Electromagnetic Calorimeter (ECL) | 55 |
| 3.3.7 | Extreme Forward Calorimeter (EFC) | 58 |
| 3.3.8 | Superconducting Magnet | 59 |
| 3.3.9 | K_L / Muon Detector (KLM) | 60 |
| 3.4 | Trigger & Data Acquisition (DAQ) | 63 |
| 4 | $B^0 \rightarrow J/\psi K_L$ Selection and Background Suppression | 66 |
| 4.1 | Introduction | 66 |
| 4.2 | Hadronic Event Selection | 68 |
| 4.3 | Identifying Good J/ψ Candidates | 71 |
| 4.4 | Identifying Good K_L Candidates | 77 |
| 4.4.1 | KLM candidates | 77 |
| 4.4.2 | ECL-only candidates | 79 |
| 4.4.3 | Additional K_L vetos, and treatment of multiple K_L candidates | 85 |
| 4.5 | $B^0 \rightarrow J/\psi K_L$ Selection | 86 |
| 4.5.1 | The General Principle | 86 |
| 4.5.2 | Exclusive Mode Vetos | 86 |
| 4.5.3 | Inclusive Veto via Likelihood Cut | 88 |
| 4.5.4 | Other Cuts | 93 |
| 4.5.5 | Calculation of p_B^{CMS} | 97 |
| 4.5.6 | Correction for Drift of Beam Energies | 98 |
| 5 | Backgrounds in the Event Sample | 103 |
| 5.1 | Non- J/ψ Background | 104 |
| 5.2 | Non-Upsilon Backgrounds | 108 |
| 5.3 | Backgrounds With a Real J/ψ | 113 |
| 5.4 | Signal and Background With a True K_L ; Verifying Beam Energy Corrections and Monte Carlo Branching Fractions | 117 |
| 5.5 | Background with a fake K_L ; Verifying Monte Carlo Fake Rates | 123 |
| 5.6 | Estimation of Signal and Background Normalizations | 132 |

| | | |
|----------|--|------------|
| 5.7 | Does the $B^0 \rightarrow J/\psi K_L$ Yield Agree with Expectations? | 140 |
| 5.8 | Discussion and Final Consistency Check of Signal and Background Yields | 144 |
| 6 | Measurement of the CP Asymmetry | 157 |
| 6.1 | Flavor Tagging: B_d^0 or \bar{B}_d^0 meson? | 158 |
| 6.1.1 | Flavor Tagging Algorithm | 158 |
| 6.1.2 | Estimating the Wrong Tag Fraction | 161 |
| 6.2 | Vertexing: Where Did the B Mesons Decay? | 163 |
| 6.2.1 | Vertexing Algorithm | 163 |
| 6.2.2 | Response function | 164 |
| 6.3 | Signal and Background Models with Time Dependence | 167 |
| 6.3.1 | $B^0 \rightarrow J/\psi K_L$ Signal PDF | 167 |
| 6.3.2 | Background PDFs | 169 |
| 6.3.3 | Normalizations | 171 |
| 6.3.4 | A Final Check | 174 |
| 6.4 | Fit for the Time Dependent CP Asymmetry | 175 |
| 7 | Systematic Uncertainties | 178 |
| 7.0.1 | Signal purity | 179 |
| 7.0.2 | Vertex Reconstruction | 181 |
| 7.0.3 | Wrong-tag Fractions | 182 |
| 7.0.4 | Resolution Function | 182 |
| 7.0.5 | Possible Fit Bias | 182 |
| 7.0.6 | Δt shape of background | 183 |
| 7.0.7 | Background composition / Individual background modes | 183 |
| 7.0.8 | Physics Parameters | 183 |
| 8 | Discussion of the Result | 184 |
| 8.1 | Relation to Published Belle Measurements | 184 |
| 8.2 | Other measurements of $\sin 2\phi_1$ | 187 |
| 8.3 | Experimental Status of the Unitarity triangle | 188 |
| A | Appendix Theory | 192 |
| A.1 | Neutral B Meson Mixing | 192 |
| A.1.1 | Time Evolution of an Initially Pure Flavor Eigenstate | 196 |
| A.2 | Time Dependent Decay Rates of an Initially Pure Flavor Eigenstates | 197 |
| A.2.1 | Decay into a Flavor Specific Final State | 197 |
| A.2.2 | Decay into a CP Eigenstate, f_{CP} | 199 |

| | |
|---|------------|
| B Appendix Other | 201 |
| B.1 Experimental Data Sample Used | 201 |
| B.2 Monte Carlo Sample Used | 201 |

List of Figures

| | | |
|------|--|----|
| 1.1 | Cartoon of the $e^+e^- \rightarrow \Upsilon(4S) \rightarrow B\bar{B}$ decay | 3 |
| 2.1 | Quark transitions due to emission of a W^- boson are proportional to V_{ij} | 16 |
| 2.2 | The CKM Unitarity Triangle | 20 |
| 2.3 | The rescaled unitarity triangle. | 21 |
| 2.4 | The two weak interaction box diagrams that are expected to dominate the $B_d^0\bar{B}_d^0$ mixing amplitude. | 24 |
| 2.5 | Mixing-induced CP violation. | 27 |
| 2.6 | Tree diagram (top) and penguin diagram (bottom) contributions to the decay $B_d^0 \rightarrow J/\psi K_L$ | 29 |
| 3.1 | KEKB daily and total integrated luminosity versus time | 34 |
| 3.2 | The KEKB accelerator. | 35 |
| 3.3 | The Belle detector. | 38 |
| 3.4 | The ACC, CDC, and TOF subdetectors provide kaon/pion separation in different momentum regions. | 39 |
| 3.5 | Silicon Vertex Detector (SVD) | 41 |
| 3.6 | Geometry of the Central Drift Chamber (CDC). | 43 |
| 3.7 | CDC cell structure | 44 |
| 3.8 | Measured mean of dE/dx versus momentum for different particle species. | 47 |
| 3.9 | Aerogel Cherenkov Counter (ACC) | 48 |
| 3.10 | Barrel and endcap ACC modules. | 49 |
| 3.11 | Time of Flight system (TOF) | 51 |
| 3.12 | Time resolution performance of the Time of Flight System (TOF), measured with μ -pair events | 53 |
| 3.13 | Pion/kaon separation performance of TOF system for hadronic events. Left: Calculated mass of charged tracks with momentum below 1.2 GeV/c. Right: Pion/Kaon separation power. See text for further explanation | 55 |

| | | |
|------|---|-----|
| 3.14 | Geometry of the Electromagnetic Calorimeter. | 56 |
| 3.15 | A single ECL counter. | 56 |
| 3.16 | ECL energy resolution, measured with Bhabha events. | 58 |
| 3.17 | Cross section of an RPC superlayer. | 60 |
| 3.18 | Cut away view of an endcap RPC superlayer module. Dimensions on the figure are in millimeters. | 61 |
| 3.19 | The level-1 trigger system. | 63 |
| 3.20 | The data acquisition (DAQ) system. | 64 |
| 4.1 | Main steps in the selection of $B^0 \rightarrow J/\psi K_L$ events. | 67 |
| 4.2 | R_2 distribution from hadronic event skim. | 72 |
| 4.3 | Invariant mass distribution of $J/\psi \rightarrow l^+l^-$ candidates | 75 |
| 4.4 | K_L candidates are formed by grouping nearby RPC hits | 78 |
| 4.5 | PDFs used to calculate the K_L -likelihood of ECL clusters | 81 |
| 4.6 | Distribution of K_L -likelihood for signal and background. | 83 |
| 4.7 | Observed ΔE distributions for vetoed B decay modes | 87 |
| 4.8 | PDFs used to calculate the $B^0 \rightarrow J/\psi K_L$ - likelihood ratio for KLM candidates. The shaded distributions show signal, the empty distributions show background. | 90 |
| 4.9 | Additional PDFs used to calculate the $B^0 \rightarrow J/\psi K_L$ - like- likelihood ratio for ECL-only candidates. The shaded distributions show signal, the empty distributions show background. | 91 |
| 4.10 | Distributions of the $B^0 \rightarrow J/\psi K_L$ - likelihood ratio for signal and background | 94 |
| 4.11 | Variation of S/B and FOM with $B^0 \rightarrow J/\psi K_L$ - likelihood ratio cut (KLM) | 95 |
| 4.12 | Variation of S/B and FOM with $B^0 \rightarrow J/\psi K_L$ - likelihood ratio cut (ECL) | 96 |
| 4.13 | In the $\Upsilon(4S)$ rest frame, the B meson momentum, p_B^{CMS} , will be constant. | 97 |
| 4.14 | Momentum spectra of observed $B^0 \rightarrow J/\psi K_L$ candidates, before and after correction of p_B^{CMS} | 102 |
| 5.1 | Estimation of real and fake (combinatorial) J/ψ components. | 105 |
| 5.2 | Estimation of combinatorial J/ψ components for $B^0 \rightarrow J/\psi K_L$ candidates from experimental data, with $p_B^{\text{CMS}} < 2.0 \text{ GeV}/c$ | 106 |
| 5.3 | p_B^{CMS} spectrum from off-resonance data (KLM) | 109 |
| 5.4 | p_B^{CMS} spectrum from off-resonance data (ECL) | 109 |
| 5.5 | Estimation of fake J/ψ component in " $B^0 \rightarrow J/\psi K_L$ " candidates from off-resonance data. | 111 |

| | | |
|------|--|-----|
| 5.6 | Venn diagram, background with fake J/ψ 's from non-Upsilon processes | 112 |
| 5.7 | Composition of charmonium inclusive background in Monte Carlo | 114 |
| 5.8 | p_B^{CMS} spectra of $J/\psi K_L$ and $J/\psi K_S$ candidates, Monte Carlo | 118 |
| 5.9 | Predicted and observed signal shape, effect of p_B^{CMS} correction | 121 |
| 5.10 | Predicted and observed p_B^{CMS} shape of background with a true kaon | 122 |
| 5.11 | Effect on the p_B^{CMS} spectrum, when rotating K_L 's around the beam axis | 126 |
| 5.12 | Observed p_B^{CMS} spectra, before and after rotating K_L 's | 127 |
| 5.13 | Predicted and observed p_B^{CMS} spectra, after rotating K_L 's (KLM) | 128 |
| 5.14 | Predicted and observed p_B^{CMS} spectra, after rotating K_L 's (ECL) | 129 |
| 5.15 | p_B^{CMS} shapes used in the yield fit (KLM) | 133 |
| 5.16 | p_B^{CMS} shapes used in the yield fit (ECL) | 134 |
| 5.17 | Fit to determine the signal and background normalizations (KLM) | 135 |
| 5.18 | Fit to determine the signal and background normalizations (ECL) | 136 |
| 5.19 | p_B^{CMS} spectrum of all $B^0 \rightarrow J/\psi K_L$ candidates found in experiment data. | 137 |
| 5.20 | K_L detection efficiency from $e^+e^- \rightarrow \phi\gamma(\phi \rightarrow K_L K_S)$ events | 143 |
| 5.21 | Consistency check using the $B^0 \rightarrow J/\psi K_L$ - likelihood ratio | 150 |
| 5.22 | Consistency check using the J/ψ 's CMS momentum, $p_{J/\psi}^{\text{CMS}}$ | 151 |
| 5.23 | Consistency check using the number of good charged tracks in the event, n_{trk} . | 152 |
| 5.24 | Consistency check using p_B^{CMS} (3-body) | 153 |
| 5.25 | Consistency check using θ_B^{CMS} | 154 |
| 5.26 | Consistency check using $E_{\text{ECL}}/E_{\text{calc}}$ | 155 |
| 5.27 | Consistency check using $R2$ | 156 |
| 6.1 | Schematic overview of the flavor tagging algorithm. | 159 |
| 6.2 | Semileptonic B meson decays via the $b \rightarrow c l \nu$ transition | 160 |
| 6.3 | B meson decays involving the $b \rightarrow c \rightarrow s$ transition | 160 |
| 6.4 | Measured time-dependent asymmetries $A(\Delta t)$ between same-flavor and opposite-flavor events | 162 |
| 6.5 | Distribution of the proper-time interval Δt , from a B -meson lifetime fit | 166 |
| 6.6 | Monte Carlo test of the background model used in the CP fit | 173 |
| 6.7 | Likelihood value, L , versus $\sin 2\phi_1$. | 176 |
| 6.8 | The (Δt) distributions from observed $B^0 \rightarrow J/\psi K_L$ candidates | 176 |
| 6.9 | The time-dependent CP asymmetry, $A(\Delta t)$ from observed $B^0 \rightarrow J/\psi K_L$ candidates | 177 |

| | | |
|-----|---|-----|
| 8.1 | Observed CP asymmetries for different event samples. | 186 |
| 8.2 | Comparison with other experiments | 187 |
| 8.3 | The rescaled unitarity triangle | 188 |
| 8.4 | $\bar{p} - \bar{\eta}$ plane with world-average $\sin 2\phi_1$ superimposed | 191 |
| A.1 | Box diagrams that dominate the $B\bar{B}$ mixing amplitude. | 196 |

List of Tables

| | | |
|------|---|-----|
| 3.1 | KEKB parameters as of October 29th, 2002 | 37 |
| 4.1 | Cross sections of the dominant physics processes at KEKB. | 70 |
| 4.2 | Preselection cuts, to select K_L 's from ECL | 80 |
| 4.3 | Preselection cuts for inclusive mode veto. | 90 |
| 5.1 | Real and fake J/ψ 's among $B^0 \rightarrow J/\psi K_L$ candidates. | 108 |
| 5.2 | Composition of $B^0 \rightarrow J/\psi K_L$ candidates in Monte Carlo (KLM). | 113 |
| 5.3 | Composition of $B^0 \rightarrow J/\psi K_L$ candidates in Monte Carlo (ECL). | 115 |
| 5.4 | Raw yield of K_L -rotated and regular $B^0 \rightarrow J/\psi K_L$ candidates. | 130 |
| 5.5 | Adjusted yield of K_L -rotated and regular $B^0 \rightarrow J/\psi K_L$ candidates. | 130 |
| 5.6 | Fitted yield of $B^0 \rightarrow J/\psi K_L$ signal and background (KLM). | 139 |
| 5.7 | Fitted yield of $B^0 \rightarrow J/\psi K_L$ signal and background (ECL). | 140 |
| 5.8 | Quantities used in predicting the $B^0 \rightarrow J/\psi K_L$ yield. | 141 |
| 5.9 | Observed and predicted yields (KLM). | 145 |
| 5.10 | Observed and predicted yields (ECL). | 145 |
| 6.1 | Wrong tag fractions (w_i) for the different tagging categories | 163 |
| 7.1 | Systematic effects in order of importance | 179 |
| 7.2 | Dependence of $\sin 2\phi_1$ on signal and background normalizations | 180 |
| B.1 | On-resonance data used. | 202 |
| B.2 | Off-resonance data used. | 202 |
| B.3 | Branching fraction of dominant $B^0 \rightarrow J/\psi K_L$ background modes | 203 |

Chapter 1

Introduction and Overview

1.1 Introduction

When CP violation was discovered in 1964 by Fitch and Cronin [1], it dashed all hopes for a perfect symmetry between matter and antimatter. While this was bad news for the lovers of symmetry, it could be good news in general, as we might not be here without it. Sakharov suggested in 1966 [2], that CP violation was a key ingredient in generating a baryon-number asymmetry in the early universe. CP violation may thus be part of the answer to the age-old question: “why is there something rather than nothing?”

That question is, of course, beyond the scope of this thesis. In the next chapters, we shall describe in detail the quantitative measurement of CP violation in the decay of B_d^0 and \overline{B}_d^0 mesons to $J/\psi K_L$ —one out of several final states where CP violation has recently been observed and measured by the Belle and BaBar experiments. These measurements of CP violation in the B system are historic,

because they provide the means to quantitatively test whether the KM scheme—one of the least constrained parts of the standard model—can give a consistent description of CP violation.

The first generation of B -Factory experiments have involved measuring CP asymmetries in decays to CP eigenstates of the form $(c\bar{c})K^0$, for which the expected asymmetry can be cleanly predicted. Among these, $J/\psi K_L$ is of interest because the statistics are large, and because the expected asymmetry has the opposite sign from what is expected in the other feasible decays. It is, however, more of a challenge experimentally. This will all be explained in due course.

A sketch of the historical developments leading up these measurements, and some theoretical background, is given in chapter 2.

1.2 Overview of the Measurement

Since our measurement of time-dependent CP violation in $B^0 \rightarrow J/\psi K_L$ decays consists of many steps, we begin by describing its overall logic.

The measurement was performed at the KEKB accelerator in Tsukuba, Japan. At KEKB, an 8.0 GeV electron beam and a 3.5 GeV positron beam are brought into collision to produce the $\Upsilon(4S)$. The $\Upsilon(4S)$ is an excited bottomonium resonance — a bound state of two b quarks — that decays predominantly into $B_d^0\bar{B}_d^0$ and B^+B^- meson pairs. These B mesons will be almost at rest in the CMS frame ($p_B^{\text{CMS}} \approx 330 \text{ MeV}/c$). Owing to the asymmetry in the beam energies, however, the B mesons receive a boost of $\gamma\beta \approx 0.425$ in the laboratory frame. Both the B_d^0 and B_u^+ lifetimes are $\approx 1.5 \text{ ps}$, allowing the B mesons to travel about

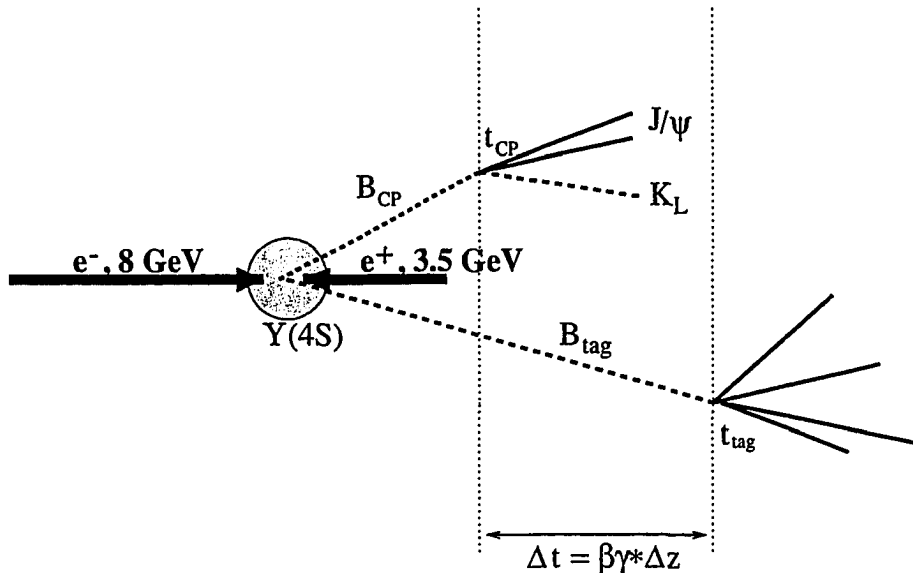


Figure 1.1: Cartoon of the $e^+e^- \rightarrow \Upsilon(4S) \rightarrow B\bar{B}$ decay in the lab frame, illustrating how the time-dependent rates of $B_d^0 \rightarrow J/\psi K_L$ and $\bar{B}_d^0 \rightarrow J/\psi K_L$ are measured.

200 μm in the direction of the electron beam before decaying. Although these decays take place inside the accelerator's beam pipe, the decay vertices can be reconstructed from the charged decay products detected outside the beam pipe, using the Belle detector, described in chapter 3.

We are interested in the case where a neutral B meson, which we call B_{CP} , decays into the CP eigenstate $J/\psi K_L$ at time $t = t_{CP}$. This situation is depicted in figure 1.1. Chapter 4 describes how we select such events from the large number of particle collisions at KEKB. The resulting event sample has a signal purity of $62 \pm 3\%$. We study and discuss the background in chapter 5. In order to obtain the time-dependent rate of $B_d^0 \rightarrow J/\psi K_L$ and $\bar{B}_d^0 \rightarrow J/\psi K_L$ from the candidate events, we also need to distinguish whether B_{CP} was a B_d^0 or \bar{B}_d^0 at some time, which we call t_{tag} , and need to measure the time interval $\Delta t = t_{CP} - t_{tag}$ between

the flavor measurement and the CP eigenstate decay. The flavor measurement is performed by using the other B meson in the pair, which we call B_{tag} . For neutral B pairs from $\Upsilon(4S)$ decays, symmetry considerations constrain the time evolution of the two B 's. Despite flavor oscillations (see appendix A.1), they must remain in states of opposite flavor until one of them decays. This entanglement of the two B mesons, a feature of quantum mechanics that Einstein, Podolsky, and Rosen once deemed a hint of underlying physics [3], is what makes our measurement possible: If we observe the decay of B_{tag} into a final state that reveals its flavor at $t = t_{\text{tag}}$, then we also know the flavor of B_{CP} at that time. Due to the boost of the B mesons in the lab frame, we can also obtain an approximate measurement of Δt from the z -displacement of their decay vertices

$$\Delta t \equiv t_{CP} - t_{\text{tag}} \approx \frac{\Delta z}{\gamma\beta c} = \frac{z_{CP} - z_{\text{tag}}}{\gamma\beta c}. \quad (1.1)$$

We are thus able to measure the proper-time difference distributions; $\Gamma_{\overline{B}_d^0 \rightarrow J/\psi K_L}(\Delta t)$ and $\Gamma_{B_d^0 \rightarrow J/\psi K_L}(\Delta t)$. The Standard Model prediction for these distributions, derived in chapter 2, contains a CP -violating term proportional to $\sin 2\phi_1$:

$$\Gamma(\Delta t)_{B_d^0/\overline{B}_d^0} \propto e^{-\frac{|\Delta t|}{\tau_B}} [1 \pm \sin 2\phi_1 \sin(\Delta m_d \Delta t)]. \quad (1.2)$$

The observed Δt distribution, however, is modified by experimental effects, such as background in the $J/\psi K_L$ sample, assignment of the wrong flavor to B_{tag} , and finite resolution of the vertex measurements. Each of these effects is discussed in chapter 6. We construct a probability density function (PDF) for the experimental Δt distribution that incorporates these effects. We then perform a

minimization procedure, which varies $\sin 2\phi_1$ in this PDF to determine the value that gives best agreement with the observed Δt distributions. The result is

$$\sin 2\phi_1 = 0.77 \pm 0.16 \text{ (statistical)} \pm 0.07 \text{ (systematic)}. \quad (1.3)$$

The statistical error is obtained directly from the fit. The systematic error is estimated by varying parameters of the PDF, and by varying cuts that affect the Δz distribution. This result, its implications, and connections to other measurements, are briefly discussed in chapter 8.

Chapter 2

Historical and Theoretical Background

2.1 Introduction

In this chapter we review selected theoretical and historical topics, so as to put our measurement in a broader context. We begin with a brief introduction to discrete symmetries and invariance principles, and discuss related experimental discoveries in elementary particle physics. We go on to show how CP violation is accommodated in the Standard Model via the Kobayashi-Maskawa (KM) mechanism, and look at some of its predictions for the B meson system. In decays of B mesons into CP eigenstates, such as $B^0 \rightarrow J/\psi K_L$, large CP violation is expected due to interference between mixing and decay. Since the B meson mixing is time dependent, so is the expected CP violation.

A more comprehensive discussion of CP violation in the Standard Model can

be found in the books by Bigi and Sanda [4] or Branco, Lavoura, and Silva [5].

2.2 Symmetries and Invariance Principles

Elementary particle physics aims at finding mathematical laws that govern nature's fundamental constituents and their interactions. We cannot perceive these laws directly, so we make do with deducing them from observations, combined with educated guesses. Symmetries are powerful tools in this regard. The presence or absence of a certain symmetry in the behavior or properties of elementary particles can constrain the allowed mathematical form of the "hidden" laws of nature, and thus provide a glimpse of the yet unknown. In a more practical sense, symmetries have also proven very useful in carrying out particle physics calculations.

What is meant by a symmetry? Let us say that we observe a physical system undergo a certain behavior. Then we can ask: "If we apply a symmetry transformation to the observed behavior, would the transformed behavior be possible in the real world?" An example of a symmetry transformation is time reversal. We can imagine recording the physical system on film.¹ Then we play this film backwards. Is the behavior that we see in the backwards-running film possible for this system? Would it be permitted by the laws of nature? If the answer is yes, no matter what we filmed in the first place, then these laws are invariant under time reversal. If not, then the laws governing the system violate time reversal symmetry. In the case of elementary particles, we often look at the rate

¹This would be a real challenge in the case of elementary particles, but never mind—this is a thought experiment!

of a process, and compare it with the rate of the symmetry-transformed process.

On the theoretical side, the behavior of a system over time is governed by equations of motion. These equations are typically the result of combining force laws or interactions with a kinematic principle. In the current description of elementary particles, quantum field theory, the interaction is contained in the Lagrangian, and the kinematic principle is the minimization of the action. From this we can derive the field equations, which are the equations of motion. Symmetries in the interaction and kinematic principle thus manifest themselves in the set of all possible motions.

2.3 Discrete symmetries

Symmetries of the Lagrangian usually correspond to conserved quantities. As a result, symmetries can also be studied by looking for conservation or non-conservation of these quantities in particle decays.

Symmetry transformations can be classified as continuous or discrete. If a symmetry transformation is continuous, then the conserved quantity is additive. If a symmetry transformation is discrete, then the conserved quantity is multiplicative. An example of a continuous symmetry transformation would be translation in space, which is connected to conservation of momentum. This thesis is concerned with the combined symmetry transformation CP , which is the discrete transformation “parity”, P , followed by the discrete transformation “charge conjugation”, C .

2.3.1 Charge Conjugation

Charge conjugation, C , is the transformation that turns particles into their antiparticles, and vice versa:

$$C|f\rangle = |\bar{f}\rangle \quad \text{and} \quad C|\bar{f}\rangle = |f\rangle, \quad (2.1)$$

where \bar{f} is the antiparticle of f .² C reverses internal quantum numbers such as electrical charge, lepton number and baryon number, but spin and momentum are left unchanged.

Only some states are eigenstates of C , and have well-defined eigenvalues, which are referred to as the C -parity of the state. In a theory where the Lagrangian is invariant under C , C -parity is conserved. Examples of eigenstates under C are flavorless, neutral mesons, i.e. bound states of quark-antiquark pairs. The C -parity of such mesons depends on the total spin, s , and relative angular momentum, l of the two quarks, and is given by $(-1)^{s+l}$. Hence, pseudo-scalar mesons ($s=0, l=0$) have positive C -parity:

$$C|\pi^0\rangle = +1|\pi^0\rangle, \quad (2.2)$$

while vectors mesons ($s=1, l=0$) have negative C -parity:

$$C|J/\psi\rangle = -1|J/\psi\rangle. \quad (2.3)$$

²The most general definition of C includes an arbitrary phase factor in the transformed state, but we choose a convention where this factor is unity. We will do the same for other symmetries, without further comments.

The photon is also an eigenstate of C . Since the electromagnetic field changes sign under reversal of charges, the photon has negative C -parity. Multiple particle states that include a particle and its antiparticle, such as the final state of $B \rightarrow \pi^+\pi^-$, can also be eigenstates of C .

2.3.2 Parity

Parity, P , is the transformation that reverses the direction of the spatial coordinate coordinates, without affecting the time coordinate:

$$P |(t, x, y, z)\rangle = |(t, -x, -y, -z)\rangle. \quad (2.4)$$

Eigenstates of parity will have eigenvalues equal to ± 1 . If parity is a symmetry of the Lagrangian, then this eigenvalue is conserved.

All hadrons are eigenstates of parity, but their parity eigenvalues vary. Quantum field theory tells us that a fermion and its antifermion have opposite parity, while a boson and its antiparticle have the same parity. By convention, quarks are assigned positive parity. The photon is a vector particle, and has negative parity. The parity of a multi-particle state is the product of the parities of the individual components, and the parity of the spatial part of the wave function. If two particles have relative angular momentum l , the parity thus receives an additional factor $(-1)^l$. As a result, pseudo scalar mesons ($l=0, s=0$) and vector mesons ($l=0, s=1$) have negative parity eigenvalues. (In fact this is the whole reason for the names "pseudo scalar" and "vector".)

2.3.3 Experimental Developments

Experimentally, the strong interaction, gravity, and electro-magnetism appear to be invariant under the discrete symmetries. To date, neither C , P , nor T violation has been observed for these interactions.

The weak interaction, however, appears to violate C and P maximally. The history of discrete symmetries and the weak interaction reveals a beautiful interplay between experimental and theoretical physics. It started in the early 1950's with the " τ - θ puzzle". The " θ " decayed into three pions (positive parity), while the " τ " decayed into two pions (negative parity). Until then, P invariance of the weak interaction had been taken for granted. Physicists at the time assumed that the τ and the θ were two different particles with opposite parity, undergoing parity conserving decays. It was puzzling why, except for their parity, these two particles had identical properties. In 1956, Lee and Yang noticed that there was no experimental evidence of parity invariance in the weak interactions [6], and suggested that the τ and θ were really the same particle, but that one decay violated parity. They proposed an experimental test of P invariance of the weak interaction. Just a year later, C.S. Wu *et al.* observed large parity violation in the weak interactions [7]. Today, the ρ and θ are known to be the same particle, namely the K^+ .

It has since been well established that parity violation in the weak interactions is "maximal". Consider the neutrino: P inversion of a left-handed neutrino yields a right-handed neutrino. If the weak interaction were P invariant, one would thus expect equal production of left- and right-handed neutrinos in weak decays.

In 1958, Goldhaber *et al.* measured the helicity of the neutrino, and it turned

out to be purely left handed. In fact, all neutrinos are left-handed. The P conjugate of the left-handed neutrino, a right handed neutrino, is not found in nature. The left-handedness of neutrinos is also C violation, since the C transformation of a left-handed neutrino yields a left-handed antineutrino, which also is not found in nature, either. All anti-neutrinos turned out to be right handed.³

On the theoretical side, when calculating the amplitude of a charged weak current transition involving a lepton and a neutrino, the vertex factor includes the sum of a vector (γ^μ) and an axial vector ($\gamma^\mu\gamma^5$):

$$\frac{-ig_w}{2\sqrt{2}}\gamma^\mu(1 - \gamma^5) \quad (2.5)$$

These two parts transform oppositely under parity, thus giving rise to parity violation in the theory. The factor $(1 - \gamma^5)$ can be interpreted as “projecting out” the left-handed component of whatever it operates on. If this happens to be a right-handed neutrino, the vertex factor vanishes.

Although the weak interaction violates C and P separately, it was for some time assumed to be invariant under the *combined* transformation CP , i.e. parity conjugation followed by charge conjugation. We can see how this is an appealing thought. If both C and P are individually maximally violated, these effects might exactly cancel. In the case of the left handed neutrino, if we apply CP , we get a right handed anti-neutrino, which is observed.

In 1964, however, Christenson, Cronin, Fitch, and Turlay discovered that the

³We assume a massless neutrino in this discussion.

weak interaction can violate CP as well [1]. They observed that a small fraction of K_L mesons decay into $\pi^+\pi^-$. It can be shown that *in the absence of CP violation*, the neutral kaon mass-eigenstates K_L and K_S would be CP eigenstates:

$$|K_S\rangle = \frac{1}{\sqrt{2}} (|K^0\rangle + |\bar{K}^0\rangle), \quad (2.6)$$

$$|K_L\rangle = \frac{1}{\sqrt{2}} (|K^0\rangle - |\bar{K}^0\rangle), \quad (2.7)$$

which makes the K_L purely CP -odd:

$$CP|K_L\rangle = CP\frac{1}{\sqrt{2}} (|K^0\rangle - |\bar{K}^0\rangle) = \frac{1}{\sqrt{2}} (-|\bar{K}^0\rangle + |K^0\rangle) = (-1)K_L \quad (2.8)$$

In a CP invariant theory, K_L cannot decay into $\pi^+\pi^-$, since this is a CP -even final state. The observation of $K_L \rightarrow \pi^+\pi^-$ is thus clear evidence of CP violation. Christenson *et al.* concluded, that the K_L is not a pure CP eigenstate, but has a small ($\epsilon = 2.3 \times 10^{-3}$) CP -even component:

$$|K_L\rangle = \frac{1}{\sqrt{2}} (|K^0\rangle - |\bar{K}^0\rangle) + \epsilon (|K^0\rangle + |\bar{K}^0\rangle). \quad (2.9)$$

The fact that $\epsilon \neq 0$ can be attributed to CP violation in the $K^0\bar{K}^0$ mixing processes, also known as *indirect CP violation*. In principle, $K_L \rightarrow \pi^+\pi^-$ decays could also arise due to a non-vanishing amplitude for the CP -violating decay of a purely CP -odd K_L into two pions. We see that this is possible if the amplitudes for $K^0 \rightarrow \pi^+\pi^-$ and $\bar{K}^0 \rightarrow \pi^+\pi^-$ don't exactly cancel. Such CP violation in the decay amplitudes is also known as *direct CP violation*. The ratio of direct to indirect CP violation in $K_L \rightarrow \pi\pi$ decays is given by $\text{Re}(\epsilon'/\epsilon)$. This parameter

has turned out to be very small, and difficult to measure. Only very recently, in 2001, have experiments at CERN and Fermilab come into agreement regarding its value. The current world average is $\text{Re}(\epsilon'/\epsilon) = 1.8 \times 10^{-3}$ [8]. Indirect CP violation is thus the dominant effect in the K -meson system. One possible explanation is the superweak model [9], which, however, does not predict direct CP violation. Thus, the superweak model either is not the only source of CP violation, or it is incorrect.

In 1973, Kobayashi and Maskawa (KM) proposed an alternative model that attributes CP violation to an irreducible complex phase in the weak-interaction quark mixing matrix [10]. The KM scheme fits naturally into the Standard Model, in the sense that it doesn't require any new interactions. It is an extension of the Cabibbo-GIM scheme, where the quark mass eigenstates are not the same as the weak interaction eigenstates, but instead "rotated" with respect to each other. Looking back, the KM scheme was a bold proposal, as it requires six quarks to violate CP . Only three quarks, u , d , and s , were known at the time. The charm quark was discovered a year later, in 1974, the bottom in 1977, and the top in 1995. The KM scheme generally predicts both indirect and direct CP violation. It is consistent with the magnitude of ϵ . The magnitude of direct CP violation presently cannot be very accurately calculated, as it involves strong interaction phases. Due to this, the measurement of $\text{Re}(\epsilon'/\epsilon)$ cannot now be used to test the KM model.

In 1980, Sanda, Bigi, and Carter showed that KM model could lead to large CP violating effects in decays of B mesons [11] [12]. It turned out that the lifetime and mixing frequency of B meson were just right to measure CP violating effects

using asymmetric e^+e^- colliders operating at the $\Upsilon(4S)$. This led to the proposal for the Belle experiment at KEK, and the BaBar experiment at SLAC.

Today, almost thirty after KM's proposal, the B factories have observed the first CP violating effects outside the neutral kaon system. In the case of B decays into CP eigenstates, such as $J/\psi K_L$, the theoretical prediction is clean. The measured CP violation can thus be related back to a combination of CKM matrix elements. This is an historic moment—the first direct test of a KM prediction of CP violation. Since in the KM model, all CP violation is due to a single complex phase in the CKM matrix, the measured values of $\sin 2\phi_1$, ϵ , as well as the magnitude of CKM matrix elements can all be related back to this phase, to check the consistency of the KM model. This will be explained below. The comparison is shown in chapter 8. At present, all experimental results are consistent with the KM-model. In particular, the measured value of $\sin 2\phi_1$ agrees very well with other constraints on the irreducible complex CKM phase.

2.4 The Kobayashi Maskawa Mechanism

This section follows closely the discussion given [13].

In the Standard Model, the coupling of the W boson to the quarks is given by the following part of the Lagrangian:

$$\mathcal{L}_w = \frac{g}{\sqrt{2}} W^\mu \sum_{\substack{i=u,c,t \\ j=d,s,b}} V_{ij} \bar{i}_L \gamma_\mu j_L + \frac{g}{\sqrt{2}} W^{\mu\dagger} \sum_{\substack{i=u,c,t \\ j=d,s,b}} V_{ij}^* \bar{j}_L \gamma_\mu i_L. \quad (2.10)$$

Here, g is the coupling strength (a real number), W is the W boson field, i_L and

j_L are the left handed projections of the up- and down-type quark fields i and j , respectively (for instance, $j_L = (1 - \gamma^5)j$), and V_{ij} are elements of the CKM matrix

$$V_{\text{CKM}} = \begin{pmatrix} V_{ud} & V_{us} & V_{ub} \\ V_{cd} & V_{cs} & V_{cb} \\ V_{td} & V_{ts} & V_{tb} \end{pmatrix} \quad (2.11)$$

The CKM matrix thus contains nine (complex) coefficients that enter the probability amplitude for transitions from down-type quarks (charge $-1/3e$) to up-type quarks (charge $+2/3e$) under emission of a W^- boson, as shown in figure 2.1 (left). If we take the CP conjugate of this process, shown in figure 2.1 (right), then the W^- is absorbed (goes into the vertex), and the complex conjugate matrix element enters the amplitude instead.

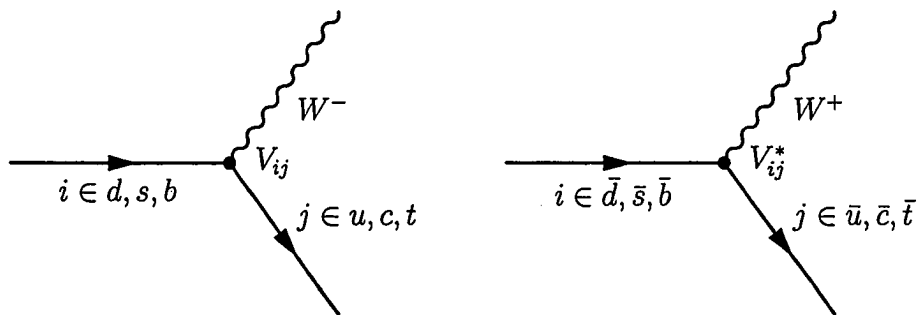


Figure 2.1: In the standard model, the amplitudes for electroweak quark transitions due to emission of a W^- boson are proportional to V_{ij} , while the amplitudes for quark transitions due to absorption of a W^- boson are proportional to V_{ij}^* , where $*$ denotes complex conjugation, and V_{ij} are the elements of the CKM matrix, discussed in the text.

In the standard model, the only constraint on the CKM matrix is that it be unitary. Future theories might predict the values of the individual matrix

elements, V_{ij} , but at present, they are simply parameters of the theory—complex numbers—that must be determined experimentally. If an element has a complex phase, $V_{ij} = |V_{ij}|e^{i\alpha}$ with $\alpha \neq 0$, so that $V_{ij} \neq V_{ij}^*$, then we obtain a different amplitude for a process and its CP conjugate process. But does this necessarily lead to measurable CP violation?

No, not necessarily. First, some phases are merely a matter of phase convention. Only irreducible, convention-independent phases can have measurable consequences. As will be explained below, the 3×3 CKM matrix allows exactly one such phase. Second, phases in quantum theory can only be measured via interference.

2.4.1 Parameter Counting: One Irreducible Phase

How many parameters are needed to determine the unitary 3×3 CKM matrix?

- A complex 3×3 matrix has $2 \times 3 \times 3 = 18$ real parameters. We can think of them as phases and mixing angles, where mixing angles are degrees of freedom that would be present in an orthogonal matrix (a purely real rotation matrix.)
- The unitarity of the matrix imposes relations between these parameters: The sum of the square of the elements in any column must add up to unity. This gives three constraints. Also, any two different column must be orthogonal. There are three such pairs of columns resulting in six additional constraints (both real and negative part of each product must be zero). Unitarity thus imposes nine constraints, so that a unitary 3×3 matrix has

nine real parameters.

- Let's compare the unitary matrix with an orthogonal matrix of the same size. The latter has nine real parameters to begin with. Again, the sum of the square of the elements in any column must add up to unity, giving three constraints. Since the elements are real, the orthogonality of different columns only gives only three constraints this time. Thus the orthogonal 3×3 matrix has three real parameters left.

Comparing the unitary and orthogonal 3×3 matrices, we conclude that the unitary matrix has nine real parameters, out of which three are rotation angles. As a result, the CKM matrix contains a maximum of six complex phases.

Now, the CKM matrix describes the coupling of six quarks. The complex phases of these quarks are a matter of convention. Redefining the phases of a quark does not change the physics, but it does change the phases of the three CKM matrix elements that describe coupling to this quark. One can thus play a game where one redefines the quark phases to remove some of the phases from the CKM matrix. Five phases, corresponding to the five relative phases of the six quarks, can be removed this way, so that *only one phase remains!*

The CKM matrix thus depends on only four parameters; three mixing angles, and a single irreducible phase. If the KM model is correct, then all CP violating phenomena are due to this single, irreducible phase.

The above argument can be repeated for a 2×2 mixing matrix, corresponding to the case of only two quark families. One then finds that the 2×2 matrix depends on a single mixing angle—the Cabibbo angle—and contains no complex

phases. The KM scheme thus needs (at least) six quarks to produce CP violation.

2.4.2 Wolfenstein Parameterization

Based on existing experimental constraints on the magnitudes and relative phases of CKM matrix elements, Wolfenstein introduced an ($\sim 3\%$) approximation to the CKM matrix [14]:

$$V_{CKM} = \begin{pmatrix} V_{ud} & V_{us} & V_{ub} \\ V_{cd} & V_{cs} & V_{cb} \\ V_{td} & V_{ts} & V_{tb} \end{pmatrix} \approx \begin{pmatrix} 1 - \frac{\lambda^2}{2} & \lambda & A\lambda^3(\rho - i\eta) \\ -\lambda & 1 - \frac{\lambda^2}{2} & A\lambda^2 \\ A\lambda^3(1 - \rho - i\eta) & -A\lambda^2 & 1 \end{pmatrix} \quad (2.12)$$

Here, the three rotation angles (λ , A , ρ) and the irreducible complex phase (η) are made explicit.

2.4.3 Unitarity Triangles

We mentioned that unitarity requires the columns of the CKM matrix to be orthogonal. For the first and third columns, the requirement is

$$V_{ud}V_{ub}^* + V_{cd}V_{cb}^* + V_{td}V_{tb}^* = 0, \quad (2.13)$$

which can be visualized as a closed triangle in the complex plane, as shown in figure 2.2. There are additional triangles involving other matrix elements, but this particular one is special because all sides are of similar length, resulting in three relatively large angles. Hence, people usually refer to it as *the* unitarity

triangle. Historically, it is also known as the “Bjorken triangle”. Although phases of the CKM matrix are convention dependent, the inner angles of this triangle are not. They are given by

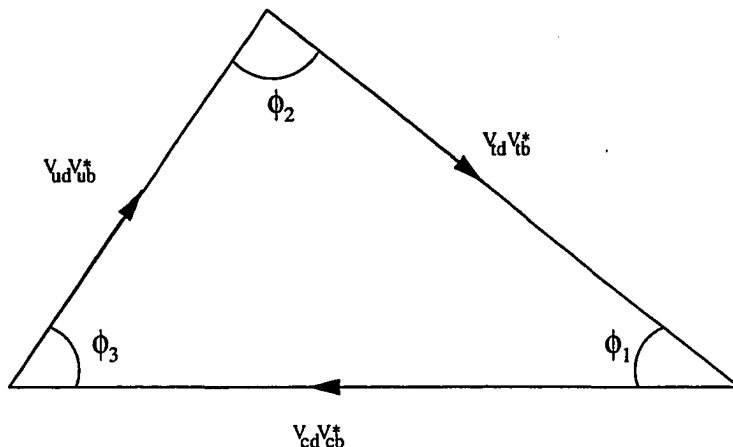


Figure 2.2: The CKM Unitarity Triangle

$$\phi_2 \equiv \alpha \equiv \arg \left(-\frac{V_{td}V_{tb}^*}{V_{ud}V_{ub}^*} \right) \approx \arctan \left(\frac{\eta}{\eta^2 - \rho(1 - \rho)} \right) \quad (2.14)$$

$$\phi_1 \equiv \beta \equiv \arg \left(-\frac{V_{cd}V_{cb}^*}{V_{td}V_{tb}^*} \right) \approx \arctan \left(\frac{\eta}{1 - \rho} \right) \quad (2.15)$$

$$\phi_3 \equiv \gamma \equiv \arg \left(-\frac{V_{ud}V_{ub}^*}{V_{cd}V_{cb}^*} \right) \approx \arctan \left(\frac{\eta}{\rho} \right), \quad (2.16)$$

where the approximations are due to the parameterization by Wolfenstein, given above. Note that ϕ_1 , ϕ_2 , and ϕ_3 all involve couplings to the b quark. The results of B physics experiments at Belle and BaBar, and the consistency of the KM scheme is commonly discussed in terms of this triangle. The work presented in this thesis is a measurement of $\sin 2\phi_1$, and thus directly constrains one angle of

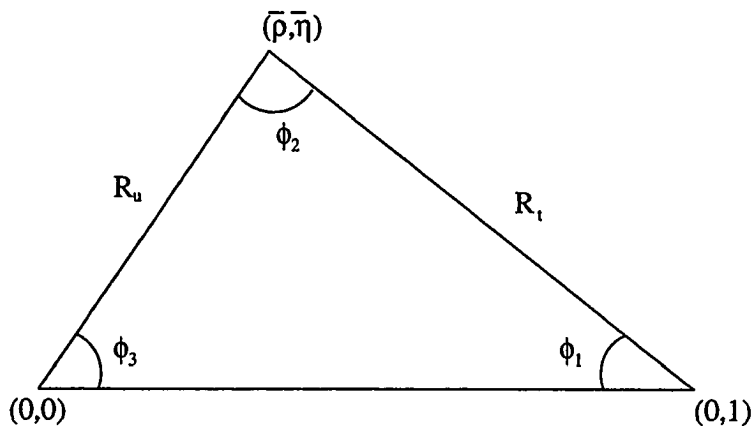


Figure 2.3: The rescaled unitarity triangle.

the unitarity triangle. Often a rescaled version of the unitarity triangle, shown in figure 2.3, is used: One divides all sides by $V_{cd}V_{cb}^*$. This defines the base of the triangle to have unit length, and to lie on the real axis. If we chose the corner with angle ϕ_3 to coincide with the origin of the complex plane, then the apex of the rescaled triangle is located at

$$\frac{V_{ud}V_{ub}^*}{V_{cd}V_{cb}^*} \approx (1 - \lambda^2/2)(\rho + i\eta) \equiv \bar{\rho} + i\bar{\eta}, \quad (2.17)$$

where the approximation is just the result of applying the Wolfenstein parameterization. The experimental status of the unitarity triangle is discussed briefly in chapter 8.

2.4.4 Measurable CP Violation Requires Interference

As noted, the irreducible phase in the CKM matrix can give different amplitudes for a weak transitions and its CP conjugate, since $V_{ij} \rightarrow V_{ij}^*$ under CP conjugation. In order to get measurable CP violation, however, interference between

two or more transitions is needed.

For instance, the amplitude of a weak decay $i \rightarrow f$ described by a single Feynman diagram is in general just a complex number, which for our purposes can be written as

$$A(i \rightarrow f) = A_{if} = |A|e^{i(\phi+\theta)}, \quad (2.18)$$

where we define ϕ to be the CP -odd component of the phase, and θ the CP -even component. The phase ϕ thus contains all phase contributions from CKM matrix elements, and is often called the weak phase. The phase θ is often called the strong phase, since it may contain contributions from strong-interaction rescattering of the final state.

The CP conjugate of $i \rightarrow f$ will be the decay $\bar{i} \rightarrow \bar{f}$, with an amplitude

$$A(\bar{i} \rightarrow \bar{f}) = A_{\bar{i}\bar{f}} = |A|e^{i(-\phi+\theta)}, \quad (2.19)$$

where the weak phase has changed sign. If we were to measure the rates of $i \rightarrow f$ and $\bar{i} \rightarrow \bar{f}$, they would be identical, since the magnitude of both amplitudes is the same.

In cases where more than one Feynman diagram contributes, the total decay amplitude can be written as

$$A(i \rightarrow f) = A_{if} = |A_1|e^{i(+\phi_1+\theta_1)} + |A_2|e^{i(+\phi_2+\theta_2)} \quad \text{and} \quad (2.20)$$

$$A(\bar{i} \rightarrow \bar{f}) = A_{\bar{i}\bar{f}} = |A_1|e^{i(-\phi_1+\theta_1)} + |A_2|e^{i(-\phi_2+\theta_2)}. \quad (2.21)$$

The rates for the two decays are then given by

$$\Gamma \propto A_{i\bar{j}}^2 = |A_1|^2 + |A_2|^2 + \cos(-\Delta\phi + \Delta\theta) \quad \text{and} \quad (2.22)$$

$$\Gamma \propto A_{i\bar{j}}^2 = |A_1|^2 + |A_2|^2 + \cos(\Delta\phi + \Delta\theta), \quad (2.23)$$

where $\Delta\phi = \phi_2 - \phi_1$ and $\Delta\theta = \theta_2 - \theta_1$. This shows that in order to obtain measurable CP violation from the decay amplitudes (this is called “direct” CP violation), there need to be at least two diagrams contributing, and they need to have both different weak and different strong phases. (The weak phase is always needed to produce CP violation, but in some cases that involve meson mixing, we can manage without strong phases.)

2.5 CP violation in the neutral B Meson System

We here look at some KM model predictions of CP violation in the mixing and decay of the B_d^0 and \bar{B}_d^0 meson. We shall distinguish between three types of CP violation: CP violation purely in the mixing, CP violation in the decay amplitudes, and mixing-induced CP violation. These are, of course, all ultimately due to a complex phase in the CKM matrix, but they differ in how the requisite interference is brought about. To preserve the flow of this discussion, explicit derivations have been relegated to the appendix.

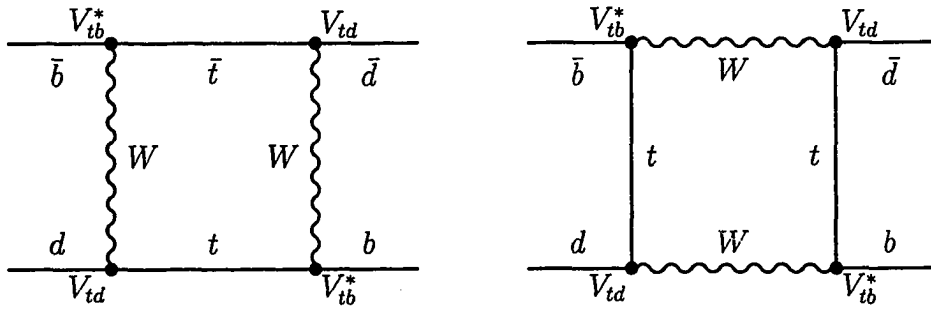


Figure 2.4: The two weak interaction box diagrams that are expected to dominate the $B_d^0 \bar{B}_d^0$ mixing amplitude.

2.5.1 CP Violation Purely in the Mixing, a.k.a. “Indirect CP Violation”

The mass eigenstates and flavor eigenstates of neutral B mesons do not coincide. This can be intuitively understood. The flavor eigenstates B_d^0 and \bar{B}_d^0 are the mesons that contain a pure \bar{b} quark and a pure b quark, respectively. Since the mixing transition $B_d^0 \rightarrow \bar{B}_d^0$ (and vice versa) can occur via the diagrams in figure 2.4, an initially pure flavor eigenstate over time acquires a component along its own anti-particle. A mass eigenstate, however, is by definition a state that evolves in time as:

$$|B(t)\rangle = |B\rangle e^{-imt}, \quad (2.24)$$

where m is the mass of the meson.⁴ Since the flavor eigenstates do not have such a simple time dependence (due to the mixing), they are not the mass eigenstates. Instead, the mass eigenstates B_H and B_L are in general given by a superposition of the flavor eigenstates:

$$|B_H\rangle = p |B_d^0\rangle + q |\bar{B}_d^0\rangle, \quad (2.25)$$

⁴If we include the possibility of decay, then $m \rightarrow \lambda = m - i\Gamma/2$.

$$|B_L\rangle = p|B_d^0\rangle - q|\overline{B}_d^0\rangle. \quad (2.26)$$

It is shown in the appendix, that if there is no CP violation in the mixing processes, then $|q/p| = 1$, and the mass eigenstates are also CP eigenstates. Conversely, if there is CP violation in the mixing, then B_H and B_L are not exactly CP eigenstates, and $|q/p| \neq 1$. Such CP violation in the mixing is also called “indirect” CP violation. It is the same effect as $\epsilon \neq 0$ in the neutral kaon system.

In the standard model, the box diagrams in figure 2.4 are expected to dominate the mixing, and to result only in a phase factor $q/p = e^{i\phi_{\text{mix}}} \approx (V_{tb}^*V_{td})/(V_{tb}V_{td}^*)$. One could measure $|q/p|$ from the asymmetry in wrong flavor B decays, such as wrong sign semileptonic B decays, where the lepton flavor is opposite of what an unmixed B would produce:

$$a_{\text{semileptonic}} = \frac{\Gamma(\overline{B}_d^0 \rightarrow \ell^+ X) - \Gamma(B_d^0 \rightarrow \ell^+ X)}{\Gamma(\overline{B}_d^0 \rightarrow \ell^+ X) + \Gamma(B_d^0 \rightarrow \ell^+ X)} = \frac{|p/q|^2 - |q/p|^2}{|p/q|^2 + |q/p|^2} \quad (2.27)$$

Since the standard model expectation is very small, any appreciable asymmetry here could be an indication of physics beyond the Standard Model.

2.5.2 Decay of B_d^0 and \overline{B}_d^0 Mesons into CP Eigenstates

Despite the expectation that $|q/p| \approx 1$, large CP violating effects are possible in decays of neutral B mesons into CP eigenstates. It is expected that $\Delta\Gamma = 0$. In this case, the time dependent rate for an initially ($t = 0$) pure flavor eigenstate

to decay into a CP eigenstate f_{CP} is given by:

$$\Gamma_{B_d^0}(t) \sim e^{-\Gamma t} \left(1 + |\lambda_f|^2 + [1 - |\lambda_f|^2] \cos \Delta m t - 2\text{Im}\lambda_f \sin(\Delta m t) \right), \quad (2.28)$$

$$\Gamma_{\overline{B}_d^0}(t) \sim e^{-\Gamma t} \left(1 + |\lambda_f|^2 - [1 - |\lambda_f|^2] \cos \Delta m t + 2\text{Im}\lambda_f \sin(\Delta m t) \right), \quad (2.29)$$

where

$$\lambda_f = \frac{q \overline{A}_f}{p A_f}, \quad (2.30)$$

with A_f and \overline{A}_f being the instantaneous amplitudes for the processes $B_d^0 \rightarrow f$ and $\overline{B}_d^0 \rightarrow f$ (i.e. when the mixing is turned off.) We see that the rates for B_d^0 and \overline{B}_d^0 differ in the sign of the coefficient in front of the sine and cosine terms. Hence we can expect CP violating effects if at least one of these coefficients does not vanish. The time dependent CP asymmetry takes a particularly simple form:

$$A(t) = \frac{\Gamma_{\overline{B}_d^0 \rightarrow J/\psi K_L} - \Gamma_{B_d^0 \rightarrow J/\psi K_L}}{\Gamma_{\overline{B}_d^0 \rightarrow J/\psi K_L} + \Gamma_{B_d^0 \rightarrow J/\psi K_L}} = \mathcal{A} \cos(\Delta m_d t) + \mathcal{S} \sin(\Delta m_d t), \quad (2.31)$$

with

$$\mathcal{A} = \frac{|\lambda_f|^2 - 1}{|\lambda_f|^2 + 1} \quad \text{and} \quad \mathcal{S} = \frac{2\text{Im}\lambda_f}{|\lambda_f|^2 + 1}.^5 \quad (2.32)$$

We see that even when $|q/p|=1$, we can still get a CP asymmetry in the following two cases:

- $|\overline{A}_f/A_f| \neq 1$: CP Violation in the decay amplitudes

⁵Note that the BaBar collaboration uses a different sign convention.

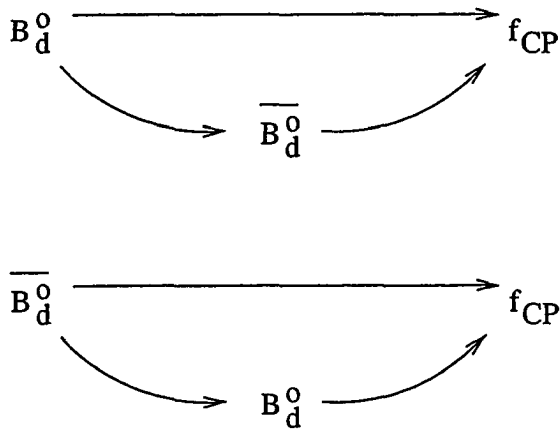


Figure 2.5: Mixing-induced CP violation.

- $\text{Im}\lambda_f \neq 0$: Mixing-induced CP violation.

2.5.3 CP Violation in the Decay Amplitudes, a.k.a. “Direct CP Violation”

We already discussed in section 2.4.4, that $|\overline{A_f}| \neq |A_f|$ occurs when at least two processes (i.e. Feynman diagrams) with different weak and strong phases contribute. This results in different rates for $i \rightarrow f$ and $\bar{i} \rightarrow \bar{f}$, where the initial state i could be either a charged or neutral B meson. In the special case of neutral B decays into CP eigenstates ($f = \bar{f}$), we see from equation 2.28 that $|\overline{A_f}| \neq |A_f|$ furthermore results in a time dependent effect, via the $\cos \Delta mt$ term.

2.5.4 Mixing-induced CP Violation in B Decays, a.k.a. “Interference CP Violation”

CP violation due to $\text{Im}\lambda_f \neq 0$ arises from interference between the direct and mixing-induced transition, as illustrated in figure 2.5. Even in the absence of both direct CP violation (so that $|\overline{A}_f/A_f| = 1$) and CP violation in the mixing (so that $|q/p| = 1$), the terms \overline{A}_f/A_f and q/p can still have different phase factors, which can interfere in a way that cannot be removed by redefining their phases. We can write this out explicitly as

$$\frac{q}{p} = e^{i2\phi_{mix}}, \text{ and } \frac{\overline{A}_f}{A_f} = e^{i2\phi_{decay}}, \quad (2.33)$$

Which gives

$$\lambda_f = \frac{q}{p} \frac{\overline{A}_f}{A_f} = e^{i2(\phi_{mix} + \phi_{decay})} \quad (2.34)$$

$$\rightarrow \text{Im}\lambda_f = \sin 2(\phi_{mix} + \phi_{decay}). \quad (2.35)$$

We see from equation 2.31 that mixing-induced CP violation manifests itself in a time dependent CP asymmetry component of the form $S\sin(\Delta m_d t)$. Particularly useful is the case when mixing-induced CP violation is the only effect. In that case $\mathcal{A} = 0$, and the CP asymmetry becomes purely sinusoidal, with amplitude $\text{Im}\lambda$. This sinusoidal asymmetry vanishes in the time-integrated case if it is measured via $\Upsilon(4S) \rightarrow B_{CP}B_{tag}$ type decays. Time-dependent analysis is thus a crucial component of studying such CP violation at the B factories. We see from equation 2.28 that mixing-induced CP violation also vanishes if the mixing

frequency is slow compared to the B lifetime, i.e. in the limit $\Delta m_d/\Gamma \rightarrow 0$. Nature has been particularly kind—the current world average for this parameter is 0.755 ± 0.015 [8]—which is about as good as one could have hoped for.

Measurements of mixing-induced CP violation provide unique opportunities for the study of the CKM matrix. Note that any strong phases in the decay amplitude cancel out in the ratio \overline{A}_f/A_f . Since $q/p \approx (V_{tb}^*V_{td})/(V_{tb}V_{td}^*)$, the phase $\phi_{mix} + \phi_{decay}$ will thus be a pure combination of CKM matrix phases, that depends on the particular final state f . For some final states, the decay phase can be predicted accurately, thus allowing a direct measurement of CKM phases.

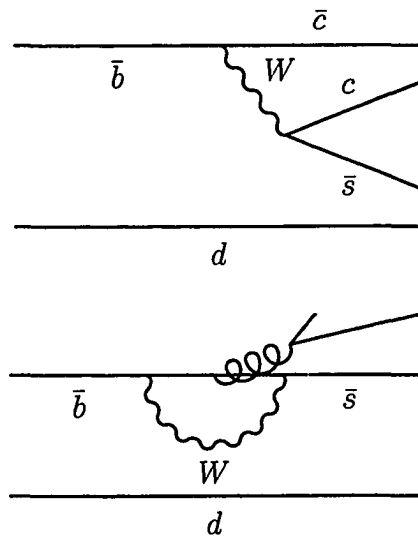


Figure 2.6: Tree diagram (top) and penguin diagram (bottom) contributions to the decay $B_d^0 \rightarrow J/\psi K_L$

The decay $B^0 \rightarrow J/\psi K_L$ et al.

The decay $B_d^0 \rightarrow J/\psi K_0$ proceeds via the quark transition $b \rightarrow c\bar{c}s$, dominated by the Feynman diagram in figure 2.6 (top). The leading order correction comes from the so-called penguin diagram in figure 2.6 (bottom), which has largely the same weak phase as the tree. The only penguin contribution with a different weak phase is suppressed by a factor of λ^2 , with $\lambda \approx 0.22$ being one of the Wolfenstein parameters. As a result, $|\lambda_f| = 1$ is thought to hold at the 1% level for this mode, making it theoretically clean. There are many $B \rightarrow (c\bar{c}) K^0$ decays that probe the $b \rightarrow c\bar{c}s$ transition, and share this cleanliness. However, owing to its large (all is relative) branching fraction and ease of reconstruction, $B \rightarrow J/\psi K_S$ is the experimentally favored among them, earning it the name “gold plated decay”. $B \rightarrow J/\psi K_L$ is more of a challenge experimentally, but particularly important, because its CP asymmetry is opposite to all other experimentally feasible modes. The decay $B^0 \rightarrow J/\psi K_L$ consists of $B^0 \rightarrow J/\psi K^0$, followed by $K^0 \rightarrow K_L$. As a result, we have

$$\lambda_{J/\psi K_L} = \frac{q}{p} \frac{\overline{A_f}}{A_f} = \frac{q}{p} \frac{A_{B_d^0 \rightarrow J/\psi K^0}}{A_{B_d^0 \rightarrow J/\psi K^0}} \frac{A_{K^0 \rightarrow K_L}}{A_{K^0 \rightarrow K_L}} \quad (2.36)$$

$$= \frac{V_{tb}^* V_{td} V_{cs}^* V_{cb} V_{cd}^* V_{cs}}{V_{tb} V_{td}^* V_{cs} V_{cb}^* V_{cd} V_{cs}^*} \quad (2.37)$$

$$= \frac{V_{tb}^* V_{td} V_{cb} V_{cd}^*}{V_{tb} V_{td}^* V_{cb}^* V_{cd}} \quad (2.38)$$

$$\rightarrow \text{Im} \lambda_{J/\psi K_L} = \sin 2 (\text{Arg} V_{tb}^* V_{td} V_{cb} V_{cd}^*) \quad (2.39)$$

$$= \sin 2 \left(\text{Arg} \frac{V_{tb}^* V_{td}}{V_{cb}^* V_{cd}} \right) \equiv -\sin 2\phi_1, \quad (2.40)$$

where ϕ_1 is one of the angles of the unitarity triangle. In the case of $J/\psi K_S$ decays, the term $A_{\bar{K}^0 \rightarrow K_L} / A_{K^0 \rightarrow K_L}$ in equation 2.36 is replaced by $A_{\bar{K}^0 \rightarrow K_S} / A_{K^0 \rightarrow K_S}$, so that the CP asymmetry flips sign.

Chapter 3

Experimental Considerations

3.1 Introduction

The Belle experiment was built to carry out precision studies of B meson decays, in particular to search for CP violation in the B meson system, and to measure the interior angles of the CKM unitarity triangle, ϕ_1 , ϕ_2 , and ϕ_3 . To achieve the first competitive measurement of the “easiest” angle, ϕ_1 , roughly 10^7 B meson decays were needed, while the current measurements with $\approx 10\%$ precision have required $\sim 10^8$ B mesons. The specific B decays probing ϕ_1 have branching fractions of order 10^{-4} . The B decay modes suitable for probing ϕ_2 and ϕ_3 have even smaller branching fractions (10^{-5} and below). In addition, decays with neutral final states, such as $B^0 \rightarrow \pi^0\pi^0$, may be needed to properly interpret these measurements in term of CKM matrix elements. Thus, even larger samples of B meson pairs will be required for accurate measurements of ϕ_2 and ϕ_3 .

The large number of B mesons required for Belle’s CP violation measure-

ments, are provided by the KEK B -factory, an asymmetric e^+e^- collider operating on the $\Upsilon(4S)$ resonance. Nearly 100% of the time, an $\Upsilon(4S)$ decays into a pair of B_d mesons, which about half of the time will be the neutral pair $B^0\bar{B}^0$. The $e^+e^- \rightarrow \Upsilon(4S)$ cross section is ~ 1.1 nb, which means we get roughly 10^6 B meson pairs for each fb^{-1} of data. The KEKB design was quite ambitious, with a design luminosity of $10^{34} \text{ cm}^{-2}\text{s}^{-1}$. KEKB recently achieved this goal. The current peak luminosity is $10.5 \times 10^{33} \text{ cm}^{-2}\text{s}^{-1}$ —the highest achieved by any particle accelerator in history. The integrated luminosity exceeds $150/\text{fb}^{-1}$. Figure 3.1 shows the daily and cumulative integrated luminosity recorded by the Belle detector versus time.

3.2 The KEKB Accelerator

The KEKB accelerator, shown schematically in figure 3.2, is located at KEK, in Tsukuba, Japan. KEK is an abbreviation for the Japanese name “Ko Enerugi Kasokuki Kenkyu Kiko”, which means “High Energy Accelerator Research Organization” [15]. KEKB consists of two separate, 3-km-long storage rings, which hold electron and positron beams at nominal energies of 3.5 and 8.0 GeV, respectively. There is only one interaction point (IP) where the beams cross to induce e^+e^- collisions. Rather than “colliding” head-on, the beams cross at a 22 mrad angle. This is one of the main differences between the design of KEKB, and that of its chief competitor, PEP-II at the Stanford Linear Accelerator Center (SLAC). The crossing angle was intended to prevent parasitic collisions near the IP, when all RF buckets are filled, as well as to avoid synchrotron radiation associated with

Integrated Luminosity (pb^{-1}) (/day)

2003/05/06 07.43

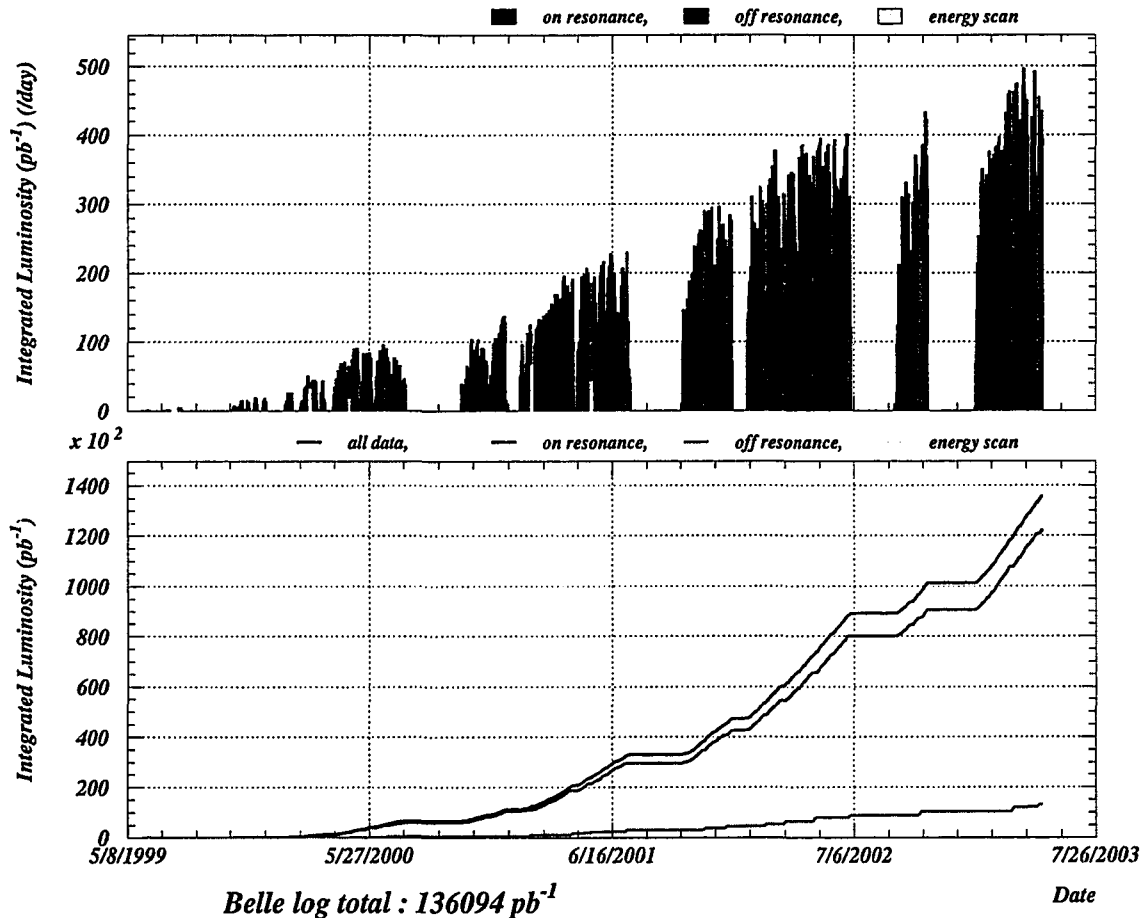


Figure 3.1: KEKB daily (upper) and total (lower) integrated luminosity, as recorded by Belle, versus time.

bending the beams to and away from “head-on” directions. This design strategy appears to have been successful, as KEKB has now surpassed PEP-II in terms of instantaneous luminosity. The parameters of KEKB are given in table 3.1. A brief introduction to accelerator physics, which explains these parameters, can be found in the section “Accelerator Physics of Colliders” in the 2002 PDG [8]. The interaction point is located below ground level in Tsukuba Hall (“Tsukuba Area” on figure 3.2), and surrounded by the Belle detector, which we will describe next.

3.3 The Belle Detector

The Belle detector, shown in figure 3.3, was designed for the precision study of B meson decays. The detector is roughly symmetric in ϕ , with the positron beam as its symmetry axis, while the electron beam comes in at a 22 mrad angle. The detector is backward/forward asymmetric, which maximizes coverage of solid angle in the boosted center-of-mass (CMS) frame. Belle’s combined detector coverage is between polar angles of 17° and 150° .

Belle’s innermost subdetector is the silicon vertex detector (SVD), which surrounds the beam pipe. It is used to measure the decay vertices of B mesons and other short-lived particles. The central drift chamber (CDC), is used for charged particle tracking and momentum measurement, as well particle identification (PID) in the lower momentum range via ionization measurement (dE/dx). The Aerogel Cherenkov Counter (ACC) system, consists of Cherenkov threshold counters situated just outside the drift chamber, providing pion/kaon separation in the momentum range 1.2 to 3.5 GeV/ c . The time of flight detector (TOF), is

| Quantity | Ring | | Units |
|--|--|----------------------|-------------------------------|
| Circumference, C | 3016.26 | | m |
| Luminosity, \mathcal{L} | 8.25×10^{33} (1.0×10^{34}) | | $\text{cm}^{-2}\text{s}^{-1}$ |
| Crossing angle, θ_x | 11 | | mrad |
| Emittance, ϵ_x/ϵ_y | $1.8 \times 10^{-8}/3.6 \times 10^{-10}$ | | m |
| Natural bunch length, σ_z | 0.4 | | cm |
| Number of bunches | 1184 | | |
| Bunch spacing, s_b | 2.4 (0.59) | | m |
| Time between collisions, τ_{coll} | 8 (2) | | ns |
| Moment. compaction factor, α_p | $1 \times 10^{-4} \sim 2 \times 10^{-4}$ | | |
| RF frequency, f_{RF} | 508.887 | | MHz |
| Harmonic number, h | 5120 | | |
| | LER | HER | |
| Energy, E | 3.5 | 8.0 | GeV |
| Energy spread, σ_E | 7.1×10^{-4} | 6.7×10^{-4} | GeV |
| Beam-beam parameters, ξ_x/ξ_y | 0.078/0.049 | 0.074/0.043 | |
| Beta function at IP, β_x^*/β_y^* | 59/0.62 | 63/0.7 | cm |
| Beam Current, I | 1.393 | 0.869 | A |
| Beam Lifetime | 98@1393 | 276@869 | min.@mA |
| Particle/Bunch, N | 3.3×10^{10} | 1.4×10^{10} | |
| Synchrotron tune, ν_s | -0.0225 | -0.0199 | |
| Betatron tune, ν_x/ν_y | 45.513/43.556 | 45.514/41.580 | |
| Energy loss/turn, U_0 | 0.81/1.5 | 3.5 | MeV |
| RF voltage, V_c | 6.6 | 12 | MV |
| Longitudinal dumping time, τ_ϵ | 43/23 | 23 | ms |
| Total beam power, P_b | 2.7/4.5 | 4.0 | MW |
| Radiation power, P_{SR} | 2.1/4.0 | 3.8 | MW |
| HOM power, P_{HOM} | 0.57 | 0.15 | MW |
| Bending radius, ρ | 16.3 | 104.5 | m |
| Length of bending magnet, l_B | 0.915 | 5.86 | m |

Table 3.1: KEKB parameters as of October 29th, 2002, with some design parameters in parenthesis.

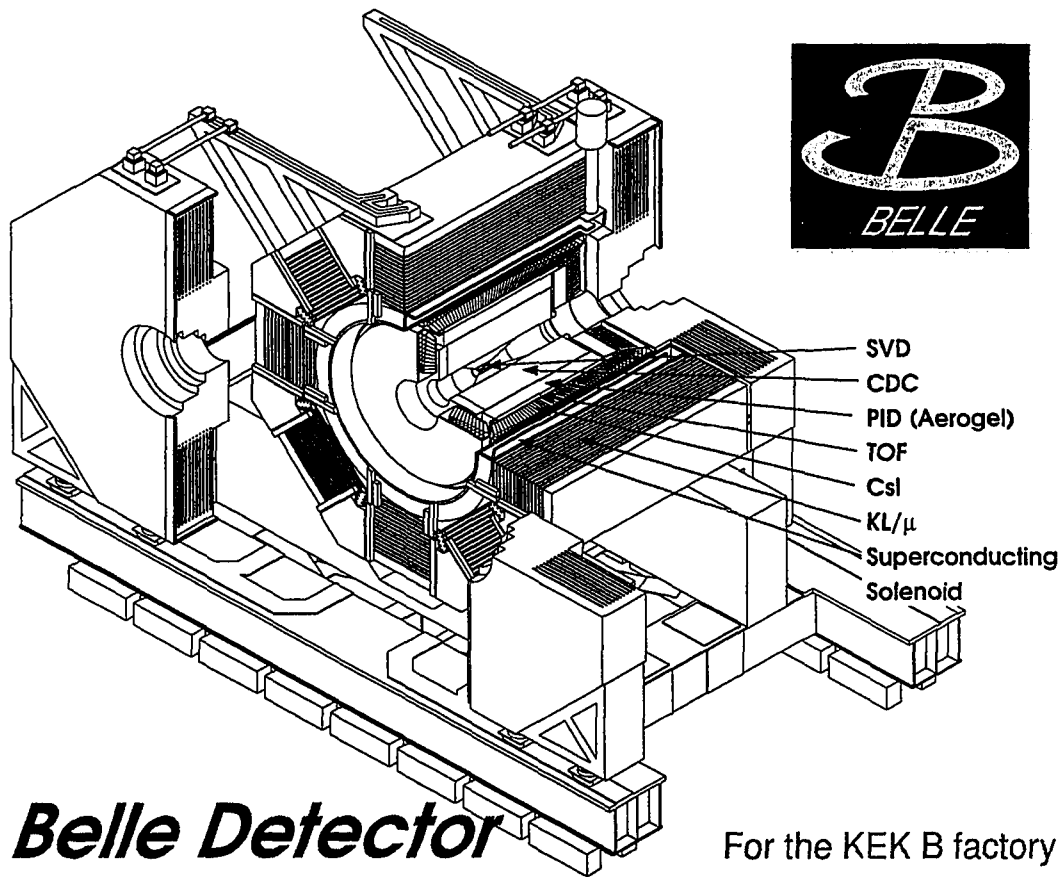


Figure 3.3: The Belle detector.

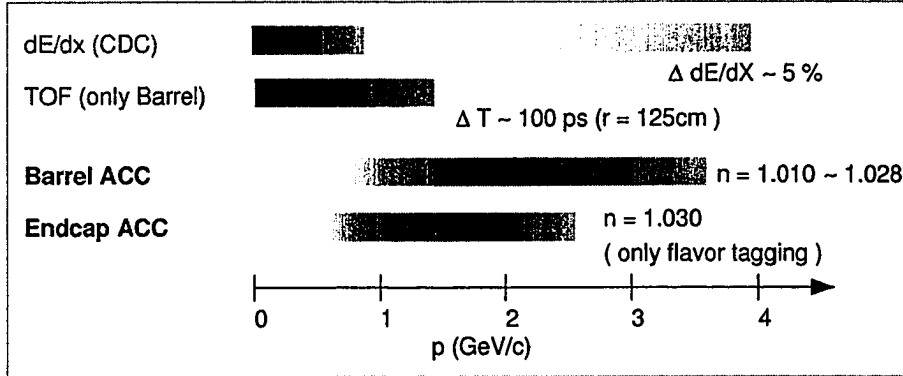


Figure 3.4: The ACC, CDC, and TOF subdetectors provide kaon/pion separation in different momentum regions.

located in the detector barrel only, and provides additional pion/kaon separation in the lower momentum range, $p < 1.2$ GeV/c, where the difference in flight time between pions and kaons can be resolved. Figure 3.4 shows how various subdetectors contribute to kaon/pion separation in different momentum ranges. The electromagnetic calorimeter (ECL), is used to detect photons and identify electrons via their electromagnetic showers. It is the last subdetector inside the magnet. The solenoidal superconducting magnet coil provides a 1.5-T magnetic field parallel to the beam axis. Outside of the magnet, iron layers making up the magnet's flux return are interspersed with resistive plate chambers that form the K_L and muon detection system (KLM). Some of the otherwise uncovered forward and backward polar angle region is covered by the extreme forward calorimeter (EFC).

Below, we will go into more detail for each subdetector, giving a brief description of the physical layout, the main physics principle used in detection, and the performance of each. The readout electronic will in general not be discussed.

For a comprehensive overview of the Belle detector, see [16], which served as the source for most figures and technical details in this chapter.

3.3.1 Coordinate System

The Belle coordinate system is defined so that the z axis points in the opposite direction of the positron beam, and the y axis points up. Since the electrons run clockwise in the accelerator (see figure 3.2), the x axis points horizontally out of the ring.

3.3.2 Beam Pipe & Silicon Vertex Detector (SVD)

The SVD provides decay vertex information, trigger information, and helps with tracking. The SVD is crucial in Belle's measurement of time dependent CP asymmetries, which involve determining the z -vertex displacement of B meson pairs, with resolution on the order of $100 \mu\text{m}$. The SVD is also used to measure the decay vertices of other particles with comparable lifetimes, such as D mesons and τ leptons.

Due to their short lifetime and low transverse momentum, B mesons from $\Upsilon(4S)$ decays at Belle typically only travel transverse distances of $\approx 30 \mu\text{m}$, and decay inside the beam pipe. The position of the decay vertices can nevertheless be reconstructed from the B 's charged decay products that move outside the beampipe, and leave tracks in the drift chamber, and hits in the SVD. These tracks are extrapolated from the CDC back into the SVD, where SVD hits are grouped into clusters, and then associated with the different tracks. Since most

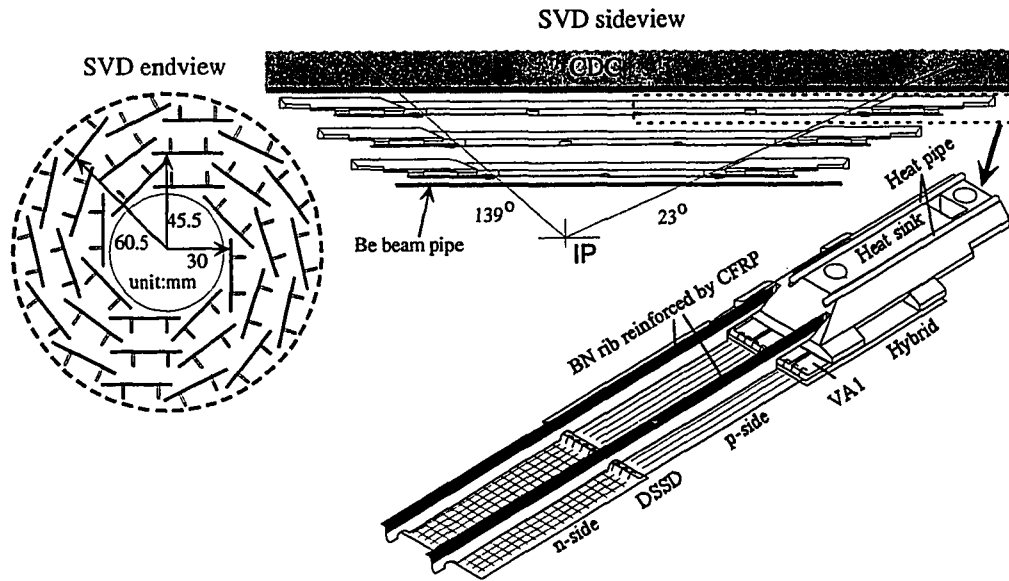


Figure 3.5: Silicon Vertex Detector (SVD)

B decay products of interest are in the momentum range of 1 GeV/ c or lower, the vertex resolution is limited mainly by multiple Coulomb scattering in any material that particles traverse before detection in the SVD. For this reason, the thickness and density of the beam pipe, as well as the mass of the SVD and its support structure, have been minimized. As the vertex resolution decreases with the distance to the first detection layer ($\sigma_z \propto r$), we want the first SVD layer as close as possible to the beam pipe. The designs of the beam pipe and SVD are thus interrelated. The current beam pipe is a double-walled cylinder, with both the inner and outer walls made out of 0.5-mm beryllium. The inner and outer walls have radii of 20 and 23.5 mm, respectively. The beam pipe is cooled by flowing helium gas in the gap between the two walls. The SVD detector is installed around the beam pipe, as shown in figure 3.5. It consists of 102 double sided silicon strip detectors (DSSDs), distributed over three cylindrical layers,

which surround the beam pipe at radial distances of 30, 35.5 and 60.5 mm, and cover the polar angle region $23^\circ < \theta < 139^\circ$. The DSSDs have sense strips on both sides. The strips on one side run in the z direction, while those on the other side are oriented in the r/ϕ direction. The former are called ϕ strips, and their pitch is $25 \mu\text{m}$, but only every second one is read out, while the latter, referred to as z -strips, are $42 \mu\text{m}$, and are read out in pairs. The strips on one side are highly n doped, strips on the other side highly p doped. A bias voltage, typically 80V, is applied to create a depletion region in the lower doped, $300 \mu\text{m}$ thick substrate between the strips. The particular DSSDs used, Hamamatsu S6936, were originally developed for the DELPHI micro-vertex detector, and a more detailed description of the DSSDs can be found in the NIM paper on that detector [17].

Charged particles traversing a DSSD ionize atoms in the depleted substrate, typically creating about 20000 electron-hole pairs. In the depletion region, electron and hole mobility is high, and the subsequent motion of the ionization charge can be read out via the induced image charge on the sense strips. Since this signal will appear only on a few z and ϕ strips, and the radius of the ladder is known, three-dimensional (3D) hit information is thus obtained. The (image) charge is collected via a charge-integrating amplifier. After integration and shaping, the signal is digitized and fed into a clustering algorithm. The probability that a CDC track (excluding K_S 's) within the SVD acceptance is associated with SVD clusters in two layers is higher than 98%. The momentum dependence of the impact parameter resolution is well described by $\theta_{xy} = 19 \oplus 50/(p\beta \sin^{3/2} \theta) \mu\text{m}$ and $\theta_z = 36 \oplus 42/(p\beta \sin^{3/2} \theta) \mu\text{m}$, where \oplus denotes addition in quadrature, and

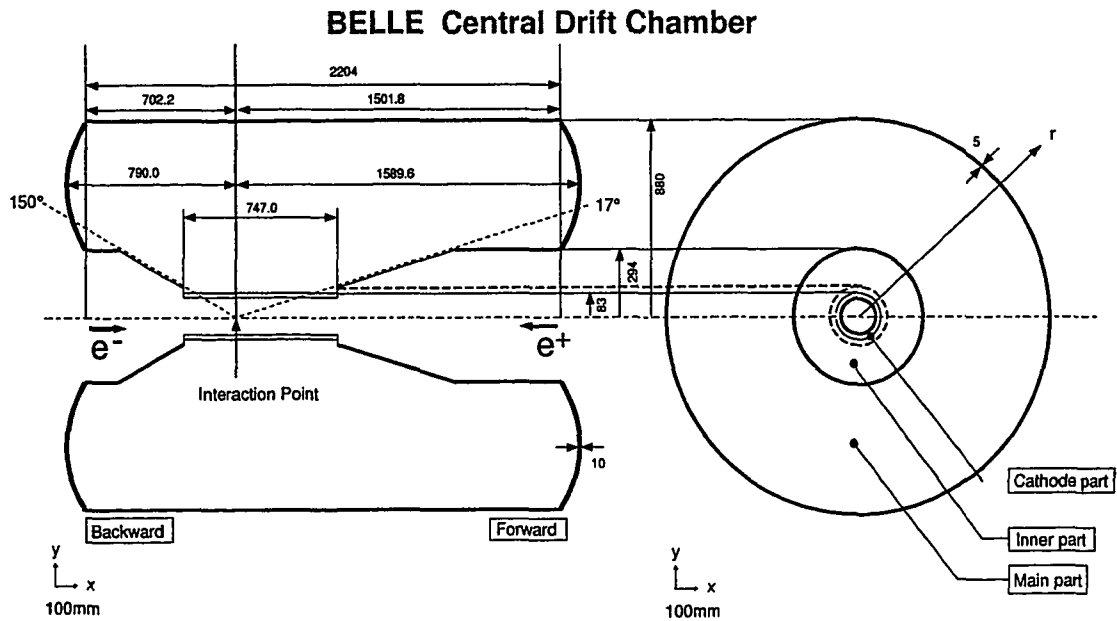


Figure 3.6: Geometry of the Central Drift Chamber (CDC).

the first and second terms are due to detector resolution and multiple scattering, respectively. Additional details on the SVD's performance can be found in [18].

3.3.3 Central Drift Chamber (CDC)

The CDC allows reconstruction and precise momentum measurement of charged tracks, provides trigger information, and helps with PID by measuring dE/dx from ionization.

The CDC geometry is shown in figure 3.6. The cylindrical design provides coverage in the polar angle region $17^\circ < \theta < 150^\circ$. The CDC has three cathode strip layers, and 50 cylindrical wire layers, each consisting of three to six sub layers with radial or stereo wires. The wires add up to 8400 drift cells. The inner- and outer-most stereo layers, together with the cathode strips, provide

BELLE Central Drift Chamber

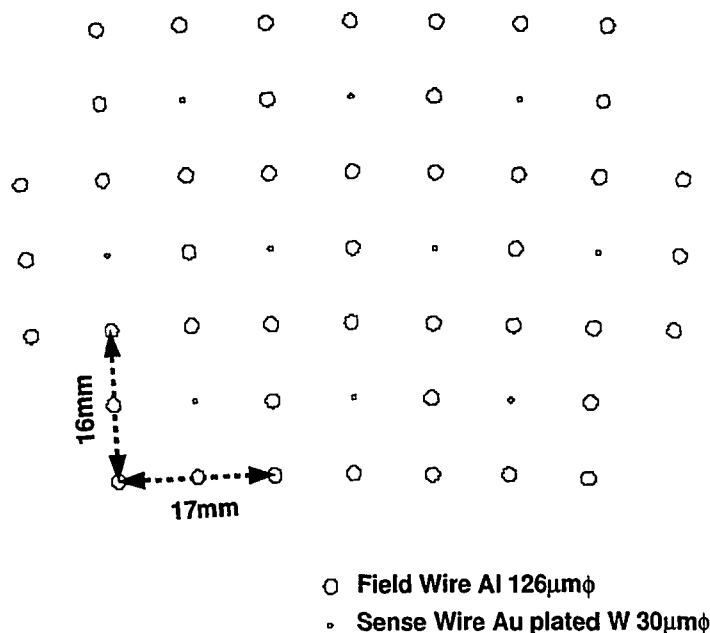


Figure 3.7: CDC cell structure

fast z -trigger information. The chamber is filled with a 50% helium, 50% ethane gas mixture, at a pressure slightly above one atmosphere.

The cell structure of the CDC is shown in figure 3.7. Sense wires of gold plated tungsten with 30 μm diameter, and field wires of unplated aluminum with 126 μm diameter, are used set up an electric field. A positive high voltage, ≈ 2.35 kV, is used for the sense wires, while the field wires and endplates of the drift chamber are kept near ground potential. The voltage on individual sense

wires varies somewhat, to keep the gas gain at the same value, roughly 10^4 , for different cell sizes.

The helium-ethane mixture has low atomic number, which minimizes multiple scattering. Charged tracks passing through the drift chamber ionize gas molecules along their path. The ionized electrons drift towards the sense wires, at a velocity which saturates at $\approx 4 \text{ cm}/\mu\text{s}$, and depends relatively weakly on the electric field strength. Only when the electrons come very close to the sense wires, does their energy become large enough to liberate fresh ions, creating an ionization avalanche with total charge proportional to the gas gain and the amount of primary ionization. The typical charge of this avalanche is thus large enough that when the liberated electrons subsequently drift toward the sense wire, the separation of positive ions and electrons produces a detectable image charge on the sense wires. Both the pulse time and the integrated charge of this signal is read out and used.

The timing ultimately provides position information: Since the drift velocity is roughly constant, the time interval between the event trigger and the sense wire signal, the "drift time," constrains the position of the original ionization seed to lie on a cylinder around the sense wire, with the radius of the cylinder proportional to the drift time. By combining the information from many sense wires, the track trajectory in the x - y plane can be reconstructed. Stereo wires, which run at a small angle with respect to the other wires in the chamber, provide additional z information. The curvature of the track's x - y plane projection in the 1.5-T magnetic field, is used to measure the transverse momentum of the track, as explained in the section on the superconducting magnet, below.

The time integrated charge of the pulse can be used for PID. The most probable amount of ionization charge depends on the passing particle's velocity, $\beta = v/c$, as given by the Bethe-Bloch formula:

$$-dE/dx = \frac{4\pi N_0 z^2 e^4 Z}{mv^2 A} \left[\ln \left(\frac{2mv^2}{I(1-\beta^2)} \right) - \beta^2 \right], \quad (3.1)$$

where m is the electron mass, z and v are the charge and velocity of the particle, e is the electron charge, N_0 is Avogadro's number, Z and A are the atomic number and mass number of the atoms of the gas, x is the path length measured in kgm^{-2} , while I is an effective ionization potential, roughly $10Z$ eV. For low velocities of the incident particle, dE/dx varies as $1/v^2$, while in the ultrarelativistic regime, it increases logarithmically as $\ln \gamma$, where $\gamma = (1 - \beta^2)^{-1/2}$ [19].

The dE/dx measurement is achieved by taking the mean of the ionization charge picked up by the various sense wires along the particle trajectory. Since the ionization charge depends on the particle velocity, and we measure momentum independently (from the trajectory's curvature), dE/dx information helps with PID in the low momentum region, where particles of different masses have a significant difference in velocity at the same momentum. Figure 3.8 shows a scatter plot of dE/dx versus particle momentum, measured in collision data. The different particle species clearly leave different distributions.

Using cosmic rays, the CDC transverse momentum resolution is measured to be $\approx 0.20 p_t\% \oplus 0.29/\beta\%$, where p_t is the transverse momentum measured in GeV/c , the first term is due to detector resolution, and the second due is to multiple scattering. The dE/dx resolution is 6-8%, with the better value for

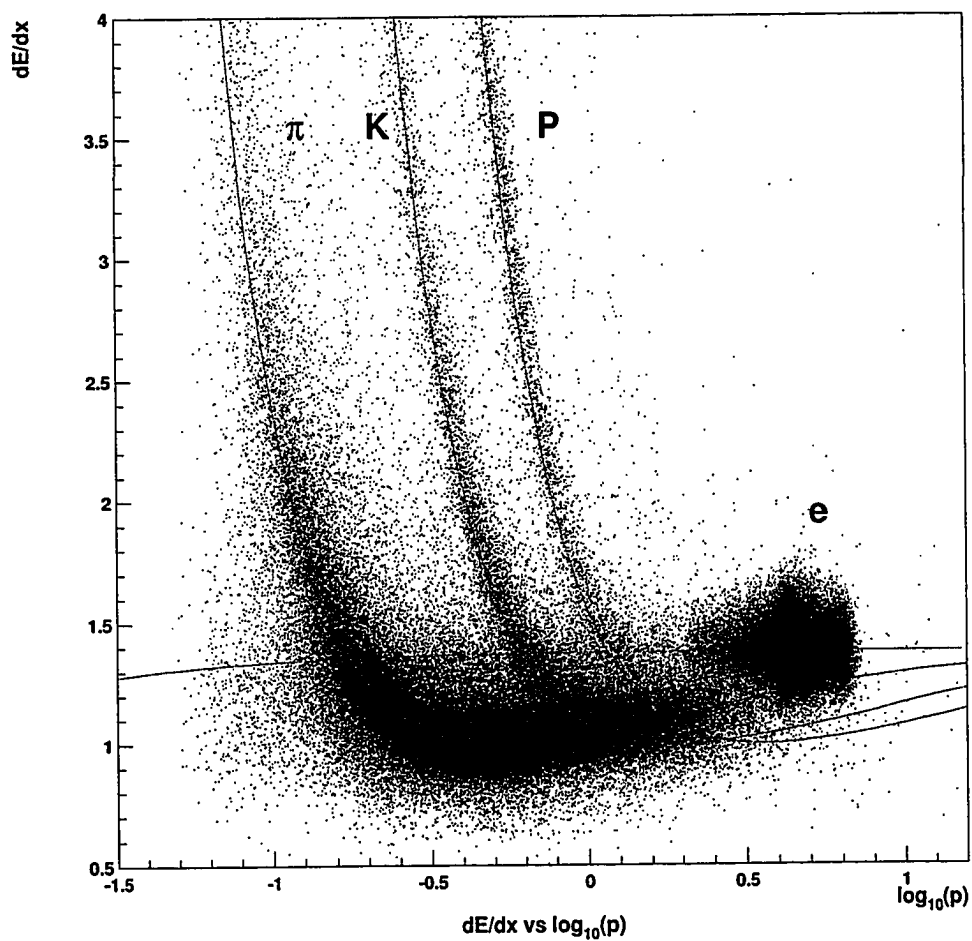


Figure 3.8: Measured mean of dE/dx versus momentum for different particle species. The curves show the expected mean energy loss.

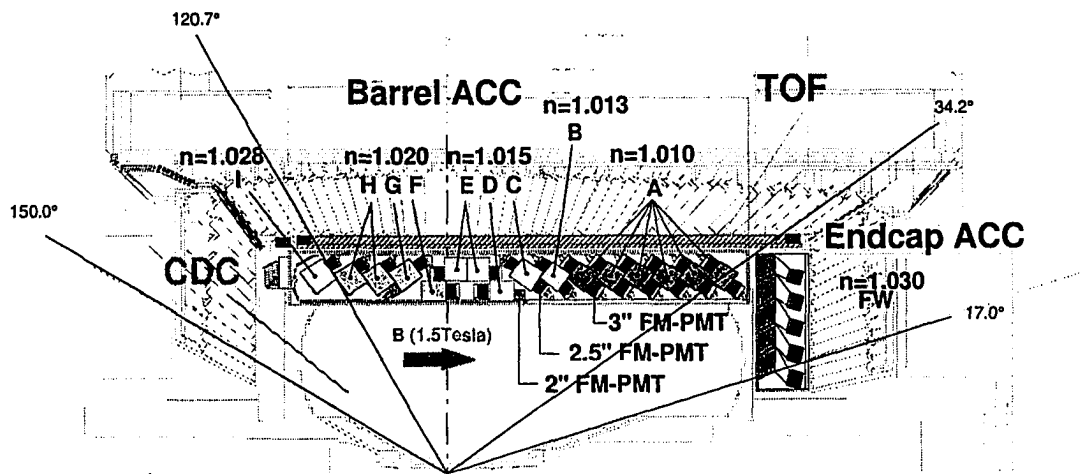


Figure 3.9: Aerogel Cherenkov Counter (ACC)

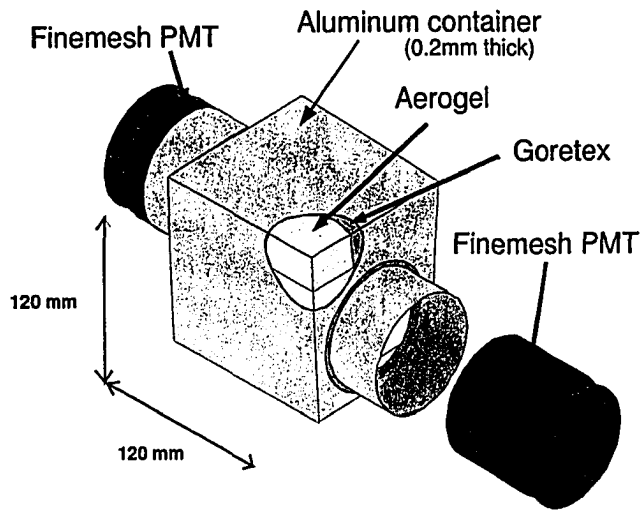
μ pair and Bhabha data, the worse for $K_S \rightarrow \pi^+\pi^-$. Spatial resolution of the tracking is about $130 \mu\text{m}$. Additional details on the CDC and its performance can be found in [20].

3.3.4 Aerogel Cherenkov Counter System (ACC)

The ACC is Belle's main means of pion/kaon separation in the higher momentum ranges, which are not well covered by the TOF system, or dE/dx measurement in the CDC, as shown in figure 3.4. The ACC consists of counter modules situated outside the CDC; 960 modules in the barrel, and 228 in the forward endcap, as shown in figure 3.9.

The modules, shown in figure 3.10, each consist of an aluminum box filled with five stacked aerogel tiles, where aerogel is a silicon based, noncrystalline

a) Barrel ACC Module



b) Endcap ACC Module

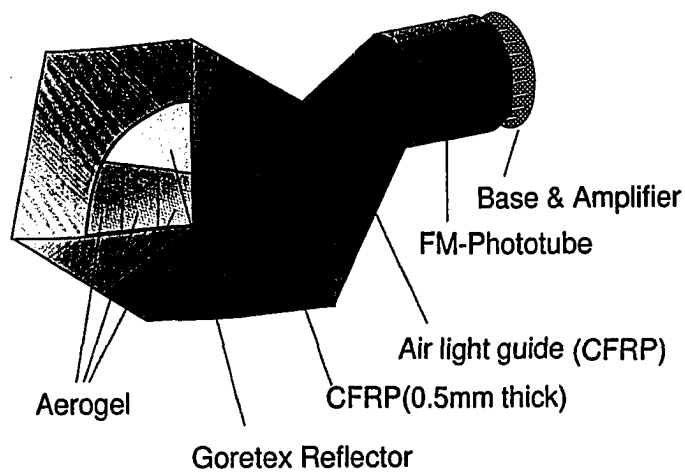


Figure 3.10: Barrel and endcap ACC modules.

solid, with very low density. One or two fine mesh photomultipliers (FM-PMTs) are attached directly to the aerogel at the sides of the box to collect the Cherenkov light, emitted by particles traversing the aerogel.

In general, charged particles traversing a medium will emit a cone of Cherenkov radiation, if the particle's velocity, $\beta = v/c$, exceeds the velocity of light in the medium, $c' = c/n$. The half angle of the Cherenkov cone, θ_c , will in that case be given by

$$\cos \theta_c = \frac{1}{n\beta}. \quad (3.2)$$

For a particle of unit charge, the number of Cherenkov photons emitted per unit path length of the particle and per unit energy interval of the photons is approximately [8]

$$\frac{d^2 N}{dE dx} = 370 \sin^2 \theta_c \text{ eV}^{-1} \text{ cm}^{-1}. \quad (3.3)$$

The Belle ACC is a threshold device, which discriminates between particles of different masses, based on whether the ACC fires or not, but doesn't make use of cone-angle information. If the index of refraction of the Cherenkov device is chosen appropriately, then at a given momentum, the lighter particle will fire the counter, while the heavier particle will move too slowly to do so. Including experimental limitations such as geometrical acceptance and quantum efficiency of the photo tubes, the Belle ACC is able to detect between 10 and 30 photons per particle above threshold (tested with muons), enough to provide good kaon/pion separation up to 3.5 GeV/c.

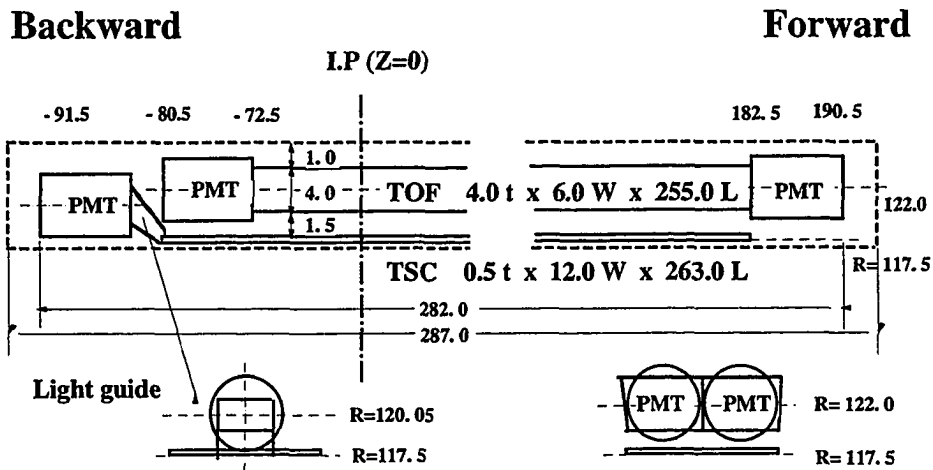


Figure 3.11: Time of Flight system (TOF)

One advantage of aerogel, is that its index of refraction can be varied in the production process. Due to the asymmetric KEKB beams, final state particles emitted at small polar angle tend to have larger momenta than those at large polar angles. Hence, as shown in figure 3.10, the refraction index of the aerogel used in the various ACC counters is varied with polar angle, to allow optimum separation of pions and kaons at all angles. The counters in the forward endcap have instead been optimized for flavor-tagging (see chapter 6.1) via kaons. This involves identifying low-momentum kaons, typically below 1.5 GeV/c, resulting from cascade decays of B_d^0 mesons via the quark level transition $b \rightarrow c \rightarrow s$. More details regarding the ACC can be found in [21].

3.3.5 Time of Flight System(TOF)

The TOF provides pion/kaon separation in the lower momentum region. It is also the subsystem that can deliver the most accurate timing of charged particles, and

thus also provides fast trigger information and timing signals to other subsystems.

The TOF system consists of 64 modules, each containing two ϕ -adjacent TOF counters, separated by a 1.5-cm radial gap from a trigger scintillation counter (TSC), as shown in figure 3.11. The TOF counters consist of $255 \times 6 \times 4$ -cm slabs of "Bicron BC408" plastic scintillator, and are read out on both ends with photo tubes, while the TSC is made out of Bicron BC412 and read out only on one end. The modules are located at a 1.2-m radius, outside the ACC in the detector barrel, as shown in figure 3.9. The TSCs were added to the design to keep the fast trigger rate below the pileup limit of 70 kHz in the presence of beam background. Due to the 1.5-T magnetic field in this region, the 1.5-cm gap between the TOF and TSC counters reduces backgrounds from electron-positron pairs created in the TSC, when the coincidence signal between the TOF and TSC counters is used.

A charged particle traversing a scintillation counter will excite molecules in its path, resulting in the subsequent emission of scintillation photons. In the case of pure organic / plastic scintillator, the scintillation photons would be in the ultraviolet, where attenuation lengths are short, on the order of millimeters [8]. This situation is circumvented by combining the scintillator with fluorescent molecules, which frequency shift the scintillation radiation to the visible, where the material is more transparent. The visible photons from the fluors then travel via internal reflection inside the scintillation counter, until they are read out with PMTs at the ends. Plastic scintillators are fast, with decay times on the order of nanoseconds, and even faster rise times.

In order to achieve good time resolution for the time-of-flight measurement,

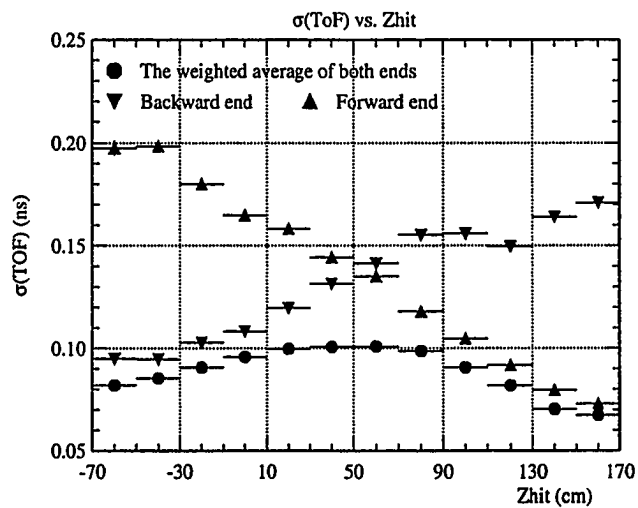


Figure 3.12: Time resolution performance of the Time of Flight System (TOF), measured with μ -pair events

PMTs are mounted directly on the scintillator without intermediate light guides, which would have reduced the timing accuracy, due to dispersion and transit time variations of the detected photons. This puts the PMTs inside the 1.5-T magnetic field region. For this reason we use fine mesh PMTs, which are less sensitive to magnetic fields than standard PMTs. Since the timing accuracy increases with the number of photons detected ($\sigma_t \propto 1/\sqrt{N}$), it is also important to use scintillators with large attenuation length, compared to the maximum photon path length, as well as large-area PMTs, resulting in good photon-collection efficiency.

Figure 3.12 shows the time resolution obtained for muon tracks from μ -pair events, as a function of z . The time resolution of the forward PMT, backward PMT, and of the weighted average are shown. The weighted average time resolution is about 100 ps or better for all values of z .

Figure 3.13 demonstrates the TOF performance for hadronic events. The left plot shows the distribution of (the absolute value of) calculated mass, which is calculated using tracks' pathlength and momentum as measured by the CDC, and the measured time-of-flight. Only tracks with momentum below 1.2 GeV/c have been used. The measurements are shown as data points, while the Monte Carlo expectation, assuming a time resolution of 100 ps, has been superimposed as a solid histogram. Clear peaks for different hadron species can be seen, and the Monte Carlo agrees reasonably well with the data.

The right plot in figure 3.13 shows the TOF system's pion/kaon separation power calculated using the equation on the figure, where μ_π and μ_K are the average flight time measured for pion and kaons, respectively, at a given momentum,

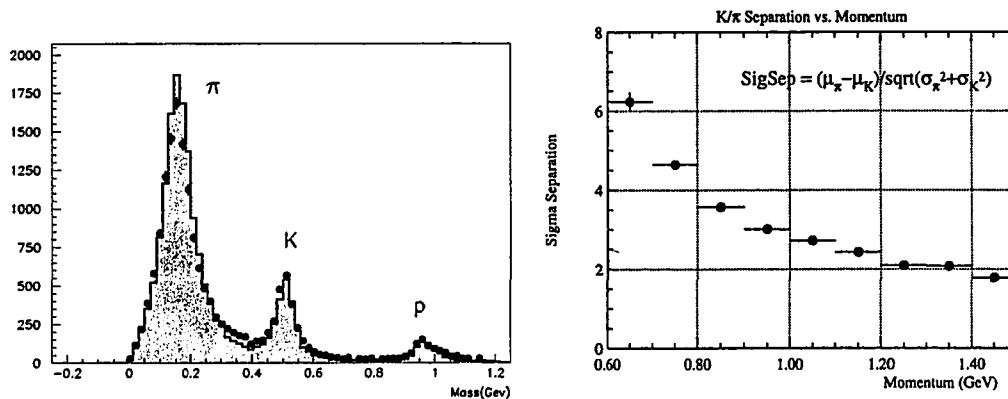


Figure 3.13: Pion/kaon separation performance of TOF system for hadronic events. Left: Calculated mass of charged tracks with momentum below 1.2 GeV/c. Right: Pion/Kaon separation power. See text for further explanation

while the σ 's are the uncertainties of these measurements. Thus the TOF achieves π/K separation $> 2\sigma$ for particle momenta up to 1.25 GeV/c.

3.3.6 Electromagnetic Calorimeter (ECL)

The ECL is designed mainly to detect photons and to identify electrons, but can also be used to detect K_L 's and minimum ionizing particles. The ECL consists of 8736 CSI(Tl) crystals, arranged inside the detector barrel and endcaps as shown in figure 3.14, and covering the polar angle region $17^\circ < \theta < 150^\circ$.

Electrons and photons are detected in crystal calorimeters via electromagnetic showers. Electromagnetic showers are the result of repeated cascades of pair production and brehmstrahlung, producing an exponential increase in the number

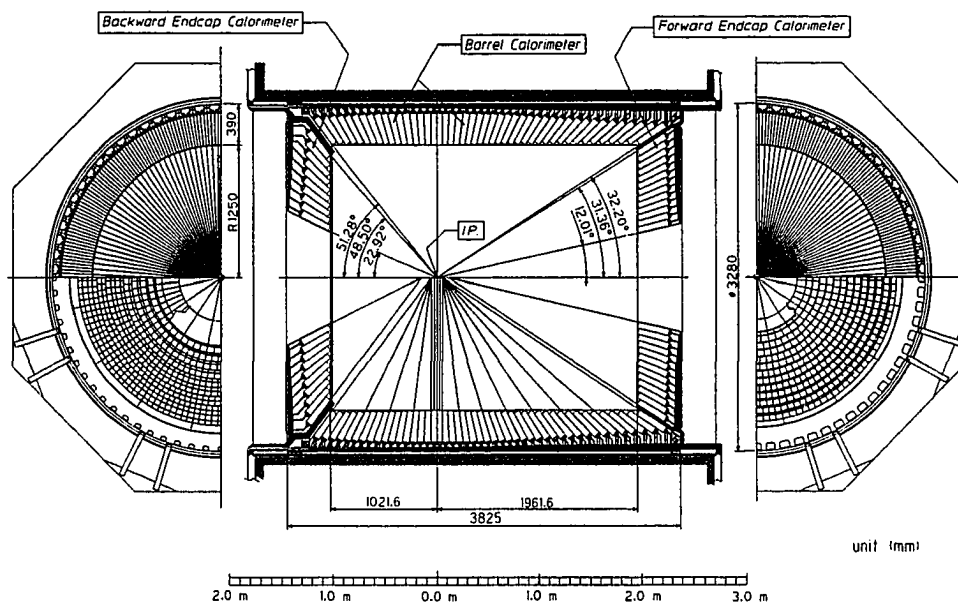


Figure 3.14: Geometry of the Electromagnetic Calorimeter.

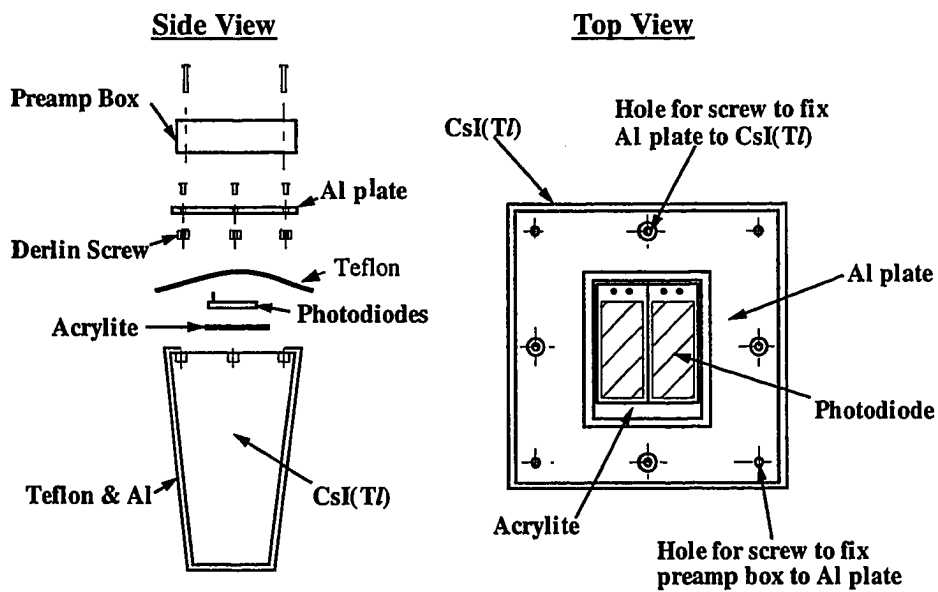


Figure 3.15: A single ECL counter.

of particles, and a corresponding decrease in particle energy until the energy is so low that ionization loss dominates, terminating the shower. Electrons and positrons in all parts of the shower have a certain probability of exciting bands in the crystal lattice that correspond to visible energies, resulting in subsequent emission of visible photons, which are read out via photo detectors. The total light yield is proportional to the combined pathlength of all electrons and positrons in the shower, which is proportional to the incident particle's energy. Electrons and photons typically deposit all their energy in the ECL. For heavier charged particles, on the other hand, brehmstrahlung is negligible, and they mainly leave energy via ionization, roughly 170 MeV for the 30-cm-long crystals. Neutral hadrons can be detected if they undergo inelastic strong interactions in the ECL, resulting in charged decay products, which can then be detected. These hadronic showers tend to be less uniform in their shape than electromagnetic showers.

The individual crystals of the Belle ECL are oriented so that they point almost towards the interaction point, but with a small tilt, to ensure that photons cannot escape through the gaps between crystals. Each crystal has a trapezoidal shape, as shown in figure 3.15. The exact dimensions of individual crystals vary with the polar angle, but their length is always 30 cm, which corresponds to 16.2 radiation lengths for electrons, and 0.8 nuclear interaction lengths for K_L 's. All sides of a crystal, except the side where the readout is attached, are covered with a 200 μm porous Teflon sheet, followed by a 25 μm sheet of aluminum and 25 μm of mylar. The Teflon serves as a diffuse reflector, while the other layers provide optical and electrical insulation. The scintillation light from each crystal is collected using two photodiodes (Hamamatsu S2744-08), attached to the crystal via a 1mm acrylicite

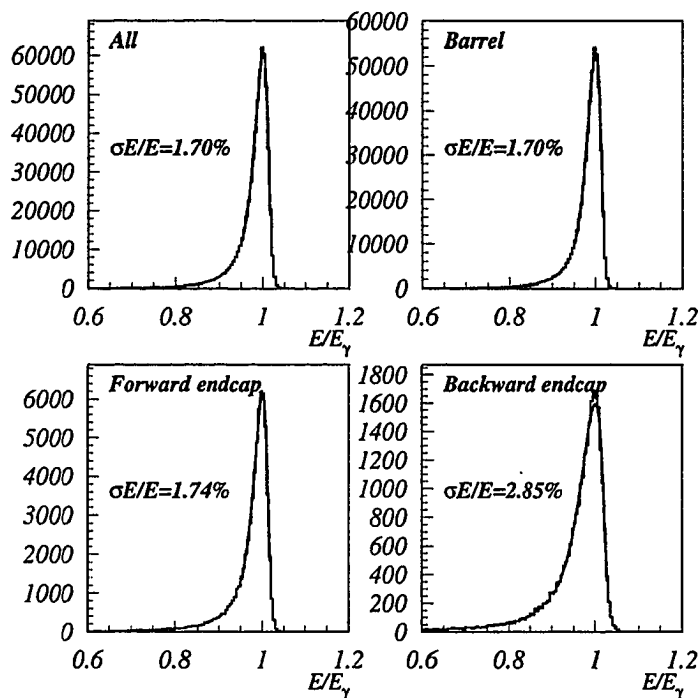


Figure 3.16: ECL energy resolution, measured with Bhabha events.

plate, and read out by charge sensitive preamplifiers.

After the commissioning of KEKB, the ECL energy measurement was calibrated counter by counter, using a large sample of Bhabha events, for which the electron energy is known as a function of the detection angle. The resulting energy resolution is shown in figure 3.16.

3.3.7 Extreme Forward Calorimeter (EFC)

The EFC consists of radiation hard Bismuth Germanate crystals. It is attached to the cryostats of the superconducting compensation solenoid magnets, which surround the beam pipe outside the interaction point in the forward and backward

region. The EFC extends the coverage of the ECL to the polar angle regions 6.5° to 11.5° and 163.3° to 171.2° . The EFC is used as a beam and luminosity monitor, as well as an effective shield from backgrounds for the central drift chamber.

3.3.8 Superconducting Magnet

The superconducting magnet, which encloses all of the abovementioned subdetectors, provides a 1.5-T axial magnetic field. The superconducting magnet coil is supported by a surrounding aluminum cylinder of 3.4-m diameter, and is cooled with liquid helium.

The axial magnetic field causes a charged particle to travel in a helix, with the x - y projections of its trajectory being a circle of radius R , related to the field B by

$$R = \frac{cp_T}{qB}, \quad (3.4)$$

where q is the charge of the particle, p_T is the particle's transverse momentum, and c is the speed of light, all in SI units. With units more useful in high energy physics, p_T measured in GeV/ c , and q in multiples of the electron charge, this becomes

$$R = \frac{p_T}{0.3qB} \quad (3.5)$$

Thus, we can determine a charged particle's momentum from the curvature of its trajectory in the drift chamber. Furthermore, we can tell the sign of the particle's charge from the direction that it curves.

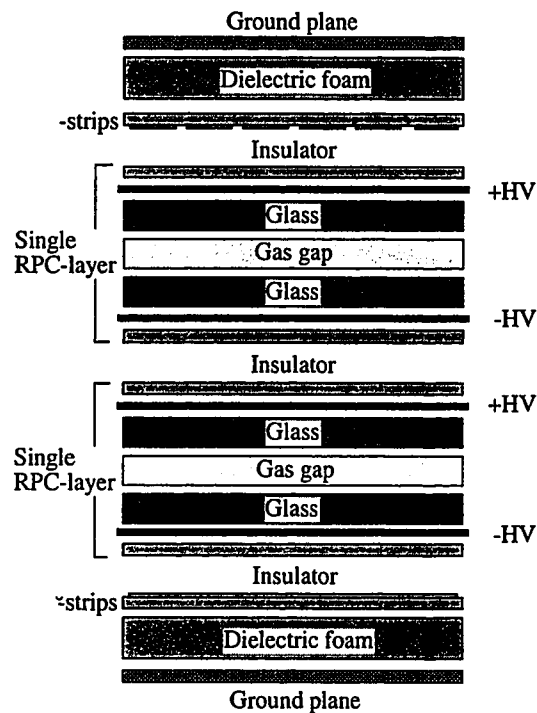


Figure 3.17: Cross section of an RPC superlayer.

3.3.9 K_L / Muon Detector (KLM)

As the name suggest, the KLM is used to identify K_L 's and muons. Located outside the magnet coil in the barrel and both endcaps, it is the last subdetector that particles encounter before leaving the detector. The KLM consists of 14 (barrel) or 15 (endcap) superlayers of Resistive Plate Chambers (RPCs), sandwiched between 4.7-cm-thick iron plates. The iron plates serve as the magnet's flux return, to induce hadronic interaction of K_L 's, and to differentiate between charged hadrons and muons based on their penetration depth and deflection in the KLM. The KLM as a whole covers the polar angle region from 20° to 155° ,

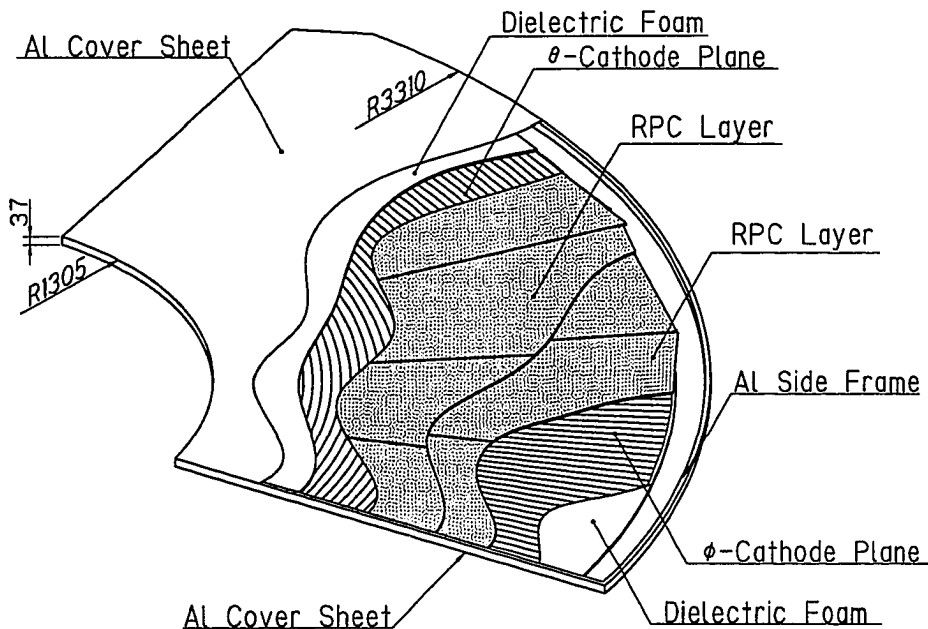


Figure 3.18: Cut away view of an endcap RPC superlayer module. Dimensions on the figure are in millimeters.

with the barrel detector covering 45° through 125° .

The RPCs used in the endcap and barrel differ somewhat in their detailed construction, but the operating principle is the same. We shall here describe the barrel detector. Each RPC superlayer contains two RPC layers, as shown in figure 3.17. Each single RPC layer consists of two glass plates, coated with conductive ink. In between the glass plates, there is a 1.9-mm gap, filled with an HFC/argon/butane gas mixture. A high voltage, typically 8000 V, is connected to conducting ink layers, which charge up the glass plates. Charged particles crossing the RPC leave a trail of ionization in the gas. This may result in a localized amount of surface charge on the glass plates discharging across the ionization trail. The image charge of this discharge is then picked up and read out via ≈ 5 -cm-wide copper pickup strips, located outside the RPCs. The pickup

strips on one side run in the z direction, while the strips on the other side run in r - ϕ direction, so that 3D information is obtained. The high resistivity of the glass ensures that the discharge will be localized to a small area in the glass plate. Even though this small area will be inactive until the charge is replenished from the conductive ink, the rest of detector area remains active during this time. Each single layer RPC typically has a detection efficiency $\approx 90\%$ for charged tracks. Since two layers are read out together via one pair of pickup strips, however, we are effectively using the “logical or” of the two layers, resulting in average efficiencies above 98%.

The RPCs thus provide 3D information on the trajectory of charged tracks in the KLM detector. Using this information, charged tracks detected in the CDC are identified as muons based on their penetration depth into the KLM, and the deviation from their expected trajectory in the KLM. Muon identification efficiency above 1.5 GeV/ c exceeds 90%, with a fake rate (from pions and kaons) of less than 5%.

The iron plates in the KLM provide a total of 3.9 interaction lengths for K_L 's traveling normal to the detector planes. If a K_L undergoes inelastic nuclear scattering in an iron layer, charged decay products can result in hits in the following RPC's. K_L 's are thus identified as clusters of RPC hits without associated charged tracks in the drift chamber, as described further in section 4.4. The K_L detection efficiency in data has been studied using $e^+e^- \rightarrow \gamma\phi(K_L K_S)$ events, where it was found to be 50% for K_L 's detected in the KLM, and 65% when the ECL is used in combination with KLM detector [22]. For more information on the KLM detector, see [23].

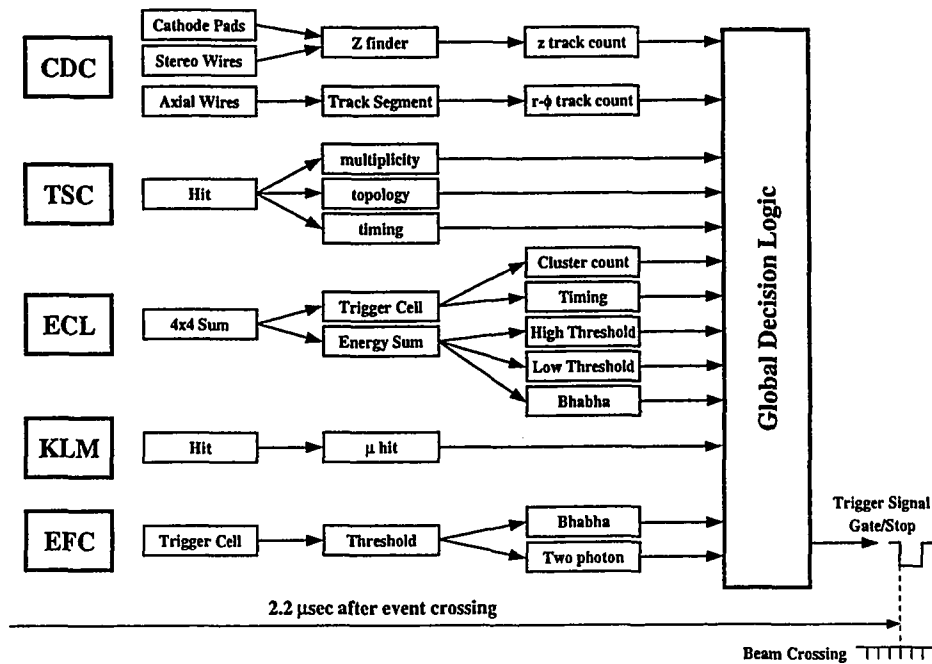


Figure 3.19: The level-1 trigger system.

3.4 Trigger & Data Acquisition (DAQ)

At KEKB's design luminosity, $10^{34} \text{ cm}^{-2}\text{s}^{-1}$, electron and positron beam bunches are spaced 60 cm apart, resulting in bunch crossings at the interaction point at a rate of about 500 MHz. During most bunch crossings, nothing happens, i.e. no e^+e^- collisions take place. As can be seen from the cross sections given in table 4.1, should a collision occur, the most probable outcome is Bhabha scattering—i.e. an electron and positron simply bounce off each other elastically. Only very rarely, $\sigma = 4.4 \text{ nb}$ (44 Hz at design luminosity), do we get $e^+e^- \rightarrow q\bar{q}$ processes, and only one out of four of these will be an $e^+e^- \rightarrow b\bar{b} \rightarrow \Upsilon(4S)$ event, which is what we are really interested in. Since we are operating at high beam currents, beam gas interactions are also quite likely.

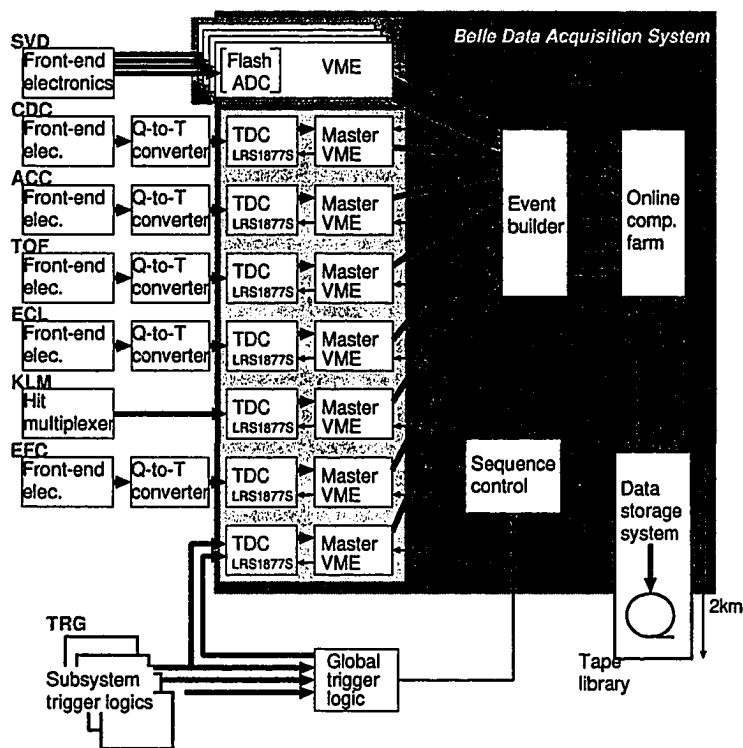


Figure 3.20: The data acquisition (DAQ) system.

The purpose of the trigger, then, is to identify bunch crossings during which a collision took place, and to determine whether this collision is of an “interesting” type, which in practice means whether all subdetectors should be read out, and whether the resulting information should be written to disk or not.

The Belle trigger system consists of the level-0 and level-1 hardware trigger, and level-3 and level-4 software triggers. The hardware trigger system is synchronized to the accelerator RF. It relies extensively on pipelined, programmable logic, providing flexible trigger options for varying beam conditions, yet retaining the low latencies associated with hardware. The level-1 system is shown in figure 3.19. The hardware triggers of the various subdetectors evaluate an event

in parallel, and provide their individual trigger decisions within $1.85 \mu\text{s}$. The subdetector triggers are fed into a Global Decision Logic (GDL) circuit, which classifies events into various types, and provides the final trigger signal $2.2 \mu\text{s}$ after the bunch crossing. Information from the SVD is presently not used by the GDL. The SVD receives a level-0 trigger signal from the TOF trigger.

Because of their large cross sections relative to $B\bar{B}$ production, Bhabha and two-photon events are prescaled at the level-1 trigger level by a factor of $1/100$. At the current luminosities, the result is a typical level-1 trigger rate of 200 Hz, with somewhat less than half due to physics processes, and the rest due to beam-related backgrounds.

A schematic of the Belle Data Acquisition (DAQ) system is shown in figure 3.20. Upon receipt of a level-1 trigger signal, the sequence control starts the data acquisition, which involves digitizing the various subdetector outputs in parallel within $200 \mu\text{s}$. The output from most subdetectors is converted from charge to timing signals before digitization, allowing a streamlined readout system. The information from the subdetectors is subsequently combined by the event builder, and then transferred to the online computer farm, which is near the detector in the Belle control room. Here, further event rate reduction (level-3 trigger) can be applied based on a fast reconstruction algorithm. Events are then sent via optical fibers to the mass storage system, located 2 km away in the KEK computer center. A final event rate reduction (level-4 trigger) is applied offline, and mainly removes beam gas events based on a fast tracking algorithm. Events passing this trigger are classified as physics events. They are fully reconstructed, and written to data summary tapes (DSTs).

Chapter 4

$B^0 \rightarrow J/\psi K_L$ Selection and Background Suppression

4.1 Introduction

This chapter explains how $B^0 \rightarrow J/\psi K_L$ candidates are selected from the large number of reconstructed Belle events. The various selection requirements, referred to as “cuts” in experimental high energy physics, are summarized in figure 4.1. Steps upstream of the hadronic event selection, such as triggers and data acquisition, were already discussed in chapter 3.

The decay $B^0 \rightarrow J/\psi K_L$ poses a special challenge among the $B_d^0 \rightarrow c\bar{c} K^0$ decays used to measure $\sin 2\phi_1$, in that the K_L 's energy cannot be measured. Due to this lack of kinematic information, signal and background cannot be very well separated. As a consequence, the particular background fraction that optimizes the statistical sensitivity to $\sin 2\phi_1$ is rather high, currently $38 \pm 3\%$. For

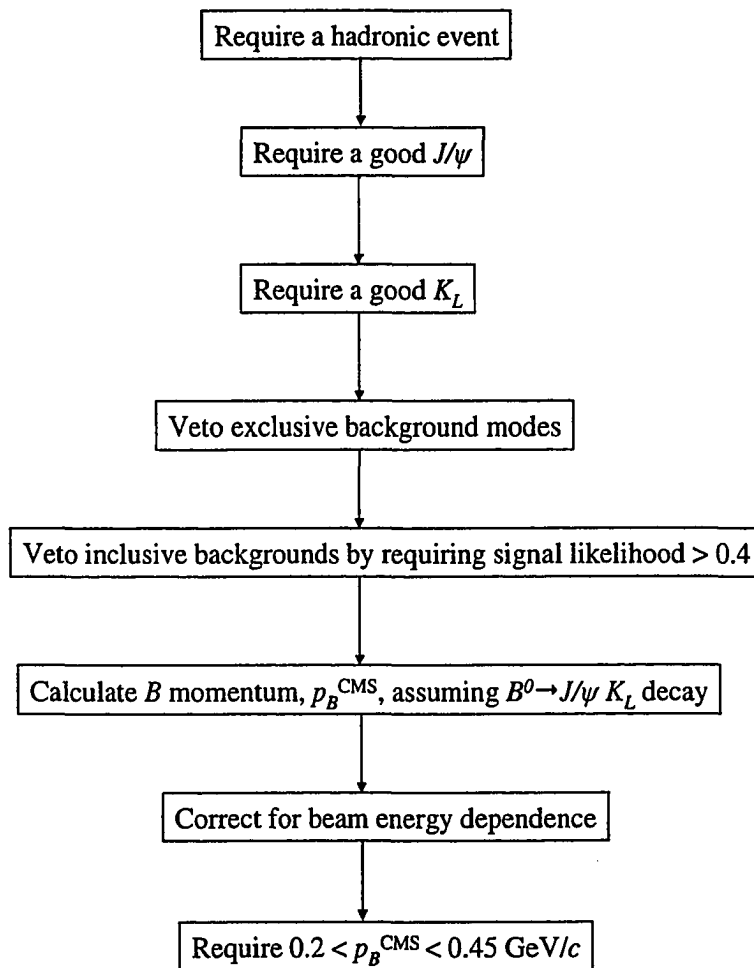


Figure 4.1: Main steps in the selection of $B^0 \rightarrow J/\psi K_L$ events.

comparison, the background fraction in Belle's $B^0 \rightarrow J/\psi K_S$ sample is currently $2.4 \pm 0.1\%$ [24]. Suppressing backgrounds, and understanding those that remain, is therefore of special importance when measuring $\sin 2\phi_1$ with $B^0 \rightarrow J/\psi K_L$ decays.

We will see below how the present background fraction is the result of tuning individual cuts to minimize the final uncertainty, when we use the selected candidate events to estimate $\sin 2\phi_1$. With the amount of data currently available, this uncertainty is dominated by its statistical component, which depends on the number of selected signal (S) and background events (B) as follows:

$$\sigma_{\sin(2\phi_1)} \propto \sqrt{\frac{1+B/S}{S}} = \frac{1}{\text{FOM}} \quad (4.1)$$

Thus, we generally tune the various steps of the event selection to maximize the figure of merit, $\text{FOM} = \sqrt{S/(1+B/S)}$. The purity could be increased further, but this would result lower statistical sensitivity, due to increased rejection of signal events. We sometimes deviate from our main strategy of optimizing the FOM, when there is a way of significantly decreasing systematic uncertainties, while either keeping the FOM constant, or only lowering it slightly.

4.2 Hadronic Event Selection

The hadronic event skim "HadronA", provided by the Belle DST group, represents the starting point for the $B^0 \rightarrow J/\psi K_L$ event selection. The HadronA skimming criteria enhance the purity of hadronic events by suppressing non-hadronic processes, which are far more likely to occur during e^+e^- collisions at

KEKB. Approximate cross sections and HadronA efficiencies for the most common physics processes are given in table 4.1. In this table, $B\bar{B}$ denotes B meson production via the Upsilon($4S$) resonance, i.e. $e^+e^- \rightarrow \Upsilon(4S) \rightarrow B_d^0\bar{B}_d^0$ or $B_u^-B_u^+$. $q\bar{q}$ denotes continuum production of quarks, $e^+e^- \rightarrow q\bar{q}$, with q being one of the four lightest quarks; up, down, charm or strange. QED denotes Bhabha scattering, $e^+e^- \rightarrow e^+e^-$, but includes radiative events with extra photons or leptons in the final state. $\tau\tau$ denotes Tau-pair production, and $\gamma\gamma$ denotes two-photon events. Beam gas denotes events where electrons or positrons from the accelerator beams interact with residual gas molecules in the beampipe, resulting in charged tracks in the drift chamber. As can be seen from the table, Bhabha scattering is the dominant physics process resulting from e^+e^- collisions at KEKB. However, due to their unique signature, Bhabhas are efficiently removed by the HadronA selection, and $e^+e^- \rightarrow q\bar{q}$ events become the dominant background in the HadronA sample. This is not surprising, since $e^+e^- \rightarrow q\bar{q}$ events are also hadronic, and the HadronA selection does not really aim at rejecting them. In addition to the HadronA skim resulting from e^+e^- collisions with $\sqrt{s} = m_{\Upsilon(4S)}$, the HadronA skim is also provided for so-called “continuum” or “off-resonance” data. These are data taken with lower beam energies, such that \sqrt{s} is 50 to 60 MeV below the Upsilon($4S$) resonance. Except for $B\bar{B}$ production, the on- and off-resonance skims will contain events due to the same physics processes. We will make use of this in our study of backgrounds in chapter 5.

The HadronA selection is based on “good” charged tracks, “good” ECL clusters, and the position of the primary event vertex. Charged tracks are assumed to be pions, and classified as good if they satisfy $|dr| < 2.0$ cm, $|dz| < 4.0$ cm,

| Process | BB | $q\bar{q}$ | $\tau\bar{\tau}$ | QED | $\gamma\bar{\gamma}$ | Beam Gas |
|--|-------|------------|------------------|-------|----------------------|----------|
| σ (nb) | 1.1 | 3.3 | 0.93 | 37.8 | 11.1 | - |
| $\epsilon_{\text{HadronA}}$ (%) | 0.994 | 0.838 | 0.240 | 0.002 | 0.008 | - |
| $\sigma \times \epsilon_{\text{HadronA}}$ (nb) | 1.09 | 2.77 | 0.22 | 0.06 | 0.09 | 0.34 |

Table 4.1: Production cross sections at nominal beam energies, efficiencies into HadronA, and effective cross sections into HadronA for the dominant physics processes at KEKB. This table was taken from [25].

and $p_t > 0.1$ GeV/ c , where $|dr|$ and $|dz|$ are the radial and z components of the impact parameter w.r.t. the nominal interaction point, and p_t is the momentum component perpendicular to the beam axis. ECL clusters are classified as good if they pass a shower quality cut, are not associated with charged tracks, and have energy larger than 100 MeV/ c^2 . The primary vertex is obtained by combining all good tracks in the event.

An event is then classified as HadronA if it satisfies the following criteria, where \sqrt{s} is the center-of-mass energy of the KEKB accelerator beams:

- Track multiplicity: 3 or more good charged tracks
- Visible energy: Sum of energy from good charged tracks and good ECL clusters in $\Upsilon(4S)$ rest frame $> 20\%$ of \sqrt{s} .
- Momentum balance: Sum of momenta of good charged tracks and good ECL clusters, measured in $\Upsilon(4S)$ rest frame, has magnitude of z component $< 50\%$ of \sqrt{s} .
- Sum of all ECL cluster energies (including clusters associated with charged tracks) in $\Upsilon(4S)$ rest frame between 10% and 80% of \sqrt{s} .

- Two or more ECL clusters (including clusters associated with charged tracks) detected in the barrel.
- Primary vertex less than 1.5 cm in radius and less than 3.5 cm in z from the nominal interaction point. If no primary vertex can be found, then this cut is not used.

Many other Belle analyses use the “HadronB” event skim, which has higher purity than HadronA. However, studies with both Monte Carlo and data show that the HadronB selection rejects roughly 5% of $B^0 \rightarrow J/\psi K_L$ signal events which pass the HadronA selection. The dominant backgrounds in $B^0 \rightarrow J/\psi K_L$ are charmonium inclusive B meson decays. Since HadronB does not offer any additional rejection of these, we use HadronA.

We remove some of the remaining backgrounds in the HadronA skim, by requiring $R2 < 0.6$, where $R2$ is the ratio of the second and zeroth Fox-Wolfram moments [26]. As can be seen from figure 4.2, our relatively loose cut was chosen so that most B decays are retained, and only obvious background is rejected at this stage.

4.3 Identifying Good J/ψ Candidates

We reconstruct J/ψ 's from their decays into two leptons of the same flavor. The combined branching fraction of $J/\psi \rightarrow e^+e^-$ and $J/\psi \rightarrow \mu^+\mu^-$ is about 12% [8]. (The J/ψ is too light to decay into two τ -leptons.)

Electron and muon candidates are selected from the sample of reconstructed charged tracks by requiring the electron or muon likelihood of the track to be

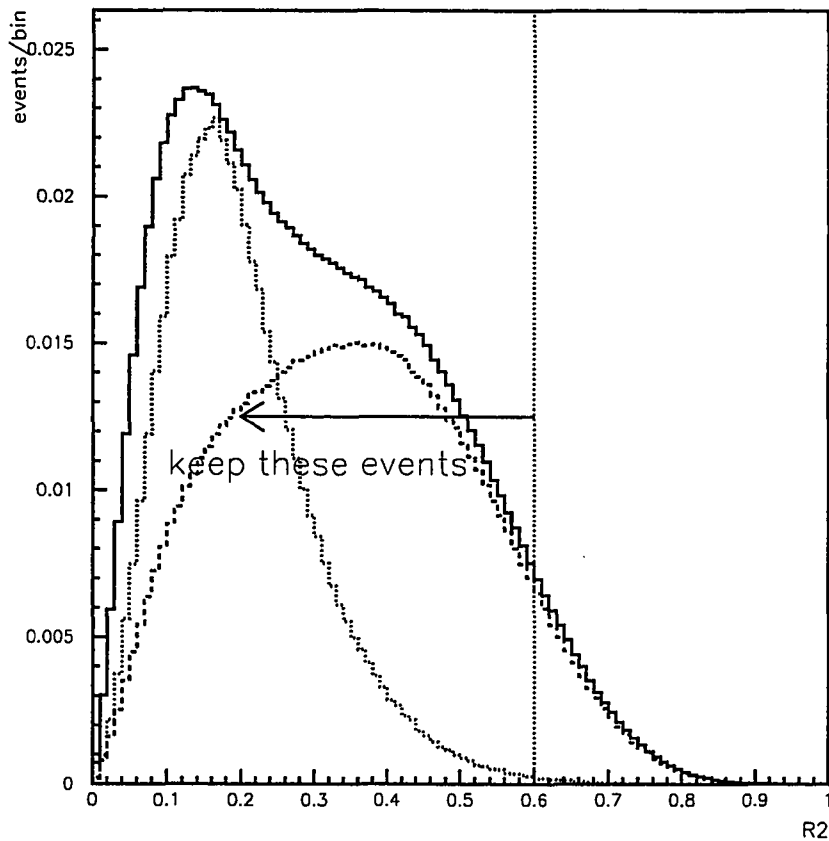


Figure 4.2: The cut $R2 < 0.6$, with $R2$ being the ratio of the second and zeroth Fox-Wolfram moments [26], is used to remove some of the remaining non-Upsilon($4S$) events from the HadronA skim. Events with high $R2$ have a prolate shape, while low $R2$ events are spherical in the CMS frame. The solid histogram shows the $R2$ distribution of hadronic events from experimental data. The superimposed, dotted histograms show the distribution of $B\bar{B}$ events (Monte Carlo) and off-resonance data, which peak at low and high $R2$, respectively.

above a certain threshold. These likelihood values range from zero to one. Although they are not intended to be probabilities in the strict sense, they behave in a similar manner.

The electron likelihood of a charged track and its associated ECL cluster is calculated based on five discriminants:

- Matching χ^2 , which quantifies agreement in azimuth and polar angle between the point where the extrapolated charged track enters the crystal calorimeter, and the actual calorimeter cluster position measured.
- E/P , the ratio of the calorimeter cluster energy to the charged track momentum measured in the drift chamber.
- $E9/E25$, the ratio of energy in a 3×3 and 5×5 array of calorimeter crystals surrounding the shower center.
- dE/dx , the track's average energy loss per unit distance, from ionization in the drift chamber.
- Light yield in the Aerogel Cherenkov counter.

The muon likelihood of a charged track is based on two discriminants:

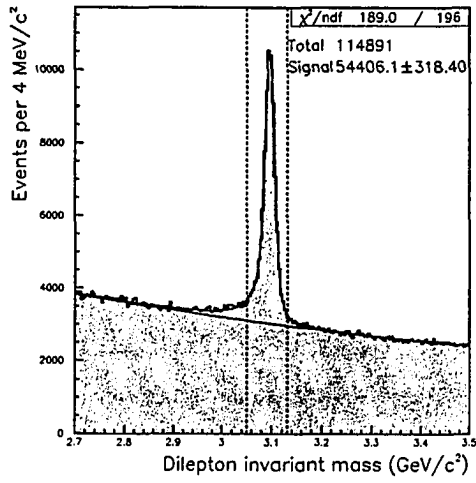
- Matching χ^2 , calculated from the transverse distance between the extrapolation of the drift chamber track into the KLM, and the actual position of RPC hits in the KLM detector.
- Matching χ^2 from comparison of the track's predicted (based on momentum measured in the drift chamber) and observed penetration depth into the KLM detector.

More details on electron- and muon-identification in Belle can be found in [27] and [28].

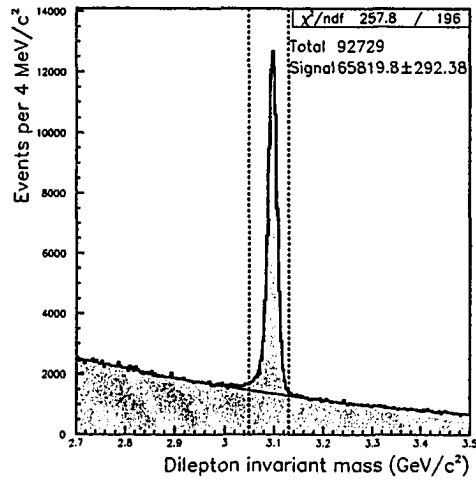
In the case of $J/\psi \rightarrow e^+e^-$ decays, we accommodate the possibility that either lepton emits a photon via bremsstrahlung. In this case the photon tends to be emitted in a direction closely aligned with the direction of the lepton at the time of emission. The bremsstrahlung process can be induced both by the electromagnetic field of the other lepton from the J/ψ decay (final state radiation), or by electromagnetic interaction with atomic nuclei from material in the detector. In either case, the photon will tend to be emitted in the lepton's travel direction. Since most of the material giving rise to bremsstrahlung events—i.e., the beampipe, the SVD, and associated support structure—is close to the interaction point, the bremsstrahlung photons will generally fall into a small angle cone ($\delta\theta < 0.05$ radians) surrounding the original direction of the lepton. By adding calorimeter clusters within this cone to the final state, we improve the J/ψ mass resolution, and increase the yield of the channel $J/\psi \rightarrow e^+e^-$. Seventeen percent of our final $B^0 \rightarrow J/\psi K_L$ candidates in experimental data are reconstructed from $J/\psi \rightarrow e^+e^-\gamma$. For a more detailed discussion of final state radiation and bremsstrahlung in $J/\psi \rightarrow e^+e^-$ decays, see [29].

J/ψ candidates are selected by requiring:

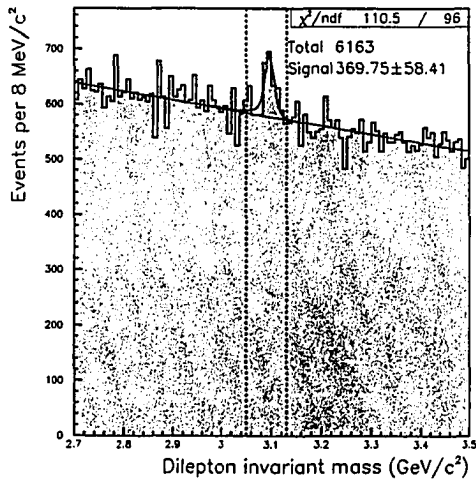
- Charge: Two oppositely charged tracks in the drift chamber.
- Particle ID: Both tracks must either have muon-likelihood greater than 0.1, or both tracks must have electron-likelihood greater than 0.01.
- SVD hits: At least one of the tracks must have one or more SVD r -strip



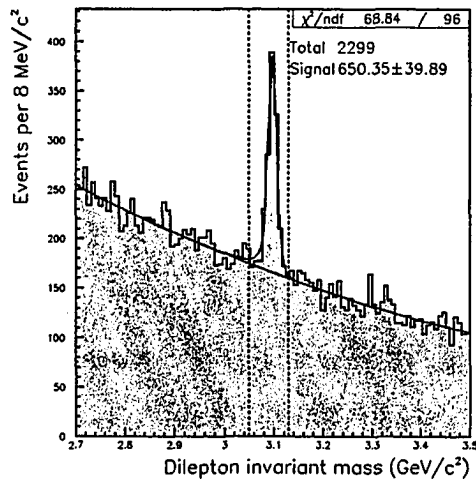
(a) $J/\psi \rightarrow e^+e^-(\gamma)$, on resonance



(b) $J/\psi \rightarrow \mu^+\mu^-$, on resonance



(c) $J/\psi \rightarrow e^+e^-(\gamma)$, off resonance



(d) $J/\psi \rightarrow \mu^+\mu^-$, off resonance

Figure 4.3: Invariant mass distribution of $J/\psi \rightarrow l^+l^-$ candidates from on-resonance (upper) and off-resonance (lower) data. The histograms show experimental data, while solid curves show the result of a fit for the signal and background components. The signal region, $3.05 < m_{J/\psi} < 3.13$ GeV/c , is marked by dotted, vertical lines. The total event yield and fitted signal yield within this region is indicated on each figure.

hits, as well as two or more SVD z -strip hits.

- Impact parameter: $|dr| < 1.0$ cm and $|dz| < 4.0$ cm for both tracks, where dr and dz are the radial and z components, respectively, of the closest approach to the run-dependent interaction point.
- Mass: The sum of the two tracks' four-momenta must have invariant mass between 3.05 and 3.13 GeV/c^2 . To account for bremsstrahlung in $J/\psi \rightarrow e^+e^-$ candidates, the four-vectors of any *ECL* clusters falling within 0.05 radians of the initial directions of the e^+ or e^- are included in the invariant mass sum.

After selection, we perform a mass- and vertex-constrained kinematic fit of the two lepton tracks, which results in a slight improvement in the J/ψ momentum resolution.

Figure 4.3 shows the invariant mass distribution of $J/\psi \rightarrow l^+l^-$ candidates found in on-resonance (upper) and off-resonance (lower) data. All cuts mentioned above, except for the invariant mass cut, have been imposed. Those events from on-resonance data that have $m_{J/\psi}$ in the signal region (between the dotted lines on the figure), are retained and subjected to the remaining cuts of the analysis. At this point, there is still a large amount of combinatoric J/ψ background left, but as we shall see in chapter 5.1, this component is drastically reduced once we also require a good K_L candidate, consistent with $B^0 \rightarrow J/\psi K_L$, in the event.

4.4 Identifying Good K_L Candidates

K_L candidates are selected in two different ways, as described below.

4.4.1 KLM candidates

The first method selects K_L candidates by grouping RPC hits in the KLM detector. See figure 4.4 (left). First, RPC-superlayer hits within 5° of each other are combined into clusters. Muons (and other charged particles) are then rejected by vetoing RPC clusters associated with charged tracks. This is done by extrapolating charged tracks in the drift chamber to the first layer of the KLM. If the line from the interaction point to the point where one of the extrapolated tracks crosses the first KLM layer is within 15° of a cluster, then the cluster is considered to be due to a charged track, and therefore vetoed.

If there is no ECL cluster with energy greater than 160 MeV within 15° of the RPC cluster, the direction of the K_L candidate is determined from the center of gravity of the RPC hits, as illustrated in figure 4.4 (middle). (S. Banerjee and G. Majumder have pointed out [31] that this is not the optimal procedure, and that somewhat better angular resolution could be obtained by using the innermost RPC hits as the K_L direction.) For K_L candidates based on KLM hits only, we require RPC hits in at least two layers.

If there is an ECL cluster with energy greater than 160 MeV within 15° of the RPC cluster, we assume that we had a K_L which left some energy in the electromagnetic calorimeter before interacting in the KLM. In this case we use the direction of the ECL cluster as the direction of the K_L candidate.

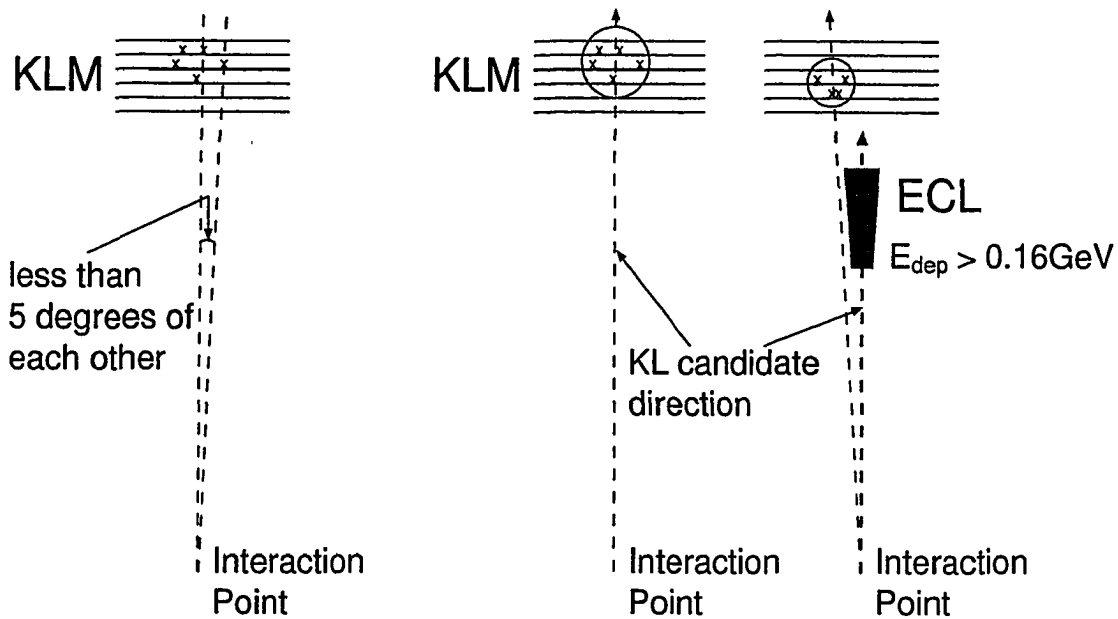


Figure 4.4: K_L candidates are formed by grouping nearby RPC hits in the KLM detector (left). The center of gravity of the RPC hits is then used as the direction of the K_L (middle), unless there is an ECL cluster in the same angular region. In the latter case, the ECL cluster is also associated with the K_L candidate, and the direction of the ECL cluster is used as the direction of the K_L (right). This figure was taken from [30].

K_L candidates that are found by the method above, will be referred to as “KLM candidates,” and are thus candidates which have hits in the KLM detector, but which may or may not have hits in the crystal calorimeter.

4.4.2 ECL-only candidates

The second method selects K_L candidates that have hits in the crystal calorimeter, but not in the K_L /muon detector. We will refer to such K_L candidates as “ECL-only candidates.” The set of all ECL clusters (charged and neutral) is used as the starting point for this selection. Since most long-lived particles produced in B decays at Belle ($e^{+/-}$, $\mu^{+/-}$, $\pi^{+/-}$, $K^{+/-}$, γ) result in ECL clusters, this initial sample has low signal purity. We then discriminate between K_L 's and other particles by using the following properties of the ECL cluster and its environment:

- Distance between the ECL cluster and the point where the closest charged track hits the ECL detector.
- Total energy of the ECL cluster.
- Mass of ECL cluster. By subdividing the ECL cluster into sub-clusters and adding up their four vectors, we obtain a four vector with non-zero mass.
- $E9/E25$, the ratio of energy in a 3×3 and 5×5 array of crystals surrounding the shower center.
- Cluster width.

| |
|---|
| distance of closest charged track > 20 cm energy of ECL cluster > 200 MeV mass of ECL cluster > 13 MeV/ c^2 $E_9/E_{25} < 0.99$ r.m.s. cluster width > 4 cm |
|---|

Table 4.2: Preselection cuts, used to remove obvious non- K_L background from the sample of all ECL clusters.

We first apply loose preselection cuts to these variables, as shown in table 4.2. These cuts are intended to remove obvious background with little loss of signal. For instance, the cut on the distance of the closest charged track will remove ECL clusters due to charged particles, while the cut on the ECL cluster energy will remove minimum ionizing particles and low energy photons. The remaining variables are useful because ECL clusters from hadronic interactions tend to be less uniform and broader than electromagnetic showers or cluster due minimum ionizing particles.

To further increase the purity of the K_L candidate sample, we use the five cluster properties to assign a K_L -likelihood ratio to each ECL cluster. The sources of fake K_L 's are varied, and several approaches are possible in the construction of a likelihood variable. We choose to optimize its performance for the $B^0 \rightarrow J/\psi K_L$ analysis by creating probability density functions (PDFs) from charmonium inclusive B decay Monte Carlo. We construct PDFs for the likelihood calculation from those particular ECL clusters in the Monte Carlo sample, which (when paired up with a good J/ψ candidate) pass all $B^0 \rightarrow J/\psi K_L$ selection cuts. Out of these ECL clusters, those from events which contain a $B^0 \rightarrow J/\psi K_L$ decay at the generator level are categorized as signal, while everything else is

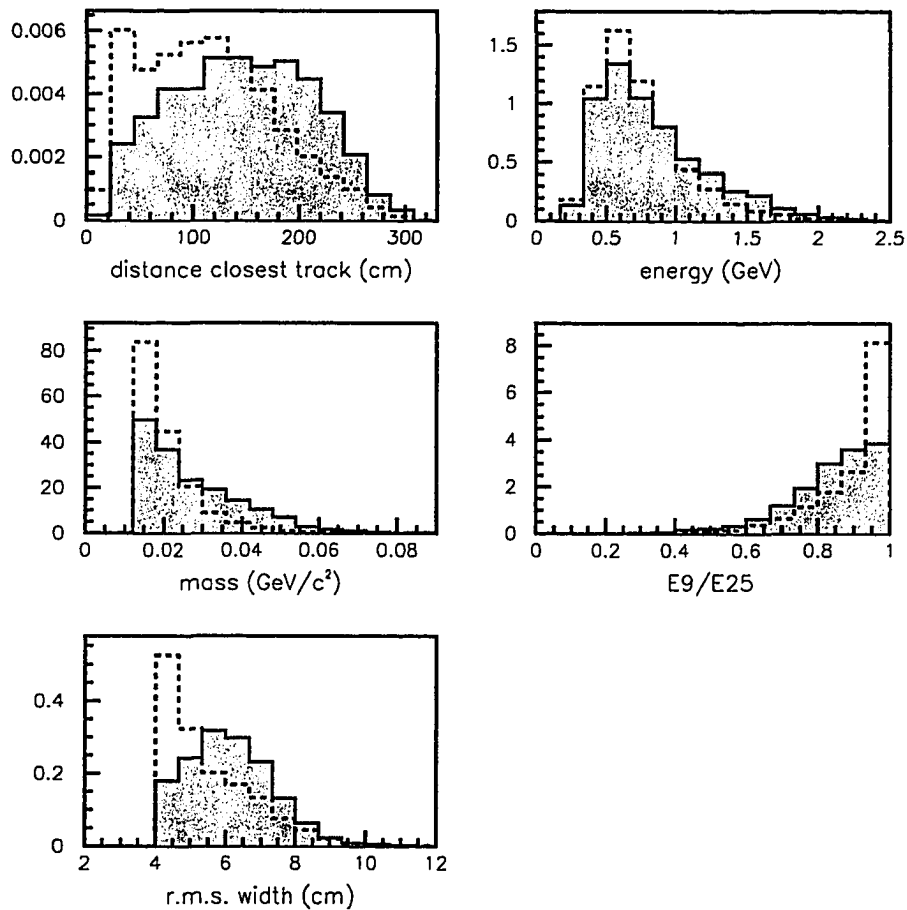


Figure 4.5: Probability density functions (PDFs) used to calculate the K_L -likelihood of ECL clusters without associated KLM hits; so called ECL-only candidates. Signal PDFs are shown as filled histograms, with the background PDFs superimposed as dotted, empty histograms. Loose preselection cuts, shown in table 4.2, have been applied. See text for further discussion.

considered background. Figure 4.5 shows the resulting signal and background distributions of the five cluster properties. Each distribution is normalized so that its integral is unity.

The idea behind our definition of signal and background, was to tailor the K_L -likelihood variable to the specific needs of the $B^0 \rightarrow J/\psi K_L$ analysis. First, our definition of background ensures that the likelihood variable will “automatically” be optimized to suppress the particular cocktail of particles that results in $B^0 \rightarrow J/\psi K_L$ backgrounds. As discussed in more detail in chapter 5, the dominant backgrounds are charmonium inclusive B meson decays, in particular those that have event topology and kinematics similar to $B^0 \rightarrow J/\psi K_L$, rather than purely combinatorial events. The sources of fake K_L 's that matter for the $B^0 \rightarrow J/\psi K_L$ analysis therefore make up a different mix of particles than the set of all ECL-clusters that are not due to K_L . Second, a substantial fraction of the background modes in our analysis contain real K_L 's, as in the decays $B^0 \rightarrow J/\psi K^{*0}(K^{*0} \rightarrow K_L\pi^0)$ and $B^+ \rightarrow J/\psi K^{*+}(K^{*+} \rightarrow K_L\pi^+)$. When such events get wrongly reconstructed as $B^0 \rightarrow J/\psi K_L$, the ECL cluster properties will distribute differently than in the case of K_L 's from real $B^0 \rightarrow J/\psi K_L$ events. For instance, the pion from $K^* \rightarrow K_L\pi$ can end up in the same region of the detector as the K_L , so that the ECL clusters of the two particles overlap. In the case of a charged pion, we will also have a charged track ending near the cluster. Our method of constructing PDFs includes such cases with real K_L 's in the background.

The K_L -likelihood of a given ECL cluster, $P(K_L \text{ from } B^0 \rightarrow J/\psi K_L)$, is calculated as follows:

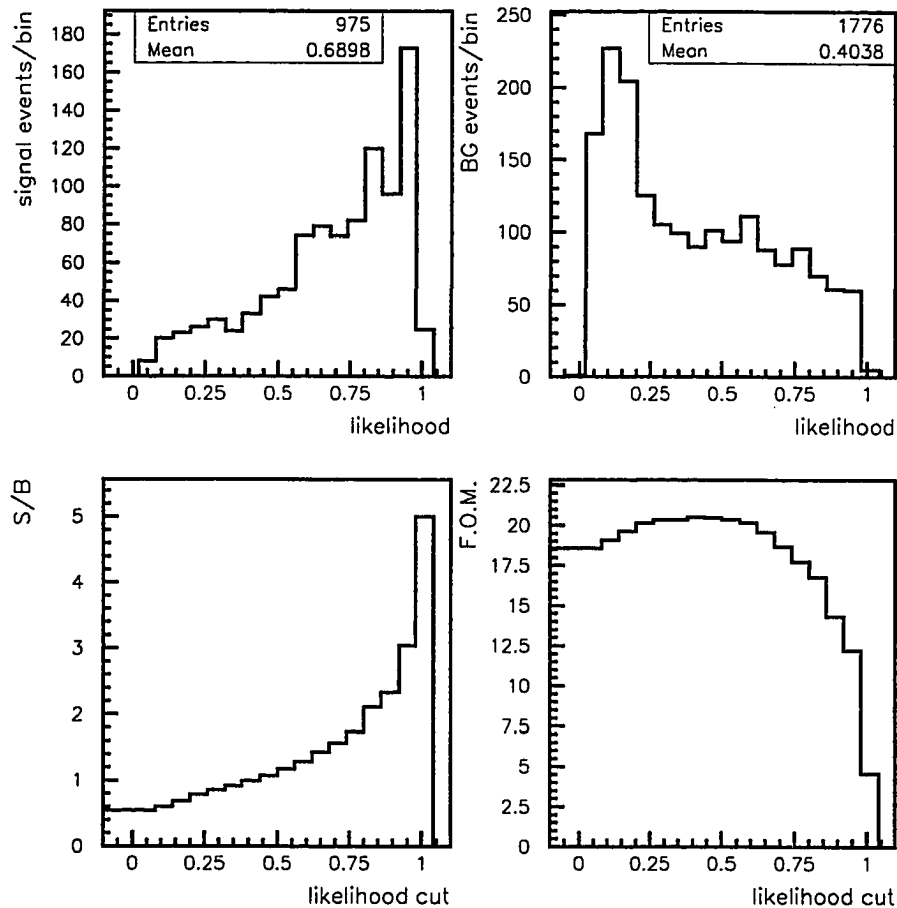


Figure 4.6: Distribution of K_L -likelihood ratio for ECL clusters from $B^0 \rightarrow J/\psi K_L$ signal Monte Carlo (upper left), and background from charmonium inclusive B decay Monte Carlo (upper right). The distributions show only ECL clusters that passed both the preselection criteria (see text), as well as all further $B^0 \rightarrow J/\psi K_L$ analysis cuts, after the K_L candidate is paired with a good J/ψ candidate. Using these signal (S) and background (B) distributions, we estimate the variation of the S/B ratio (lower left) and the FOM (lower right) as we cut on different values of the K_L -likelihood ratio.

$$P(K_L \text{ from } B^0 \rightarrow J/\psi K_L) = \frac{\prod_{i=1}^5 f_i^S(v_i)}{\prod_{i=1}^5 f_i^S(v_i) + \prod_{i=1}^5 f_i^B(v_i)}, \quad (4.2)$$

where $f_i^S()$ and $f_i^B()$ are the five signal and background PDFs shown in figure 4.5. These PDFs are evaluated at v_i , which are the values of the five variables for the given ECL cluster. The resulting K_L -likelihood ratio thus combines the information of the five variables into one discriminant, which ends up behaving similarly to a probability. For each ECL cluster, we obtain a likelihood value between 0 and 1.0. The greater the value, the more likely is it that we have a real K_L which came from a $B^0 \rightarrow J/\psi K_L$ event. The upper two histograms in figure 4.6 show the likelihood distributions for ECL clusters from signal and background Monte Carlo. It indeed works out quite nicely—ECL clusters from $B^0 \rightarrow J/\psi K_L$ events are distributed with a peak at high K_L -likelihood ratio, while ECL clusters from other charmonium inclusive B decays are distributed with a peak at low likelihood ratio.

We retain ECL clusters with high K_L -likelihood as K_L candidates, and discard the rest. The exact cutoff value is chosen so that the figure of merit, FOM, is optimized, as discussed in the introduction of this chapter. The lower plots in figure 4.6 show the variation of the signal to background ratio, S/B , and the FOM with the likelihood cutoff value. Based on these plots, we retain ECL clusters with likelihood ratio > 0.5 as K_L candidates. To avoid self bias in our estimation of the the optimum likelihood cut, the Monte Carlo event sample used to make

figure 4.6 is separate from the sample that was used to make the PDFs.

4.4.3 Additional K_L vetos, and treatment of multiple K_L candidates

Both KLM candidates and ECL-only candidates are subject to the following two vetos:

- K_L candidates that include an ECL cluster are vetoed if the ECL cluster is consistent with being a photon from $\pi^0 \rightarrow \gamma\gamma$. We thus reject K_L candidates if the ECL cluster, when paired up with a photon candidate, reconstructs to a good π^0 -mass, $120 \text{ MeV}/c^2 < m_{\gamma\gamma} < 150 \text{ MeV}/c^2$. However, in order to reduce the rate of fake vetos, we only veto the K_L if the π^0 's momentum in the $\Upsilon(4S)$ rest frame is greater than $1.2 \text{ GeV}/c$ (for ECL-only candidates) or $0.8 \text{ GeV}/c$ (for KLM candidates with an associated ECL cluster).
- Since the drift chamber only allows us to reconstruct charged tracks in the region $17^\circ < \theta < 150^\circ$, K_L candidates in the very forward and very backward detector regions have a larger fake rate due to charged particles, when selected as described above. We improve the purity of our K_L candidate sample by imposing the requirement $|\cos \theta_{K_L}| < 0.95$ for all K_L candidates.

In order to avoid double counting due to overlap between the two classes of K_L candidates, we only look for ECL-only candidates in an event, if the event contained no KLM candidates which resulted in a $B^0 \rightarrow J/\psi K_L$ candidate surviving further event selection cuts. This is the only exception to our general

rule, which is to keep multiple particle candidates until the end of the analysis, where we select one $B^0 \rightarrow J/\psi K_L$ candidate per event based on the B meson's CMS momentum, p_B^{CMS} .

4.5 $B^0 \rightarrow J/\psi K_L$ Selection

4.5.1 The General Principle

If we find at least one good J/ψ candidate, and one good K_L candidate in an event, we take all combinations of J/ψ 's and K_L 's as potential $B^0 \rightarrow J/\psi K_L$ candidates. Backgrounds are suppressed in two steps. Some background modes can easily be fully reconstructed and cleanly vetoed. The remaining charmium modes are suppressed with an inclusive veto, based on a likelihood variable. Finally, we calculate the CMS momentum of each B candidate, p_B^{CMS} . After a correction for beam energy dependence, candidates with $0.20 < p_B^{\text{CMS}} < 0.45$ GeV/ c are retained for the measurement of $\sin 2\phi_1$. When there are multiple $B^0 \rightarrow J/\psi K_L$ candidates in an event, the candidate with p_B^{CMS} closest to the expected signal peak position is kept.

4.5.2 Exclusive Mode Vetos

For each $B^0 \rightarrow J/\psi K_L$ candidate, we take the J/ψ candidate and also attempt to reconstruct each of the following B decays:

- $B^0 \rightarrow J/\psi K_S (K_S \rightarrow \pi^+ \pi^-)$
- $B^0 \rightarrow J/\psi K^{*0} (K^{*0} \rightarrow K^+ \pi^- \text{ and } K_S \pi^0)$

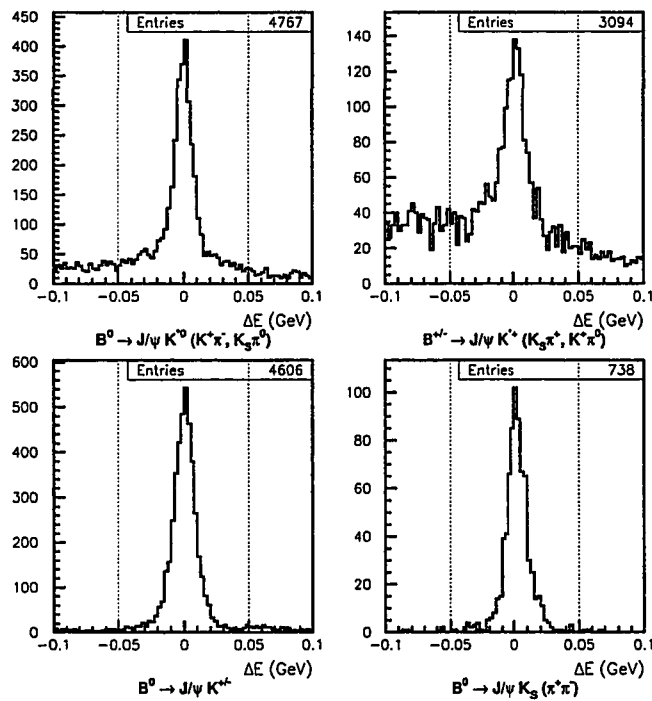


Figure 4.7: ΔE distributions from experimental data, for B decay modes that are fully reconstructed and vetoed. The cut $5.27 < M_{bc} < 5.29 \text{ GeV}/c^2$ has been applied. The vertical, dotted lines show the signal region in ΔE .

- $B^{+/-} \rightarrow J/\psi K^{*+} (K^{*+/-} \rightarrow K^{+/-}\pi^0 \text{ and } K_S\pi^{+/-})$
- $B^{+/-} \rightarrow J/\psi K^{+/-}$

Since these decay channels can be fully reconstructed, we end up with two variables, reflecting the known values of the B meson's energy and momentum. The most commonly used variables are $\Delta E = E_B^{\text{CMS}} - E_{\text{CMS}}/2$, and beam constrained mass, $M_{bc} = \sqrt{(E_{\text{CMS}}/2)^2 - (p_B^{\text{CMS}})^2}$. This is in contrast to the $B^0 \rightarrow J/\psi K_L$ reconstruction, where we don't know the K_L 's momentum, and as a result are left with only one variable at the end; p_B^{CMS} . Figure 4.7 shows histograms of ΔE for B meson candidates from experimental data, reconstructed with the various decay hypotheses above. If we find a candidate for any of these modes that satisfies $|\Delta E| < 50$ MeV and $5.27 < M_{bc} < 5.29$ GeV/c², then the $B^0 \rightarrow J/\psi K_L$ candidate is discarded.

4.5.3 Inclusive Veto via Likelihood Cut

We construct another likelihood variable, this one aimed at separating $B^0 \rightarrow J/\psi K_L$ events from any charmonium inclusive B decay background that remains after all other selection cuts have been applied. This likelihood variable, which we shall refer to as the " $B^0 \rightarrow J/\psi K_L$ - likelihood ratio," is calculated from the following variables:

- $p_{J/\psi}^{\text{CMS}}$: Momentum of the J/ψ candidate in the $\Upsilon(4S)$ rest frame.
- $\cos(\text{"Marlow veto angle"})$: Cosine of the (lab frame) angle between the K_L candidate and the nearest charged track with momentum above 700 MeV/c.

We calculate the angle using the initial direction of charged tracks, i.e. the direction of tracks as they emerge from the interaction point.

- N_{trk} : Number of “good” charged tracks in the event. See section 4.2 for the definition of a good track.
- p_B^{CMS} (3-body): Calculated momentum of reconstructed B meson in the $\Upsilon(4S)$ rest frame, when we add a charged pion to the $J/\psi K_L$ final state, and assume that the three-body decay $B \rightarrow J/\psi K^{*\pm} (K^{*\pm} \rightarrow K_L \pi^\pm)$ took place. This variable is only used when a good $B \rightarrow J/\psi K^*$ candidate, satisfying $p_B^{\text{CMS}}(3\text{-body}) < 0.8 \text{ GeV}/c$, $852 \text{ MeV}/c^2 < m_{K^*} < 930 \text{ MeV}/c^2$, and $p_\pi^{\text{CMS}} > 350 \text{ MeV}/c$ is found. The pion must come from the interaction point. When there are multiple candidates, the one with m_{K^*} closest to the PDG value [8] is used.
- $\cos(\theta_B^{\text{CMS}})$: Angle of reconstructed B meson with respect to beam axis, measured in the $\Upsilon(4S)$ rest frame.
- $E_{\text{ECL}}/E_{\text{calc.}}$: Ratio of the K_L candidate’s energy deposit in the ECL, to the calculated K_L energy, when assuming a $B^0 \rightarrow J/\psi K_L$ decay. This variable is only used when the K_L candidate has some associated ECL energy.

The procedure for constructing this second likelihood variable is very similar to the procedure for constructing the K_L -likelihood ratio, which was described in section 4.4.2. We first apply loose preselection cuts, shown in table 4.3, to remove obvious background. We then use a large Monte Carlo sample of charmonium inclusive B decays to create signal- and background-PDFs for the abovementioned

$1.4 \text{ GeV}/c < p_{J/\psi}^{\text{CMS}} < 2.0 \text{ GeV}/c$
 "Marlow veto angle": no hard cut
 $2 < N_{trk} < 13$
 $p_B^{\text{CMS}}(3\text{-body})$: see text
 $\cos(\theta_B^{\text{CMS}})$: no hard cut
 $0 < E_{\text{ECL}}/E_{\text{calc.}} < 1.0$

Table 4.3: Preselection cuts for inclusive mode veto.

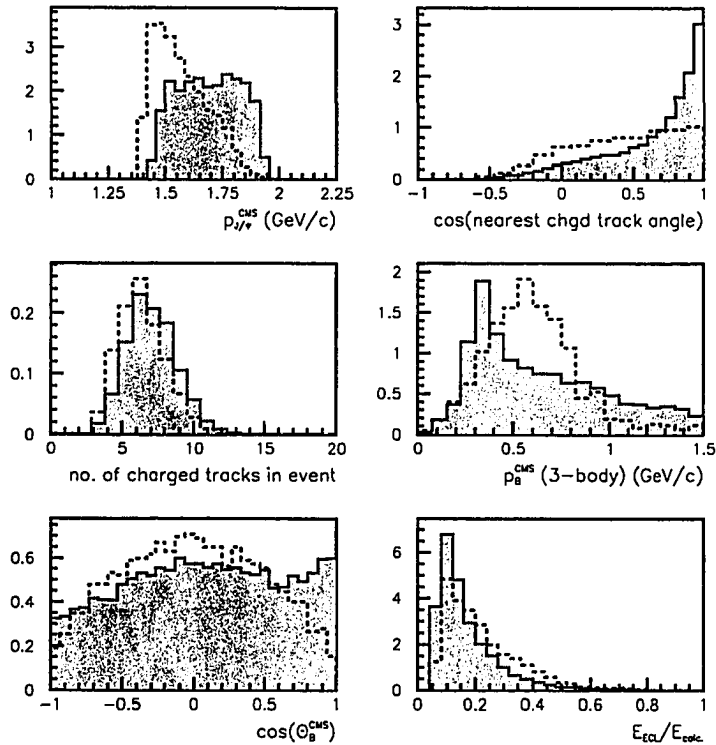


Figure 4.8: PDFs used to calculate the $B^0 \rightarrow J/\psi K_L$ - likelihood ratio for KLM candidates. The shaded distributions show signal, the empty distributions show background.

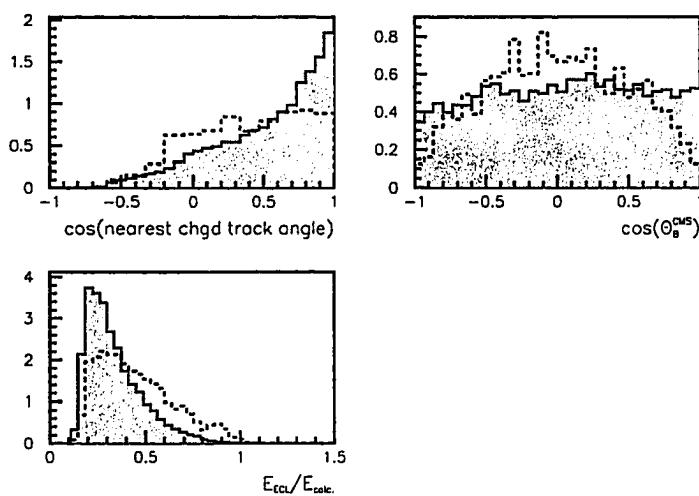


Figure 4.9: Additional PDFs used to calculate the $B^0 \rightarrow J/\psi K_L$ - likelihood ratio for ECL-only candidates. The shaded distributions show signal, the empty distributions show background.

variables. For this purpose, we apply all event selection cuts discussed so far, and use $B^0 \rightarrow J/\psi K_L$ candidates with $p_B^{\text{CMS}} < 2.0 \text{ GeV}/c$. Signal and background events are separated by looking at the generator-level information of the Monte Carlo events. Any event containing $B^0 \rightarrow J/\psi K_L$ is classified as signal, all other events are classified as background. The resulting PDFs for KLM candidates are shown in figure 4.8. The distributions of the variables $\cos(\theta_B^{\text{CMS}})$, $E_{\text{ECL}}/E_{\text{calc.}}$, and $\cos(\text{“Marlow veto angle”})$ are significantly different between KLM candidates and ECL-only candidates. Hence we use a different set of PDFs, shown in figure 4.9, for these variables when calculating the likelihood ratio for ECL-only candidates. The $B^0 \rightarrow J/\psi K_L$ - likelihood ratio for a given candidate, $P_{B^0 \rightarrow J/\psi K_L}$, is then calculated as follows:

$$P_{B^0 \rightarrow J/\psi K_L} = \frac{\prod_{i=1}^6 f_i^{\text{S}}(v_i)}{\prod_{i=1}^6 f_i^{\text{S}}(v_i) + \prod_{i=1}^6 f_i^{\text{B}}(v_i)}, \quad (4.3)$$

where $f_i^{\text{S}}()$ and $f_i^{\text{B}}()$ are the signal and background PDFs, respectively, shown in figures 4.8 and 4.9. These PDFs are evaluated at v_i , which are the values of the six variables for the given $B^0 \rightarrow J/\psi K_L$ candidate.

Further explanation is needed to make our likelihood procedure repeatable: not all of the six variables (and corresponding PDFs) are used each time we calculate the likelihood value for a $B^0 \rightarrow J/\psi K_L$ candidate. The energy ratio, $E_{\text{ECL}}/E_{\text{calc.}}$, is used only when the K_L candidate has an associated ECL cluster, while p_B^{CMS} (3-body) is only used when a good $B \rightarrow J/\psi K^*$ candidate exists.

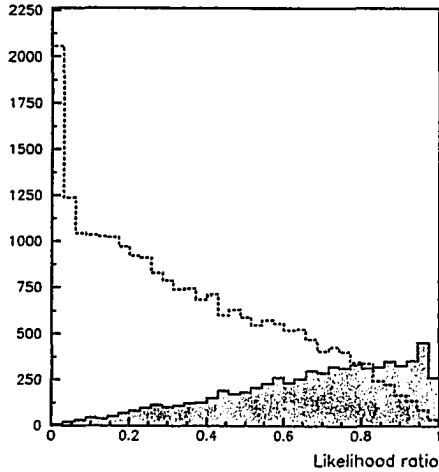
The rationale behind these exceptions is simply that we increase the efficiency of the likelihood ratio if we don't include variables in the calculation when they have no meaning.

Distributions of the $B^0 \rightarrow J/\psi K_L$ - likelihood ratio for signal and background events from Monte Carlo are shown in figure 4.10. We again estimate the optimal likelihood cut by considering the variation of the signal to background ratio, S/B , and the FOM, with the cut value, as shown in figures 4.11 and 4.12. Based on these plots, we only retain signal candidates with $B^0 \rightarrow J/\psi K_L$ - likelihood ratio greater than 0.4.

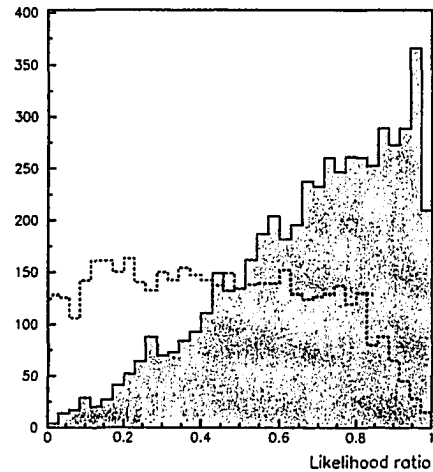
4.5.4 Other Cuts

We also apply a K_L "cone angle cut," a legacy cut that may no longer be needed. It results in a weak suppression of events at high p_B^{CMS} . We predict the K_L direction, $\vec{r}_{\text{expected}}$, based only on the detected J/ψ candidate. This is done by approximating the four-momentum of the parent B with its average value, which is the four momentum of the $\Upsilon(4S)$, divided by two. If we assume a $B^0 \rightarrow J/\psi K_L$ decay, the four momentum of the K_L is then given by the difference between the four momentum of the B , and the four momentum of the J/ψ . We reject events where the measured K_L direction, \vec{r}_{K_L} , is too far from the expected direction by requiring

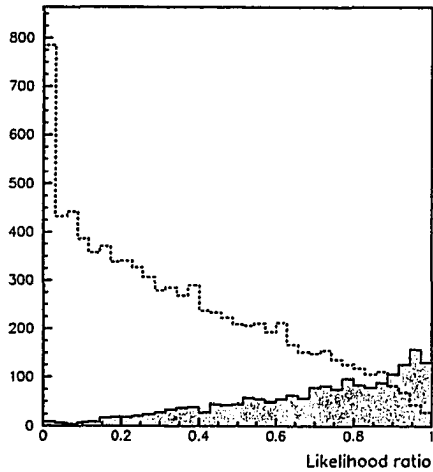
$$\cos(\angle(\vec{r}_{\text{expected}}, \vec{r}_{K_L})) > 0.8. \quad (4.4)$$



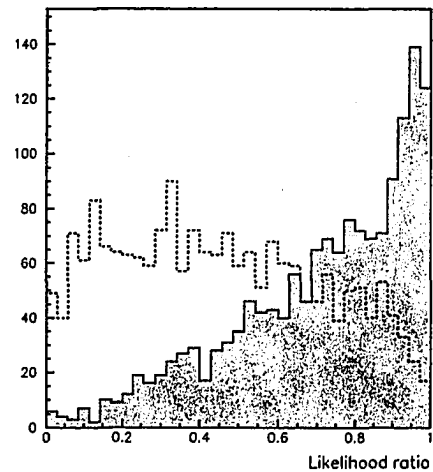
(a) $p_B^{\text{CMS}} < 2.0 \text{ GeV}/c$
 K_L in KLM



(b) $0.2 < p_B^{\text{CMS}} < 0.45 \text{ GeV}/c$
 K_L in KLM



(c) $p_B^{\text{CMS}} < 2.0 \text{ GeV}/c$
 K_L in ECL only



(d) $0.2 < p_B^{\text{CMS}} < 0.45 \text{ GeV}/c$
 K_L in ECL only

Figure 4.10: Distributions of the $B^0 \rightarrow J/\psi K_L$ - likelihood ratio for signal (shaded histograms) and background (empty histograms) events from charmonium inclusive Monte Carlo. The upper histograms show KLM candidates, while the lower histograms show ECL-only candidates. All event selection cuts, except for that on the likelihood ratio, have been applied. For plots a) and c), the p_B^{CMS} cut has been widened as indicated.

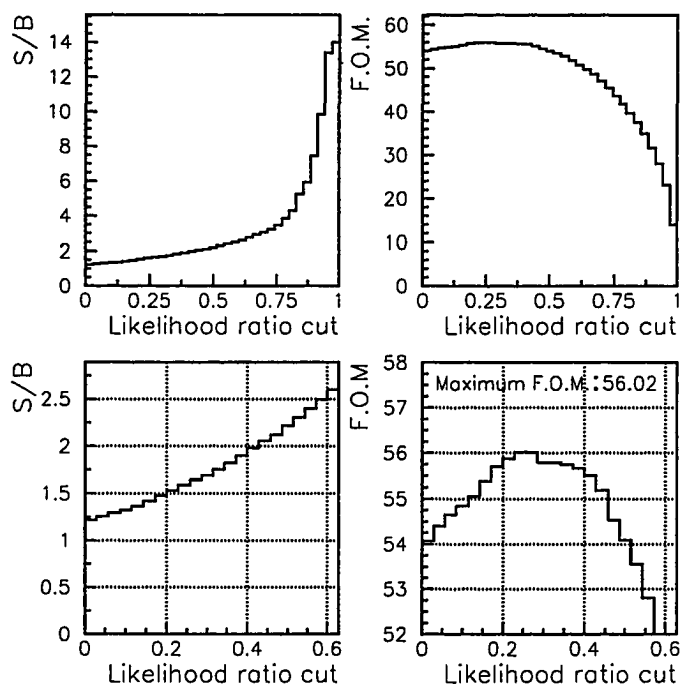


Figure 4.11: Variation of the S/B ratio (left) and the figure of merit (right) as we cut on different values of the $B^0 \rightarrow J/\psi K_L$ - likelihood ratio, for KLM candidates. The signal (S) and background (B) distributions are those shown in figure 4.10 b). The lower plots show a blow-up of the lower likelihood region.

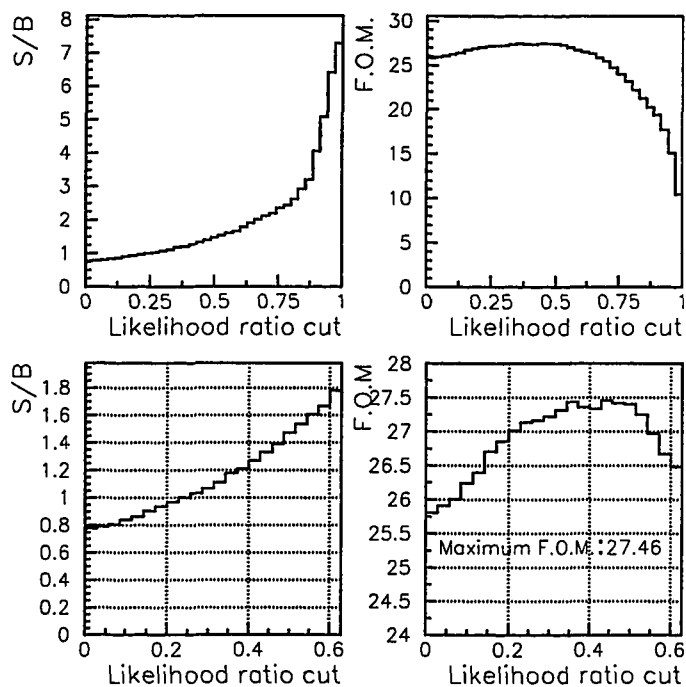


Figure 4.12: Variation of the S/B ratio (left) and the figure of merit (right) as we cut on different values of the $B^0 \rightarrow J/\psi K_L$ - likelihood ratio, for ECL-only candidates. The signal (S) and background (B) distributions used are those shown in figure 4.10 d).

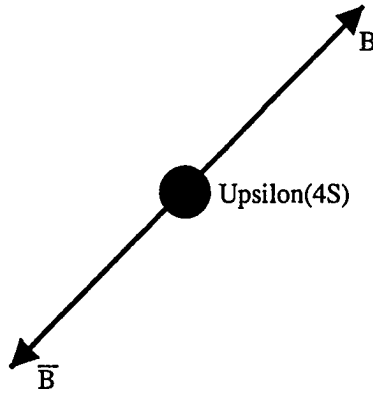


Figure 4.13: In the $\Upsilon(4S)$ rest frame, the B meson momentum, p_B^{CMS} , will be constant.

4.5.5 Calculation of p_B^{CMS}

As illustrated in figure 4.13, if we have an $\Upsilon(4S) \rightarrow B\bar{B}$ decay, then in the $\Upsilon(4S)$ rest frame, the B mesons will each carry away half the energy of the $\Upsilon(4S)$. Ignoring beam energy fluctuations (see section 4.5.6) and detection uncertainties, the resulting B mesons will always have the same momentum:

$$p_B^{\text{CMS expected}} = \sqrt{E_B^2 - m_B^2} = \sqrt{(E_{\text{CMS}}/2)^2 - m_B^2} \approx 330 \text{ MeV}/c^2. \quad (4.5)$$

Since our method of detecting K_L 's does not provide an accurate measurement of the K_L energy, we are not able to measure the B momentum directly. But if a $B^0 \rightarrow J/\psi K_L$ decay took place, then the K_L momentum, \vec{p}_K , must satisfy

$$m_B^2 = \left(E_{J/\psi} + \sqrt{p_K^2 + m_K^2} \right)^2 - \left| \vec{p}_K + \vec{p}_{J/\psi} \right|^2 \quad (4.6)$$

$$= \left(E_{J/\psi} + \sqrt{p_K^2 + m_K^2} \right)^2 - p_K^2 - p_{J/\psi}^2 - 2p_K p_{J/\psi} \cos \theta, \quad (4.7)$$

where all quantities are measured in the lab frame, and θ is the angle between the J/ψ and K_L momenta. The magnitude $p_K = |\vec{p}_K|$ is the only unknown in this equation, so that the K_L direction combined with the J/ψ momentum and direction provide enough information to calculate p_K . We can then boost \vec{p}_K to the CMS frame, and as a result we can calculate p_B^{CMS} .

The calculation of p_K assumes that a $B^0 \rightarrow J/\psi K_L$ decay took place. We can then verify the $B^0 \rightarrow J/\psi K_L$ hypothesis by comparing the calculated value of the B momentum in the CMS frame, p_B^{CMS} , to the value predicted by equation 4.5. For true signal events, we expect a peak in the p_B^{CMS} spectrum at $p_B^{\text{CMS}} = p_B^{\text{CMS}}_{\text{expected}}$. In the actual experiment, this peak will have finite width due primarily to resolution effects, such as angular resolution in the K_L detection and fluctuations in the beam energies. Figures 5.15 a) and 5.16 a) show the p_B^{CMS} distribution predicted by $B^0 \rightarrow J/\psi K_L$ signal Monte Carlo, which includes these effects. We select $B^0 \rightarrow J/\psi K_L$ candidates by keeping events in the range $0.20 < p_B^{\text{CMS}} < 0.45$ GeV/c. Figures 5.15 and 5.16 also show the p_B^{CMS} distribution of various backgrounds. As discussed extensively in chapter 5, the main backgrounds in this analysis are charmonium inclusive B meson decays, which remain even after the final p_B^{CMS} cut.

4.5.6 Correction for Drift of Beam Energies

Ideally, we would like the KEKB beam energies to be constant in time, so that the CMS energy in the e^+e^- collisions, \sqrt{s} , always equals the $\Upsilon(4S)$ rest energy. In the actual experiment, however, this is not possible, since the particles in both accelerator beams are distributed in energy. As a result, \sqrt{s} differs from event

to event. The boost vector between the lab frame and the CMS frame, also changes with the beam energies. These variations in the beam energies affect our analysis, in that they result in a broadening of the $B^0 \rightarrow J/\psi K_L$ signal peak in p_B^{CMS} . This effect is taken into account in the Monte Carlo generation by using a distribution for the beam energies.

In addition to the event-to-event variations, the mean beam energies drift on a time scale of weeks. Typically, \sqrt{s} drifts away from the $\Upsilon(4S)$ after a while, and the $B\bar{B}$ production rate decreases. The CMS energy can also change abruptly after energy scans, when the accelerator group adjusts the energy to recenter the machine on the $\Upsilon(4S)$ peak. These changes affect the p_B^{CMS} distributions, and must be corrected in the analysis.

In particular, we correct for the $B^0 \rightarrow J/\psi K_L$ signal peak position's dependence on \sqrt{s} in experimental data. Neglecting the beam crossing angle and the electron mass, we find that the *expected* value of p_B^{CMS} is given by

$$p_B^{\text{CMS}} = \sqrt{(LH - m_B^2)}, \quad (4.8)$$

where L and H are the energies of the positron and electron beams, respectively. Note that it is the actual CMS machine energy that matters, and not the nominal mass of the $\Upsilon(4S)$. Using the nominal beam energies of 3.5 GeV and 8.0 GeV, and $m_B = 5.2794 \text{ GeV}/c^2$, we find that a 1 MeV change in the LER results in a 10 MeV/ c change in p_B^{CMS} . With the actual drift of beam energies in the experiment, which is \pm a few MeV, the expected p_B^{CMS} value varies over a range of more than 50 MeV/ c .

The p_B^{CMS} signal peak position has thus a slow time dependence in the experiment. We apply the requisite correction to experimental data after reconstruction. This is possible because the drift in \sqrt{s} is slow enough that it can be measured by fully reconstructing other B decay channels. At Belle, the run-dependent B meson energy is thus available as a convenient function, $\text{benergy}()$, in the reconstruction software. For each $B^0 \rightarrow J/\psi K_L$ candidate from data, we adjust the B momentum after reconstruction, $p_B^{\text{CMS}}{}_{(\text{uncorrected})}$, as follows:

$$p_B^{\text{CMS}}{}_{(\text{corrected})} = p_B^{\text{CMS}}{}_{(\text{uncorrected})} - p_B^{\text{CMS}}{}_{(\text{beam})} + p_B^{\text{CMS}}{}_{(\text{MC})}, \quad (4.9)$$

Here $p_B^{\text{CMS}}{}_{(\text{beam})} = \sqrt{\text{benergy}()^2 - m_{B_d^0}^2}$ is the *expected* momentum for a B^0 meson in data. It is derived from $\text{benergy}()$, which depends on the experiment and run number. $p_B^{\text{CMS}}{}_{(\text{MC})}$ is the *expected* B meson momentum for Monte Carlo, which is a constant: 0.335110 GeV/ c . It was calculated from the beam parameters used in the Monte Carlo generation, $L = 3.5000$ GeV, $H = 7.9965$ GeV, and the 22-mrad crossing angle. All calculations use the world average B_d^0 mass, 5.2794 GeV/ c^2 [8], which was also used in the Monte Carlo production. (We emphasize that all quantities are “*expected*” p_B^{CMS} values to avoid getting into other complicating experimental effects, such as limited angular resolution of K_L detection and fluctuations of the beam energies around the run-dependent mean values. These also affect the mean signal peak position.) The drifting beam energies also affect the boost vector between the CMS and lab frame. However, we use a run-independent boost vector even for reconstruction of experimental data. We use the same boost vector that was used to measure the $\text{benergy}()$ values in

the first place, resulting in a self-consistent procedure.

The result of applying the p_B^{CMS} correction to $B^0 \rightarrow J/\psi K_L$ candidates from experimental data, experiment 7-19, is shown in figure 4.14. The dotted histograms are the raw p_B^{CMS} distributions, while the superimposed solid histograms show the same events after correction. Since these histograms are made using the same candidate events, any difference is due to the p_B^{CMS} -correction. The bottom right plot shows the distribution of correction values; i.e. the distribution of $-p_B^{\text{CMS}}(\text{beam}) + p_B^{\text{CMS}}(\text{MC})$, the values which have been added to p_B^{CMS} . The average p_B^{CMS} -correction is +25 MeV/c, which reflects the higher beam energy of the Monte Carlo relative to the data. The correction values are distributed over a range of 60 MeV/c, due to the run-dependent drift of the mean beam energies.

After applying the p_B^{CMS} correction to $B^0 \rightarrow J/\psi K_L$ candidates from experimental data, we obtain improved agreement with the p_B^{CMS} spectrum from Monte Carlo, see section 5.6. In section 5.4, we also provide an independent verification of the p_B^{CMS} correction, using a sample of $B^0 \rightarrow J/\psi K_S$ events. For a future $B^0 \rightarrow J/\psi K_L$ analysis with increased statistics, p_B^{CMS} correction after reconstruction may prove insufficiently accurate. It may become necessary to generate charmonium Monte Carlo with run-dependant beam energies, to maintain good agreement between simulation and experiment.

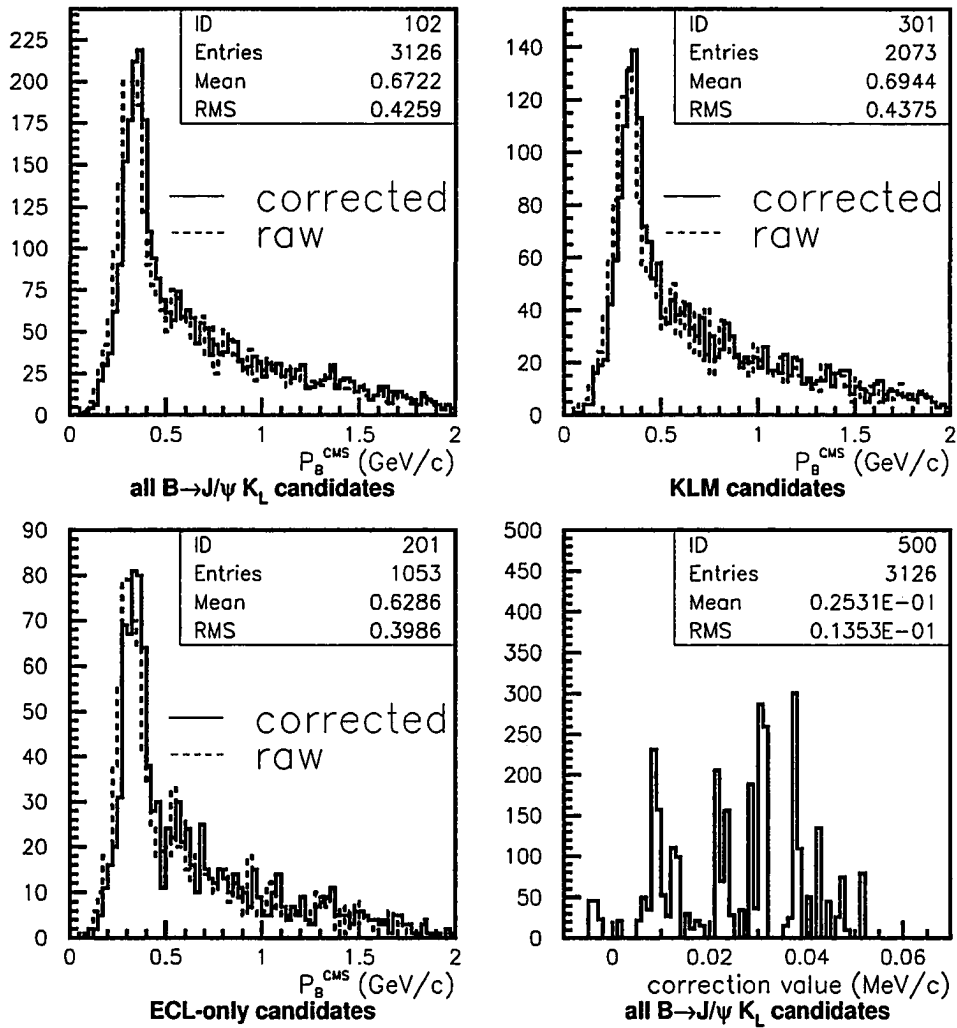


Figure 4.14: Momentum spectra for $B^0 \rightarrow J/\psi K_L$ candidates from Belle experiments 7 through 19, before (dotted) and after (solid) the correction of p_B^{CMS} for drift in the beam energies. Events where the K_L was detected in the KLM (ECL) are also shown separately in the top right (bottom left). The bottom right plot shows the distribution of correction values. See text for discussion.

Chapter 5

Backgrounds in the Event Sample

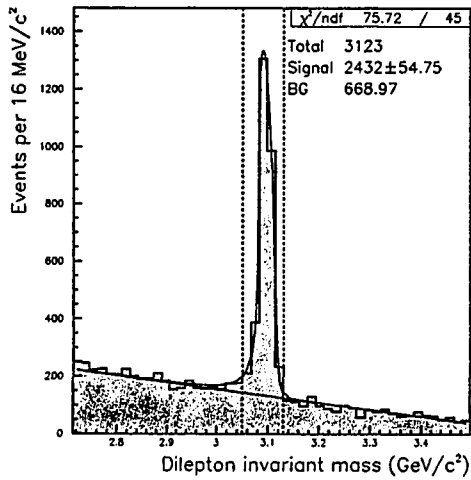
The Standard Model of particle physics predicts a time dependent CP asymmetry in the decay-time distribution of $B^0 \rightarrow J/\psi K_L$ decays, with amplitude equal to $\sin 2\phi_1$. Experimental effects will, however, change the amplitude of the measured asymmetry, so that it no longer equals $\sin 2\phi_1$. To obtain an unbiased measurement, it is necessary to understand and correctly model these effects. The most important ones are wrong flavor assignment during flavor tagging, limited vertex resolution, and the presence of backgrounds (including CP eigenstates) in the final event sample. While wrong-flavor tagging and vertex resolution effects (discussed in chapter 6) are common to all analyses that measure $\sin 2\phi_1$ via $B \rightarrow c\bar{c} K^0$ type decays, $B^0 \rightarrow J/\psi K_L$ poses a special experimental challenge in that the background fraction is large. We therefore devote special attention to backgrounds.

In the present chapter, we use various techniques to estimate the type and magnitude of significant background components. We consider backgrounds from

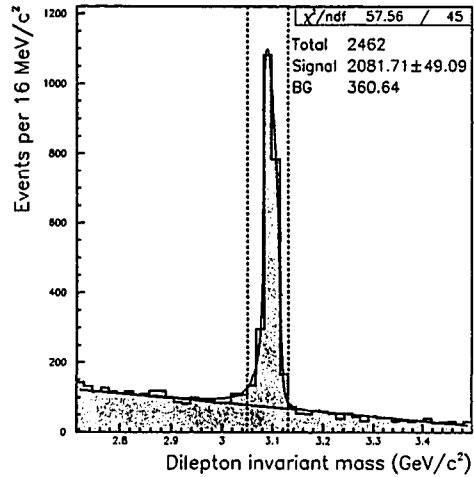
the viewpoint of their p_B^{CMS} distribution. The decay-time distribution of the different backgrounds will be discussed subsequently, in chapter 6.3. We first show that $96 \pm 3\%$ of all candidate events (signal and background alike) contain a real J/ψ . This greatly simplifies the study of the background composition. Roughly half of the fake J/ψ background is shown to be due to non-Upsilon events. We then use a large sample of charmonium inclusive Monte Carlo events to estimate the more detailed composition of events from B decays with a true J/ψ in the final state. We present a number of tests of whether this Monte Carlo actually describes the experimental data properly. We conclude that the simulation models the experiment well, except for the detection efficiency of K_L 's in the KLM. We accommodate this difference in our analysis, by treating backgrounds with a real K_L , and backgrounds with a fake K_L separately. We then determine the normalization of signal and background components from a fit to the observed p_B^{CMS} spectrum. We perform a series of cross checks on these normalizations. These cross checks also confirm that the Monte Carlo distributions we used in the event selection are in good agreement with experimental data.

5.1 Non- J/ψ Background

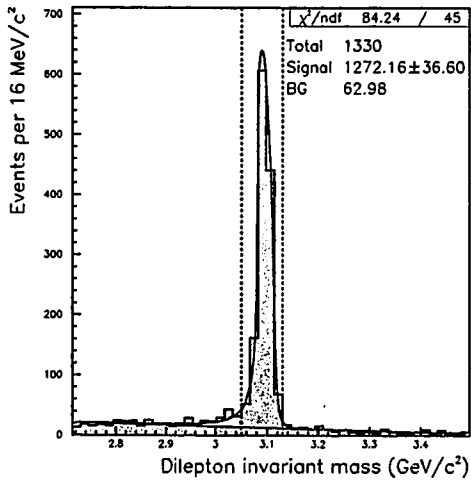
The initial J/ψ selection leaves us with a fair amount of fake J/ψ 's, as shown in figure 4.3. But a fake J/ψ combined with an arbitrary K_L candidate is very unlikely to result in a low calculated value of p_B^{CMS} , which we expect for $B^0 \rightarrow J/\psi K_L$ decays. Thus, candidates with fake J/ψ 's are rejected by the final event selection, which includes the cut $0.2 < p_B^{\text{CMS}} < 0.45$ GeV/c. We can



(a) $0.0 < p_B^{\text{CMS}} < 2.0 \text{ GeV}/c$

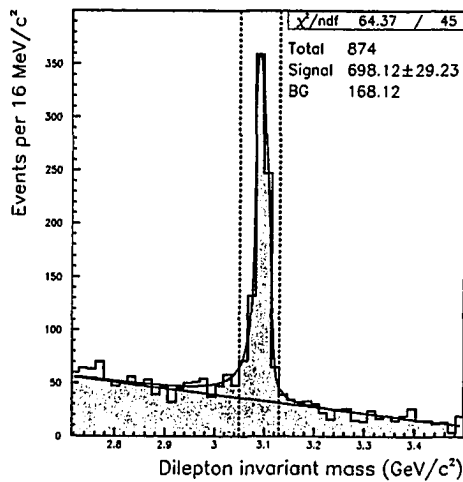


(b) $0.0 < p_B^{\text{CMS}} < 1.0 \text{ GeV}/c$

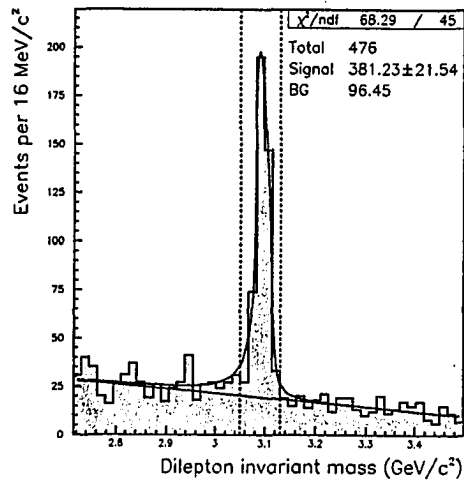


(c) $0.2 < p_B^{\text{CMS}} < 0.45 \text{ GeV}/c$

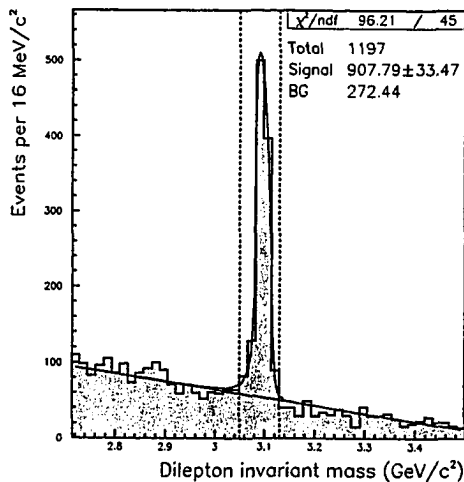
Figure 5.1: Estimation of real and fake (combinatorial) J/ψ components. The histograms show experimental data, while the solid curves show the fitted real (upper) and combinatorial (lower) J/ψ components. Events in the signal region, $3.05 < m_{J/\psi} < 3.13 \text{ GeV}/c$, marked by the dotted vertical lines, are used in the final analysis. The total event yield and fitted signal yield in this region are indicated on each figure. Note how the fake J/ψ fraction goes down as we tighten the p_B^{CMS} cut.



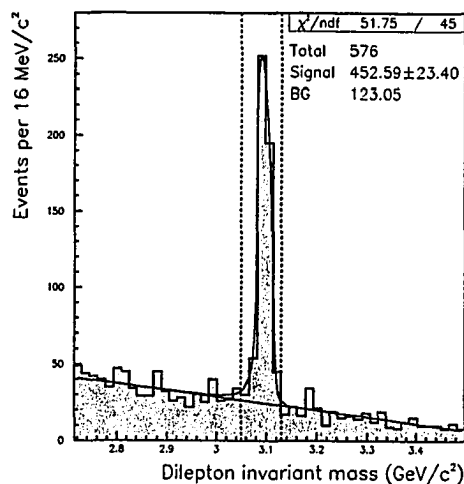
(a) $J/\psi \rightarrow e^+e^-(\gamma)$, K_L detected in KLM



(b) $J/\psi \rightarrow e^+e^-(\gamma)$, K_L detected in ECL only



(c) $J/\psi \rightarrow \mu^+\mu^-$, K_L detected in KLM



(d) $J/\psi \rightarrow \mu^+\mu^-$, K_L detected in ECL only

Figure 5.2: Estimation of combinatorial J/ψ components for $B^0 \rightarrow J/\psi K_L$ candidates from experimental data, with $p_B^{\text{CMS}} < 2.0 \text{ GeV}/c$.

verify this directly from experimental data: figure 5.1 shows the invariant mass distribution of only those J/ψ 's that result in good $B^0 \rightarrow J/\psi K_L$ candidates, when paired up with a good K_L . That requirement alone drastically reduces the combinatorial J/ψ background "under" the J/ψ signal peak, when the sample is limited to events with $p_B^{\text{CMS}} < 2.0 \text{ GeV}/c$. Tighter cuts on the calculated p_B^{CMS} value further reduce the combinatorial background. Restricting the signal region to $0.2 < p_B^{\text{CMS}} < 0.45 \text{ GeV}/c$ (figure 5.1 c), leaves little combinatorial background. The fit indicates that $96 \pm 3\%$ of the 1330 signal candidates contain a real J/ψ .

We can therefore focus our background study on processes producing real J/ψ 's, which are mainly J/ψ -inclusive B meson decays ($e^+e^- \rightarrow \Upsilon(4S) \rightarrow B\bar{B} \rightarrow J/\psi X$). We will also look at a possible contribution from non-Upsilon processes, such as continuum ($e^+e^- \rightarrow q\bar{q} \rightarrow J/\psi X$) events.

In section 5.6 we will estimate the normalization of $B^0 \rightarrow J/\psi K_L$ signal and background components in experimental data, by performing a fit to the p_B^{CMS} spectrum. Here we estimate the normalization of background with fake J/ψ 's in such a way that it can then be held fixed in that fit. This reduces systematic uncertainties related to the signal purity. Since the p_B^{CMS} fit is performed for all candidate events with $p_B^{\text{CMS}} < 2.0 \text{ GeV}/c$, and for ECL-only candidates and KLM candidates separately, we estimate the fake J/ψ fractions for these two subsets separately. Furthermore, we again divide these subsets into $J/\psi \rightarrow e^+e^-$ and $J/\psi \rightarrow \mu^+\mu^-$, since these two decay channels result in different J/ψ mass spectra, due to the possibility of final state radiation in the electron channel. This results in four fits, shown in figures 5.2 a) through d). Table 5.1 summarizes

| Subsample | Real J/ψ | fake J/ψ |
|---------------------|---------------------|--------------------|
| K_L in KLM (+ECL) | 1605.91 ± 44.44 | 467.09 ± 44.44 |
| K_L in ECL only | 833.82 ± 31.80 | 219.18 ± 31.80 |

Table 5.1: Estimated number of real and fake J/ψ 's among $B^0 \rightarrow J/\psi K_L$ candidates with $p_B^{\text{CMS}} < 2.0$ GeV/c, obtained from fits to the J/ψ mass spectra, shown in figures 5.2 a) through d).

the fit results. ¹

5.2 Non-Upsilon Backgrounds

The e^+e^- collisions at KEKB yield significant rates of $e^+e^- \rightarrow q\bar{q}$ (with $q = u, d, c, s$) and non-hadronic processes. To estimate the importance of such non-Upsilon processes, we can make use of off-resonance experimental data, which is e^+e^- collision data taken with \sqrt{s} set 50 to 60 MeV below the $\Upsilon(4S)$ resonance. This reduction in \sqrt{s} ensures that we are below the energy threshold for $q\bar{q} \rightarrow B\bar{B}$ production. At the same time, the 0.5% reduction in \sqrt{s} is small enough, that the rate of other processes remains virtually unchanged. For instance, the cross-sections of $e^+e^- \rightarrow q\bar{q}$ and $e^+e^- \rightarrow l^+l^-$ are proportional to $1/s$, so that the change in rates is about 1%.

We can thus use the off-resonance data to estimate the number of non- $\Upsilon(4S)$ events in the $B^0 \rightarrow J/\psi K_L$ candidate sample from on-resonance data. Figures

¹A careful reader may have noticed that the J/ψ mass distributions for $B^0 \rightarrow J/\psi K_L$ candidates with $p_B^{\text{CMS}} < 2.0$ GeV/c have three (out of 3126) events less in the J/ψ signal region than the p_B^{CMS} spectra shown in other sections. This is because these three events have multiple signal candidates, where the candidate with the best p_B^{CMS} value has a J/ψ mass outside the signal region, and only one candidate per events is shown. This effect is too small to affect the result of our analysis. In table 5.1, these three events have been included in the fake J/ψ category.

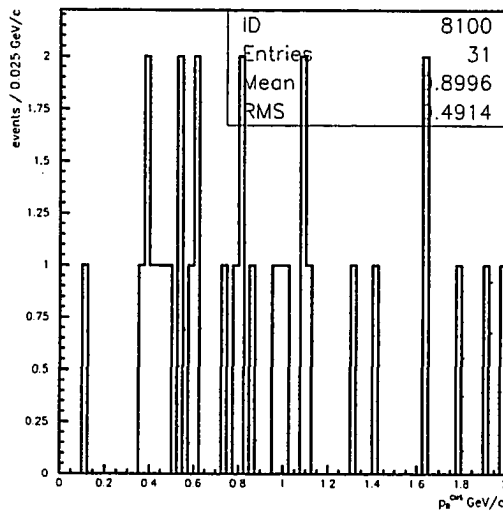


Figure 5.3: “Signal” candidates with the K_L detected in the KLM, after applying the $B^0 \rightarrow J/\psi K_L$ event selection to off-resonance data.

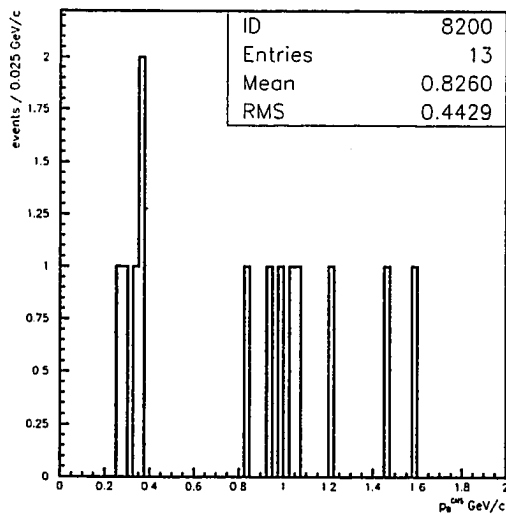
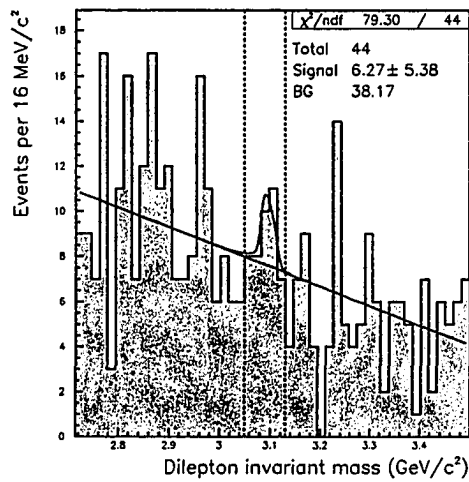


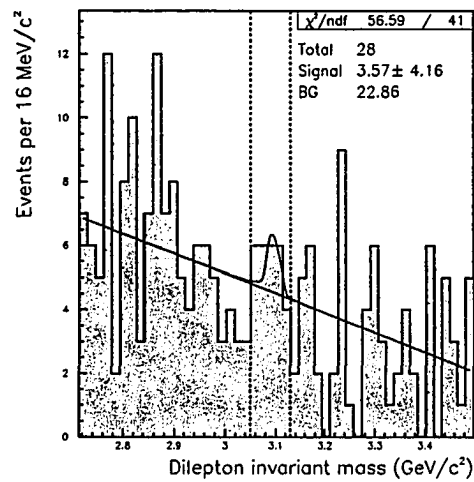
Figure 5.4: “Signal” candidates with the K_L detected in the ECL only, after applying $B^0 \rightarrow J/\psi K_L$ event selection to off-resonance data.

5.3 and 5.4 show the resulting p_B^{CMS} spectra, when applying the regular event selection to 8.83 fb^{-1} of off-resonance data. After all event selection cuts, except for the final cut on p_B^{CMS} , have been applied, 31 KLM candidates, and 13 ECL-only candidates remain. Scaling these yields by the ratio of the on-resonance to the off-resonance luminosity, $78.1 \text{ fb}^{-1} / 8.83 \text{ fb}^{-1}$, we estimate that 274 ± 49 KLM candidates and 114 ± 32 ECL-only candidates out of our 3096 on-resonance candidates with $p_B^{\text{CMS}} < 2.0 \text{ GeV}/c$ are due to non- $\Upsilon(4S)$ processes. (The uncertainties given here are simply the Poisson errors of the off-resonance yields, scaled by the luminosity ratio).

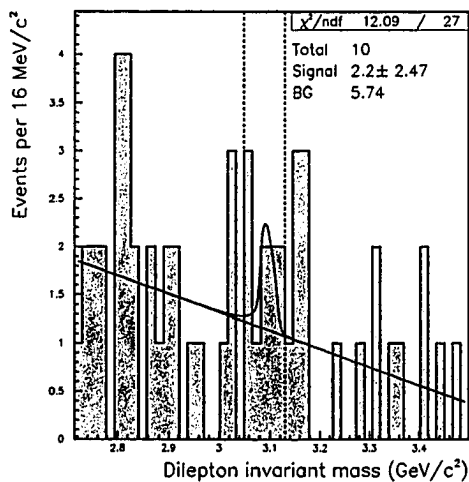
In section 4.3, we showed that there is appreciable J/ψ production in the off-resonance data. This begs us to ask what fraction of the non- $\Upsilon(4S)$ backgrounds in our $B^0 \rightarrow J/\psi K_L$ candidate sample contain real J/ψ 's. We address this question by again looking at the invariant mass distribution. Figures 5.5 a) to c) show the J/ψ mass spectra for those $B^0 \rightarrow J/\psi K_L$ candidates from off-resonance data that pass all event selection cuts, but with wider cuts on p_B^{CMS} and $m_{J/\psi}$, as indicated. ECL-only candidates and KLM candidates are shown together to get increased statistics. The 44 candidates that fall into the J/ψ signal region of figure 5.5 a) (marked by dotted lines on the figure), are thus the same events that are shown in figures 5.3 and 5.4. We perform a fit for the J/ψ signal and background components. There is only a weak hint of a component with real J/ψ 's, at the one-sigma level. Based on this, we continue our analysis with the simplifying assumption that background from non- $\Upsilon(4S)$ processes does not contain real J/ψ 's. This means that we assume the backgrounds due to non-Upsilon processes are a subset of backgrounds due to combinatorial J/ψ 's,



(a) $0.0 < p_B^{\text{CMS}} < 2.0 \text{ GeV}/c$



(b) $0.0 < p_B^{\text{CMS}} < 1.0 \text{ GeV}/c$



(c) $0.2 < p_B^{\text{CMS}} < 0.45 \text{ GeV}/c$

Figure 5.5: Estimation of real and fake (combinatorial) J/ψ components in " $B^0 \rightarrow J/\psi K_L$ " candidates from off-resonance experimental data. The histogram show the data, while the solid curves show the fitted signal and background yields. The total event yield and fitted signal event yield in the region $3.05 < m_{J/\psi} < 3.13 \text{ GeV}/c^2$ is indicated on each figure.

accounting for roughly half of this component, as illustrated by the Venn diagram in figure 5.6 a).

The fits shown in figure 5.5 leave open the possibility that a small fraction of non- $\Upsilon(4S)$ background contains real J/ψ 's. In that case, the non- $\Upsilon(4S)$ background would no longer be a subset of the combinatorial J/ψ background, as illustrated in figure 5.5 b). The total background from non- $\Upsilon(4S)$ processes and fake J/ψ 's combined would in that case be larger than the background due to fake J/ψ 's. This may become significant with increased statistics. In the present analysis, we include this possibility in the systematic error study. The resulting contribution to the total systematic error is small.

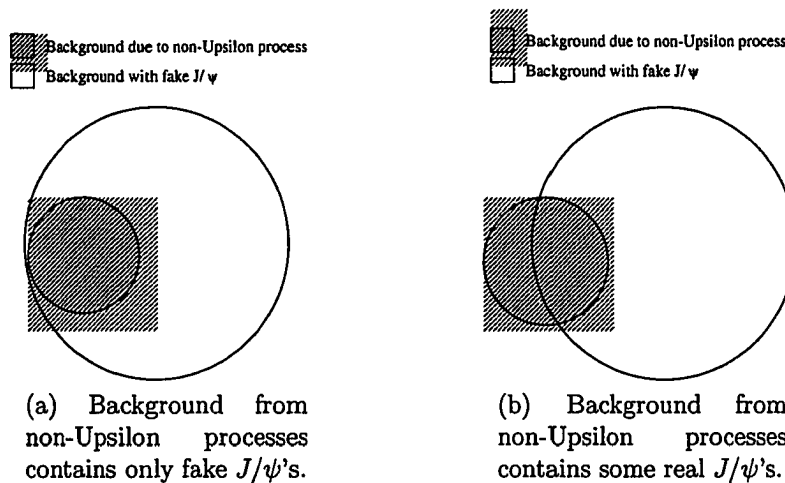


Figure 5.6: If the background from non- $\Upsilon(4S)$ processes doesn't have J/ψ 's in the final state (a), then background due to non- $\Upsilon(4S)$ events is a subset of fake J/ψ backgrounds. In that case, the background estimate obtained from the J/ψ -mass spectrum of $B^0 \rightarrow J/\psi K_L$ signal candidates already includes the whole non- $\Upsilon(4S)$ background. If some of the background from non-Upsilon processes does have real J/ψ 's in the final state (b), then the total background due to non- $\Upsilon(4S)$ events and fake J/ψ events combined can be larger than the estimate obtained from J/ψ -mass spectrum.

| Decay mode | $p_B^{\text{CMS}} < 2.0 \text{ GeV}/c$ | | $0.2 < p_B^{\text{CMS}} < 0.45 \text{ GeV}/c$ | |
|---------------------------|--|------------|---|------------|
| | true K_L | fake K_L | true K_L | fake K_L |
| $J/\psi K_L$ | 25125 | 1123 | 22118 | 102 |
| all background | 25780 | 14371 | 9343 | 2502 |
| $J/\psi K^{*\pm}$ | 9514 | 3263 | 4064 | 489 |
| $J/\psi K^{*0}(K_L\pi^0)$ | 5727 | 745 | 2367 | 118 |
| $J/\psi K^\pm$ | 353 | 1440 | 54 | 333 |
| $J/\psi K_S$ | 473 | 2041 | 56 | 543 |
| $\chi_{C1} K_L$ | 912 | 59 | 459 | 4 |
| $J/\psi \pi^0$ | 57 | 155 | 3 | 62 |
| $\psi(2S) K_L$ | 267 | 18 | 136 | 3 |

Table 5.2: Composition of $B^0 \rightarrow J/\psi K_L$ candidates where the K_L was detected in the KLM, when subjecting 5 Million charmonium inclusive B decay Monte Carlo events to the $B^0 \rightarrow J/\psi K_L$ event selection. Only important background modes are shown explicitly.

5.3 Backgrounds With a Real J/ψ

In section 5.1, we estimated that $96 \pm 3\%$ of our $B^0 \rightarrow J/\psi K_L$ signal candidates are due to decays with a real J/ψ in the final state. We have also concluded that background from non- $\Upsilon(4S)$ processes is included in the non- J/ψ background, meaning that the events with a real J/ψ are all due to B decays. The overall $B^0 \rightarrow J/\psi K_L$ signal purity in our data sample is estimated to be $62 \pm 3\%$ from a fit to the p_B^{CMS} distribution, which is presented in section 5.6. This means that about 34% of the final event sample is background from B meson decays with a real J/ψ in the final state.

In order to obtain an unbiased measurement of $\sin 2\phi_1$, we need to know the composition of such J/ψ inclusive background, in particular the contribution of CP eigenstates other than $B^0 \rightarrow J/\psi K_L$. The branching fractions of many such decays have been measured by both CLEO and the B factories. We use a

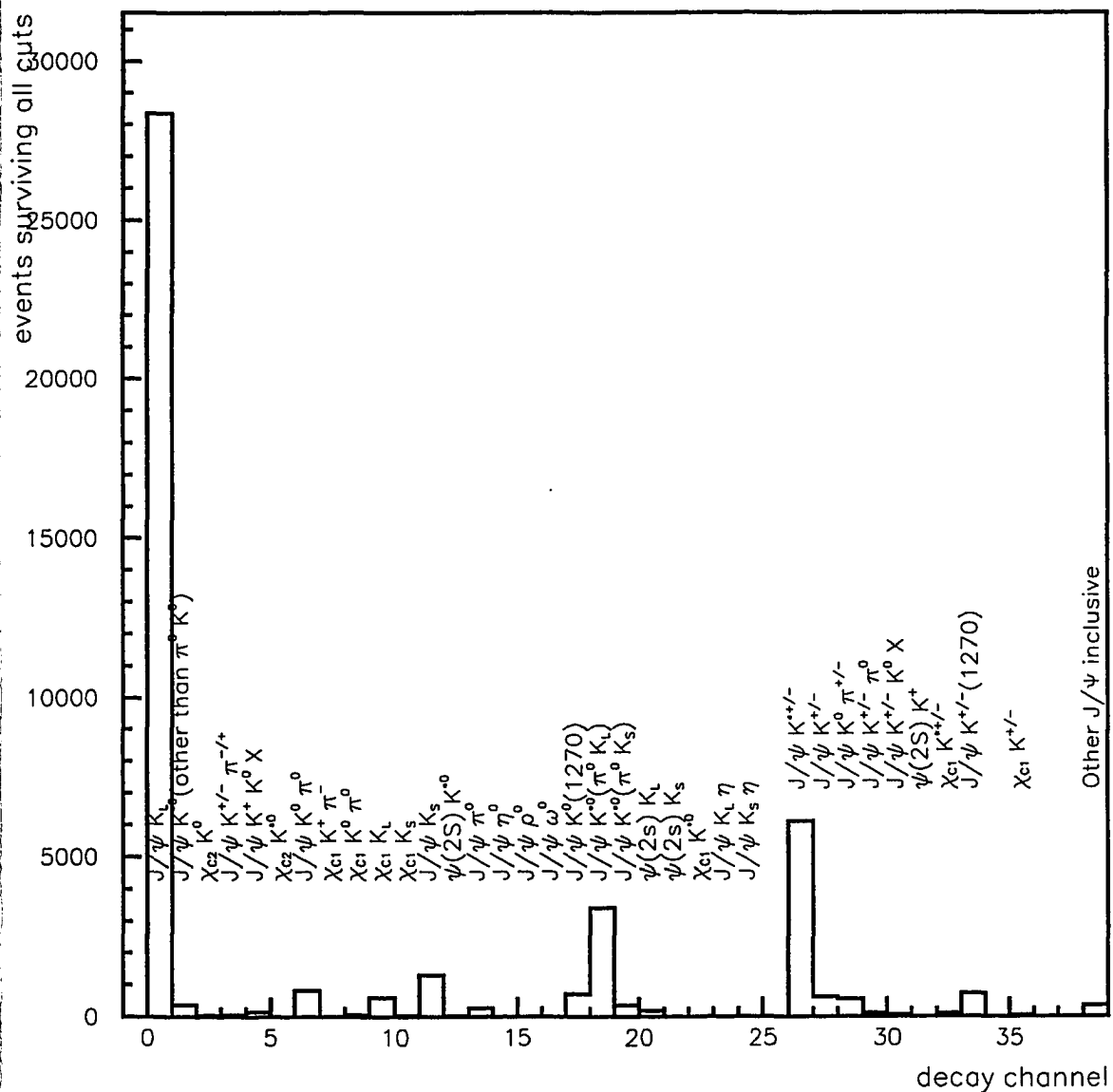


Figure 5.7: Charmonium inclusive Monte Carlo events satisfying all $B^0 \rightarrow J/\psi K_L$ selection criteria, including the cut $0.2 < p_B^{CMS} < 0.45 \text{ GeV}/c$. Events have been classified based on their decay chain at the generator level.

| Decay mode | $p_B^{\text{CMS}} < 2.0 \text{ GeV}/c$ | | $0.2 < p_B^{\text{CMS}} < 0.45 \text{ GeV}/c$ | |
|---------------------------|--|------------|---|------------|
| | true K_L | fake K_L | true K_L | fake K_L |
| $J/\psi K_L$ | 6508 | 261 | 6127 | 15 |
| all background | 7930 | 7339 | 3033 | 2147 |
| $J/\psi K^{*\pm}$ | 2835 | 1462 | 1235 | 316 |
| $J/\psi K^{*0}(K_L\pi^0)$ | 1936 | 331 | 834 | 74 |
| $J/\psi K^\pm$ | 115 | 641 | 22 | 213 |
| $J/\psi K_S$ | 168 | 1552 | 25 | 685 |
| $\chi_{c1} K_L$ | 277 | 14 | 142 | 1 |
| $J/\psi \pi^0$ | 25 | 252 | 8 | 192 |
| $\psi(2S) K_L$ | 73 | 5 | 46 | 2 |

Table 5.3: Composition of $B^0 \rightarrow J/\psi K_L$ candidates where the K_L was detected in the ECL only, when subjecting 5 Million charmonium inclusive B decay Monte Carlo events to the $B^0 \rightarrow J/\psi K_L$ event selection. Only important background modes are shown explicitly.

large Monte Carlo event sample based on the measured branching fractions to determine the acceptance of our analysis to the dominant J/ψ -inclusive B decay products. This Monte Monte Carlo sample generally includes feed down from higher $c\bar{c}$ -resonances, such as $\chi_{c1} \rightarrow \gamma J/\psi$. See Appendix B.2 for further details.

Since the detection efficiency of K_L 's is not very reliably predicted by Monte Carlo, we will consider charmonium inclusive decays with real and fake K_L 's separately, and float their relative normalization in the p_B^{CMS} fit for the signal purity. Since the detection efficiency and fake rate are expected to depend on whether the K_L candidate was detected in the ECL or KLM subdetectors, we further consider KLM candidates (which includes K_L candidates with hits in both subdetectors) and ECL-only candidates separately.

We feed 5 million charmonium inclusive B decay Monte Carlo events through the $B^0 \rightarrow J/\psi K_L$ event selection software, which includes the $B^0 \rightarrow J/\psi K_L$

reconstruction, hadronic event selection, and the level 4 trigger. Lower-level triggers are not simulated, but are not important in this context, since they correspond to looser selection criteria than the hadronic event selection. Figure 5.7 shows the detailed composition of those events that were selected as $B^0 \rightarrow J/\psi K_L$ candidates. The events are classified by their decay channel, which was determined from their associated Monte Carlo event generator information. The decays $B^\pm \rightarrow J/\psi K^{*\pm}$ and $B_d^0 \rightarrow J/\psi K^{*0}$ are the largest single background components after all cuts. The B_d^0 decays into CP eigenstates, such as $B_d^0 \rightarrow J/\psi K^{*0}(K_L\pi^0)$ are especially important in the context of our CP analysis, since they can enhance or dilute the CP asymmetry, depending on their CP eigenvalue. They must thus be treated properly in the CP fit. A more detailed breakdown of the dominant event types, in particular the pure CP eigenstates, is given in tables 5.2 and 5.3. Here, the events are divided further into candidates with true and fake K_L . Any event which contains a K_L at the generator level within 0.3 radians of the reconstructed K_L candidate, is classified as true K_L . The p_B^{CMS} distributions and time dependence of these backgrounds are discussed in more detail in the context of the CP fit in chapter 6.3.2.

5.4 Signal and Background With a True K_L ; Verifying Beam Energy Corrections and Monte Carlo Branching Fractions

How can we gauge whether the charmonium inclusive Monte Carlo provides a good model of J/ψ -inclusive events in experimental data? We may know the dominant background modes, but do the many partial rates used in producing the Monte Carlo sample really provide a realistic inclusive picture of events that pass the $B^0 \rightarrow J/\psi K_L$ selection in experimental data? In particular, how do we know that the p_B^{CMS} spectra predicted by Monte Carlo are realistic?

We first consider the simplest case, where the K_L candidate is a true K_L . Since CP violation in the K system is small, for each decay of the type $B \rightarrow J/\psi K_L X$ (X being any particle, or collection of particles), there is also a decay $B \rightarrow J/\psi K_S X$ with the same partial rate. We can thus reconstruct the K_S modes in such a way that we learn about the K_L modes. Since we can reconstruct both the full momentum and decay vertex of K_S candidates, we have more information in the case of K_S modes than in the case of K_L modes. This allows us to positively identify K_S 's, as well as distinguish between $B \rightarrow J/\psi K_S$ signal and $B \rightarrow J/\psi K_S X$ background in experimental data.

We reconstruct $B \rightarrow J/\psi K_S$ candidates in a way that mimics the $B \rightarrow J/\psi K_L$ reconstruction, as follows: we initially pretend that we don't know the K_S 's energy. Instead, we calculate the K_S 's energy in the same way as we normally would for K_L 's (see chapter 4.5.5). The resulting p_B^{CMS} spectrum

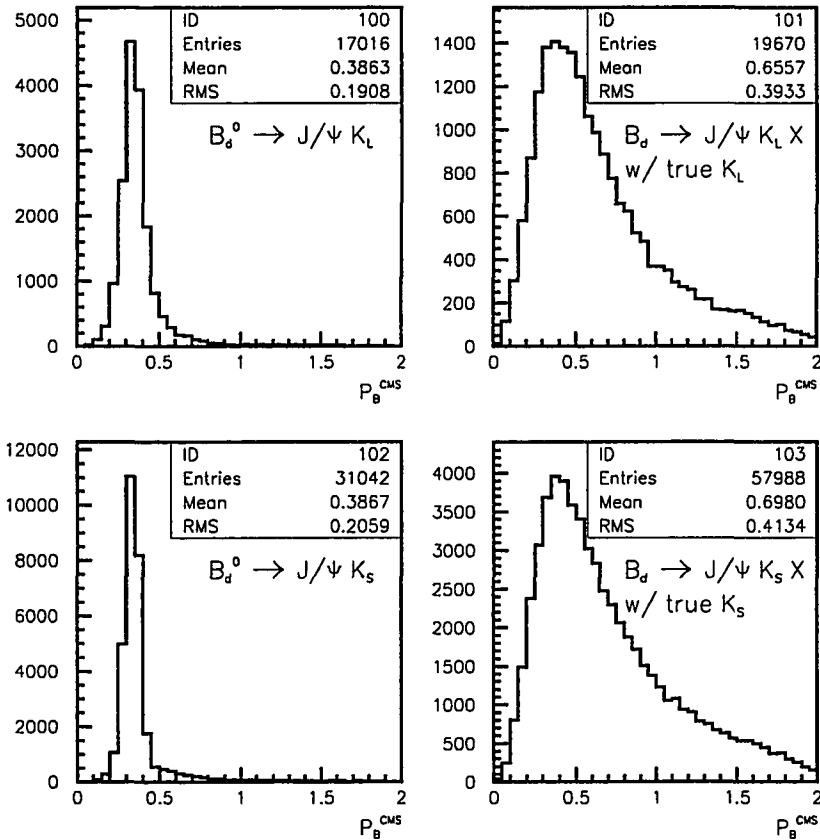


Figure 5.8: Comparison between p_B^{CMS} spectra of $J/\psi K_L$ (upper) and $J/\psi K_S$ (lower) candidates from charmonium inclusive Monte Carlo. Fake K_L 's and K_S 's have been removed using generator information, so that only signal and background with a true kaon remains. To mimic the $J/\psi K_L$ reconstruction, p_B^{CMS} of the $J/\psi K_S$ candidates is calculated ignoring our knowledge of the K_S 's energy. See text for further explanation.

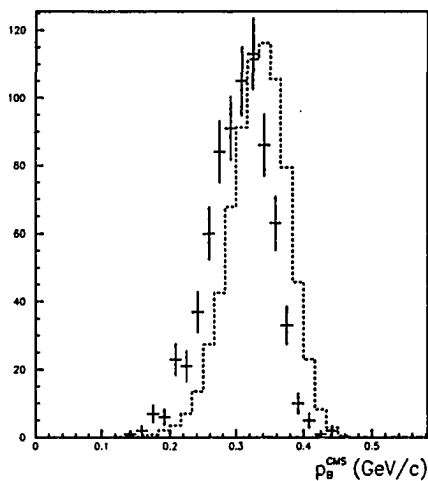
should contain the same $B \rightarrow J/\psi K^0 X$ background modes that we get in the $B^0 \rightarrow J/\psi K_L$ analysis. Since the sources and rates of fake K_L 's and K_S 's are different, only the backgrounds with a true kaon can be expected to be the same in the two analyses. If we want to be able to get the same p_B^{CMS} distribution from $B \rightarrow J/\psi K_S$ as from $B \rightarrow J/\psi K_L$, we need to make sure that the same cuts are applied in the event selection. In practice this is not so easy. For instance, the charged tracks from the K_S need to be intentionally ignored throughout the analysis, in places such as the charged track veto, the inclusive likelihood veto (which uses the number of charged tracks), in the 3-body veto, and so on. The exclusive mode vetoes also need to be turned off, since these are not "symmetric" with respect to K_S 's and K_L 's. K_L 's detected fully or partially in the ECL cannot be used, since the inclusive mode veto makes use of the ECL energy in this case, and there would have been no way to model this for K_S candidates. Generally, we went quite far trying to remove any differences between K_S and K_L modes.

The result of applying the $B^0 \rightarrow J/\psi K_L$ analysis without likelihood veto, and the $B \rightarrow J/\psi K_S$ analysis designed to "mirror" it, to the charmonium Monte Carlo sample, can be seen in figure 5.8. Since this is Monte Carlo, we can remove fake kaons, and separate signal and background, even in the K_L case, using generator information. The two p_B^{CMS} spectra for background with a true kaon are similar, but not identical. The remaining difference is mainly due to a different momentum dependence in the detection efficiencies of K_L 's and K_S 's. The background fraction in the K_S case is larger, because the K_S detection efficiency extends to lower momentum than that of the K_L . Some analysis cuts upstream of the $B^0 \rightarrow J/\psi K_L$ selection, such as the hadronic event selection

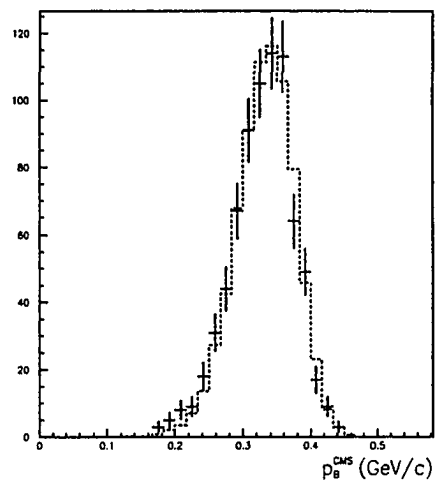
and $R2$ calculation, are also not symmetrical with respect to K_S 's and K_L 's. Differences between the p_B^{CMS} shapes of the $B \rightarrow J/\psi K_L$ and $B \rightarrow J/\psi K_S$ signal are mainly due to the difference in angular resolution of the K_L and K_S detection.

For our purpose, it is not crucial that the p_B^{CMS} shapes of K_S and K_L backgrounds be identical, but that the background samples contain contributions from the same decay channels. The generator information of the Monte Carlo events confirms this is the case. It is crucial, however, that the particular background cocktail predicted by Monte Carlo matches the data. In the $B^0 \rightarrow J/\psi K_L$ case, we can neither separate signal from background, nor separate true from fake K_L 's in experimental data, to check individual components against Monte Carlo. However, in the case of $B \rightarrow J/\psi K_S$, where we ignored the K_S 's energy, we can make use of the K_S energy after reconstruction. This allows us, even in experimental data, to reject fake K_S 's with high accuracy, and to separate $B \rightarrow J/\psi K_S$ signal from $B \rightarrow J/\psi K_S X$ background with a true K_S . Fake K_S 's are rejected with a cut on the invariant mass of $K_S \rightarrow \pi\pi$ candidates. $B \rightarrow J/\psi K_S$ signal and background are separated by requiring $|\Delta E| < 50 \text{ MeV}/c$ and $5.27 < M_{bc} < 5.29 \text{ GeV}/c^2$ for signal. (ΔE and M_{bc} are defined in chapter 4.5.2. They can only be measured independently, if the K_S energy is measured.)

After separating signal and background in both Monte Carlo and experiment with the abovementioned cuts, the p_B^{CMS} distributions from simulation and experiment can be compared. The result is shown in figures 5.9 (signal) and 5.10 (background). After subtracting the differing fake J/ψ components in data and Monte Carlo (which have been constrained in the manner described in chap-



(a) Before p_B^{CMS} correction.



(b) After p_B^{CMS} correction.

Figure 5.9: Comparison between p_B^{CMS} spectra of $B \rightarrow J/\psi K_S$ signal candidates from charmonium inclusive Monte Carlo (dotted histogram) and experimental data (points with error). In order to mimic the $J/\psi K_L$ reconstruction, p_B^{CMS} of the $J/\psi K_S$ candidates is calculated, ignoring our knowledge of the K_S 's energy. The left and right histograms show the same candidates, before and after correcting p_B^{CMS} for drift in the accelerator beam energies. See text for further discussion.

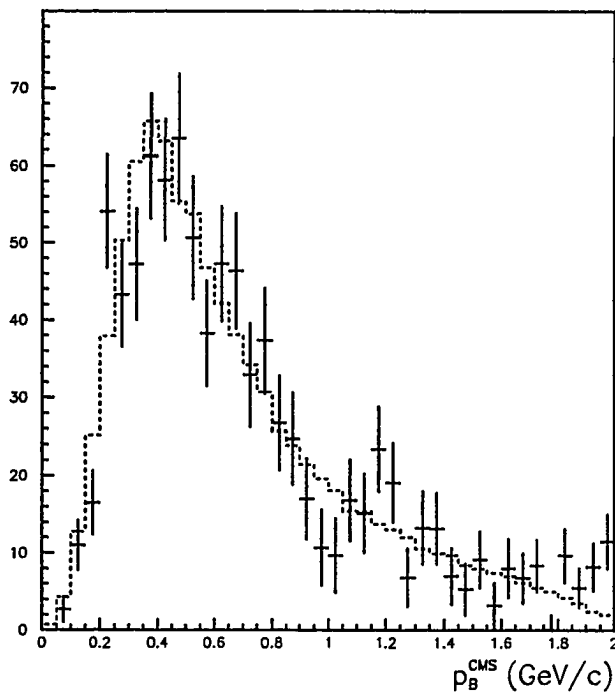


Figure 5.10: Comparison between p_B^{CMS} spectra of $B \rightarrow J/\psi K_S$ background from charmonium inclusive Monte Carlo (dotted histogram) and experimental data (points with error). In order to mimic the $J/\psi K_L$ reconstruction, p_B^{CMS} of the $J/\psi K_S$ candidates is calculated, ignoring our knowledge of the K_S 's energy. Both distributions have been background subtracted for a fake J/ψ component. The statistical errors shown are based on the pre-subtracted event yield. See text for further explanation.

ter 5.1), the p_B^{CMS} spectra from experiment and Monte Carlo agree well. The width of the signal distribution (figure 5.9) is dominated by angular resolution and beam energy fluctuations. The general shape agrees well between data and Monte Carlo, indicating that these effects are properly modeled in the simulation. The signal peak position depends on the mean beam energy. Note how the beam energy correction of p_B^{CMS} (see chapter 4.5.6) shifts the experimental distribution in figure 5.9, and brings it into good agreement with the Monte Carlo distribution, validating our correction method. A small excess of events is seen in the Monte Carlo distribution at low p_B^{CMS} . We include a possible difference between simulation and experiment in the low p_B^{CMS} region in our systematic error study. The agreement between simulation and experiment for background with a true K_S (figure 5.10) is a nice confirmation that the branching fractions used in our charmonium Monte Carlo generation are realistic. It also is an indication that the many variables used in the event selection, and specifically those used to calculate the inclusive likelihood veto, are realistically modeled. We show additional, explicit checks of the latter in section 5.8. There is a small excess of events in the observed background distribution at $p_B^{\text{CMS}} > 1.8$ GeV/c. This is due to a small component of events with fake K_S 's, which has not been subtracted.

5.5 Background with a fake K_L ; Verifying Monte Carlo Fake Rates

In the previous section, we verified that the p_B^{CMS} spectrum of $B^0 \rightarrow J/\psi K_L$ candidates where a true kaon is detected, is well described by Monte Carlo. This

suggests that the many branching fractions used to produce charmonium inclusive Monte Carlo are realistic, and that things are under control at the generator level. We proceed to assess whether K_L fake rates in the Monte Carlo are realistic as well. The fake rate in Monte Carlo could be off if there are problems at the detector simulation level. We could also have unexpectedly large backgrounds with fake K_L 's in the experiment, if there are important background sources that have not have been included in the Monte Carlo.

For K_L 's, we have no mass measurement, and thus cannot determine the fraction of fake particles directly, as we did in the case of J/ψ 's. Instead, we study backgrounds with fake K_L 's that pertain to our analysis via a less direct method, the "method of rotated K_L 's". The basic idea is that during reconstruction of $B^0 \rightarrow J/\psi K_L$, we rotate all K_L candidates 180 degrees around the beam axis in software, before we combine them with J/ψ candidates and calculate p_B^{CMS} as usual. (All cuts related directly to the K_L cluster and its environment, such as the charged track veto, are applied before rotating.) The net effect of rotating the K_L 's is a strong suppression of candidates with real K_L 's, resulting in a sample of $B^0 \rightarrow J/\psi K_L$ candidates where the K_L 's are largely fake. This allows us to compare backgrounds with fake K_L 's in experimental data and Monte Carlo.

The idea behind the K_L rotation, is that it on average tends to suppress (move to higher p_B^{CMS}) events where the K_L and the J/ψ direction are correlated. On the other hand, event types where the J/ψ and K_L direction are not correlated should remain unaffected by the rotation of the K_L 's, with the p_B^{CMS} distributions in these events remaining unchanged. These "uncorrelated" events are largely events with fake K_L 's. This makes intuitive sense for backgrounds due to "random" fake K_L 's,

such as machine background due to beam/gas interactions. We don't expect the direction of these K_L 's to be correlated with the direction of other particles in the event. Since such backgrounds are expected to be symmetrically distributed in ϕ , we expect them to be statistically unaffected by the K_L rotation. Other event types where we expect the K_L and J/ψ direction to be uncorrelated, are combinatorial J/ψ events, and $\Upsilon(4S) \rightarrow BB$ events where the J/ψ and K_L candidates (either true or fake) come from different B mesons.

On the other hand, we expect some correlation between the J/ψ and the K_L direction, when both particles have a common parent (or grandparent) particle. Examples of this would be decays of the type $B \rightarrow J/\psi K_L X$, $B \rightarrow J/\psi X$ followed by $X \rightarrow K_L Y$, and $B \rightarrow J/\psi X$ with X resulting in a fake K_L . More generally, any $\Upsilon(4S) \rightarrow BB$ decay where only one of the B 's gives rise to both the J/ψ and the K_L candidate (either a true or fake K_L), should result in the J/ψ and K_L direction being correlated.

The extent to which the rotation method works has been checked by Monte Carlo. The result is shown in figure 5.11. By comparing the upper left and lower left histograms, we see that as a result of applying the K_L rotation, the "correlated events" are highly suppressed, and make up only 15% of the event sample obtained after rotating, while the "uncorrelated events" remain largely unaffected. Furthermore, by comparing reconstructed K_L candidates against Monte Carlo generator level information, we learn that about two thirds of the "uncorrelated events" contain a fake K_L . This result is encouraging. It means that the p_B^{CMS} spectrum obtained after rotating the K_L candidates, can be used to obtain a rough estimate of the shape and normalization of combinatorial background due

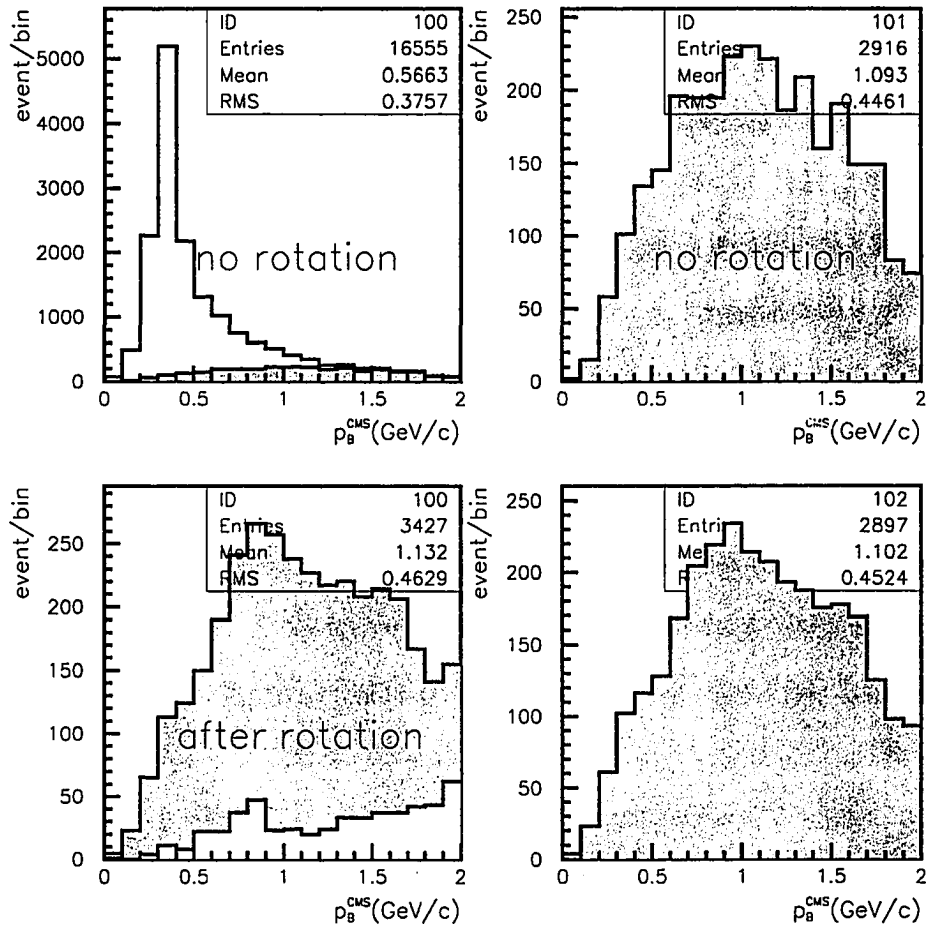


Figure 5.11: Monte Carlo study with charmonium inclusive B decays, to demonstrate the effect of rotating the K_L candidates 180 degrees around the beam axis, before reconstructing $B^0 \rightarrow J/\psi K_L$ and calculating p_B^{CMS} as usual. The filled part of each histogram shows those events where the K_L and J/ψ candidates are due to two different B mesons, while the white parts shows those events for which both candidates are due to the same B meson. The upper plots show the p_B^{CMS} spectrum obtained without rotation, while the lower plots show the resulting p_B^{CMS} spectrum for the same data sample, when the K_L 's are first rotated. The right plots show only those events where the J/ψ and K_L come from separate B mesons. The p_B^{CMS} distributions of these events appears largely unaffected by the K_L rotation, while other event types are highly suppressed.

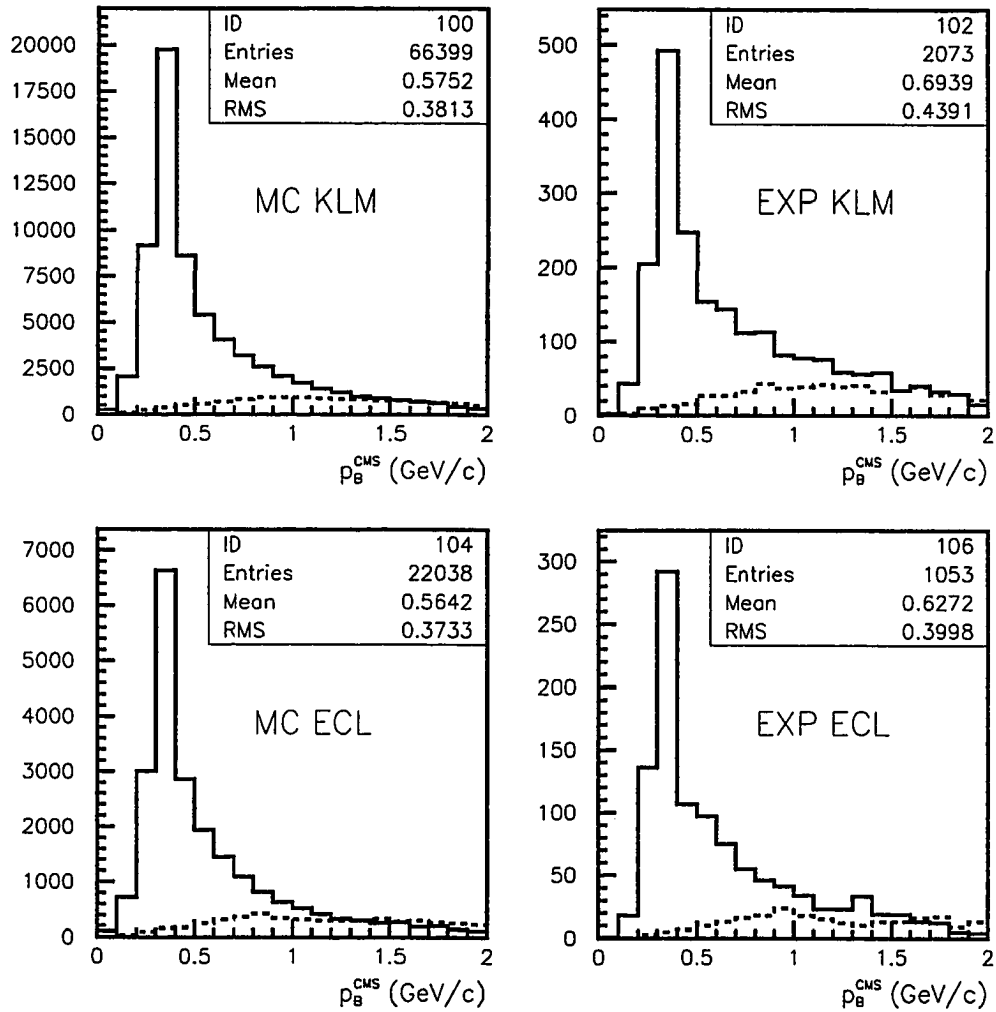


Figure 5.12: p_B^{CMS} distributions of $B^0 \rightarrow J/\psi K_L$ candidates from charmonium Monte Carlo (left) and experimental data (right). KLM candidates (upper) and ECL-only candidates (lower) are shown separately. The solid histograms are the result of regular $B^0 \rightarrow J/\psi K_L$ reconstruction, while the superimposed, dotted histograms are the result of rotating all K_L 's in each data sample 180 degrees around the beam axis before running the reconstruction.

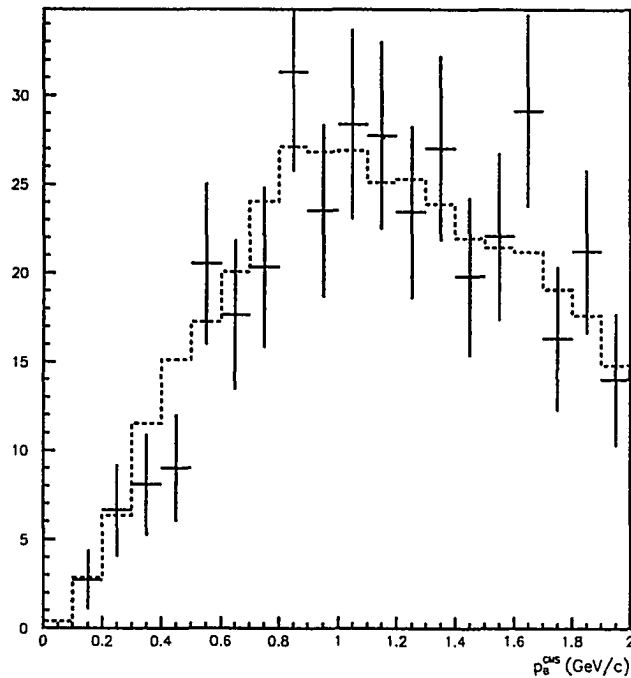


Figure 5.13: p_B^{CMS} spectra for $B^0 \rightarrow J/\psi K_L$ candidates (with the K_L detected in the KLM) from charmonium inclusive Monte Carlo (dotted) and experimental data (points with errors). K_L candidate were rotated 180 degrees around the beam axis before reconstruction, which suppresses real K_L 's. The agreement between Monte Carlo and experiment confirms that fake- K_L backgrounds are properly modeled in Monte Carlo.

to combining J/ψ 's with random (and to a large extent fake) K_L 's. Since we can easily rotate the K_L candidates in experimental data as well, we proceed to compare experiment and simulation.

Figure 5.12 shows the p_B^{CMS} spectra obtained by running the $B^0 \rightarrow J/\psi K_L$ event selection on Monte Carlo and experimental data, with and without rotating the K_L candidates. Candidate events with K_L 's detected in the KLM are shown separately from those where the K_L was detected in the ECL only, since we

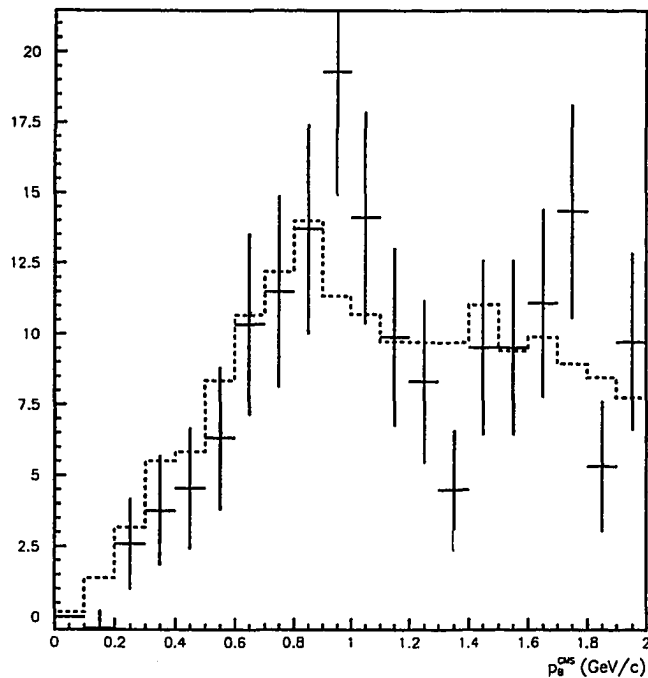


Figure 5.14: p_B^{CMS} spectra for $B^0 \rightarrow J/\psi K_L$ candidates (with the K_L detected in the ECL only) from charmonium inclusive Monte Carlo (dotted) and experimental data (points with errors). K_L candidate were rotated 180 degrees around the beam axis before reconstruction, which suppresses real K_L 's. The general agreement between Monte Carlo and experiment confirms that fake- K_L backgrounds are properly modeled in Monte Carlo, although there may be a small discrepancy at low p_B^{CMS} values. See text for discussion.

| | total | signal | | background | | |
|-------------------|-------|------------|------------|------------|------------|---------------|
| | | true K_L | fake K_L | true K_L | fake K_L | fake J/ψ |
| MC, KLM, regular | 66399 | 25125 | 1123 | 25780 | 14371 | $\approx 1\%$ |
| MC, KLM, rotated | 12710 | 736 | 1104 | 3838 | 7032 | $\approx 1\%$ |
| MC, ECL, regular | 22038 | 6508 | 261 | 7930 | 7339 | $\approx 1\%$ |
| MC, ECL, rotated | 5055 | 406 | 455 | 1162 | 3032 | $\approx 1\%$ |
| exp, KLM, regular | 2073 | | | | | 427 |
| exp, KLM, rotated | 551 | | | | | 182 |
| exp, ECL, regular | 1053 | | | | | 206 |
| exp, ECL, rotated | 232 | | | | | 64 |

Table 5.4: Raw yields of $B^0 \rightarrow J/\psi K_L$ candidates with $p_B^{\text{CMS}} < 2.0 \text{ GeV}/c$ from charmonium inclusive Monte Carlo and experimental data. “Regular” refers to candidates remaining after the nominal event selection, while “rotated” refers to candidates obtained when K_L candidates are rotated 180 degrees around the beam axis before the event selection.

| | yield regular | yield rotated | rotated/regular |
|---------------------------|---------------|---------------|-----------------|
| K_L in KLM, experiment | 1646 | 369 | 0.224 |
| K_L in KLM, Monte Carlo | 42514 | 10564 | 0.248 |
| K_L in ECL, experiment | 847 | 168 | 0.198 |
| K_L in ECL, Monte Carlo | 23134 | 5174 | 0.224 |

Table 5.5: Adjusted yield of $B^0 \rightarrow J/\psi K_L$ candidates from experimental data and charmonium inclusive Monte Carlo. The data samples used for this table are the same as those used to make table 5.4, but with fake J/ψ components subtracted, and Monte Carlo components rescaled to account for the discrepancy in K_L reconstruction efficiency. (See text for more details.)

expect different fake rates for these two classes of K_L 's. Table 5.4 shows a more detailed breakdown of the same events. For a comparison between experiment and simulation to be meaningful, we must first deal with two known limitations of the simulation. First, the charmonium inclusive Monte Carlo contains a true J/ψ in each event. (Although some combinatorial J/ψ 's arise during reconstruction, this component is only about 1% of reconstructed events.) In order to compare Monte Carlo and experimental data, we therefore need to estimate and subtract out the fake J/ψ component in experimental data. This is done by performing a fit to the J/ψ mass distribution of each data sample, using the same procedure as in chapter 5.1. Second, the K_L detection efficiency in the KLM is known to be higher in Monte Carlo than in the experiment. This has been observed both for $B^0 \rightarrow J/\psi K_L$ and $e^+e^- \rightarrow \phi\gamma, \phi \rightarrow K_L K_S$ events [22]. As show in chapter 5.8, the K_L detection efficiency in the KLM is about 47% lower than the Monte Carlo prediction. As a consequence, a somewhat larger fraction of K_L 's than predicted (about 7%), is detected in the ECL only.

Table 5.5 summarizes event yields that follow from table 5.4, after subtracting the fake J/ψ component from experimental event yields, and after rescaling the normalization of Monte Carlo components to correct for the discrepancy between K_L detection efficiencies in data and Monte Carlo. We see from table 5.5 that after these adjustments, the fraction of rotated to unrotated candidate events agree at the 10% (or roughly 1.5σ) level between experimental data and simulation. The K_L fake rate in both the KLM and ECL detectors is well described in the simulation. Finally, figures 5.13 and 5.14 compare the p_B^{CMS} spectra of "rotated- K_L -events" from Monte Carlo and experimental data. Again, Monte

Carlo distributions have been rescaled to account for the discrepancy in K_L detection efficiency, and the distributions from experimental data have been background subtracted for fake J/ψ 's. Generally, the p_B^{CMS} shape predicted by Monte Carlo matches the distribution observed in the experiment well.

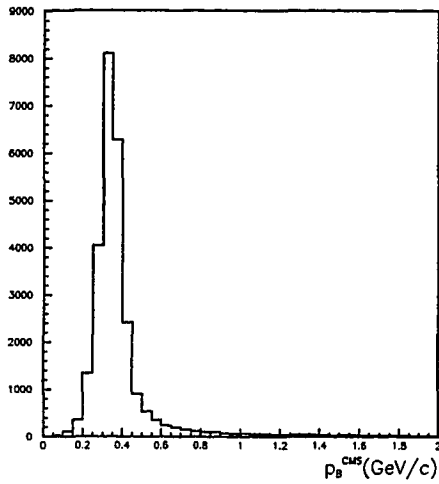
In the case of K_L 's detected in the ECL only however, there may be a small discrepancy for $p_B^{\text{CMS}} < 200 \text{ MeV}/c$. While this difference is not statistically significant, a similar but larger discrepancy is seen when comparing the "unrotated" p_B^{CMS} spectra in experiment and simulation, see figure 5.18 in the next section. We include a possible difference between simulation and experiment in the low p_B^{CMS} region in our systematic error study.

5.6 Estimation of Signal and Background Normalizations

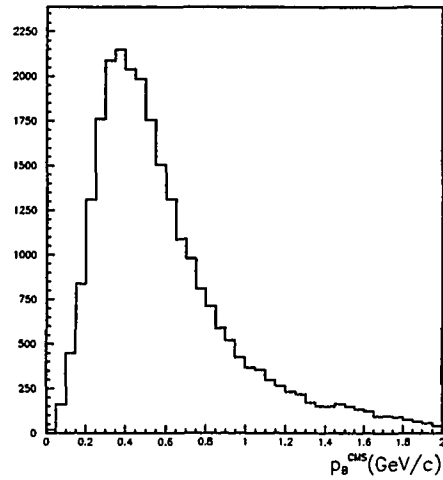
To estimate the $B^0 \rightarrow J/\psi K_L$ signal purity, as well as the relative normalization of different backgrounds in experimental data, we perform a binned likelihood fit to the p_B^{CMS} distribution of $B^0 \rightarrow J/\psi K_L$ candidates with $p_B^{\text{CMS}} < 2.0 \text{ GeV}/c$. In this fit, we allow the normalization of three components to vary:

1. $B^0 \rightarrow J/\psi K_L$ signal
2. $B \rightarrow J/\psi K_L X$ backgrounds where the K_L candidate is a true K_L
3. $B \rightarrow J/\psi K_L X$ backgrounds where the K_L candidate is a fake K_L

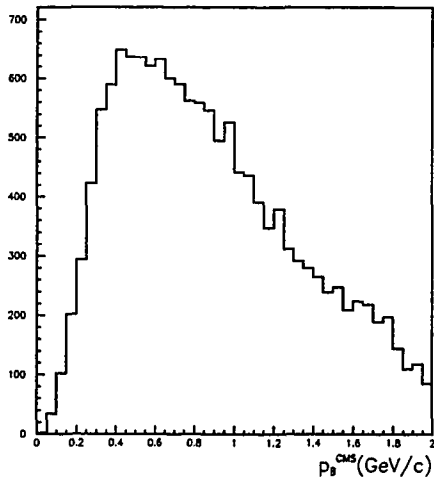
The p_B^{CMS} position of the $B^0 \rightarrow J/\psi K_L$ signal peak is also allowed to vary in the fit. The normalization of a fourth component, events with a combinatorial



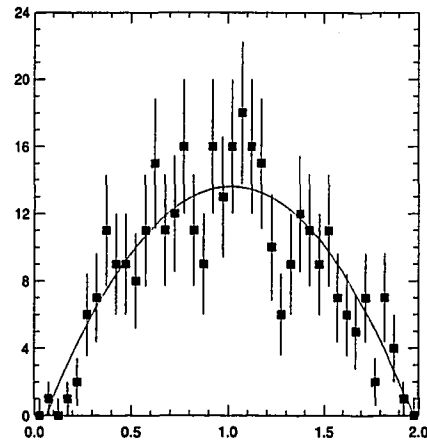
(a) $B^0 \rightarrow J/\psi K_L$ signal



(b) $B \rightarrow J/\psi K_L X$, true K_L

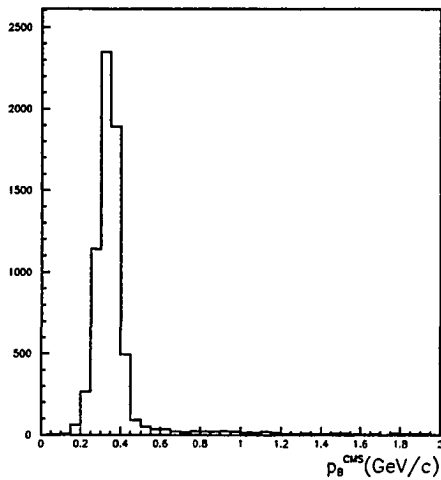


(c) $B \rightarrow J/\psi K_L X$, fake K_L

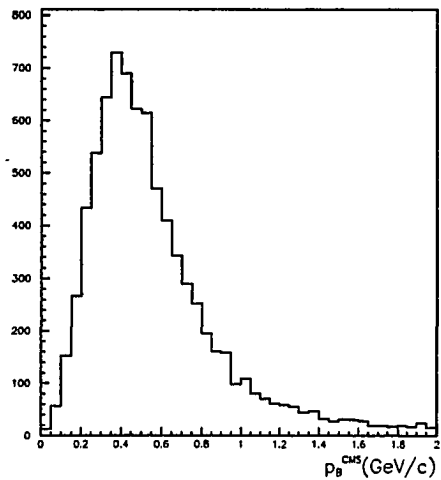


(d) Combinatorial J/ψ background

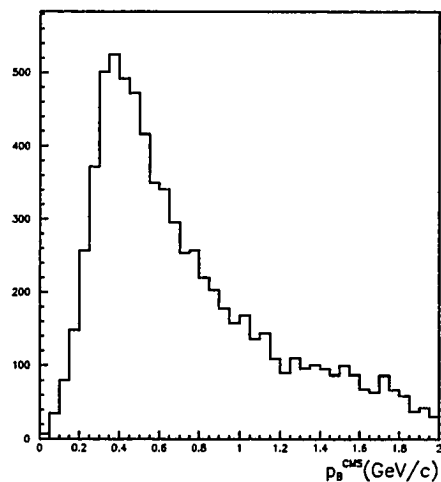
Figure 5.15: p_B^{CMS} shapes for $B^0 \rightarrow J/\psi K_L$ signal and various background components, for the case that the K_L candidate was detected in the KLM detector. Shapes a) through c) are Monte Carlo predictions. The combinatorial J/ψ background shape is estimated using $e\mu$ pairs from experimental data. See text for further discussion.



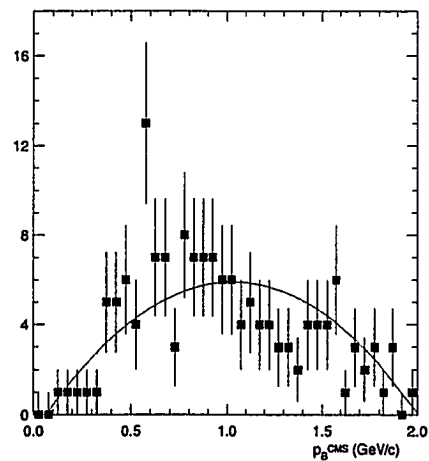
(a) $B^0 \rightarrow J/\psi K_L$ signal



(b) $B \rightarrow J/\psi K_L X$, true K_L



(c) $B \rightarrow J/\psi K_L X$, fake K_L



(d) Combinatorial J/ψ background

Figure 5.16: p_B^{CMS} shapes for $B^0 \rightarrow J/\psi K_L$ signal and various backgrounds, for the case that the K_L candidate was detected only in the ECL subdetector. Shapes a) through c) are Monte Carlo predictions. The combinatorial J/ψ background shape is estimated using $e\mu$ pairs from experimental data. See text for further discussion.

MINUIT Likelihood Fit to Plot

9999&0

v3: exp 7-19 P_B^* (corr) KLM
 File: pbcn_ichep2002.hbk
 Plot Area Total/Fit 2073.0 / 2073.0
 Func Area Total/Fit 2081.0 / 2081.0

11-MAY-2003 13:35
 Fit Status 3
 E.D.M. 2.118E-20

Likelihood = 37.3

$\chi^2 = 35.4$ for 40 - 4 d.o.f.,

C.L. = 49.5%

| Errors | | Parabolic | Minos | |
|------------------------------|-------------|--------------------|--------------|--------------|
| Function 1: Smooth Histogram | 1 | 0(1) Normal errors | | |
| NORM | 637.51 | ± 46.10 | - 45.78 | + 46.42 |
| OFFSET | 1.09882E-02 | $\pm 3.7925E-03$ | - 3.7960E-03 | + 3.7953E-03 |
| Function 2: Histogram | 2 | 0 Normal errors | | |
| NORM | 497.24 | ± 93.68 | - 93.19 | + 94.19 |
| Function 3: Histogram | 3 | 0 Normal errors | | |
| NORM | 479.42 | ± 75.37 | - 74.74 | + 76.01 |
| Function 4: POLY | | | | |
| *MN-NORM | -33.788 | $\pm 0.$ | - 0. | + 0. |
| *MN-P1 | 590.03 | $\pm 0.$ | - 0. | + 0. |
| *MN-P2 | -290.09 | $\pm 0.$ | - 0. | + 0. |
| *MN-OFFSET | 0. | $\pm 0.$ | - 0. | + 0. |
| *REAL-NORM | 1.3736 | $\pm 0.$ | - 0. | + 0. |

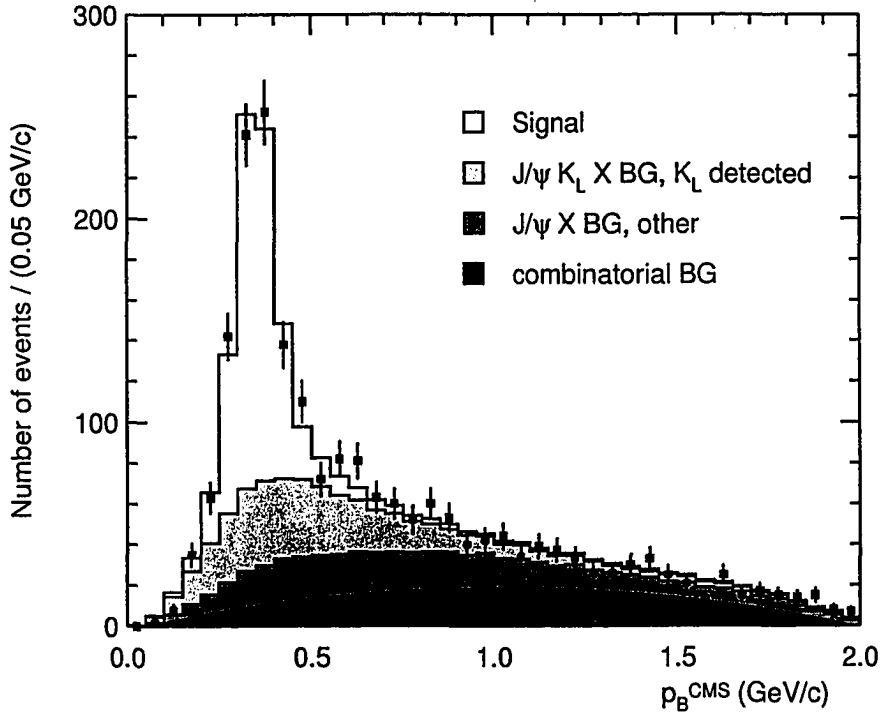


Figure 5.17: Fit to determine the signal and background normalizations among $B^0 \rightarrow J/\psi K_L$ candidates from Belle experiments 7 through 19, for those events where the K_L candidate was detected fully or partially in the KLM detector. The data points with error show the experimental data, while the fit result has been superimposed.

MINUIT Likelihood Fit to Plot

9999&0

v3: exp 7-19 P_B^* (corr) ECL
 File: pbcn_ichep2002.hbk
 Plot Area Total/Fit 1053.0 / 1053.0
 Func Area Total/Fit 1053.5 / 1053.5

11-MAY-2003 13:48
 Fit Status 3
 E.D.M. 8.425E-13

Likelihood = 49.2

$\chi^2 = 44.3$ for 40 - 4 d.o.f.,

C.L. = 16.2%

| Errors | | Parabolic | | Minos | |
|------------------------------|-------------|------------------|---------------|-------|---------|
| Function 1: Smooth Histogram | 1 | 0(1) | Normal errors | | |
| NORM | 325.63 | \pm 27.89 | - | 27.59 | + 28.22 |
| OFFSET | 1.35587E-09 | \pm 1.7915E-08 | - | 0. | + 0. |
| Function 2: Histogram | 2 | 0 | Normal errors | | |
| NORM | 341.69 | \pm 83.86 | - | 84.33 | + 83.59 |
| Function 3: Histogram | 3 | 0 | Normal errors | | |
| NORM | 166.95 | \pm 81.88 | - | 80.51 | + 83.40 |
| Function 4: POLY | | | | | |
| *MN-NORM | -15.764 | \pm 0. | - | 0. | + 0. |
| *MN-P1 | 258.70 | \pm 0. | - | 0. | + 0. |
| *MN-P2 | -125.02 | \pm 0. | - | 0. | + 0. |
| *MN-OFFSET | 0. | \pm 0. | - | 0. | + 0. |
| *REAL-NORM | 1.4328 | \pm 0. | - | 0. | + 0. |

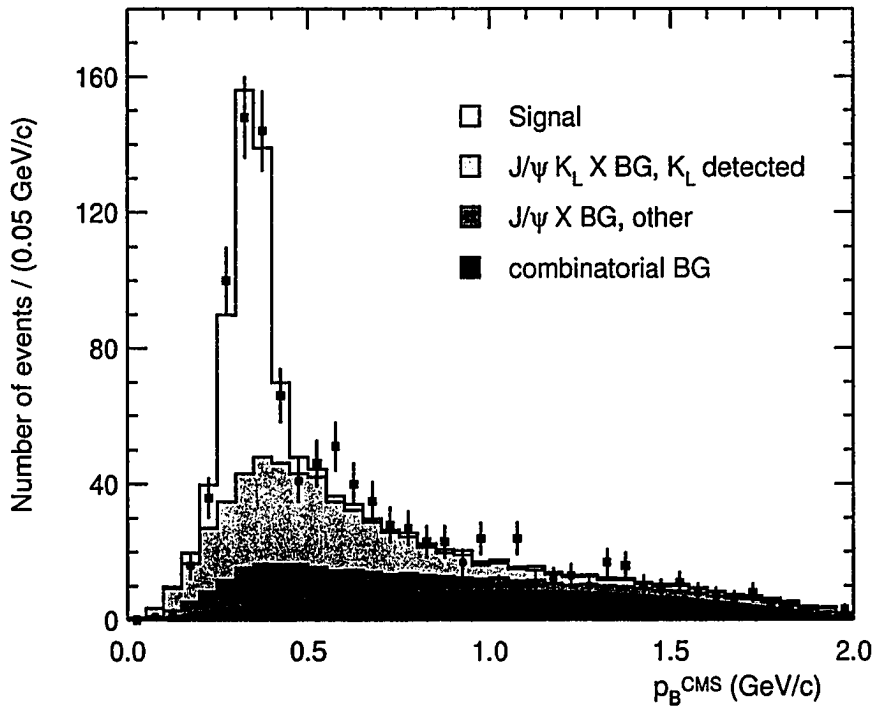


Figure 5.18: Fit to determine the signal and background normalizations among $B^0 \rightarrow J/\psi K_L$ candidates from Belle experiments 7 through 19, for those events where the K_L candidate was detected only in the ECL detector. The data points with error show the experimental data, while the fit result has been superimposed.

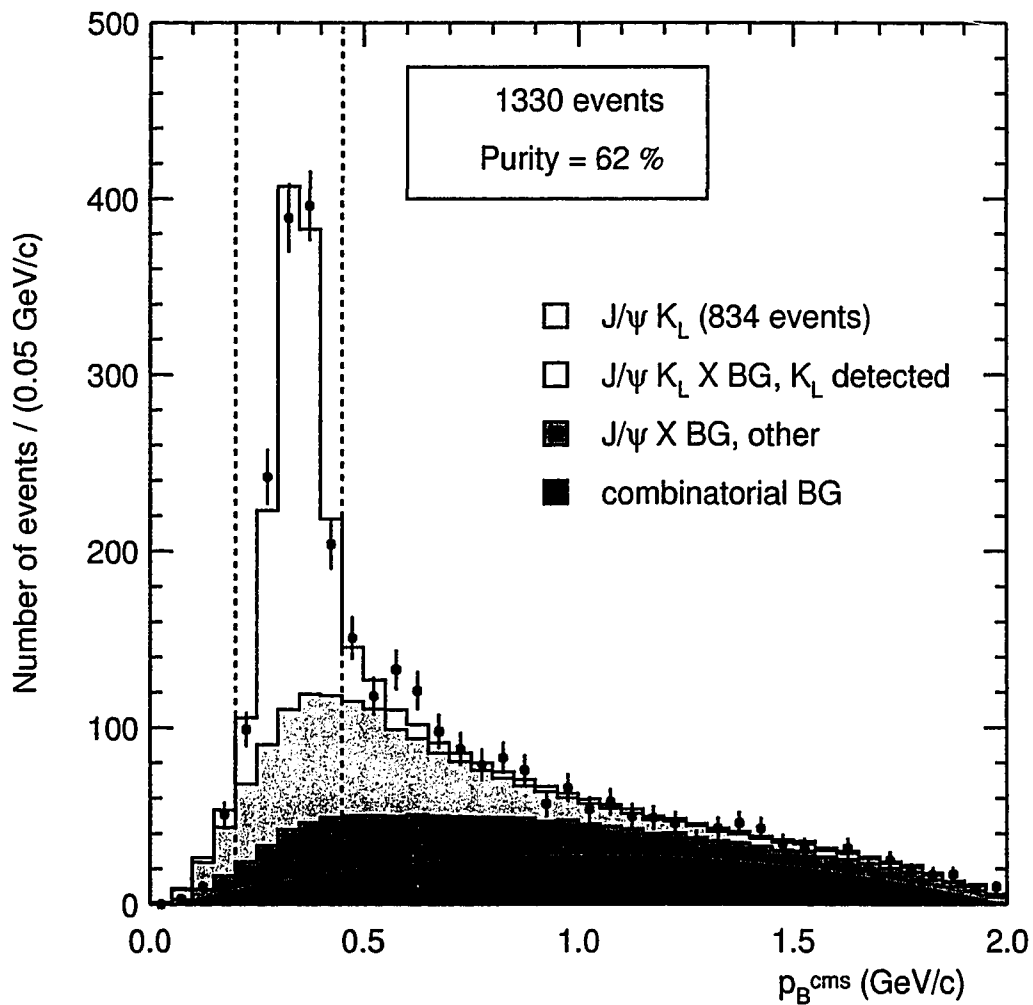


Figure 5.19: p_B^{CMS} distribution of all $B^0 \rightarrow J/\psi K_L$ candidates from Belle experiments 7 through 19 (data points with errors). The normalizations of signal and background components, shown superimposed, were estimated by performing separate fits depending on whether the K_L was detected in the KLM detector or only in the ECL detector (see figures 5.17 and 5.18).

J/ψ , is not allowed to vary in the fit. Rather, it is held fixed at the level estimated in section 5.1. Some alternative fitting schemes are included in the systematic error study.

The p_B^{CMS} shapes of the three B decay components are obtained from charmonium inclusive Monte Carlo, but have been cross checked in several ways against data, as described in detail in chapters 5.3 through 5.5. A final set of cross checks will also be presented in the next section, chapter 5.8. The p_B^{CMS} shape of the fake J/ψ component has been estimated from experimental data, by repeating the $B^0 \rightarrow J/\psi K_L$ reconstruction, using positively identified $e^\pm\mu^\mp$ pairs to form J/ψ candidates, rather than the actual decay channels e^+e^- or $\mu^+\mu^-$.

We perform separate fits for ECL-only candidates and KLM candidates, since the relative normalization of the different background components is expected to depend on how the K_L is detected. The four p_B^{CMS} shapes used in each of the two fits are shown in figures 5.15 and 5.16. Since the sample of fake J/ψ events is small, we approximate the p_B^{CMS} shape of this background component with a second-order polynomial in the p_B^{CMS} fit, as shown in figures 5.15 c) and 5.16 c).

The result of the fit for $B^0 \rightarrow J/\psi K_L$ signal and background components in all available experimental data (Belle experiments 7 through 19), is shown graphically in figures 5.17 and 5.18, and summarized in tables 5.6 and 5.7. The confidence level of the fits is reasonable, although it is better for KLM candidates than for ECL-only candidates. This is largely due to a deficit of observed ECL-only candidates with $p_B^{\text{CMS}} < 0.2 \text{ GeV}/c$. Preliminary simulations suggest that this deficit is a side-effect of the p_B^{CMS} correction. Although the correction successfully aligns the signal peak's p_B^{CMS} position in experiment and simulation,

| | $p_B^{\text{CMS}} < 2.0 \text{ GeV}/c$ | $0.20 < p_B^{\text{CMS}} < 0.45 \text{ GeV}/c$ |
|------------------------|--|--|
| $\chi^2/\text{n.d.f.}$ | 0.98 | - |
| Signal purity | 30.6% | 63.7% |
| Signal | 637.51 ± 46.10 | 532.58 |
| BG w/ true K_L | 497.24 ± 93.68 | 179.97 |
| BG w/ fake K_L | 479.42 ± 75.37 | 83.27 |
| BG w/ fake J/ψ | 467.09 | 43.21 |
| Fitted total | 2081.2 | 839.0 |
| Actual total | 2073.0 | 836.0 |

Table 5.6: Fitted yield of signal and various backgrounds, for those $B^0 \rightarrow J/\psi K_L$ candidates from experimental data where the K_L candidate was detected fully or partially in the KLM detector.

it slightly distorts the background shapes outside the signal region, mainly for $p_B^{\text{CMS}} < 0.2 \text{ GeV}/c$. We include the effect on our final result in the systematic error study, where it is found to be small.

Finally, figure 5.19 shows the combined p_B^{CMS} spectrum for all $B^0 \rightarrow J/\psi K_L$ candidate events, obtained by combining KLM candidates and ECL-only candidates into one figure. The 1330 events in the signal region, $0.20 < p_B^{\text{CMS}} < 0.45 \text{ GeV}/c$, are passed on to the CP analysis, i.e. the measurement of $\sin 2\phi_1$, presented in chapter 6. Based on the result of the yield fits, the average signal purity of these events is $62 \pm 3\%$.

| | $p_B^{\text{CMS}} < 2.0 \text{ GeV}/c$ | $0.20 < p_B^{\text{CMS}} < 0.45 \text{ GeV}/c$ |
|------------------------|--|--|
| $\chi^2/\text{n.d.f.}$ | 1.23 | - |
| Signal purity | 30.9% | 59.7% |
| Signal | 325.63 ± 27.89 | 294.76 |
| BG w/ true K_L | 341.69 ± 83.86 | 130.50 |
| BG w/ fake K_L | 166.95 ± 81.88 | 48.75 |
| BG w/ fake J/ψ | 219.18 | 19.51 |
| Fitted total | 1053.5 | 493.5 |
| Actual total | 1053.0 | 494.0 |

Table 5.7: Fitted yield of signal and various backgrounds, for those $B^0 \rightarrow J/\psi K_L$ candidates from experimental data where the K_L candidate was detected only in the ECL detector.

5.7 Does the $B^0 \rightarrow J/\psi K_L$ Yield Agree with Expectations?

We have already mentioned that the K_L reconstruction efficiency in our Monte Carlo sample is higher than what we observe in the experiment. In this section, we make this statement quantitative by comparing the expected and observed yield of $B^0 \rightarrow J/\psi K_L$ signal events. The expected yield is calculated from known branching ratios and the $B^0 \rightarrow J/\psi K_L$ reconstruction efficiency in Monte Carlo. We start this calculation from the number of $B\bar{B}$ pairs, rather than the integrated luminosity, since the former has been measured to high accuracy using the $R2$ distributions of hadronic events [32]. This way we avoid dealing with uncertainties in the CMS beam energies and the $e^+e^- \rightarrow \Upsilon(4S)$ cross section. The number of $B^0 \rightarrow J/\psi K_L$ ($J/\psi \rightarrow l^+l^-$) events we would expect to reconstruct,

| Quantity | Best estimate | reference |
|---|--------------------------------|---------------|
| $N_{B\bar{B}}$ | $(85.0 \pm 0.5) \times 10^6$ | [32] |
| $\Gamma_{\Upsilon(4S) \rightarrow B^+ B^-} / \Gamma_{\Upsilon(4S) \rightarrow B^0 \bar{B}^0}$ | 1.02 ± 0.14 | [8] |
| $\text{BF}_{B^0, \bar{B}^0 \rightarrow J/\psi K^0}$ | $(8.7 \pm 0.5) \times 10^{-4}$ | [8] |
| $\text{BF}_{J/\psi \rightarrow l^+ l^- \text{ with } l=e, \mu}$ | 0.1181 ± 0.007 | [8] |
| $\epsilon_{\text{rec}}(KLM)(0 < p_B^{\text{CMS}} < 2.0 \text{ GeV}/c)$ | 27.78% | MC Prediction |
| $\epsilon_{\text{rec}}(KLM)(0.2 < p_B^{\text{CMS}} < 0.45 \text{ GeV}/c)$ | 23.74% | MC Prediction |
| $\epsilon_{\text{rec}}(ECL)(0 < p_B^{\text{CMS}} < 2.0 \text{ GeV}/c)$ | 7.00% | MC Prediction |
| $\epsilon_{\text{rec}}(ECL)(0.2 < p_B^{\text{CMS}} < 0.45 \text{ GeV}/c)$ | 6.17% | MC Prediction |

Table 5.8: Quantities used in predicting the $B^0 \rightarrow J/\psi K_L$ yield.

$N_{B^0 \rightarrow J/\psi K_L}$, is then given by

$$N_{B^0 \rightarrow J/\psi K_L} = N_{B\bar{B}} \times \frac{1}{1 + \Gamma_{\Upsilon(4S) \rightarrow B^+ B^-} / \Gamma_{\Upsilon(4S) \rightarrow B^0 \bar{B}^0}} \times 2 \quad (5.1)$$

$$\times \text{BF}_{B^0 \rightarrow J/\psi K^0} \times \text{BF}_{K^0 \rightarrow K_L} \times \text{BF}_{J/\psi \rightarrow l^+ l^-} \times \epsilon_{\text{recon}}, \quad (5.2)$$

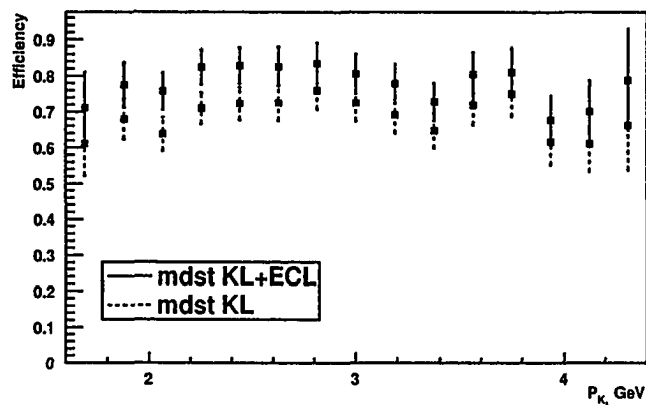
where $\text{BF}_{X \rightarrow Y}$ is the branching fraction of X into decay product Y , and ϵ_{recon} is the fraction of $B^0 \rightarrow J/\psi K_L$ ($J/\psi \rightarrow l^+ l^-$) events that can be reconstructed successfully. The multiplicative factor of two accounts for the fact that in addition to $B^0 \rightarrow J/\psi K^0 \rightarrow J/\psi K_L$, we also have $\bar{B}^0 \rightarrow J/\psi \bar{K}^0 \rightarrow J/\psi K_L$. Note that even though mixing and CP violation in the Standard Model affect the time-dependent decay rate of $B^0 \rightarrow J/\psi K_L$, this effect averages out when we measure the total (time-independent) decay rate of $B^0 \rightarrow J/\psi K_L$. Hence, mixing and CP violation in the B system can here be disregarded. We can also ignore indirect CP violation in the K system (which is small in any case), and use $\text{BF}_{K^0 \rightarrow K_L} = 0.5$.

Best estimates for the values and errors of the variables entering (5.1), are

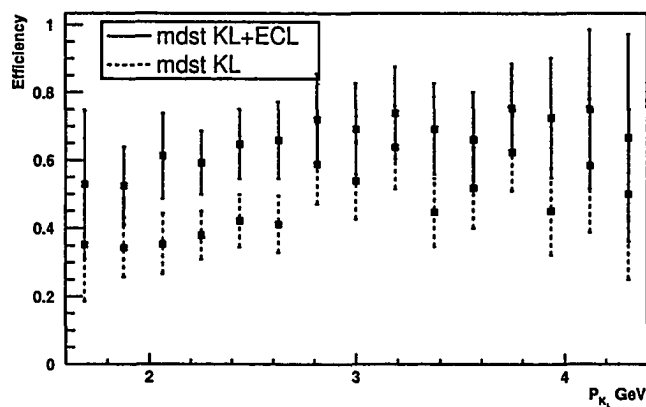
given in table (5.8). By substituting these values, and adding uncertainties in quadrature, we arrive at an expected yield of 1201 ± 130 KLM candidates, and 303 ± 33 ECL-only candidates, both for $p_B^{\text{CMS}} < 2.0$ GeV/c. The observed yields are 637.51 ± 46.09 and 325.63 ± 27.90 , respectively. This means that we observe about 47% less KLM candidates than expected, while the yield of ECL-only candidates is either consistent with, or only slightly larger than expectation.

The yield of signal with K_L hits in the KLM is thus only half of the Monte Carlo prediction. The same trend has been independently observed in the study of $e^+e^- \rightarrow \phi\gamma(\phi \rightarrow K_L K_S)$ events at Belle [22]. As explained in detail in [22], reconstruction of the photon and K_S in these events provides enough information to predict the complete four-momentum of the K_L . By then counting the fraction of such events where a K_L is actually detected, one can thus directly measure the momentum-dependent K_L detection efficiency. The result of applying this procedure to both Monte Carlo and experimental data, is shown in figure 5.20. A 40-50% deficit of K_L 's detected in the KLM is seen in experiment, relative to Monte Carlo. Due to a different event environment, such as the number and direction of charged tracks, the K_L detection efficiency may not be identical in $B^0 \rightarrow J/\psi K_L$ and $e^+e^- \rightarrow \phi\gamma(\phi \rightarrow K_L K_S)$ events. Nevertheless, the $\phi\gamma$ study confirms that the discrepancy between experiment and simulation is a feature of K_L detection in general, and not a problem specific to the $B^0 \rightarrow J/\psi K_L$ analysis.

A pure scaling between the K_L detection efficiency in simulation and experiment, does not introduce problems to our CP asymmetry measurement. However, the unreliable Monte Carlo prediction raises the concern that the momen-



(a) Monte Carlo



(b) Experimental data

Figure 5.20: K_L detection efficiency versus K_L momentum, estimated using $e^+e^- \rightarrow \phi\gamma(\phi \rightarrow K_L K_S)$ events from Monte Carlo and experiment. In each plot, the lower data points show the efficiency for events where the K_L left hits in the KLM detector, which includes events with hits in both the KLM and ECL. The upper data points includes so-called ECL-only events, where the K_L only left hits in the ECL. Note that in the momentum range below 2.7 GeV/c, which covers both signal and background in the $B^0 \rightarrow J/\psi K_L$ analysis, the KLM detection efficiency is 40-50% lower experiment than in the simulation, while the momentum dependence has the same tendency. Special thanks to Alexei Tchouvikov for providing these plots [22].

tum dependence of the K_L detection may not be well modeled in Monte Carlo. This could lead to a different background composition in Monte Carlo and experiment, which would lead to systematic bias on $\sin 2\phi_1$ if the relative fraction of CP -violating background modes with different CP eigenvalues were altered. However, the K_L efficiency measurements in figure 5.20 show that the Monte Carlo / experiment discrepancy is mainly a pure scaling. The $B^0 \rightarrow J/\psi K_L$ analysis depends on K_L 's with momenta below 2.7 GeV/ c . In this momentum range, no large difference in momentum dependence is observed between the detection efficiency in experiment and simulation; a similar weak increase with increasing momentum is seen in both cases.

5.8 Discussion and Final Consistency Check of Signal and Background Yields

In the two previous sections, we obtained the normalization of $B^0 \rightarrow J/\psi K_L$ signal and background components, by performing fits to observed p_B^{CMS} spectra. We learned that when the K_L is detected in the KLM, the signal yield is significantly lower than what we expect from Monte Carlo. We also showed that the K_L detection efficiency in the KLM is lower in experiment than in Monte Carlo for $e^+e^- \rightarrow \phi\gamma$ [22] events, roughly by the same amount as the observed $B^0 \rightarrow J/\psi K_L$ signal deficit. A reduced KLM detection efficiency for hadrons has also been observed in other studies [33]. We therefore concluded that the reduced K_L efficiency alone explains the lower-than-expected signal yield in $B^0 \rightarrow J/\psi K_L$ decays.

| | fit result, experiment | Monte Carlo |
|------------------|------------------------|-------------|
| Signal purity | 30.6% (39.4%) | 39.4% |
| Signal | 637.51±46.10 | 5218 |
| BG w/ true K_L | 497.24±93.68 | 5188 |
| BG w/ fake K_L | 479.42±75.37 | 2850 |
| comb. BG | 467.09 | - |
| Total | 2081.26 | 13256 |

Table 5.9: Fitted yield of $B^0 \rightarrow J/\psi K_L$ candidates (and various background types) where the K_L candidate was detected fully or partially in the KLM detector. Two signal-purity values are given for experimental data. The first value is based on total signal yield, while the value in parentheses is calculated excluding events with a fake J/ψ .

| | fit result | MC prediction |
|---------------------|---------------|---------------|
| Signal purity | 30.9% (39.0%) | 30.8% |
| Signal | 325.63±27.89 | 1368 |
| BG w/ true K_L | 341.69±83.86 | 1615 |
| BG w/ fake K_L | 166.95±81.88 | 1461 |
| BG w/ fake J/ψ | 219.18 | - |
| Total | 1053.5 | 4444 |

Table 5.10: Fitted yield of $B^0 \rightarrow J/\psi K_L$ candidates (and various background types) where the K_L candidate was detected only in the ECL. Two signal-purity values are given for experimental data. The first value is based on total signal yield, while the value in parentheses is calculated excluding events with a fake J/ψ .

A consequence of the lower K_L efficiency in experimental data is that the observed and predicted normalization of signal and background components differ, as can be seen from tables 5.9 and 5.10. We allowed signal and background normalizations to vary independently in the yield fit, and did separate fits, depending on whether the K_L was detected using the KLM or not. This procedure is the safest way to avoid bias due to the known discrepancy between Monte Carlo and experimental data. The fitting uncertainty on the background fractions is included in the systematic error on $\sin 2\phi_1$.

In the present section, we present a set of final cross-checks of the signal and background normalizations obtained from the p_B^{CMS} fit. At the same time, these checks serve to verify the validity of the Monte Carlo distributions of variables that were used in the event selection. The idea behind these checks is as follows: If the normalizations of signal and the various backgrounds that we obtained from the p_B^{CMS} fit are correct, then we should be able to use these normalizations to predict the distribution of other variables in experimental data. In figures 5.21 through 5.27, we show a comparison of the predicted and observed distribution for a number of variables. We will use figure 5.22 as an example, to explain the procedure. This figure shows distributions of the J/ψ 's CMS momentum, $p_{J/\psi}^{\text{CMS}}$, for the four event types we considered in the p_B^{CMS} fit:

1. $B^0 \rightarrow J/\psi K_L$ signal
2. $B \rightarrow J/\psi K_L X$ backgrounds where the K_L candidate is a true K_L
3. $B \rightarrow J/\psi K_L X$ backgrounds where the K_L candidate is a fake K_L
4. fake J/ψ background

These four event types all have a different $p_{J/\psi}^{\text{CMS}}$ distribution. As in the case of p_B^{CMS} , we predict the $p_{J/\psi}^{\text{CMS}}$ distribution for the first three components using charmonium inclusive Monte Carlo. As before, we predict the distribution for fake J/ψ events with experimental data, using $B^0 \rightarrow J/\psi K_L$ candidates with fake J/ψ 's made from $e^\pm \mu^\mp$ pairs. The resulting distributions for the four components are shown in the upper left (KLM candidates) and lower left (ECL-only candidates) plots of figure 5.22. Events with $p_B^{\text{CMS}} < 2.0 \text{ GeV}/c$ are used. Each of the distributions has been normalized to the result of the p_B^{CMS} fit, as given in tables 5.6 and 5.7. If these normalizations are good estimates of the actual normalizations in experimental data, then we should be able to add up the four $p_{J/\psi}^{\text{CMS}}$ distributions, and predict the $p_{J/\psi}^{\text{CMS}}$ distribution of the 2073 $B^0 \rightarrow J/\psi K_L$ KLM candidates and 1053 ECL-only candidates in data. This is what's shown in the upper and lower right plots of figure 5.22. The dotted histogram is the sum of the distributions shown in the left plots, while the superimposed data points show the $p_{J/\psi}^{\text{CMS}}$ distribution for the $B^0 \rightarrow J/\psi K_L$ candidates from experimental data. (Note that although we don't show errors on the sum of the four distributions, this sum of course inherits the statistical uncertainties of the four components, which are largest for the fake J/ψ distribution, where the signal yield is very low. Some apparent discrepancies are simply due to this, and become evident after studying the plots closely.) Although only events with $0.20 < p_B^{\text{CMS}} < 0.45 \text{ GeV}/c$ are ultimately used in the measurement of $\sin 2\phi_1$, we use events with $p_B^{\text{CMS}} < 2.0 \text{ GeV}/c$ in these tests. That is because this larger set of events needs to be understood well for the p_B^{CMS} fit to be trustworthy. Due to the larger statistics, we also obtain a more stringent test of the agreement between simulation and experiment for

the various variables.

The agreement between the predicted and observed distributions is remarkably good. Not only in the case of $p_{J/\psi}^{\text{CMS}}$, but for all the distributions shown, both for KLM candidates and ECL-only candidates. Especially for those variables where some of the signal and background components have very different distributions, the agreement provides a nice confirmation that our normalizations can be trusted, and that our method of estimating them is sound. For instance, the agreement between the predicted and observed $R2$ distributions for high $R2$ values, shows that we really did estimate the fraction of events with fake J/ψ 's correctly, and that modeling this component with fake J/ψ 's from $e^+\mu^-$ pairs works. Furthermore, agreement between the predicted and experimentally observed distributions of the $B^0 \rightarrow J/\psi K_L$ - likelihood ratio (figure 5.21), and of the various variables that are used to calculate it (figures 5.22 through 5.27), is another nice confirmation that the likelihood calculation, which uses p.d.f.'s from Monte Carlo, works well in the actual experiment. The largest deviation between predicted and observed distributions, is seen for the ratio between predicted and measured ECL energy, for K_L candidates that have both KLM and ECL hits (figure 5.26, upper right plot). This is not surprising, given that the K_L detection efficiency in the KLM is not well described by Monte Carlo. But even for this variable, in the case that the K_L was detected in the ECL only, the predicted and observed energy ratio distributions agree very well.

We have thus shown that our estimates of the signal and background normalizations in the $B^0 \rightarrow J/\psi K_L$ candidate event sample are realistic. The observed distributions of variables used in the event selection agree with their

Monte Carlo predictions. In sections 5.4 and 5.5, we also showed that the p_B^{CMS} shapes of signal and background components are well modeled by charmonium Monte Carlo. We conclude that our event selection procedure is sound.

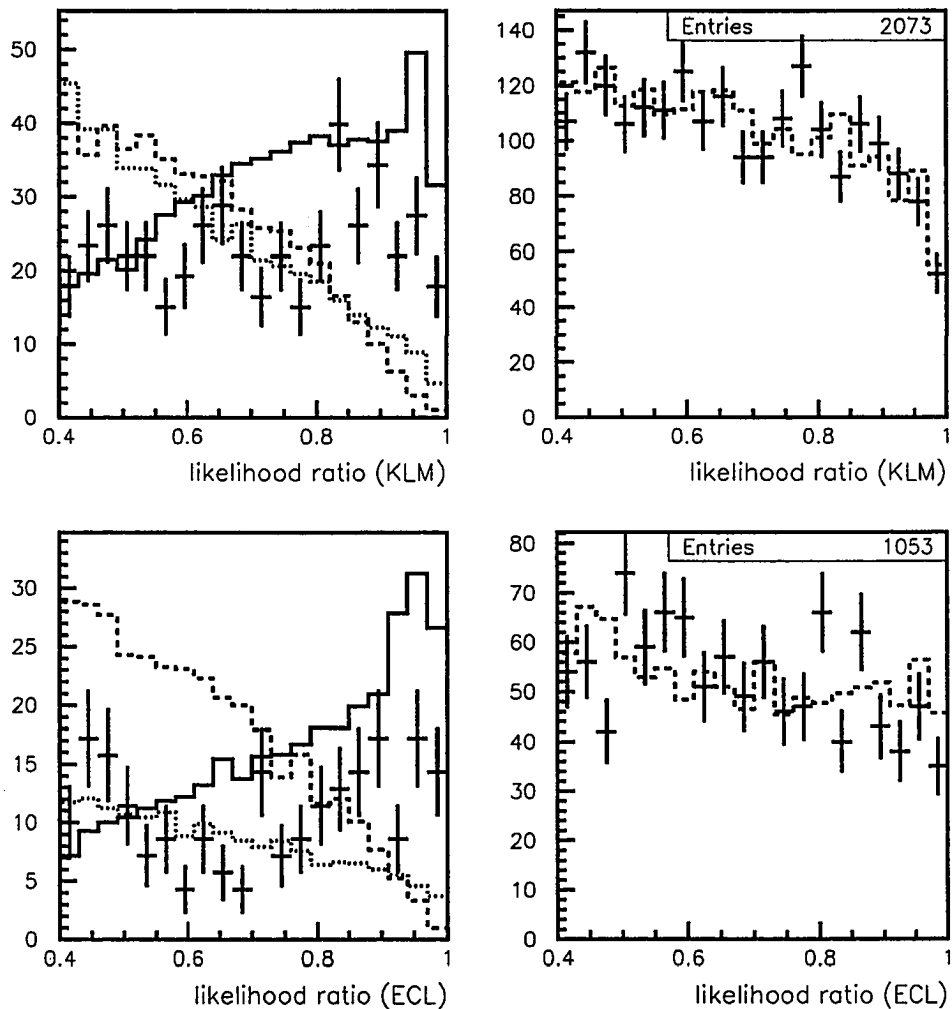


Figure 5.21: Consistency check using the $B^0 \rightarrow J/\psi K_L$ - likelihood ratio. The left plots show the likelihood distribution for signal Monte Carlo (solid), background Monte Carlo with a true K_L (dotted), background Monte Carlo with a fake K_L (finer dots), and experimental data with combinatorial J/ψ 's (points with errors). Each of these distributions has been scaled to the normalization determined by the yield fit, given in tables 5.6 and 5.7. The sum of these four distributions is shown as a dotted histogram in the plots on the right, together with the likelihood ratio distribution from experimental data (points with error). See text for discussion.

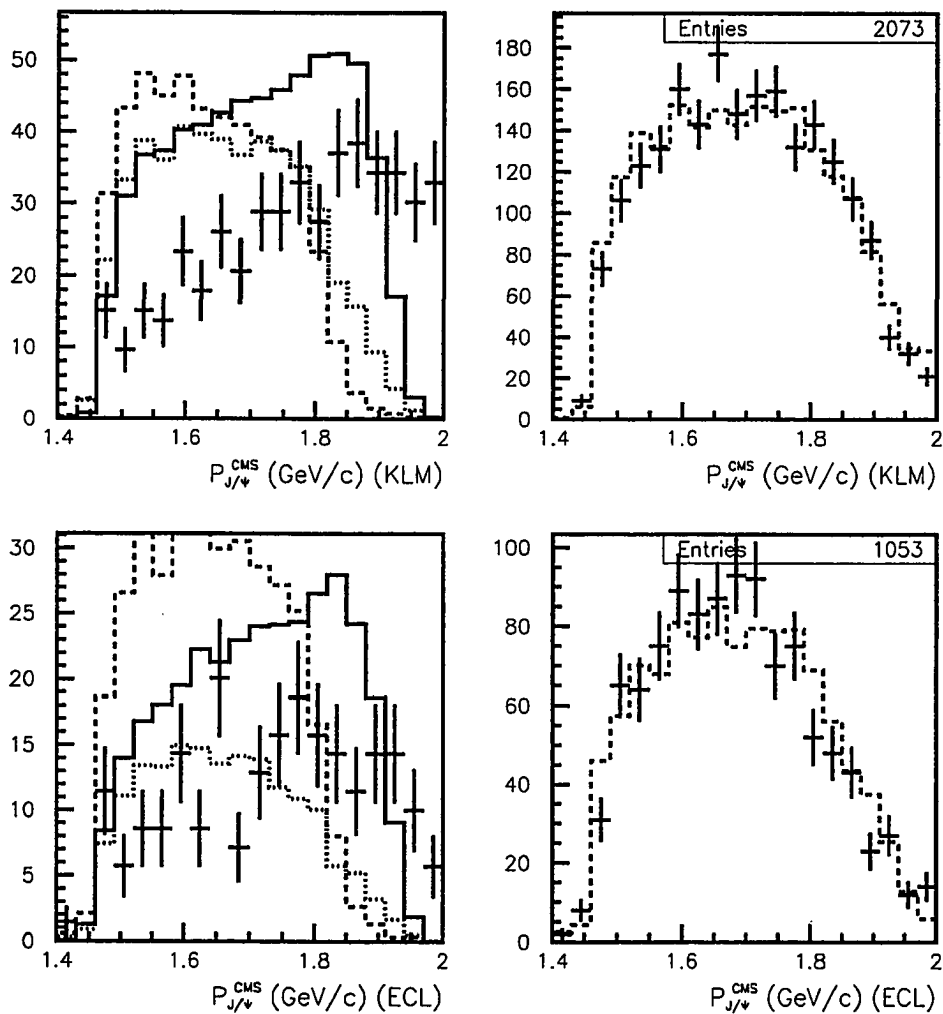


Figure 5.22: Consistency check using the J/ψ 's CMS momentum, $p_{J/\psi}^{\text{CMS}}$. The left plots show the likelihood distribution for signal Monte Carlo (solid), background Monte Carlo with a true K_L (dotted), background Monte Carlo with a fake K_L (finer dots), and experimental data with combinatorial J/ψ 's (points with errors). Each of these distributions has been scaled to the normalization determined by the yield fit, given in tables 5.6 and 5.7. The sum of these four distributions is shown as a dotted histogram in the plots on the right, together with the $p_{J/\psi}^{\text{CMS}}$ distribution from experimental data (points with error). See text for discussion.

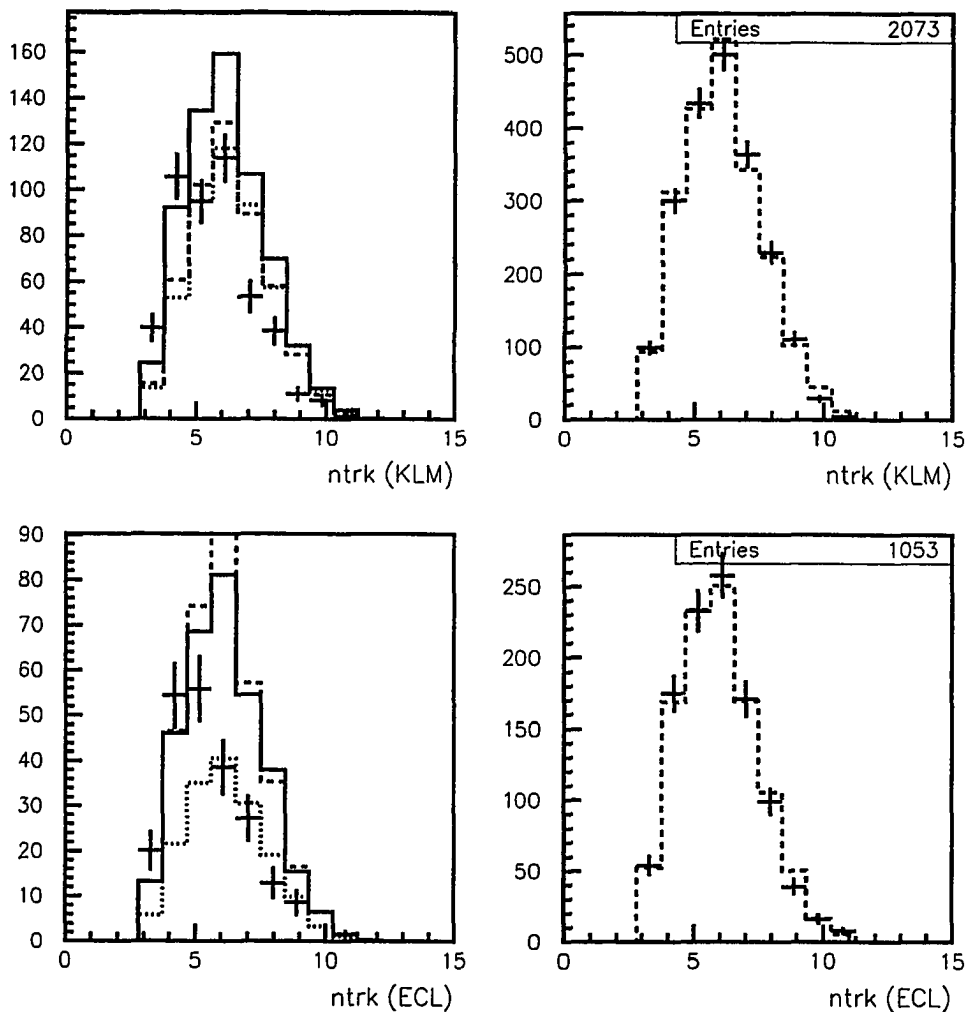


Figure 5.23: Consistency check using the number of good charged tracks in the event, $ntrk$. The left plots show the likelihood distribution for signal Monte Carlo (solid), background Monte Carlo with a true K_L (dotted), background Monte Carlo with a fake K_L (finer dots), and experimental data with combinatorial J/ψ 's (points with errors). Each of these distributions has been scaled to the normalization determined by the yield fit, given in tables 5.6 and 5.7. The sum of these four distributions is shown as a dotted histogram in the plots on the right, together with the $ntrk$ distribution from experimental data (points with error). See text for discussion.

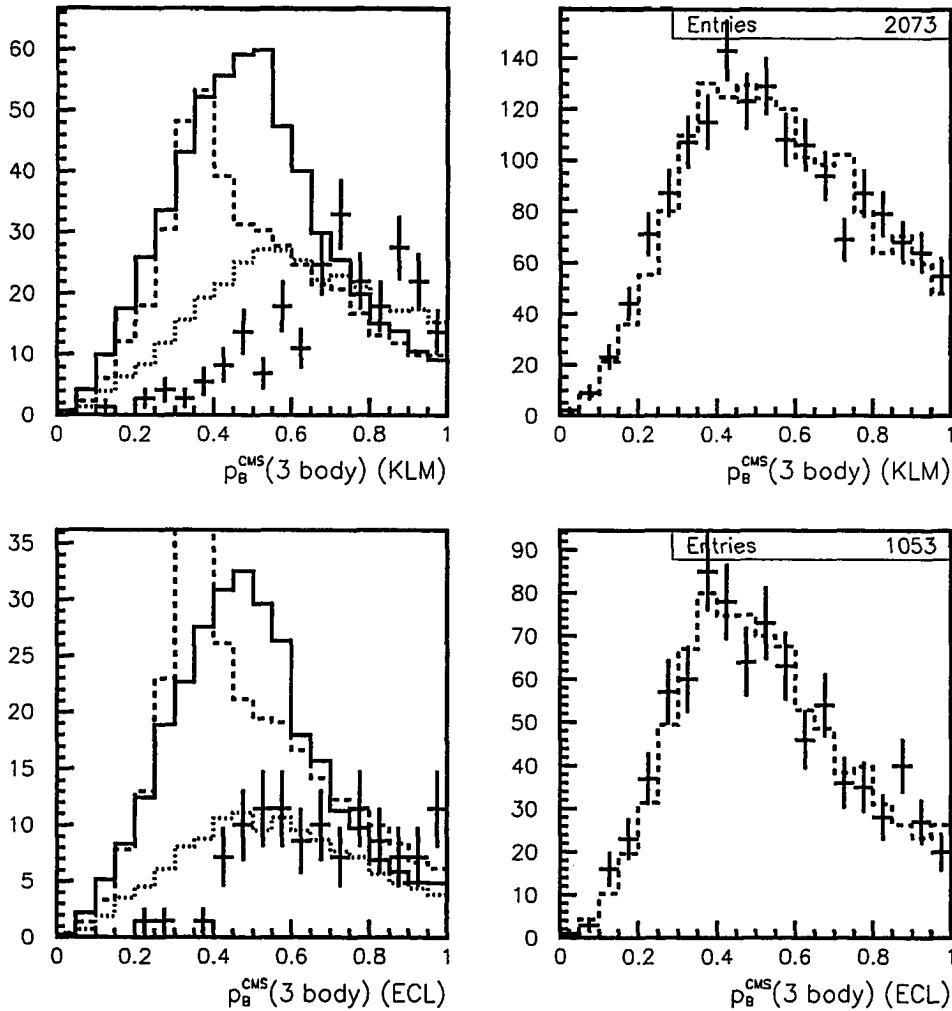


Figure 5.24: Consistency check using $p_B^{\text{CMS}}(3\text{-body})$ (see chapter 4.5.3). The left plots show the likelihood distribution for signal Monte Carlo (solid), background Monte Carlo with a true K_L (dotted), background Monte Carlo with a fake K_L (finer dots), and experimental data with combinatorial J/ψ 's (points with errors). Each of these distributions has been scaled to the normalization determined by the yield fit, given in tables 5.6 and 5.7. The sum of these four distributions is shown as a dotted histogram in the plots on the right, together with the $p_B^{\text{CMS}}(3\text{-body})$ distribution from experimental data (points with error). See text for discussion.

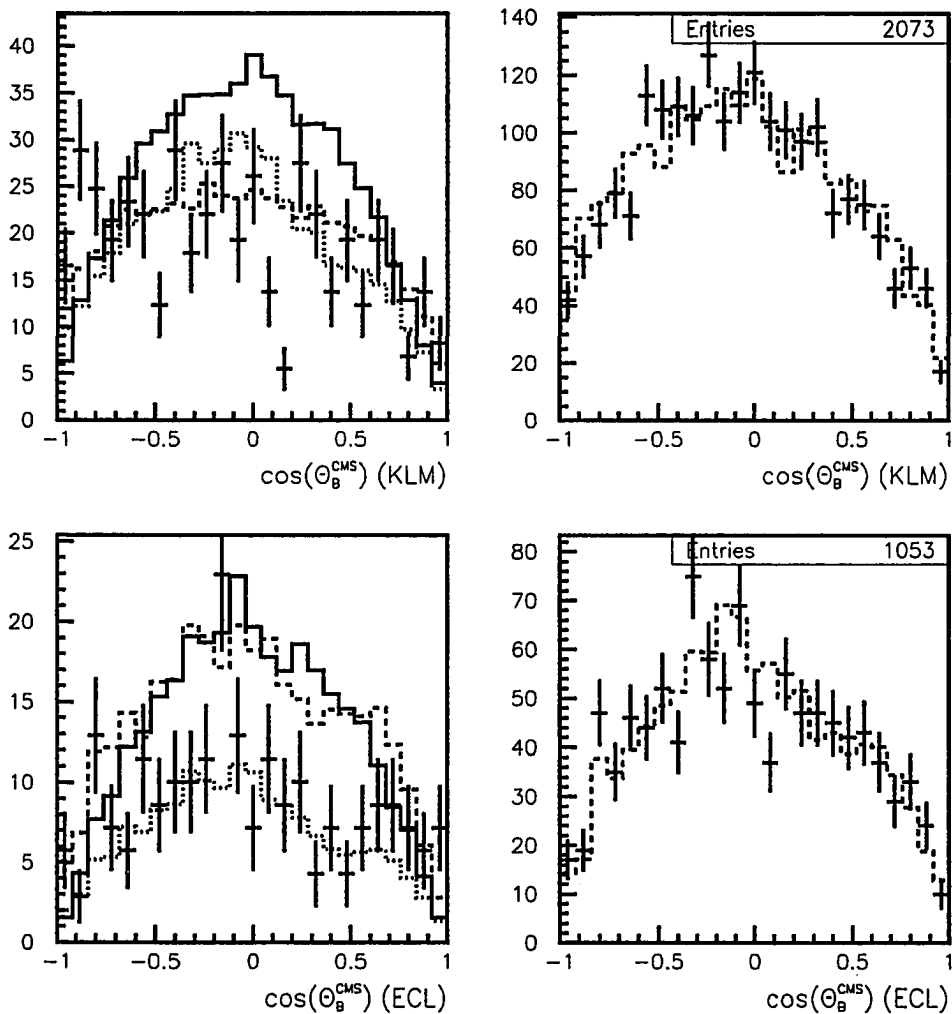


Figure 5.25: Consistency check using the cosine of the CMS-frame polar angle of the $B^0 \rightarrow J/\psi K_L$ candidate, θ_B^{CMS} . The left plots show the likelihood distribution for signal Monte Carlo (solid), background Monte Carlo with a true K_L (dotted), background Monte Carlo with a fake K_L (finer dots), and experimental data with combinatorial J/ψ 's (points with errors). Each of these distributions has been scaled to the normalization determined by the yield fit, given in tables 5.6 and 5.7. The sum of these four distributions is shown as a dotted histogram in the plots on the right, together with the θ_B^{CMS} distribution from experimental data (points with error). See text for discussion.

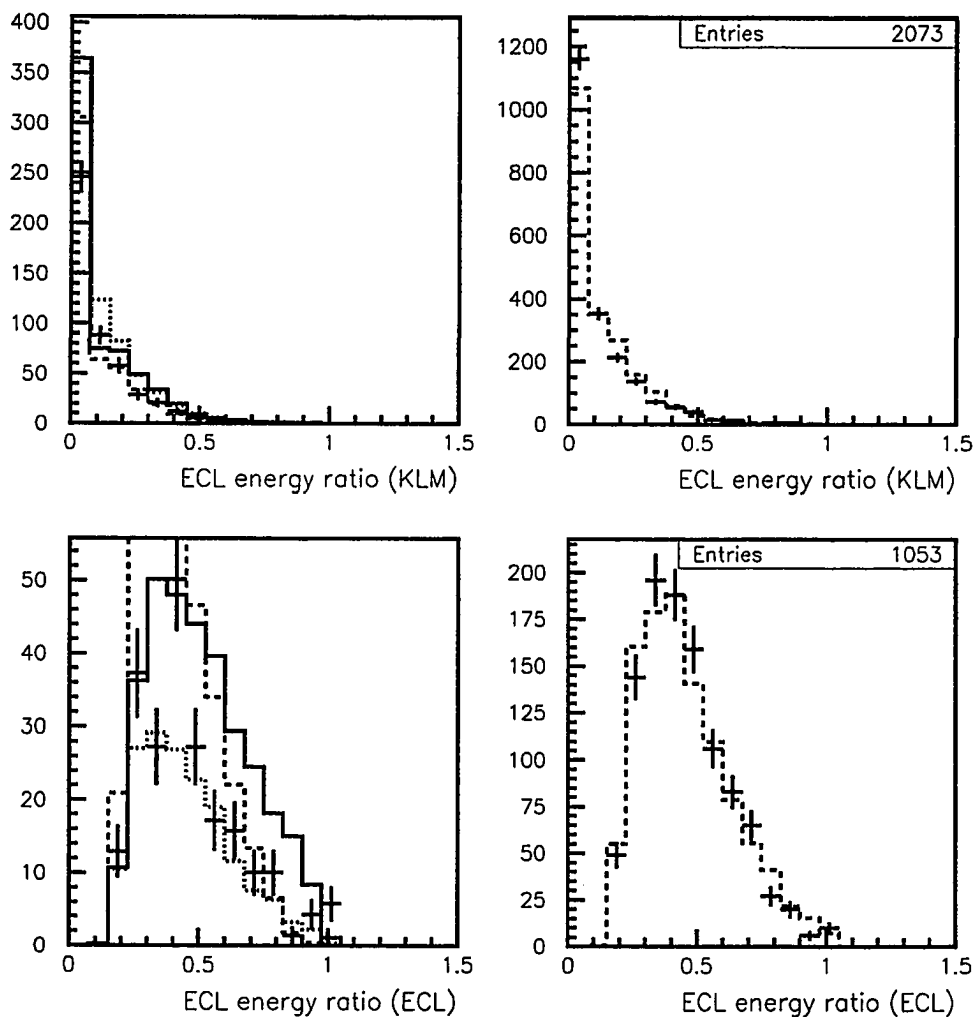


Figure 5.26: Consistency check using the ratio of measured to calculated energy deposited by the K_L in the ECL, $E_{\text{ECL}}/E_{\text{calc}}$ (see chapter 4.5.3). The left plots show the likelihood distribution for signal Monte Carlo (solid), background Monte Carlo with a true K_L (dotted), background Monte Carlo with a fake K_L (finer dots), and experimental data with combinatorial J/ψ 's (points with errors). Each of these distributions has been scaled to the normalization determined by the yield fit, given in tables 5.6 and 5.7. The sum of these four distributions is shown as a dotted histogram in the plots on the right, together with the actual $E_{\text{ECL}}/E_{\text{calc}}$ distribution from experimental data (points with error). See text for discussion.

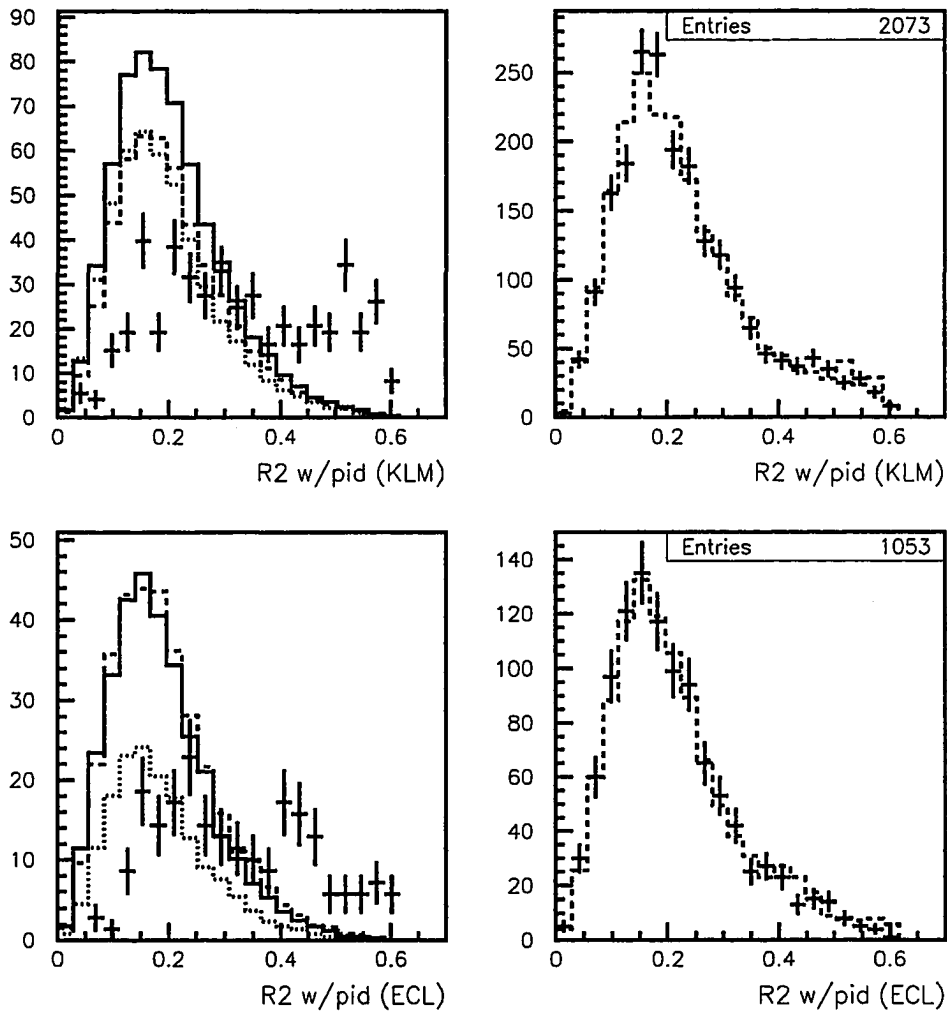


Figure 5.27: Consistency check using $R2$ (see chapter 4.2). The left plots show the likelihood distribution for signal Monte Carlo (solid), background Monte Carlo with a true K_L (dotted), background Monte Carlo with a fake K_L (finer dots), and experimental data with combinatorial J/ψ 's (points with errors). Each of these distributions has been scaled to the normalization determined by the yield fit, given in tables 5.6 and 5.7. The sum of these four distributions is shown as a dotted histogram in the plots on the right, together with the $R2$ distribution from experimental data (points with error). See text for discussion.

Chapter 6

Measurement of the CP Asymmetry

The present chapter describes how $\sin 2\phi_1$ is measured. The event selection yielded 1330 $e^+e^- \rightarrow \Upsilon(4S) \rightarrow B\bar{B}$ candidate events, where one B meson most likely decayed into $J/\psi K_L$. We will refer to this meson as B_{CP} . For each event, we identify the flavor of the accompanying B meson, B_{tag} , from its decay products (section 6.1). We obtain the proper time interval between the decay of the two B mesons, Δt , from the z -displacement of their decay vertices (section 6.2). The B flavor and vertex assignment is successful for 1230 of our $B^0 \rightarrow J/\psi K_L$ candidates. We measure $\sin 2\phi_1$ with an unbinned likelihood fit to the asymmetry in the Δt distribution of these events (section 6.4), a procedure which we will refer to simply as “the CP fit.”

In order to obtain a reliable measurement, the CP fit needs to incorporate non-ideal, but unavoidable, real-world aspects of each analysis step, such as the

fraction of wrong B flavor assignments, the finite resolution of the B vertex measurements, and the effect of background events on the Δt distribution. These issues will be discussed as we go along.

6.1 Flavor Tagging: B_d^0 or \overline{B}_d^0 meson?

Distinguishing between B_d^0 and \overline{B}_d^0 mesons is referred to as flavor tagging, and is a central part of all time-dependent CP violation measurements at Belle. As a result, the tagging algorithm has become quite sophisticated. It is performed with a software package called “Hamlet” (“To B or not to B ?”). We will here only give an overview of the procedure. An in-depth description can be found in [34].

6.1.1 Flavor Tagging Algorithm

Reconstruction of a $J/\psi K_L$ final state yields no information on whether the parent B was a B_d^0 meson or a \overline{B}_d^0 meson, since both $B_d^0 \rightarrow J/\psi K_L$ and $\overline{B}_d^0 \rightarrow J/\psi K_L$ decays are possible. If we assume that we had an event of the form $e^+e^- \rightarrow \Upsilon(4S) \rightarrow B_{\text{tag}}B_{\text{CP}}$, followed by $B_{\text{CP}} \rightarrow J/\psi K_L$, then particles other than the J/ψ and K_L in the event must be due to B_{tag} . We can use these remaining particles to identify the flavor of B_{tag} , since some decays yield decay products whose charges are correlated with the flavor of B_{tag} . Figures 6.2 and 6.3 show the most important types of such flavor specific B meson decays. The semileptonic decay in figure 6.2 results in a high-momentum lepton, which will have the same electric charge as the b quark in the decaying B meson, thus

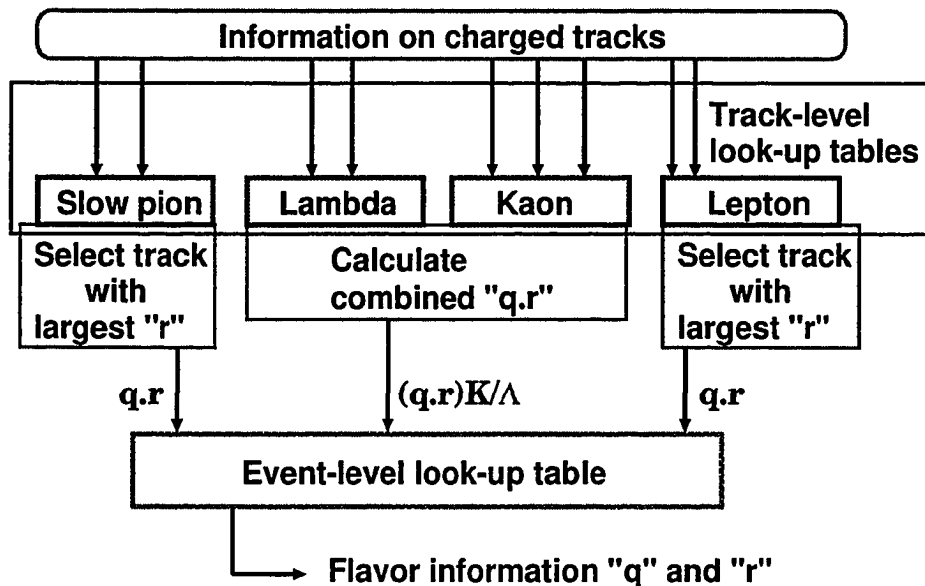


Figure 6.1: Schematic overview of the flavor tagging algorithm.

revealing the B meson's flavor. Similarly, the $\bar{b} \rightarrow \bar{c} \rightarrow \bar{s}$ transition in figure 6.3 results in an \bar{s} quark that can hadronize into a charged kaon, with the sign of the kaon's charge opposite of the decaying b quark.

The exercise of flavor tagging is non-trivial because one needs to consider many decay channels of the B meson, in order to get good efficiency. Also, many commonly occurring flavor-specific decays cannot be fully reconstructed. For both of these reasons, exclusive reconstruction is not useful. Instead, the flavor assignment is based on inclusive information regarding remaining particles in the event. As illustrated in figure 6.1, information regarding remaining charged leptons, pions, kaons and Λ baryons is used and combined. Combining this information involves the calculation and combination of several likelihood quantities, but the process essentially amounts to a lookup table, constructed using a large B decay Monte Carlo sample. The overall result is to assign each

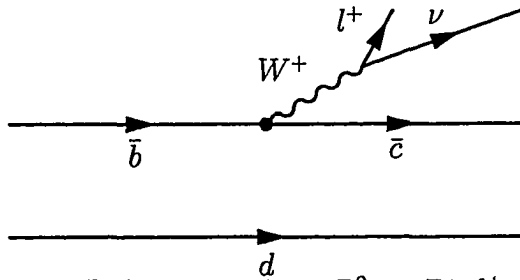


Figure 6.2: Semileptonic B decays, such as $B_d^0 \rightarrow D^{*-} l^+ \nu$, proceed via the $b \rightarrow c l \nu$ transition. Since the final-state lepton has the same electric charge as the decaying b quark, we can distinguish B_d^0 and \overline{B}_d^0 decays.

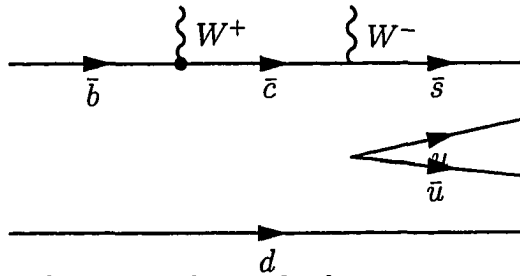


Figure 6.3: B meson decays involving the $b \rightarrow c \rightarrow s$ transition can result in charged kaons, where the charge of the kaon depends on the B 's flavor.

event two values: “ q ” and “ r ”. The value of q denotes the most likely flavor of B_{tag} : $q = +1$ means B_{tag} is likely to be a B_d^0 (which contains the positively charged \bar{b} quark), while $q = -1$ means B_{tag} is likely to be a \overline{B}_d^0 (which contains the negatively charged b quark). The parameter r ranges from zero to one, and is the reliability of the q value assignment, as estimated by Monte Carlo. An r value of zero means the q value is essentially a random variable, while an r value of one means the flavor assignment is certain to be correct. Although the r value is a good approximation of the tagging reliability, it is only used to classify events into tagging bins (“ r bins”) in our analysis. As will be explained in the next section, the actual tagging reliability used in our measurement is obtained

using experimental data.

The tagging reliability is often less than one, because the tagging is based on inclusive event information, rather than exclusive reconstruction. As a result we have large backgrounds, and often end up assigning the incorrect flavor to B_{CP} . The fraction of the time this happens is commonly called the “wrong tag fraction”, denoted by w . If our Monte Carlo were perfect, then the r value from the tagging algorithm would equal $1 - 2w$.

6.1.2 Estimating the Wrong Tag Fraction

Any error in the assumed wrong tag fraction could translate into a systematic shift in the measured $\sin 2\phi_1$ value. We safeguard against such bias, by measuring the wrong tag fraction, w , using experimental data. For this purpose, we group events into six bins, based on their assigned r values.

For each r bin, we then determine w as follows. We reconstruct exclusive decays of B_d^0 and \overline{B}_d^0 into the self-tagged final states $D^{*\pm} l^\mp \nu$, $D^{*\mp} \pi^\pm$, and $D^{*\mp} \rho^\pm$, where the charges of the decay products tell us the flavor of the decaying B meson. We then use the flavor-tagging algorithm to assign flavor to the other B meson in the event. Now that we have assigned a flavor to both B mesons, we can split the sample into events where the B mesons have the same flavor (SF), and where they have opposite flavor (OF). As derived in appendix A, the time-dependent mixing asymmetry of such events is given by

$$A(\Delta t) = \frac{P_{\text{OF}} - P_{\text{SF}}}{P_{\text{OF}} + P_{\text{SF}}} = (1 - 2w) \cos(\Delta m_d \Delta t). \quad (6.1)$$

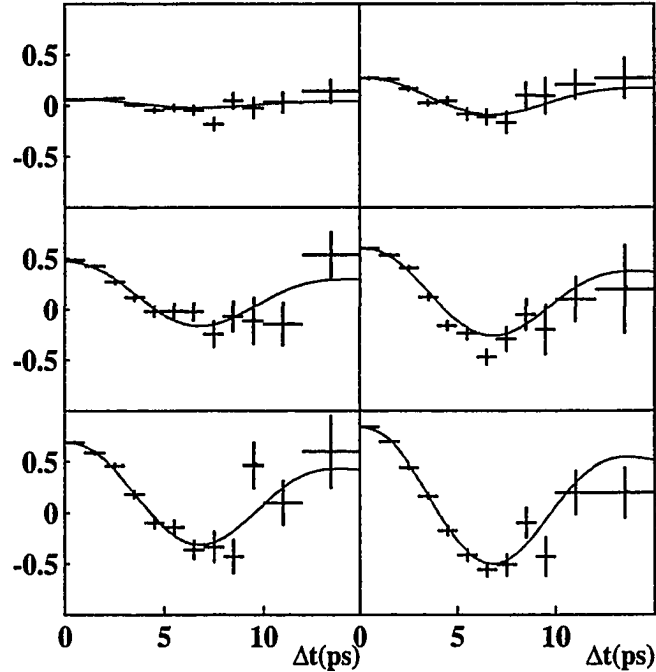


Figure 6.4: Measured time-dependent asymmetries $A(\Delta t)$ (equation 6.1 in text) between same-flavor and opposite-flavor events, for each of the six tagging categories (“ r -bins”). $B \rightarrow D^{*\pm} l^{\mp} \nu$ decays are used to determine the flavor of one B meson, while the flavor tagging algorithm is used to determine that of the other.

By measuring the amplitude of this asymmetry for the events in each r bin separately, we can obtain $(1 - 2w)$, and hence the wrong tag fraction w for each r bin. The result of a fit to the asymmetry from $B \rightarrow D^* l \nu$ decays, is shown in figure 6.4. The final result for all three decay channels combined is given in table 6.1. The errors on the six wrong tag fractions are used when estimating the systematic error on $\sin 2\phi_1$, which is described in chapter 7.

| l | r | w_l |
|-----|-------------|-------------------|
| 1 | 0.000-0.250 | 0.458 ± 0.006 |
| 2 | 0.250-0.500 | 0.336 ± 0.009 |
| 3 | 0.500-0.625 | 0.228 ± 0.010 |
| 4 | 0.625-0.750 | 0.160 ± 0.009 |
| 5 | 0.750-0.875 | 0.112 ± 0.009 |
| 6 | 0.875-1.000 | 0.020 ± 0.006 |

Table 6.1: Wrong-tag fractions (w_l) for the different tagging categories (r bins). The quoted errors on w include both statistical and systematic uncertainties.

6.2 Vertexing: Where Did the B Mesons Decay?

6.2.1 Vertexing Algorithm

The decay vertex of $B_{CP} \rightarrow J/\psi K_L$ is reconstructed using the two leptons from $J/\psi \rightarrow e^+e^-(\gamma)$ or $J/\psi \rightarrow \mu^+\mu^-$. Since the lifetime of the J/ψ (about 8×10^{-21} s), is much shorter than that of the B_d^0 meson (about 1.5 ps), the decay vertex of the J/ψ is effectively identical to that of the B meson. On the software level, the decay vertex of B_{CP} is obtained using the “kvertexfitter” package.

The vertex of B_{tag} is obtained from a fit that uses remaining, well-reconstructed charged tracks in the event. Tracks due to $K_S \rightarrow \pi^+\pi^-$ decays are excluded, as they might bias the vertex position. If any tracks have an unusually large contribution to the χ^2 obtained from the vertex fit, they are also removed, and the fit is repeated. See [35] for more details. On the software level, the “TagV” package is used to obtain the decay vertex of B_{tag} .

Both vertex positions are required to be consistent with the (run-dependent)

profile of the interaction point, which is convolved in the r - ϕ plane to account for the flight of the B . Because of this constraint, even a single track can give us information on the z position of the decay vertex. The RMS resolutions obtained for the B meson vertices are roughly $75 \mu\text{m}$ for B_{CP} , and $140 \mu\text{m}$ for B_{tag} , obtained from a Monte Carlo simulation [35]. For comparison, the impact parameter resolution along the z axis, for single tracks perpendicular to the SVD, is about $55 \mu\text{m}$.

6.2.2 Response function

We estimate the proper-time interval between the decay of B_{CP} and B_{tag} from z_{CP} and z_{tag} , the z positions of the decay vertices, using the approximation

$$\Delta t = \frac{\Delta z}{\gamma\beta c} = \frac{z_{CP} - z_{\text{tag}}}{\gamma\beta c}. \quad (6.2)$$

When Δt is obtained this way, it is smeared by a number of experimental effects, so that it differs from the actual proper-time interval. In the CP fit, we model this smearing of Δt with an effective response function, $R_{\text{sig}}(\Delta t)$. This function takes into account the four dominant smearing effects for signal events, and is obtained by convolving components modeling each effect:

- Finite resolution of the z_{CP} measurement.
- Finite resolution of the z_{tag} measurement.
- Smearing due to using equation 6.2, which ignores the B mesons' motion in the $\Upsilon(4S)$ frame.

- Shift of the z_{tag} measurements due to secondary tracks from longer-lived (charmed) particles.

The final resolution function, $R_{\text{sig}}(\Delta t)$, is computed on an event-by-event basis from the z errors given by the two B -vertex fits. We will not delve into the details of this scheme here. Suffice it to say that twelve parameters of $R_{\text{sig}}(\Delta t)$ are obtained from Belle's measurement of the charged and neutral B meson lifetimes. That measurement also involves exclusive reconstruction of one B meson, and an inclusive measurement of the vertex of the other B , so that the same parameterization of $R_{\text{sig}}(\Delta t)$ applies. However, the exclusive decay channels used in the lifetime measurement, $B \rightarrow D^\pm \pi^\mp$, $D^{*\pm} \pi^\mp$, $D^{*\pm} \rho^\mp$, $J/\psi K_S$, $J/\psi K^{*0}$, $D^0 \pi^\mp$, and $J/\psi K^\mp$, result in much higher statistics than what we have in the $B^0 \rightarrow J/\psi K_L$ analysis, thus providing a more stringent test of the resolution function. All fine details regarding $R_{\text{sig}}(\Delta t)$, and how its parameters are determined, can thus be found in the description of the lifetime measurement [36]. For the present analysis, the parameters were re-evaluated using the full 78.1 fb^{-1} data sample. Figure 6.5 shows the result of this updated lifetime fit. We see that there is good agreement between the experimental data points and the PDF used in the fit, out to Δt values roughly ten times the B lifetime.

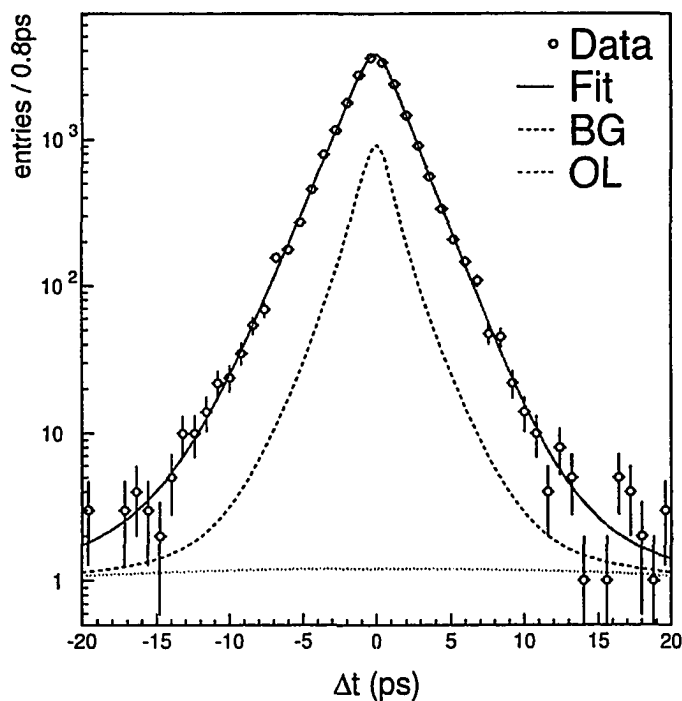


Figure 6.5: Distribution of the proper-time interval Δt , from a B -meson lifetime fit, using 78.1 fb^{-1} of data. One B is fully reconstructed from hadronic decays, while the other B 's vertex is determined from the remaining charged tracks in the event. The points with error show the experimental data, while the solid line is the fitted PDF. It was obtained by smearing the theoretical expectation with the event-dependent resolution function, $R(\Delta t)$. The yellow line shows a small component of broad outliers, while the blue line shows the sum of all background, including outliers. Excellent agreement between the PDF and experimental data is seen out to ten times the B_d^0 lifetime.

6.3 Signal and Background Models with Time Dependence

In the CP fit for $\sin 2\phi_1$, each $B^0 \rightarrow J/\psi K_L$ candidate event is assigned a likelihood value;

$$P_i(\Delta t, \sin 2\phi_1, p_B^{\text{CMS}}, \dots) = (1 - f_{\text{ol}}) [f_{\text{sig}} P_{\text{sig}} + (1 - f_{\text{sig}}) P_{\text{bkg}}] + f_{\text{ol}} P_{\text{ol}}, \quad (6.3)$$

where P_{sig} and P_{bkg} are PDFs describing signal and background events. In general, they are obtained by modifying the theoretically expected Δt distributions, to take into account experimental effects. The background PDF consists of four components, as will be described later. The signal fraction, f_{sig} , is calculated from each B candidate's CMS momentum, p_B^{CMS} , and also depend on whether the K_L was detected in the KLM or only in the ECL. The outlier component, P_{ol} , is a wide gaussian, intended to account for a small number of signal and background events with large Δt . Its normalization, f_{ol} , is small; 1.65×10^{-4} for events with multiple track vertices, and 0.027 for events with at least one single-track vertex, as determined from the B lifetime measurement. Below, we will discuss in more detail how the PDFs, the signal fraction, and the normalizations of different background components are calculated.

6.3.1 $B^0 \rightarrow J/\psi K_L$ Signal PDF

As derived in chapter 3, a meson produced in a state of pure flavor, decays with proper time distribution given by

$$\Gamma(t) \sim e^{-t/\tau_{B^0}} [1 \pm \eta_f \sin 2\phi_1 \sin(\Delta m_d t)], \quad (6.4)$$

where the plus (minus) sign denotes the case where the B meson started out as a B_d^0 (\overline{B}_d^0), η_f is the CP eigenvalue of the final state ($\eta = +1$ for $J/\psi K_L$), τ_{B^0} is the neutral B -meson lifetime, and m_d is the mass difference between the B^0 mass eigenstates. At Belle, we have $\Upsilon(4S) \rightarrow B_{\text{tag}} B_{\text{CP}}$ events, with B_{CP} decaying to a CP eigenstate, and B_{tag} decaying to a self-tagged final state, revealing its flavor. At the time when B_{tag} decays, B_{CP} can be considered collapsed into a flavor eigenstate with the opposite flavor of B_{tag} . Denoting the proper-time difference between the two B mesons decays as $\Delta t = t_{CP} - t_{\text{tag}}$, the proper-time difference distribution for $\Upsilon(4S) \rightarrow B_{\text{tag}} B_{\text{CP}}$ decays is therefore given by

$$\Gamma(\Delta t) \sim e^{-|\Delta t|/\tau_{B^0}} [1 - q\eta_f \sin 2\phi_1 \sin(\Delta m_d \Delta t)], \quad (6.5)$$

where q is the flavor assigned to B_{tag} by the tagging algorithm. This expression is also valid for negative values of Δt , which is the case when B_{CP} decays before B_{tag} . Taking into account finite vertex resolution, wrong flavor assignment, and normalizing the PDF to unity, we arrive at

$$P_{\text{sig}} = \frac{e^{-|\Delta t|/\tau_{B^0}}}{4\tau_{B^0}} [1 - q\eta_f(1 - 2w_l) \sin 2\phi_1 \sin(\Delta m_d \Delta t)] \otimes R_{\text{sig}}(\Delta t), \quad (6.6)$$

where w_l is the wrong tag fraction for the l th r -bin (given in table 6.1), and

$\otimes R_{\text{sig}}(\Delta t)$ denotes convolution with the resolution function:

$$f(\Delta t) \otimes R_{\text{sig}}(\Delta t) \equiv \int_{-\infty}^{+\infty} f(\Delta t') R_{\text{sig}}(\Delta t' - \Delta t) d\Delta t' \quad (6.7)$$

Yield losses, such as limited reconstruction efficiency, tagging efficiency, or vertex finding efficiency, result in fewer signal events, but do not alter the signal distribution. The Δt distribution is affected only when we make a “mistake”—e.g., reconstruct background instead of signal, or assign the wrong flavor to a B meson.

6.3.2 Background PDFs

Our background model incorporates four different background types, A through D:

- A. B^0 decays into CP -eigenstate background modes will have the Δt distribution given in equation 6.6 for signal, but with η_f depending on the CP eigenvalue of the specific final state. We thus use the signal PDF to describe the background modes $B \rightarrow \psi(2S) K_L$, $B \rightarrow \chi_{c1} K_L$, and $B \rightarrow J/\psi \pi^0$, with $\eta_f = +1$; and $B \rightarrow J/\psi K_S$, with $\eta_f = -1$. In the special case of $B \rightarrow J/\psi K^{*0}$ ($K^{*0} \rightarrow K_L \pi^0$) decays, the CP eigenvalue depends on the relative orbital angular momentum of the J/ψ and the K^{*0} . We use the effective CP eigenvalue $\eta_f = -0.62 \pm 0.11$ for these decays, based on Belle’s own measurement [37]. The resolution function used for CP eigenstate backgrounds is R_{sig} .

B. Other B^0 decays (not into CP eigenstates) are not expected to exhibit any CP asymmetry, so the Δt distribution is modeled by the simpler form

$$P_B = \frac{e^{-|\Delta t|/\tau_{B^0}}}{4\tau_{B^0}} \otimes R_{\text{sig}}(\Delta t). \quad (6.8)$$

C. The lifetime of the charged B^\pm mesons is different from that of the neutral B 's. Hence backgrounds from B^\pm decays are modeled separately. Some of these decays also have final states of the type $J/\psi K_L + X$, where X results in charged tracks. Since we mistakenly assume a $B^0 \rightarrow J/\psi K_L$ decay took place, tracks due to X can thus be included when measuring the vertex of B_{tag} , resulting in a shorter Δt , and effectively lowering the B^\pm lifetime. We thus model the combined background from charged B decays as

$$P_C = \frac{e^{-|\Delta t|/\tau_{B_{\text{eff}}^\pm}}}{4\tau_{B_{\text{eff}}^\pm}} \otimes R_{\text{sig}}(\Delta t), \quad (6.9)$$

where $\tau_{B_{\text{eff}}^\pm}$ is an effective lifetime, somewhat shorter than the actual lifetime of the charged B meson. Using our charmonium inclusive Monte Carlo sample, we estimate $\tau_{B_{\text{eff}}^\pm} = 1.558 \pm 0.026$ ps. (Based on the same Monte Carlo study, this effective shortening of the B lifetime, does not appear to take place for neutral B decays.)

D. Combinatorial background with fake J/ψ 's is due to several event types, such as B decays with true leptons, $e^+e^- \rightarrow q\bar{q}$ continuum events, and non-hadronic e^+e^- events such as Bhabha scattering. We model the Δt distribution of these events with a sum of two components; one with finite

lifetime, and a delta function to represent prompt decays. The combinatorial background is modeled with its own resolution function, R_{comb} , different from R_{sig} . We estimate parameters of the combinatorial background PDF (its lifetime, and fraction of prompt decays), as well as the parameters of R_{comb} , using experimental data. We employ a sample of $B^0 \rightarrow J/\psi K_L$ candidates with fake J/ψ , constructed from $e^\pm\mu^\mp$ pairs with invariant mass in our acceptance region. (The same event sample was also used to estimate the p_B^{CMS} shape of combinatorial events, see chapter 5.6.)

6.3.3 Normalizations

We now obtain the relative normalizations of signal and these background components, used in the CP fit. For each $B^0 \rightarrow J/\psi K_L$ candidate event, the signal and background PDFs are combined linearly to construct the event-dependent likelihood

$$P_i = f_{\text{sig}}P_{\text{sig}} + (1 - f_{\text{sig}})(f_A P_A + f_B P_B + f_C P_C + f_D P_D). \quad (6.10)$$

Each of the normalizations f_{sig} , f_A , f_B , f_C , and f_D is actually a function of p_B^{CMS} , and therefore evaluated on an event-by-event basis. For each event $f_A + f_B + f_C + f_D = 1$. From the p_B^{CMS} fit presented in chapter 5.6, we know the relative normalization and p_B^{CMS} dependence of four components: signal, background events with a true K_L , background with a fake K_L , and combinatorial background. The signal fraction, f_{sig} , and the fraction of combinatorial events within the background, f_C , can therefore be taken directly from the result of the p_B^{CMS} fit.

Obtaining f_A , f_B , and f_C , is a bit more tedious, since components A, B, and C don't correspond directly to the way background is divided in the p_B^{CMS} fit. Our procedure is as follows: Different classes of background events are identified in Monte Carlo using generator level information. Events are separated into background with true and fake K_L 's. These two components are then scaled to the result of the p_B^{CMS} fit. Within these two components, we identify the background components A, B and C, from which we obtain f_A , f_B , and f_C . In order to obtain the correct Δt dependence for background A (CP -eigenstate decays), we need to know the relative normalization of decays with $\eta_f = +1$ and $\eta_f = -1$. We accomplish this by identifying the most significant CP -eigenstate decays (the ones mentioned explicitly above) at the generator level. Some remaining, less commonly occurring CP -eigenstate decays are not identified, and as a result included in background component B. As shown below, a Monte Carlo study measures no significant bias due to ignoring the less significant CP eigenstates, but we include a possible effect on $\sin 2\phi_1$ in the systematic error.

The p_B^{CMS} dependence of background components A, B, and C (with A subdivided by decay channel), is shown in figure to follow ECL-only candidates. In the calculation of f_A , f_B , and f_C , the smooth functions shown in the figures are used. Since only events in the signal region $0.2 < p_B^{\text{CMS}} < 0.45$ GeV/ c are used in the CP fit, agreement between these functions and the actual distributions outside the signal region is not important.

CP-fit of $J/\psi K_L$ candidates from charmonium MC

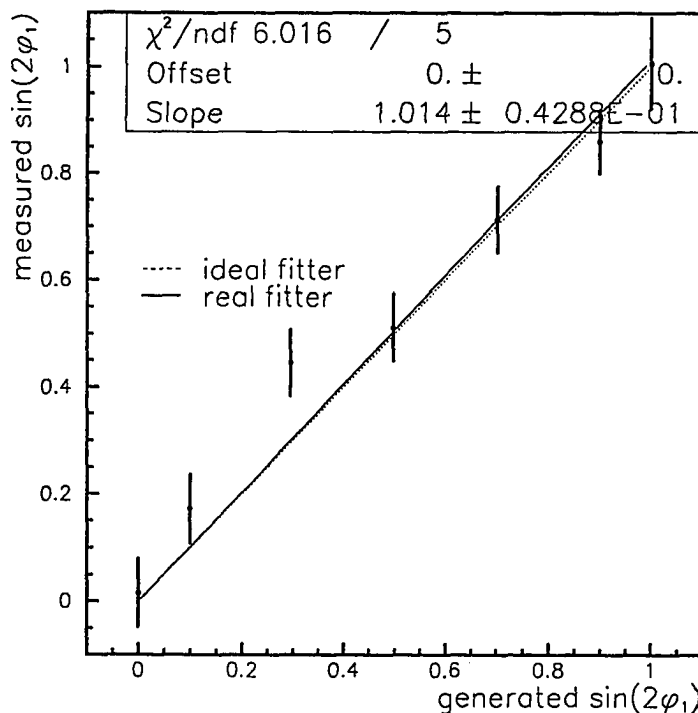


Figure 6.6: Monte Carlo test of the background model used in the CP fit. The five data points show the generated (horizontal) and fitted (vertical) values of $\sin 2\phi_1$ for each Monte Carlo sample. The solid line is the result of a fit to the data points, using a straight line that is confined to go through the origin. A dotted line with slope 1 is drawn for reference. For instance, bias due to omitting important CP eigenstates in the background treatment, would likely result in the solid line having a slope different from unity. The result is consistent with no such bias.

6.3.4 A Final Check

In the end, the background model is quite complicated, but all its ingredients have been well tested. Tagging and vertexing have been independently verified using experimental data, as described earlier in this chapter. Checks of the validity of our charmonium inclusive Monte Carlo have been presented in chapter 5. The normalizations obtained from the p_B^{CMS} fit have been checked in chapter 5.8.

We here provide one final check, to safeguard against trivial mistakes in the implementation, when all these ingredients are combined. Since the same CP fitter is used to measure $\sin 2\phi_1$ in many different decay channels, it has been extensively tested by the collaboration for linearity and fit bias. The purpose of our check is to test that the rescaling procedure of the different background components, which is specific for $B^0 \rightarrow J/\psi K_L$, is implemented correctly, and that omitting the less frequent CP -eigenstate backgrounds in this scheme does not lead to any fit bias. We perform a fit for $\sin 2\phi_1$ using five samples of charmonium inclusive Monte Carlo events. Each sample is subjected to the $B^0 \rightarrow J/\psi K_L$ event selection. The overall normalization of signal, background with a true K_L , and background with a fake K_L in each sample, is taken from the Monte Carlo (rather than doing p_B^{CMS} fits), in order to minimize the statistical errors in our check. Since this is Monte Carlo, we don't have a combinatorial J/ψ component. The result of the five CP fits is summarized in figure 6.6, which shows measured versus generated $\sin 2\phi_1$ values for the five samples. A fit for the slope of the five data point gives 1.014 ± 0.04 . An ideal fitter with infinite Monte Carlo statistics would yield unity slope. We conclude that we see no significant bias from our background model.

6.4 Fit for the Time Dependent CP Asymmetry

Finally, we measure $\sin 2\phi_1$ with an unbinned maximum-likelihood fit to the Δt distribution in experimental data. Each of the 1230 candidate events that survived flavor tagging and vertexing, is assigned a likelihood value, P_i , using equation 6.10. For particle properties entering the PDF, such as Δm_d and $\tau_{B_d^0}$, we use the world average values from 2002 [8]. Each likelihood value also depends on $\sin 2\phi_1$. We vary $\sin 2\phi_1$ in the PDF to maximize the combined likelihood of all signal candidates, given by

$$L = \prod_{i=1}^{i=1230} P_i(\sin 2\phi_1, \Delta t, \dots), \quad (6.11)$$

while all other parameters of P_i are held constant. The value with the highest likelihood is

$$\sin 2\phi_1 = 0.77 \pm 0.16 \text{ (statistical)} \pm 0.07 \text{ (systematic)}. \quad (6.12)$$

The quoted statistical error is obtained from the values of $\sin 2\phi_1$ where $-2 \ln L$ increases 1.0 over its minimum. The likelihood curve is shown in figure 6.7. The evaluation of the systematic error is presented in the next chapter. The significance of our result, and relation to other measurements, is discussed in chapter 8. There is no one way to visualize the result of an unbinned likelihood fit, but we show two possibilities in figures 6.8 and 6.9.

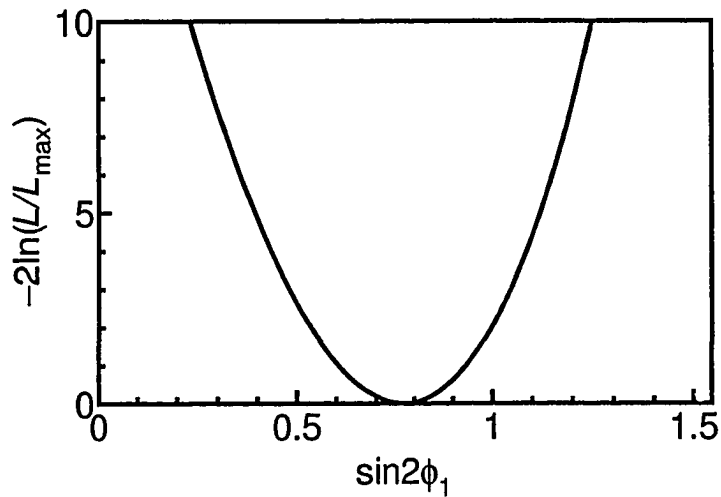


Figure 6.7: Likelihood value, L , versus $\sin 2\phi_1$.

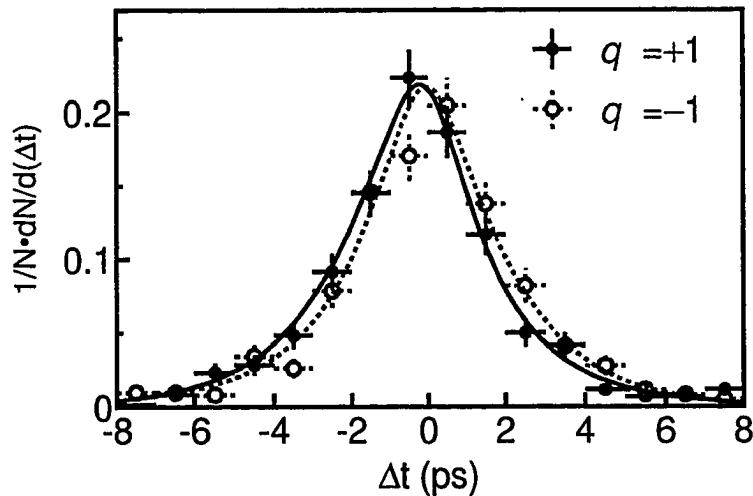


Figure 6.8: The Δt distribution for 1230 $J/\psi K_L$ candidates found in Belle experiments 7 through 19. Events classified as $B_d^0 \rightarrow J/\psi K_L$ ($q = -1$) are shown as hollow data points with errors, while events classified as $B_d^0 \rightarrow J/\psi K_L$ ($q = +1$) are shown as filled data points with errors. The superimposed curves show the sum of the fitting PDFs used for the two event classes, evaluated with $\sin 2\phi_1$ equal to our final result. The displacement of the two curves is a consequence of CP violation.

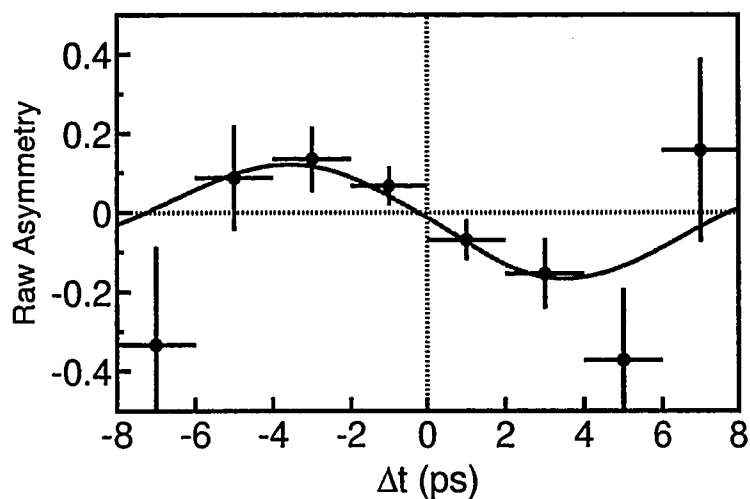


Figure 6.9: The time-dependent “raw” CP asymmetry, $A(\Delta t)$, obtained from 1230 $B^0 \rightarrow J/\psi K_L$ candidates found in Belle experiments 7 through 19. The superimposed curve shows the sum of the fitting PDFs used for each event, evaluated with $\sin 2\phi_1$ equal to our final result. The amplitude of this curve is proportional to the observed CP violation.

Chapter 7

Systematic Uncertainties

In this chapter, we examine how the observed $\sin 2\phi_1$ -value depends on the parameters of the fitting PDF, and on cuts that affect the Δt distribution. We increase and decrease each experimentally measured parameter in the PDF by one standard deviation, repeat the fit for $\sin 2\phi_1$, and record the resulting deviation in the fit result. Parameters estimated from Monte Carlo are varied by two standard deviations. For cuts, the procedure differs from case to case. Table 7.1 gives a summary of the observed deviations in $\sin 2\phi_1$. By adding these in quadrature, we obtain the total systematic error:

$$\sigma_{\text{sys}} = 0.07. \tag{7.1}$$

Below, we give more details regarding cuts and parameters we have considered.

| class of parameters | systematic error |
|------------------------|------------------|
| signal purity | 0.050 |
| BG composition | 0.034 |
| vertex reconstruction | 0.024 |
| resolution function | 0.023 |
| fit bias | 0.011 |
| wrong-tag fractions | 0.009 |
| physics parameters | 0.008 |
| BG shape in Δt | 0.005 |
| total | 0.07 |

Table 7.1: Contributions to the systematic error on $\sin 2\phi_1$. Each entry shows the cumulative uncertainty arising from a class of cuts and parameters used toward the CP fit.

7.0.1 Signal purity

The signal purity depends on the normalization of four components: signal, background with true K_L 's, background with fake K_L 's, and background with fake J/ψ 's. The first three of these were determined simultaneously from a fit to the observed p_B^{CMS} spectrum. Since the total normalization of signal and background is constrained to the observed number of events in this fit, any two of these normalizations are anti-correlated. We take this into account as follows: we repeat the p_B^{CMS} fit several times, with each of these three normalizations in turn fixed to $\mu \pm \sigma$, where μ and σ are the nominal normalizations and their statistical errors, given in tables 5.6 and 5.7. We thus obtain several new sets of signal and background normalizations, and repeat the fit for $\sin 2\phi_1$ with these. The resulting deviations in $\sin 2\phi_1$ are given in table 7.2. The largest deviations seen, $^{+0.016}_{-0.017}$ for KLM candidates, and $^{+0.013}_{-0.021}$ for ECL-only candidates, are taken as the systematic error.

| parameter | variation | $\Delta \sin 2\phi_1$ (KLM) | $\Delta \sin 2\phi_1$ (ECL) |
|--------------------------|-------------------------------|-----------------------------|-----------------------------|
| signal | $-\sigma$ | 0.016 | 0.007 |
| signal | $+\sigma$ | -0.017 | -0.021 |
| BG w/ true K_L | $-\sigma$ | -0.014 | -0.012 |
| BG w/ true K_L | $+\sigma$ | 0.013 | 0.013 |
| BG w/ fake K_L | $-\sigma$ | -0.008 | 0.006 |
| BG w/ fake K_L | $+\sigma$ | 0.007 | -0.005 |
| BG w/ fake J/ψ | $-\sigma$ | 0.001 | -0.003 |
| BG w/ fake J/ψ | $+\sigma$ | -0.003 | -0.006 |
| p_B^{CMS} range | exclude $< 0.2 \text{ GeV}/c$ | 0.016 | 0.020 |
| signal peak | fixed | 0.038 | 0.0 |

Table 7.2: Deviations in $\sin 2\phi_1$ when the signal and background normalizations are varied by their statistical uncertainties, or obtained with an alternative yield fit. See text for further explanation.

The normalization of background with fake J/ψ 's was estimated from the J/ψ invariant mass spectrum. In addition to the statistical uncertainty from that fit, we have the uncertainty due to a possible background with true J/ψ 's from non- $\Upsilon(4S)$ events. We vary the fake J/ψ component by $\pm\sigma$ (which includes terms for both uncertainties), repeat the p_B^{CMS} fit, and then the CP fit. The observed deviation is added in quadrature to the systematic error associated with the other signal and background components.

We saw in the chapter 5 that the p_B^{CMS} shapes of signal and background shapes are generally well described by Monte Carlo, but noticed a potential discrepancy in the region $p_B^{\text{CMS}} < 0.2 \text{ GeV}/c$. To evaluate possible bias from this, we repeat the p_B^{CMS} fit, excluding this region. We thus obtain a new set of signal and background normalizations, and repeat the fit for $\sin 2\phi_1$ with these.

In the nominal p_B^{CMS} fit, we allow the signal peak to move in p_B^{CMS} . In the case of ECL-only candidates, the peak fitted peak position equals the Monte

Carlo prediction, while we observe a shift of 11 ± 4 MeV/ c for KLM candidates. We repeat the p_B^{CMS} fit with the signal peak position fixed to the Monte Carlo prediction. We repeat the CP fit with the resulting normalizations, and include the change in $\sin 2\phi_1$ in the systematic error.

7.0.2 Vertex Reconstruction

We check for bias due to outliers by repeating the CP fit without the nominal cut $\Delta t < 70$ ps, and also by tightening it to $\Delta t < 5$ ps.

The assignment of vertex errors involves a scale factor. We study its effect by repeating the CP fit with the scale factor to unity.

We consider the effects of the vertex-quality cut by varying it from $\xi < 50$ to $\xi < 200$.

We relax and tighten the track-quality criterion for the tag-side vertex reconstruction by 10%.

Charge-dependent bias of tracks' z -position measurement could result in a detector-induced CP asymmetry. We estimate that the position bias is small (± 3 μm), using cosmic rays and $\gamma\gamma \rightarrow \rho^0\rho^0 \rightarrow \pi^+\pi^-\pi^+\pi^-$ events. We study the effect on $\sin 2\phi_1$ by repeating the CP fit with the track's z positions shifted by ± 3 μm . We find the effect on $\sin 2\phi_1$ negligible (0.002).

The transverse smearing of the IP constraint is varied by ± 10 μm . The change in $\sin 2\phi_1$ is found to be negligible (0.001).

7.0.3 Wrong-tag Fractions

We repeat the CP fit, with the wrong-tag fraction of each r bin in turn varied by its error, given in table 6.1. The observed deviations in $\sin 2\phi_1$ are added in quadrature.

We also consider deviations due to a charge asymmetry in the wrong tag fractions by repeating the fit with charge dependent wrong-tag fractions.

7.0.4 Resolution Function

All parameters of the resolution function are in turn varied by $\pm\sigma$ ($\pm 2\sigma$ for parameters determined from Monte Carlo), and the CP fit is repeated. The observed deviations in $\sin 2\phi_1$ are added in quadrature.

We also check the dependence on the functional form of the resolution function, by using a different parameterization, and repeating the fit.

7.0.5 Possible Fit Bias

In section 6.3.4 we checked against bias due to omitting rare CP eigenstates in the background treatment, and measured bias on the level of $1.4 \pm 4.3\%$ of the central value, consistent with no bias. We assign 1.4% of our observed $\sin 2\phi_1$ value, 0.011, as a systematic error due to possible fit bias. This error includes the effect of a difference between the wrong-tag fractions in $B^0 \rightarrow J/\psi K_L$ decays and in the flavor-specific B decays used to measure the wrong tag fractions. This error also includes misalignment effects, since these are included in the Monte Carlo.

7.0.6 Δt shape of background

The effective lifetime of the background from charged B decays was determined to be $\tau_{B^+}^{\text{eff}} = 1.558 \pm 0.026$ ps from a Monte Carlo simulation. Is it varied by twice its error.

Parameters describing the Δt shape of the combinatorial background are varied by their errors.

7.0.7 Background composition / Individual background modes

We consider systematic effects from uncertainties in the normalization and p_B^{CMS} shape of individual background modes, in particular CP eigenstates, which were determined from Monte Carlo. We vary all parameters describing the p_B^{CMS} distributions of individual modes by twice their error. The observed deviations in $\sin 2\phi_1$ are added in quadrature.

7.0.8 Physics Parameters

In the nominal CP fit, the neutral B meson lifetime, mass, and mixing parameter are held fixed at their world average values; $\tau_{B^0} = 1.542 \pm 0.016$ ps, $m_{B^0} = 5.2794 \pm 0.0005$ GeV/ c^2 , $\Delta m_d = 0.489 \pm 0.008$ [8]. Each parameter is varied by its error.

The effective CP eigenvalue of $J/\psi K^{*0}(K_L\pi^0)$ decays, $\eta_f = -0.62 \pm 0.11$ [37], is varied by its error.

Chapter 8

Discussion of the Result

Using 78 fb^{-1} of e^+e^- collision data, collected with the Belle detector at the KEKB accelerator, we reconstructed 1330 $B^0 \rightarrow J/\psi K_L$ candidates, with an estimated signal purity of $62 \pm 3\%$. Using 1230 of these candidates, we measured

$$\sin 2\phi_1 = 0.77 \pm 0.16 \text{ (statistical)} \pm 0.07 \text{ (systematic)}. \quad (8.1)$$

8.1 Relation to Published Belle Measurements

Using the same data sample as in this thesis, the Belle collaboration has published a measurement of $\sin 2\phi_1$ based on several decay channels of the B_d^0 meson[24]. The author of this thesis was responsible for the $B^0 \rightarrow J/\psi K_L$ selection and related aspects of that measurement, and this thesis is to a large degree a detailed account of the author's work towards that result.

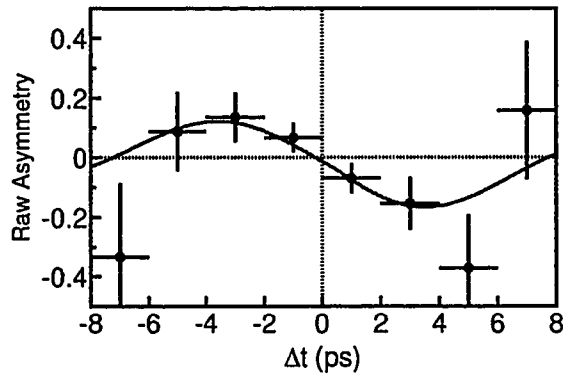
As there has been time for minor refinements and further cross-checks while writing this thesis, the analysis presented here differs in some details from that

in [24]. For instance, in this work we used the J/ψ mass spectrum to constrain the normalization of the fake J/ψ component. This allowed us to hold this component fixed in the p_B^{CMS} fit, resulting in smaller errors on the J/ψ -inclusive background normalization. The candidate event sample in [24] and this thesis are identical, and the measured value of $\sin 2\phi_1$ using $B^0 \rightarrow J/\psi K_L$ candidates has remained virtually unchanged, from $\sin 2\phi_1 = 0.78 \pm 0.17$ (stat.) in [24], to $\sin 2\phi_1 = 0.77 \pm 0.16$ (stat.) in this thesis.

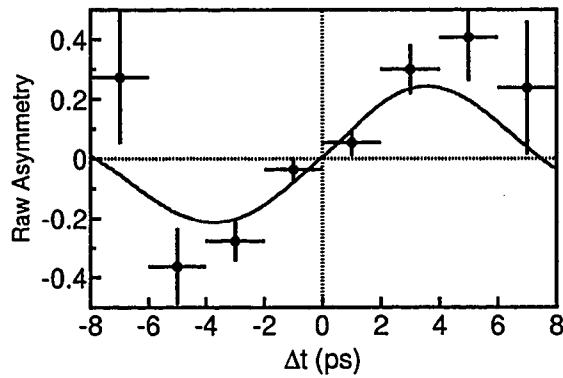
Figure 8.1 shows the CP asymmetry we observed in $B^0 \rightarrow J/\psi K_L$ decays ($\eta_{CP} = +1$), together with the asymmetry in $B \rightarrow (c\bar{c}) K_S$ decays ($\eta_{CP} = -1$) and the asymmetry in non- CP eigenstate decays ($B^0 \rightarrow D^{(*)-}\pi^+, D^{*-}\rho^+, J/\psi K^{*0}(K^+\pi^-), D^{*-}l^+\nu$) from [24]. We showed in chapter 2 that the CP asymmetries in $B^0 \rightarrow J/\psi K_L$ and $B \rightarrow (c\bar{c}) K_S$ decays are expected to be equal in magnitude, but opposite in sign. The opposite sign is clearly observed, and the measured values of $\sin 2\phi_1$ are consistent. Note that the raw asymmetries shown are diluted by backgrounds in the event samples. The amplitude of the fitted curves is thus smaller than $\sin 2\phi_1$, and cannot be directly compared between the plots, since the background fractions differ. The asymmetry in the control sample is consistent with zero, as expected.

The combined Belle result, obtained from a simultaneous unbinned maximum likelihood fit to all $\eta_{CP} = +1$, $\eta_{CP} = -1$, and $J/\psi K^{*0}(K_S\pi^0)$ decays, is $\sin 2\phi_1 = 0.719 \pm 0.074(\text{stat.}) \pm 0.035(\text{syst.})$ [24].

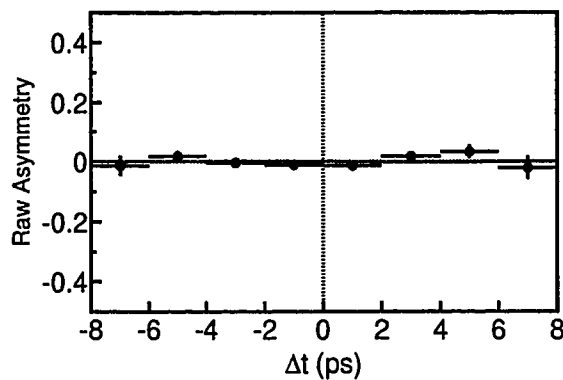
Based on theoretical expectation, our measurement of $\sin 2\phi_1$ has assumed the absence of direct CP violation, i.e. that $|\lambda| = 1$. We performed a fit for the amplitude \mathcal{S} of a CP asymmetry of the form $\mathcal{S} \sin(\Delta m_d \Delta t)$, and if $|\lambda| = 1$



(a) $B^0 \rightarrow J/\psi K_L$: $\sin 2\phi_1 = 0.77 \pm 0.16$



(b) $B \rightarrow c\bar{c} K_S$: $\sin 2\phi_1 = 0.72 \pm 0.08$



(c) control sample: " $\sin 2\phi_1$ " = 0.005 ± 0.015

Figure 8.1: Observed (raw) CP asymmetries in $B^0 \rightarrow J/\psi K_L$ decays ($\eta_{CP} = +1$), $B \rightarrow (c\bar{c}) K_S$ ($\eta_{CP} = -1$), and a control sample of decays into non- CP eigenstates.

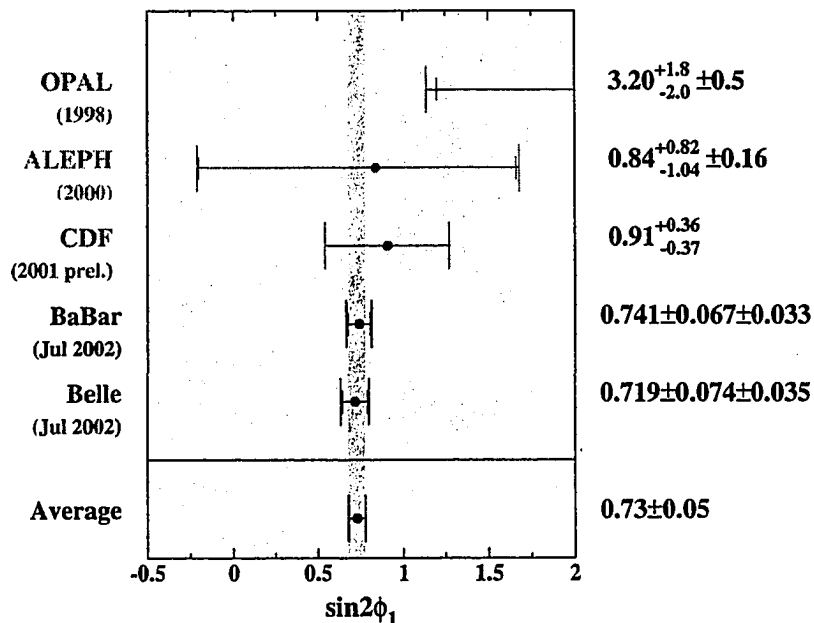


Figure 8.2: Comparison with other experiments

holds, then $\mathcal{S} = \text{Im}\lambda = \sin 2\phi_1$. This assumption has been verified by [24], where a simultaneous fit for $|\lambda|$ and $\text{Im}\lambda$ yielded $|\lambda| = 0.950 \pm 0.049$ (stat.) ± 0.025 (syst.).

8.2 Other measurements of $\sin 2\phi_1$

The other statistically significant measurement of $\sin 2\phi_1$ comes from the BaBar experiment, and is in good agreement with Belle's. The most recent results from different experiments are shown in figure 8.2. The average of these is $\sin 2\phi_1 = 0.73 \pm 0.05$.

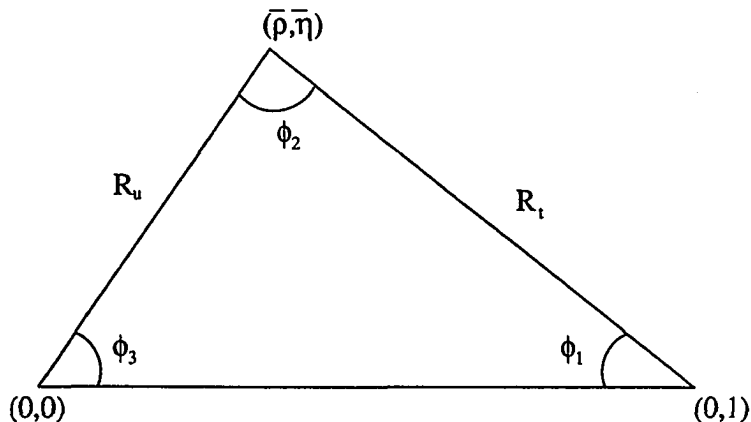


Figure 8.3: The rescaled unitarity triangle

8.3 Experimental Status of the Unitarity triangle

The world-average value of $\sin 2\phi_1$ has now reached a precision that allows a comparison with other measurements that probe the CKM matrix, in order to check the consistency of the KM model.

This is done by considering how different measurements constrain the unitarity triangle, introduced in section 2.4.3. The rescaled version of this triangle, is shown in figure 8.3. In the Wolfenstein approximation, the apex of this triangle is located at $(\bar{\rho} + i\bar{\eta})$ in the complex plane. Figure 8.4 shows the preferred values of $\bar{\rho}$ and $\bar{\eta}$ for different classes of measurements, represented by bands of different colors. This plot is generated by the CKM fitter group [38]. We will discuss the constraints shown briefly.

The two legs of the rescaled unitarity triangle that are not on the real axis

have lengths

$$R_u = \left| \frac{V_{ud}V_{ub}^*}{V_{cd}V_{cb}^*} \right| \approx \sqrt{\rho^2 + \bar{\eta}^2} \approx (1 - \lambda^2/2) \frac{1}{\lambda} \left| \frac{V_{ub}}{V_{cb}} \right| \quad \text{and} \quad (8.2)$$

$$R_t = \left| \frac{V_{td}V_{tb}^*}{V_{cd}V_{cb}^*} \right| \approx \sqrt{(1 - \bar{\rho})^2 + \bar{\eta}^2} \approx \frac{1}{\lambda} \left| \frac{V_{td}}{V_{cb}} \right|. \quad (8.3)$$

The absolute values of CKM-matrix elements, and hence the length of these two legs, can be measured using flavor-changing, CP -conserving processes. The least well measured elements, which limit the precision of the unitarity triangle are ¹

- $|V_{ub}| = (3.6 \pm 0.7) \times 10^{-3}$ is measured using inclusive and exclusive semileptonic B decays, involving the $b \rightarrow u$ transition. The dominant part of the error is theoretical.
- $|V_{cb}| = (41.2 \pm 2.0) \times 10^{-3}$ is measured using inclusive and exclusive semileptonic B decays involving the $b \rightarrow c$ transition.
- $|V_{td}|$ can be obtained from B mesons mixing measurements. For instance, B_d^0 meson mixing is governed by the box diagram in figure 2.4, so that $\Delta m_d \propto |V_{tb}^*V_{td}|$. The world average $\Delta m_d = 0.489 \pm 0.008$ can thus be turned into the CKM constraint $|V_{tb}^*V_{td}| = 0.0079 \pm 0.0015$, where the larger uncertainty in the latter is due to imprecisely known hadronic matrix elements. This uncertainty can be reduced when the B_s mixing frequency is known as well. Although Δm_s has not yet been measured, the present limit can be used to constrain V_{td} further, also shown in figure 8.4.

¹The values quoted are the world averages from 2002 [8]. The CKM fitter group uses slightly different values, see [38] for details.

In the KM model, measurement of CP violating processes yield direct measurements of CKM phases. A specific value of ϵ (which denotes indirect CP violation in the neutral K system—see equation 2.9) constrains the apex on the unitarity angle to lie on a hyperbola [5]. Although the measurement error on ϵ is small, the hyperbola has large width due to imprecisely known hadronic matrix elements.

Finally, as shown in chapter 2 the measurement of CP asymmetries in B decays to CP eigenstates that proceed via the $b \rightarrow c\bar{c}s$ transition tells us $\sin 2\phi_1$, with ϕ_1 being one of the inner angles of the unitarity triangle. Each measured value $\sin 2\phi_1$ corresponds to four possible values of ϕ_1 .

When we compare the regions of \bar{p} and $\bar{\eta}$ pointed to by CP -conserving and CP -violating measurements, we find that they agree well. One of the solutions for ϕ_1 that corresponds to the current world average $\sin 2\phi_1$, is in excellent agreement with the value expected based on the value of ϵ , and measurements of CKM matrix elements. The KM-model is thus able to give a consistent description of all calculable CP violating phenomena that have been observed to date.

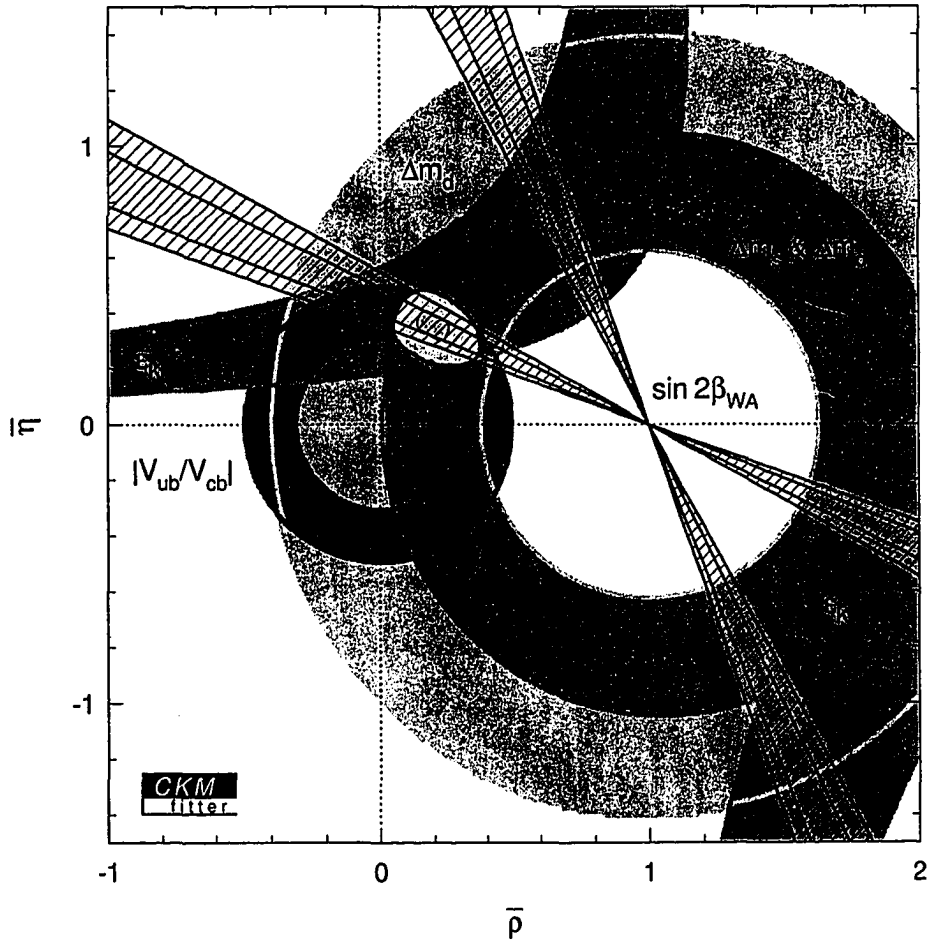


Figure 8.4: $\bar{\rho}-\bar{\eta}$ plane with constraints from different measurements. The hatched areas are the four ϕ_1 solutions that correspond to the 68% and 95% confidence-level intervals of the world-average $\sin 2\phi_1$. The 95% confidence-level regions from other measurements are shown shaded.

Appendix A

Appendix Theory

A.1 Neutral B Meson Mixing

The neutral meson pairs $B_s^0\overline{B}_s^0$, $B_d^0\overline{B}_d^0$, $D^0\overline{D}^0$, and $K^0\overline{K}^0$, are the only relatively long lived mesons for which the Standard Model predicts the phenomenon known as mixing. Mixing denotes the fact that any of these eight mesons with time will evolve into a state which includes an admixture of its antiparticle. We will here look at mixing in the B_d^0 meson system (we'll omit the explicit d subscript from now on), following the discussion in [13]. The treatment of the B_s^0 , D^0 and K^0 systems is similar.

A state describing an admixture of a neutral B^0 meson and its antiparticle \overline{B}^0 can be described using a basis of only two eigenstates. In the $B^0\overline{B}^0$ basis, the

time evolution is given by

$$i\frac{\partial}{\partial t} \begin{bmatrix} a(t) \\ \bar{a}(t) \end{bmatrix} = \mathcal{M} \begin{bmatrix} a(t) \\ \bar{a}(t) \end{bmatrix}, \quad (\text{A.1})$$

where $a(t)$ and $\bar{a}(t)$ are the amplitudes for measuring a B^0 and a \bar{B}^0 , respectively, at time t , and \mathcal{M} is the neutral B meson mass matrix

$$\mathcal{M} = \begin{bmatrix} \mathcal{M}_{11} & \mathcal{M}_{12} \\ \mathcal{M}_{21} & \mathcal{M}_{22} \end{bmatrix}. \quad (\text{A.2})$$

This matrix is the effective Hamiltonian of the system. Since both B meson components decay with time, the matrix is not Hermitian, and its eigenvalues, λ_H and λ_L , will be complex numbers. The mass eigenstates, $|B_H\rangle$ and $|B_L\rangle$, are by definition the particular linear combinations of B_d^0 and \bar{B}_d^0 that don't mix with time, but have the following simple time dependence:

$$|B(t)\rangle = |B_H\rangle e^{-i\lambda_H t} + |B_L\rangle e^{-i\lambda_L t} \quad (\text{A.3})$$

$|B_H\rangle$ and $|B_L\rangle$ are thus the eigenvectors of \mathcal{M} , with λ_H and λ_L as their respective eigenvalues. We see from equation A.3 that the real part of the eigenvalues is the mass of the mass eigenstates, while the complex part of the eigenvalues is the width of the mass eigenstates. The diagonal elements of \mathcal{M} can be written $\mathcal{M}_{11} = m_{B^0} - i\Gamma_{B^0}/2$ and $\mathcal{M}_{22} = m_{\bar{B}^0} - i\Gamma_{\bar{B}^0}/2$. It can be shown that CPT invariance implies $\mathcal{M}_{11} = \mathcal{M}_{22}$. If we consider the real and complex parts separately, this is the more familiar statement that a particle and its antiparticle

must have equal masses and lifetimes. The off-diagonal matrix elements contain the transition amplitudes for $B^0 \rightarrow \overline{B^0}$ and vice versa.

Imposing only CPT symmetry, we can thus solve for the complex eigenvalues of \mathcal{M} :

$$\lambda_{H/L} \equiv m_{H/L} - \frac{i}{2}\Gamma_{H/L} = m_{B^0} - i\Gamma_{B^0}/2 \pm \sqrt{\mathcal{M}_{12}\mathcal{M}_{21}}. \quad (\text{A.4})$$

We can then solve for the eigenvectors, which will be the mass eigenstates:

$$|B_L\rangle = p|B^0\rangle + q|\overline{B^0}\rangle, \quad (\text{A.5})$$

$$|B_H\rangle = p|B^0\rangle - q|\overline{B^0}\rangle, \quad (\text{A.6})$$

with

$$\frac{q}{p} = \mp \sqrt{\frac{\mathcal{M}_{21}}{\mathcal{M}_{12}}} \quad (\text{A.7})$$

Let us consider q/p in two cases: First, assuming the Hamiltonian is CP invariant as well (no CP violation in the mixing processes), we have $\mathcal{M}_{12} = \mathcal{M}_{21}$, giving $q/p = \mp 1$, and the eigenstates of \mathcal{M} become $\frac{1}{\sqrt{2}}(|B^0\rangle + |\overline{B^0}\rangle)$ and $\frac{1}{\sqrt{2}}(|B^0\rangle - |\overline{B^0}\rangle)$, which are exactly the CP eigenstates. So in the absence of CP violation, the mass eigenstates will also be CP eigenstates.

Second, in the Standard Model, the box diagrams of fig. A.1 are thought to dominate the mixing transition $B^0 \rightarrow \overline{B^0}$, while the CP conjugate diagrams are responsible for $\overline{B^0} \rightarrow B^0$. From this, it is expected that $\mathcal{M}_{12} = \mathcal{M}_{21}^*$. In this case, $\mathcal{M}_{12}\mathcal{M}_{21}$ is real and positive, so that the square-root in eq. A.4 is real and positive. Equating the complex parts of eq. A.4, we discover that the two mass

eigenstates have equal decay rates, so that

$$\Delta\Gamma = \Gamma_H - \Gamma_L = 0. \quad (\text{A.8})$$

$\Delta\Gamma/\Gamma \approx 0$ is thought to be a safe prediction, even if the diagrams in fig. A.1 don't dominate the mixing. The reason is that, unlike the neutral kaon system, neither B mass eigenstate has a decay mode with appreciable partial width (i.e. a large fraction of the total width), that is unavailable to the other mass eigenstate.

Finally, if the diagrams of fig. A.1 dominate the mixing, then the complex phase of \mathcal{M}_{12} is due to CKM matrix elements appearing in them, while the complex conjugate CKM matrix elements appear in \mathcal{M}_{21} . (See section 2.4.) Using the eigenvalues of eq. A.4 to find the eigenvectors of \mathcal{M} , we obtain that neutral B meson mass eigenstates in this case are given by

$$|B_{H/L}\rangle = |B^0\rangle \pm e^{-i\phi_{MIX}} |\overline{B^0}\rangle, \quad (\text{A.9})$$

where ϕ_{MIX} is the weak mixing phase

$$\phi_{MIX} = \arg(V_{TB}^* V_{TD}). \quad (\text{A.10})$$

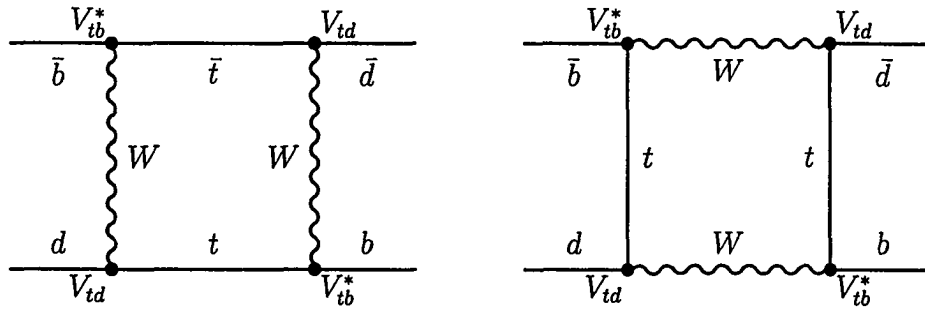


Figure A.1: The two weak interaction box diagrams which carry the main contribution to the $B\bar{B}$ mixing amplitude. The weak phase shift for $B \rightarrow \bar{B}$ via any of these diagrams will be $\phi_{MIX} = \arg(V_{TB}^* V_{TD})$.

A.1.1 Time Evolution of an Initially Pure Flavor Eigenstate

Consider a B^0 meson that starts out in a state of pure flavor, i.e. either as a B_d^0 or a \bar{B}_d^0 , at $t = 0$. Since the mass eigenstates have the simplest time-dependance, we invert equation A.6 to get

$$|B^0\rangle = \frac{1}{2p} (|B_L\rangle + |B_H\rangle) \quad \text{and} \quad (\text{A.11})$$

$$|\bar{B}^0\rangle = \frac{1}{2q} (|B_L\rangle - |B_H\rangle). \quad (\text{A.12})$$

In the meson's rest frame, the time evolution for $t > 0$ is then given by

$$|B^0(t)\rangle = \frac{e^{-\Gamma t/2}}{2p} (e^{-im_L t} |B_L\rangle + e^{-im_H t} |B_H\rangle) \quad \text{and} \quad (\text{A.13})$$

$$|\bar{B}^0(t)\rangle = \frac{e^{-\Gamma t/2}}{2q} (e^{-im_L t} |B_L\rangle - e^{-im_H t} |B_H\rangle), \quad (\text{A.14})$$

where we have used the same decay rate Γ for both neutral B mesons, as justified in the previous section. Since these states decay via their B_d^0 and \bar{B}_d^0 components,

it is useful to rewrite the time-dependant states in terms of these:

$$|B^0(t)\rangle = e^{-\Gamma t/2} e^{-i\bar{m}t} \left(\cos(\Delta mt/2) |B^0\rangle + i\frac{q}{p} \sin(\Delta mt/2) |\bar{B}^0\rangle \right), \quad (\text{A.15})$$

$$|\bar{B}^0(t)\rangle = e^{-\Gamma t/2} e^{-i\bar{m}t} \left(i\frac{p}{q} \sin(\Delta mt/2) |B^0\rangle + \cos(\Delta mt/2) |\bar{B}^0\rangle \right), \quad (\text{A.16})$$

where $\bar{m} = \frac{1}{2}(m_H + m_L)$, $\Delta m = m_H - m_L$.

A.2 Time Dependent Decay Rates of an Initially Pure Flavor Eigenstates

Given the time dependence of an initial B_d^0 or \bar{B}_d^0 in equation A.15, we derive the decay-time distribution for final states relevant to our analysis.

A.2.1 Decay into a Flavor Specific Final State

Some decay products can only be produced by either the B_d^0 or \bar{B}_d^0 component of a neutral B . Let us consider a final state f for which $\langle f|H|B^0\rangle \neq 0$ and $\langle \bar{f}|H|\bar{B}^0\rangle \neq 0$ but $\langle \bar{f}|H|B^0\rangle = 0$ and $\langle f|H|\bar{B}^0\rangle = 0$, where H is the weak interaction Hamiltonian. Although a pure B^0 at $t = 0$ cannot decay into \bar{f} , if we wait until $t > 0$, the B meson will acquire a \bar{B}^0 component via the mixing, and this component can in turn decay into \bar{f} . We call this a “mixed” or “opposite sign” (OS) decay. Its rate is readily obtained from equation A.15:

$$\Gamma_{\text{OS}} = \Gamma_{B^0(t) \rightarrow \bar{f}} = \left| \langle \bar{f}|H|B^0(t)\rangle \right|^2 = \left| \langle \bar{f}|H|\bar{B}^0\rangle \right|^2 e^{-\Gamma t} \left| \frac{q}{p} \right|^2 \sin^2 \left(\frac{\Delta mt}{2} \right). \quad (\text{A.17})$$

Similarly, the rate of unmixed or “same sign” (SS) decay of an initially pure B^0 is given by

$$\Gamma_{\text{SS}} = \Gamma_{B^0(t) \rightarrow f} = \left| \langle f | H | B^0(t) \rangle \right|^2 = \left| \langle f | H | B^0 \rangle \right|^2 e^{-\Gamma t} \cos^2 \left(\frac{\Delta m t}{2} \right). \quad (\text{A.18})$$

In time-dependent mixing analyses, such as the measurement of the wrong tag fractions w_t in our analysis, one makes use of the time dependent mixing asymmetry, $A(t) = (\Gamma_{\text{SS}} - \Gamma_{\text{OS}})/(\Gamma_{\text{SS}} + \Gamma_{\text{OS}})$. Let us assume $|q/p| = 1$ (no CP violation in the mixing), and $|\langle f | H | B^0 \rangle| = |\langle \bar{f} | H | \bar{B}^0 \rangle|$ (no CP violation in the decay amplitudes) for simplicity. If a certain fraction, w , of the B^0 decays are wrongly classified as \bar{B}^0 (and vice versa), then we have

$$\Gamma_{\text{OS}} \propto (1 - w) \sin^2 \left(\frac{\Delta m t}{2} \right) + w \cos^2 \left(\frac{\Delta m t}{2} \right) \quad \text{and} \quad (\text{A.19})$$

$$\Gamma_{\text{SS}} \propto (1 - w) \cos^2 \left(\frac{\Delta m t}{2} \right) + w \sin^2 \left(\frac{\Delta m t}{2} \right), \quad (\text{A.20})$$

which gives

$$A(t) = (1 - 2w) \left[\cos^2 \left(\frac{\Delta m t}{2} \right) - \sin^2 \left(\frac{\Delta m t}{2} \right) \right] = (1 - 2w) \cos(\Delta m t). \quad (\text{A.21})$$

When flavor specific decays are used to measure the wrong tag fractions (see section 6.1.2), we have two B mesons per event. One B is fully reconstructed via a flavor specific final state, while the flavor of the other is determined using the flavor tagging algorithm. Since the B mesons from $\Upsilon(4S) \rightarrow BB$ have opposite flavor when the first one decays, same flavor decays means that one of the B 's underwent a mixed decay. Same flavor (SF) decays thus correspond to mixed

decays (OS) of one B , while opposite flavor (OF) decays correspond to unmixed (SS) decays of one B .

A.2.2 Decay into a CP Eigenstate, f_{CP}

CP eigenstates are special final states, because both the B^0 and the \bar{B}^0 component can decay into them. The time-dependent amplitude for an initially pure B^0 to decay into a CP eigenstate, f_{CP} , is therefore given by summing the amplitudes for the (in principle indistinguishable) contributing processes $B^0 \rightarrow f_{CP}$ and $B^0 \rightarrow \bar{B}^0 \rightarrow f_{CP}$:

$$A_{B^0(t) \rightarrow f_{CP}} = \langle f_{CP} | B^0 \rangle \langle B^0 | B^0(t) \rangle + \langle f_{CP} | \bar{B}^0 \rangle \langle \bar{B}^0 | B^0(t) \rangle \quad (\text{A.22})$$

$$= e^{-\Gamma t/2} e^{-i\bar{m}t} \left(A_f \cos(\Delta mt/2) + i \frac{q}{p} \bar{A}_f \sin(\Delta mt/2) \right), \quad (\text{A.23})$$

where we introduced the shorthand

$$A_f = \langle f_{CP} | H | B^0 \rangle \quad (\text{A.24})$$

$$\bar{A}_f = \langle f_{CP} | H | \bar{B}^0 \rangle. \quad (\text{A.25})$$

The time dependent decay rate is obtained by taking the amplitude squared. The final result can be written in the following simple form:

$$\Gamma_{B^0}(t) \sim e^{-\Gamma t} \left(1 + |\lambda_f|^2 + [1 - |\lambda_f|^2] \cos \Delta mt - 2 \text{Im} \lambda_f \sin(\Delta mt) \right), \quad (\text{A.26})$$

where

$$\lambda = \frac{q \bar{A}_f}{p A_f}. \quad (\text{A.27})$$

Similarly, starting with a pure \bar{B}^0 at $t = 0$, we obtain the time-dependent decay rate

$$\Gamma_{\bar{B}_d^0}(t) \sim e^{-\Gamma t} \left(1 + |\lambda_f|^2 - [1 - |\lambda_f|^2] \cos \Delta m t + 2 \text{Im} \lambda_f \sin(\Delta m t) \right). \quad (\text{A.28})$$

Appendix B

Appendix Other

B.1 Experimental Data Sample Used

The data used for this thesis originates from Experiment 7 through 19 at KEK, which took place from January 2000 through June 2002. At KEK, each fill of the accelerator is referred to as a “run” (with some exceptions we won’t get into). Each longer period of data taking, between shut-downs of the facility, is called an experiment. Tables B.1 and B.2 lists the data samples that were used in the present analysis, together with the corresponding luminosities. The luminosity estimates were kindly provided by Victor Zhilich [39].

B.2 Monte Carlo Sample Used

To study the acceptance of our analysis to $\Upsilon(4S) \rightarrow B\bar{B}$ decays with a real J/ψ in the final state, we generated a sample of 5 Million Monte Carlo events.

| Eperiment | dates of data taking | runs | Integ. luminosity [fb ⁻¹] | dst file version |
|--------------|----------------------|------|---------------------------------------|------------------|
| 7 | 13 Jan - 23 Jul 2000 | 2012 | 5.928 | b20020416 |
| 9 | 13 Oct - 17 Dec 2000 | 974 | 4.440 | b20020416 |
| 11 | 20 Jan - 21 Apr 2001 | 978 | 8.132 | b20020416 |
| 13 | 21 Apr - 16 Jul 2001 | 1206 | 10.739 | b20020416 |
| 15 | 06 Oct - 25 Dec 2001 | 904 | 12.682 | b20020405 |
| 17 | 18 Jan - 13 Mar 2002 | 659 | 11.181 | b20020416 |
| 19 | 15 Mar - 01 Jul 2002 | 1302 | 25.055 | b20020416 |
| sum of above | | | 78.13 ± 1.4% | |

Table B.1: On-resonance data used.

| Eperiment | dates of data taking | runs | Integ. luminosity [fb ⁻¹] | dst file version |
|--------------|----------------------|------|---------------------------------------|------------------|
| 7 | 13 Jan - 23 Jul 2000 | 154 | 0.594 | b20020416 |
| 11 | 20 Jan - 21 Apr 2001 | 134 | 1.211 | b20020416 |
| 13 | 21 Apr - 16 Jul 2001 | 126 | 1.203 | b20020416 |
| 15 | 06 Oct - 25 Dec 2001 | 94 | 1.411 | b20020405 |
| 17 | 18 Jan - 13 Mar 2002 | 55 | 0.853 | b20020416 |
| 19 | 15 Mar - 01 Jul 2002 | 202 | 3.575 | b20020416 |
| sum of above | | | 8.83 ± 1.4% | |

Table B.2: Off resonance data used. For experiment 9 we didn't take any off-resonance data.

| decay channel | BF, decay table | BF, word average |
|--|-----------------|------------------------|
| $B^0 \rightarrow J/\psi K^0$ | 8.9 | 8.7 ± 0.5 |
| $B^0 \rightarrow J/\psi K^{*0}$ | 14.9 | 13.1 ± 0.9 |
| $B^0 \rightarrow J/\psi \pi^0$ | 0.30 | 0.21 ± 0.05 |
| $B^0 \rightarrow J/\psi K(1270)^0$ | 14.5 | 13 ± 5 |
| $B^0 \rightarrow \psi(2S) K^0$ | 6.2 | 5.7 ± 1.0 |
| $B^0 \rightarrow \chi_{c1} K^0$ | 4.9 | $4.0^{+1.2}_{-1.0}$ |
| $B^\pm \rightarrow J/\psi K^{*\pm}$ | 14.9 | 13.9 ± 1.3 |
| $B^\pm \rightarrow J/\psi K^\pm$ | 8.9 | 10.1 ± 0.5 |
| $B^\pm \rightarrow J/\psi K(1270)^\pm$ | 14.5 | $18.0 \pm 3.4 \pm 3.9$ |

Table B.3: Branching fractions used in Monte Carlo generation, and their world average values, in units of 10^{-4} . Only the dominant $B^0 \rightarrow J/\psi K_L$ background modes are shown.

This sample, which we refer to as the “charmonium inclusive Monte Carlo”, was created as follows: A modified version of the BaBar collaboration’s “EvtGen” was used to create decay chains describing generic B decays. Only events with a true J/ψ at the generator level were kept and reconstructed. The final event sample thus contains J/ψ inclusive decays of charged and neutral B mesons, as well as feed-down from B decays to final states including higher charmonium resonances, such as $\psi(2S)$ and χ_{c1} . The interaction of particles with the detector material was simulated using GEANT3.

The branching fractions of the decay channels that are most relevant to our analysis are given in table B.3, along with the current world averages [8]. The ratio of charged to neutral B decays used in the event generation was unity.

Bibliography

- [1] J. H. Christenson, J. W. Cronin, V. L. Fitch and R. Turlay, *Phys. Rev. Lett.* **13**, 138 (1964).
- [2] A. D. Sakharov, *Pisma Zh. Eksp. Teor. Fiz.* **5**, 32 (1967).
- [3] A. Einstein, B. Podolsky and N. Rosen, *Phys. Rev.* **47**, 777 (1935).
- [4] I. I. Bigi and A. I. Sanda, *CP Violation* (Cambridge University Press, Cambridge, UK, 2000).
- [5] G. C. Branco, L. Lavoura and J. P. Silva, *CP Violation* (Carendon Press, Oxford, UK, 1999).
- [6] T. D. Lee and C.-N. Yang, *Phys. Rev.* **104**, 254 (1956).
- [7] C. S. Wu, E. Ambler, R. W. Hayward, D. D. Hoppes and R. P. Hudson, *Phys. Rev.* **105**, 1413 (1957).
- [8] K. Hagiwara *et al.*, *Physical Review D* **66**, 010001 (2002).
- [9] L. Wolfenstein, *Phys. Rev. Lett.* **13**, 562 (1964).
- [10] M. Kobayashi and T. Maskawa, *Prog. Theor. Phys.* **49**, 652 (1973).

- [11] A. Carter and A. I. Sanda, *Phys. Rev.* **D23**, 1567 (1981).
- [12] I. I. Bigi and A. I. Sanda, *Nucl. Phys.* **193**, 851 (1981).
- [13] B. Kayser, *Proceedings of Trieste Summer School in HEP and Cosmology* (June-July 1995).
- [14] L. Wolfenstein, *Phys. Rev. Lett.* **51**, 1945 (1983).
- [15] M. Yokoyama, private communication.
- [16] A. Abashian *et al.*, *Nucl. Instrum. Meth.* **A479**, 117 (2002).
- [17] V. Chabaud *et al.*, *Nucl. Instrum. Meth.* **A368**, 314 (1996).
- [18] Belle, G. Alimonti *et al.*, *Nucl. Instrum. Meth.* **A453**, 71 (2000).
- [19] D. H. Perkins, *Introduction to High Energy Physics* (Addison-Wesley, Reading, MA, 1982).
- [20] H. Hirano *et al.*, *Nucl. Instrum. Meth.* **A455**, 294 (2000).
- [21] T. Iijima *et al.*, *Nucl. Instrum. Meth.* **A453**, 321 (2000).
- [22] A. Tchouvikov *et al.*, Belle Note no. 580 (unpublished).
- [23] Belle, A. Abashian *et al.*, *Nucl. Instrum. Meth.* **A449**, 112 (2000).
- [24] Belle, K. Abe *et al.*, *Phys. Rev.* **D66**, 071102 (2002).
- [25] B. Casey, Belle Note no. 390 (unpublished).
- [26] G. C. Fox and S. Wolfram, *Phys. Rev. Lett.* **41**, 1581 (1978).

- [27] K. Hanagaki, H. Kakuno, H. Ikeda, T. Iijima and T. Tsukamoto, Nucl. Instrum. Meth. **A485**, 490 (2002).
- [28] L. Piilonen *et al.*, Belle Note no. 338 (unpublished).
- [29] A. V. Ershov, *Beauty meson decays to charmonium*, PhD thesis, Harvard University, 2001.
- [30] M. Yamaga, *Measurement of CP violation in $B^0 \rightarrow J/\psi + K_L$ decay at KEK B-factory*, PhD thesis, Tohoku University, 2001.
- [31] S. Banerjee and G. Majumder, Belle Note no. 515 (unpublished).
- [32] B. Casey, Belle Note no. 296 (unpublished).
- [33] S. Kumar, Belle Note no. 351 (unpublished).
- [34] H. Kakuno, Belle Note no. 384, to be submitted to Nucl. Instrum. Meth. (in preparation).
- [35] Belle, K. Abe *et al.*, Phys. Rev. **D66**, 032007 (2002).
- [36] Belle, K. Abe *et al.*, Phys. Rev. Lett. **88**, 171801 (2002).
- [37] Belle, K. Abe *et al.*, Phys. Lett. **B538**, 11 (2002).
- [38] A. Hocker, H. Lacker, S. Laplace and F. L. Diberder, European Physical Journal C **21**, 225 (2001).
- [39] D. Beylin *et al.*, Belle Note no. 465 (unpublished).